

Université du Québec  
Institut National de la Recherche Scientifique (INRS)  
Centre Énergie, Matériaux et Télécommunications (EMT)  
Università degli Studi di Palermo (UNIPA)  
Dipartimento di Ingegneria

## **INVESTIGATION, REALIZATION, AND ENTANGLEMENT CHARACTERIZATION OF COMPLEX OPTICAL QUANTUM STATES**

Par  
Stefania Sciara

Mémoire ou thèse présentée pour l'obtention du grade de  
Philosophiae doctor (Ph.D.)  
en sciences de l'énergie et des matériaux (INRS-EMT)  
et  
Information and Communication Technologies (ICT, UNIPA)

### **Jury d'évaluation**

Président du jury et examineur interne	Prof. Sergei Manzhos INRS-EMT
Examineur externe	Prof. Li Qian University of Toronto
Examineur externe	Prof. Daniel F. V. James University of Toronto
Directeur de recherche	Prof. Roberto Morandotti INRS-EMT
Codirecteur de recherche	Prof. Alfonso Carmelo Cino Università degli Studi di Palermo



*To my mom,  
who is my whole life.*

# Acknowledgement

First of all, I really thank my advisor at INRS-EMT Prof. Roberto Morandotti. His mentorship has been crucial for me to be a good scientist with clear ideas and targets, as well as to be an open-minded researcher, bold enough to pursue new research horizons. I also thank my advisor at University of Palermo Prof. Alfonso Carmelo Cino, who has been always present and willing despite the distance.

I am deeply grateful to Prof. Morandotti to give me the opportunity to study in a unique research institute, in which I could work as well as collaborate at a distance with excellent physicists and scientists. A special thanks goes to Prof. Michael Kues, whose presence, mentorship, and support have been extremely meaningful to me. The numerous discussions with him have helped me to broaden my research visions and thus to elaborate new ideas, while his moral support has taught me to never get discouraged in front of the many obstacles affecting research. I really want to thank Prof. William (Bill) J. Munro, a worldwide expert in quantum theory. It has been an honor, as well as crucial for my researcher formation, to collaborate with him. How can I forget the intricate and fruitful discussions we had about entanglement, cluster states, stabilizers, and witness? I would like to thank also Dr. Lucia Caspani, an excellent theoretician with whom I have had the greatest pleasure to exchange ideas. Finally, I cannot but thank my closest research colleagues Dr. Christian Reimer and Piotr Roztock, as well as our lab technician Rob Helsten.

Beyond the scientific results I have obtained during my PhD studies, I feel I have learnt an extremely important lesson, i.e. to be an independent researcher in quantum physics. This is mainly thanks to my advisor Roberto Morandotti, my research team and collaborators, who have always considered and welcomed my opinions and research ideas, giving me the chance to investigate the research directions I was proposing.

A very special thanks goes to my friends here at INRS for the great moments I have experienced with them throughout these years.

Last but not least, I would like to thank my family, who has always supported me despite the physical distance. My thought to them has been the fuel for me to keep going as well as to overcome the several obstacles I have met throughout these years. I really thank my sister Roberta, my brightest star, who has been a constant figure in my life, and her husband Salvo that I mostly consider a brother. My thoughts also go to Marianna,

a person who left us too soon. She will always be in our hearts. Special thanks go to my dad Michele, who is the lighthouse of my life. Finally, I foremost thank my mom Mariella, my whole life, the only person who has always understood and supported me despite everything and even when all other people turned me away. It is to my mom that I dedicate this thesis.

# Contents

<b>Résumé</b>	<b>i</b>
<b>Abstract</b>	<b>xviii</b>
<b>Sommario</b>	<b>xxiv</b>
<b>1 Introduction to quantum mechanics</b>	<b>1</b>
1.1 Fundamentals of quantum mechanics . . . . .	1
1.2 Formalism of quantum mechanics . . . . .	3
1.2.1 Dirac’s notation . . . . .	3
1.2.2 Observables, operators, and matrices . . . . .	5
1.3 Measurements in quantum mechanics . . . . .	6
1.4 Density matrix . . . . .	8
1.5 Qubits and qudits . . . . .	9
1.6 Quantum states of light: photons . . . . .	12
1.7 The Pauli matrices . . . . .	13
1.8 The generalized Pauli matrices . . . . .	16
<b>2 Entanglement</b>	<b>20</b>
2.1 The concept of entanglement . . . . .	20
2.2 The Bell states . . . . .	23
2.2.1 Two-level (qubit) Bell states . . . . .	24
2.2.2 Multi-level (qudit) Bell states . . . . .	25
2.2.3 Generating Bell states: SPDC and SFWM . . . . .	26
2.3 Bell’s inequality and Quantum Interference . . . . .	30
2.3.1 High-dimensional Bell inequalities . . . . .	34

2.4	Schmidt mode decomposition . . . . .	35
2.5	Multipartite entangled states . . . . .	37
2.5.1	Greenberger-Horne-Zeilinger (GHZ) states . . . . .	39
2.5.2	Hyper-entangled states . . . . .	40
2.6	Quantum state tomography . . . . .	41
<b>3</b>	<b>Cluster states</b>	<b>44</b>
3.1	Two-level (qubit) cluster states . . . . .	49
3.2	Stabilizer formalism for qubit cluster states . . . . .	49
3.3	Entanglement witness . . . . .	51
3.3.1	Entanglement witness for qubit cluster states . . . . .	53
3.3.2	Noise tolerance of qubit cluster states . . . . .	55
3.4	Multi-level (qudit) cluster states . . . . .	56
3.4.1	Stabilizer formalism for qudit cluster states . . . . .	57
<b>4</b>	<b>High-dimensional frequency-entangled photon pairs</b>	<b>60</b>
4.1	Generation of frequency-entanglement . . . . .	61
4.2	Quantum state analysis . . . . .	63
4.2.1	State dimensionality through Schmidt mode decomposition . . . . .	63
4.2.2	Quantum interference measurement . . . . .	68
4.2.3	Quantum state tomography . . . . .	71
4.2.4	Experimental scheme for quantum state manipulation . . . . .	72
<b>5</b>	<b>Universal multipartite <math>d</math>-level entanglement witness</b>	<b>79</b>
5.1	Approach for the witness derivation . . . . .	81
5.2	Entanglement witness for multipartite $d$ -level cluster states with two measurement settings . . . . .	84
5.2.1	Noise tolerance of multipartite $d$ -level cluster states . . . . .	87
5.3	Tailoring the witness to realistic measurement settings . . . . .	91
5.3.1	Application to optical cluster states given some measurement restrictions . . . . .	91
5.3.2	Detecting multi-level entanglement via two-level projections . . . . .	95

<b>6</b>	<b>Demonstration of a four-partite three-level photon cluster state</b>	<b>99</b>
6.1	Wave function of a four-partite three-level cluster state . . . . .	99
6.2	Cluster state realization . . . . .	101
6.2.1	Time- and frequency-bin hyper-entanglement . . . . .	102
6.2.2	Controlled phase gate for the cluster state realization . . . . .	107
6.3	Witness for four-partite three-level cluster states . . . . .	109
6.3.1	Stabilizers . . . . .	110
6.3.2	Entanglement witness . . . . .	111
6.3.3	Witness distribution and noise tolerance of cluster states . . . . .	114
6.4	One-way quantum computing operations . . . . .	117
	<b>Conclusions</b>	<b>125</b>
	<b>Conclusions</b>	<b>134</b>
	<b>Conclusioni</b>	<b>139</b>
<b>A</b>	<b>Origin of the Bell inequality for qubits</b>	<b>140</b>
<b>B</b>	<b>Origin of the Bell inequality for qudits</b>	<b>142</b>
<b>C</b>	<b>Examples of GHZ states</b>	<b>145</b>
<b>D</b>	<b>Quantum state tomography formalism</b>	<b>147</b>
<b>E</b>	<b>Examples of qubit cluster states</b>	<b>153</b>
<b>F</b>	<b>Witness for four-partite qubit cluster states</b>	<b>157</b>
<b>G</b>	<b>Examples of qudit cluster states</b>	<b>159</b>
<b>H</b>	<b>Projection measurements for quantum interference and quantum state tomography</b>	<b>161</b>
<b>I</b>	<b>Maximal eigenvalue of <math>\Theta</math></b>	<b>164</b>
<b>J</b>	<b>List of the 81 cluster state stabilizers</b>	<b>167</b>
	<b>List of publications in scientific journals</b>	<b>169</b>

List of presentations	172
List of conference proceedings	174
Bibliography	179

# List of Figures

1.1	Qubit state in the Bloch sphere . . . . .	10
2.1	Bell-type experiment with a polarization entangled two-photon state . . .	25
2.2	Generation and characterization of time-bin entanglement . . . . .	29
2.3	Convex set of multipartite separable and inseparable quantum states . .	39
3.1	Different structures of cluster states lattices . . . . .	45
3.2	Four-partite qubit linear cluster state. Chain structure and scheme for its experimental realization . . . . .	46
3.3	Geometric representation of a witness . . . . .	52
4.1	Experimental setup for the generation and control of high-dimensional frequency-entangled photon pairs . . . . .	61
4.2	Properties of the microring resonator used for the generation of entangled photons . . . . .	62
4.3	Characterization of the quantum state dimensionality through Schmidt mode decomposition of the correlation matrix and second-order coherence function . . . . .	64
4.4	Bell inequality violation and quantum state tomography of high-dimensional frequency-entangled photon pairs . . . . .	70
4.5	Scheme for the coherent manipulation of high-dimensional frequency-entangled states . . . . .	74
4.6	Coherent mixing of multiple frequency modes . . . . .	76
5.1	Complexity of the measurement settings required to detect a witness vs the witness noise tolerance . . . . .	83

5.2	Entanglement witness and convex set of multipartite separable and inseparable states . . . . .	91
6.1	Scheme for the generation of time-frequency hyper-entanglement. . . . .	104
6.2	Experimental setup for generation of $d$ -level cluster-states and for measurement-based quantum operations . . . . .	106
6.3	Generation of cluster states with a controlled phase gate . . . . .	108
6.4	Measurement of the entanglement witness expectation value . . . . .	114
6.5	Witness distribution towards incoherent, phase, and amplitude noise . . . . .	116
6.6	Measured photon projections on the 81 diagonal elements of the cluster state density matrix . . . . .	118
6.7	Quantum interference measurements for high-dimensional one-way computation operations . . . . .	119
6.8	Implementation of one-way quantum computing on $d$ -level hyper-entangled cluster states . . . . .	124

# List of Tables

6.1	Phases and visibilities of the two-partite entangled states obtained from cluster state projections. These values are extracted via quantum interference characterization . . . . .	115
D.1	Set of projection measurements for a typical quantum state tomography analysis . . . . .	149

# List of Symbols

$\mathcal{H}$	Hilbert space
$ \cdot\rangle$	Ket (quantum state)
$\langle\cdot $	Bra (dual of the ket)
$\dagger$	Transpose conjugate
$*$	Complex conjugate
$d$	Single-state dimensionality
$N$	Number of parties of a quantum system
$ \psi\rangle$	Quantum state wave function
$\langle\psi \phi\rangle$	Scalar product (probability amplitude)
$ \langle\psi \phi\rangle ^2$	Probability
$ u\rangle \otimes  v\rangle \equiv  u, v\rangle$	Tensor product
$ u\rangle\langle v $	Outer product
$\rho =  \psi\rangle\langle\psi $	Quantum state density matrix
$O, A, B, M$	Observables
$[A, B]$	Commutator
$\langle\psi M \phi\rangle = \langle M\rangle$	Expectation value
$ 0\rangle,  1\rangle$	Qubit
$ 0\rangle,  1\rangle,  2\rangle, \dots,  d-1\rangle$	Qudit
$\sigma_0 \equiv \mathbb{I}$	Identity matrix
$\sigma_{x,y,z}$	Pauli matrices
$X, Z, Y, V$	Generalized Pauli matrices
$H$	Hadamard matrix
$W$	Walsh-Hadamard matrix
$ \Phi^\pm\rangle,  \Psi^\pm\rangle$	Bell states
$s, i$	Signal and Idler photons

$ k\rangle$	Photon's frequency mode (frequency-bin)
$ 1\rangle,  2\rangle,  3\rangle$	Time-bin qutrit
$ a\rangle,  b\rangle,  c\rangle$	Frequency-bin qutrit
$V_d$	Visibility
$F_d$	Quantum state Fidelity
$K$	Schmidt number
$\mathcal{W}$	Witness operator
$ \phi_{N,d}\rangle$	$N$ -partite $d$ -level linear cluster state
$ C_{N,d}\rangle$	$N$ -partite $d$ -level compact cluster state
$\mathcal{S}_k^{(\phi_{N,d})}$	Stabilizer operator of linear cluster states
$\mathcal{S}_k^{(C_{N,d})}$	Stabilizer operator of compact cluster states
$\varepsilon$	White noise
$\varepsilon_{\text{th}}$	Noise tolerance (threshold)
$\mathcal{W}_{\text{th}}^{\text{opt}}$	Theoretically optimal entanglement witness
$\mathcal{W}_{\text{exp}}^{\text{opt}}$	Experimentally optimal entanglement witness

# Résumé

## Introduction : problématiques et motivation

La mécanique quantique est la seule branche de la physique capable de décrire les propriétés ainsi que la dynamique de systèmes microscopiques, comme par exemple, les particules élémentaires, les atomes et les molécules. Cela rend l'étude de la mécanique quantique cruciale pour une meilleure compréhension de la physique fondamentale. Un concept d'importance essentielle de la mécanique quantique et dépourvu de tout analogue classique est l'« enchevêtrement » (communément connu comme « entanglement »). Ce phénomène décrit des corrélations entre deux ou plusieurs systèmes microscopiques, qui ne dépendent pas de la distance physique entre les systèmes ou de la base dans laquelle ils sont mesurés. C'est ce dernier aspect qui fait de l'enchevêtrement un phénomène exclusivement quantique. Cependant, l'importance de la mécanique quantique et de l'enchevêtrement va bien au-delà de l'étude de la physique fondamentale. En particulier, la mécanique quantique et l'enchevêtrement ont un rôle clé à la fois pour le développement de nouvelles technologies et pour surmonter les capacités et les limitations des technologies qui sont actuellement disponibles. Par exemple, les principes de la mécanique quantique ainsi que l'enchevêtrement permettent de réaliser des ordinateurs (appelés précisément ordinateurs quantiques) avec une puissance et une efficacité de calcul bien supérieures à celles de l'analogie classique et qui sont aussi capables de stocker et de traiter une quantité d'informations plus élevée. L'enchevêtrement entre deux ou plusieurs systèmes permet également de communiquer et de transmettre des données (ou, en général, une information) en toute sécurité. Pour que la mécanique quantique, avec ses principes et ses phénomènes, soit efficacement introduite dans la technologie, il est nécessaire d'utiliser des états complexes enchevêtrés, sans lesquels cet objectif ne serait pas réalisable. Pour cette raison, de nombreux efforts ont été consacrés à la réalisation expérimentale des ces

états.

Cependant, une pleine exploitation de l’enchèvement sous toutes ses facettes nécessite une compréhension profonde de ce phénomène, ainsi qu’une caractérisation complète des états enchevêtrés. Ceci reste encore une question ouverte, en particulier dans le cas d’états quantiques complexes caractérisés par un grand nombre de parties et / ou de niveaux (c’est-à-dire multipartites et / ou multidimensionnels). Les états quantiques avec deux niveaux (discrets) sont appelés « qubits », tandis que les états quantiques caractérisés par plusieurs niveaux discrets (c’est-à-dire «  $d$  ») sont appelés « qudits ».

À ce jour, il n’existe pas d’approche universelle capable d’étudier et de caractériser l’enchèvement de tout état quantique arbitrairement complexe. En outre, la réalisation d’états complexes enchevêtrés dans des plates-formes pratiques, évolutives et à faible coût, selon les exigences des technologies modernes, reste toujours un grand objectif à atteindre.

Motivés par l’importance et par le rôle crucial de l’enchèvement, nous avons orienté notre activité de recherche vers la réalisation d’états enchevêtrés complexes et aussi à la théorisation d’une approche universellement valable qui est capable de caractériser pleinement l’enchèvement. Un objectif important que nous nous sommes fixés pour élaborer cette approche est celle-ci devrait permettre de caractériser l’enchèvement par des mesures qui nécessite le moins d’effort expérimental possible. La faisabilité expérimentale est en effet la base pour appliquer l’enchèvement dans la technologie moderne.

## **Réalisation et caractérisation de l’enchèvement de paires de photons multidimensionnels et enchevêtrés en fréquence**

Pour atteindre cet objectif, nous avons d’abord exploré les états quantiques qui fournissaient les conditions préalables (c’est-à-dire la multi-dimensionnalité) pour obtenir des états enchevêtrés plus complexes, c’est-à-dire consistant en plusieurs parties et niveaux (ou dimensions).

Cette étude nous a conduit à démontrer pour la première fois dans une plate-forme optique intégrée (on-chip) la réalisation de paires de photons multidimensionnels et enchevêtrés en fréquence. En outre, nous avons manipulé et traité ces états de manière cohérente afin de caractériser leur dimensionnalité par décomposition en modes de Schmidt et leur enchevêtrement par interférence quantique, violation des inégalités de Bell et to-

mographie quantique. Cette analyse nous a fourni une base pour développer l’approche universelle susmentionnée visant à une caractérisation complète de l’enchèvement.

Afin de générer les paires de photons enchevêtrés en fréquence, nous avons exploité le phénomène du mélange à quatre ondes spontané (« spontaneous four-wave mixing » - SFWM) dans un micro-résonateur en forme d’anneaux « microring » non linéaire à quatre ports, caractérisé par une plage spectrale libre (« free spectral range » - FSR, relative à la séparation spectrale entre les modes de résonance adjacentes) de 200 GHz et un facteur de qualité  $Q$  de 235,000. En particulier, nous avons excité une seule résonance du micro-résonateur en forme d’anneaux avec un laser à mode bloqué filtré spectralement à une longueur d’onde de 1,550 nm. Cette excitation a pour résultat la génération de paires de photons corrélées (c’est-à-dire un photon de type (s)ignal et (i)dlér) qui sont spectralement symétriques au champ d’excitation et qui couvre plusieurs résonances. En particulier, les deux photons ont été générés sur un peigne fréquence quantique (quantum frequency combs - QFCs), c’est-à-dire un nombre important de modes de fréquences également espacés (voir la Figure 1).

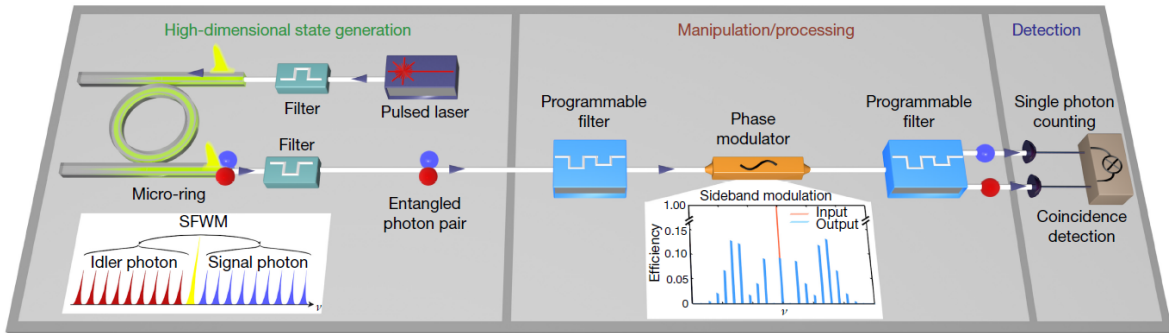


**Figure 1** – Configuration expérimentale pour la génération et le contrôle d’états quantiques multidimensionnels. Un laser à mode bloqué de type passive a été couplé au micro-résonateur intégré après avoir été filtré spectralement pour exciter précisément une seule résonance. Le phénomène de SFWM (voir encadré de gauche) a conduit à la génération de paires de photons (signal et idler) qui sont spectralement symétriques à l’excitation et qui sont une superposition quantique des modes de fréquence. Des filtres programmables et un modulateur de phase ont été utilisés pour manipuler l’état. Ensuite, les photons signal et idler ont été détectés par deux compteurs à photons unique. [6]

De cette façon, les deux photons ont été générés chacun dans une superposition de modes de fréquence multiples. Une telle superposition, associée à la conservation d’énergie lié au SFWM, a permis de générer un enchevêtré multidimensionnel en fréquence (voir la Figure 1). Nous avons généré des photons ayant une dimension allant jusqu’à

$d = 10$  pour chaque photon. La dimensionnalité de chaque photon a été démontrée en déterminant le nombre de Schmidt  $K$ , qui donne le nombre de modes de fréquence orthogonaux dans un système quantique. Plus précisément, nous avons évalué une limite inférieure et une limite supérieure pour  $K$  (c'est-à-dire,  $K_{low}$  et  $K_{up}$ , respectivement). Ensuite, nous avons comparées les deux valeurs.  $K_{low}$  a été déterminé en utilisant une matrice de corrélation, qui peut être obtenue en effectuant des mesures de coïncidence résolues spectralement entre le signal et l'idler (voir la Figure 2-a). A partir de la décomposition en valeurs singulières de la matrice de corrélation, nous avons extrait la limite inférieure du nombre de Schmidt, qui était  $K_{low} = 9.4$ . Afin d'estimer la limite supérieure  $K_{up}$ , nous avons utilisé la fonction de cohérence signal-idler du second ordre  $g_{s,i}^{(2)}(t)$  dans le domaine temporel, qui est directement corrélée au nombre de modes effectifs dans le système (voir la Figure 2-b). Cela a été mesuré avec un montage optique comprenant un diviseur de faisceau 50 : 50 et un système de détection de photon à coïncidence. En sélectionnant individuellement dix résonances à la fois pour le signal et pour l'idler, nous avons validé le fait que la résonance de chaque photon était dans un état quantique extrêmement pur, c'est-à-dire chaque mode de résonance a un nombre de Schmidt approximativement égal à un (voir la Figure 2-b). Dans cette expérience, nous avons considéré les paires de résonance et nous avons additionné le nombre de Schmidt de chacune d'elles. Nous avons ainsi obtenu la limite supérieure du nombre de Schmidt, qui était  $K_{up} = 10.45 \pm 0.53$  (voir la Figure 2). Comme les limites inférieure et supérieure  $K_{low}$  et  $K_{up}$  coïncidaient dans la barre d'erreur, nous en avons conclu que le nombre de modes orthogonaux pertinents était de dix, ce qui signifie que chaque photon était généré dans un état de fréquence à 10 dimensions.

Afin de vérifier l'enchevêtrement et la qualité des états de photons générés, nous avons effectué des mesures d'interférences et de tomographie quantiques. Dans ce cas, nous avons exploité les technologies à base de fibres afin de contrôler de manière cohérente les états enchevêtrés en fréquence et donc de réaliser les projections au niveau  $d$  nécessaires pour réaliser à la fois l'interférence et la tomographie quantiques. Ces projections ont été effectuées par décalage de phase et par le mélange de fréquence, qui ont été réalisés en utilisant respectivement deux filtres de phase programmables et un modulateur électro-optique (voir la Figure 1). La manipulation cohérente des états quantiques était possible, avec le montage optique actuel, pour  $d = 2, 3$  et  $4$  par photon. Parmi les trois figures

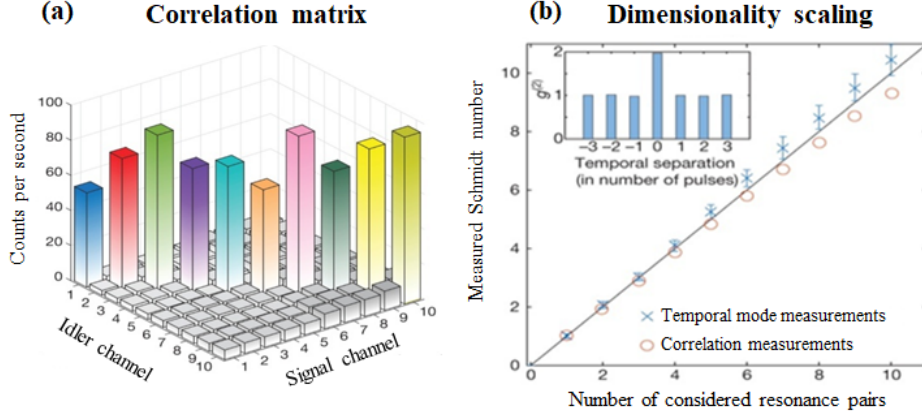


**Figure 2** – Caractérisation de la dimensionnalité de l'état quantique. (a) JSI mesuré de l'état quantique multidimensionnel, montrant les coïncidences de photons uniquement à des paires de modes symétriques (c'est-à-dire, sur la diagonale de la matrice) et révélant une corrélation de fréquence. (b) Nombre de Schmidt en fonction des paires de résonance considérées, symétriques à la fréquence d'excitation, avec la limite supérieure (croix bleues) obtenue à partir de la fonction de cohérence du second ordre, et la limite inférieure (cercles rouges) calculée à partir de la matrice de corrélation. L'encart en (b) montre la fonction de cohérence de second ordre mesurée d'un photon unique émis à une résonance spécifique avec un maximum de  $1.92 \pm 0.03$ , correspondant à  $1.086 \pm 0.03$  modes effectifs. [6]

d'interférence quantique, nous avons extrait les visibilitées respectives, qui étaient  $V_2 = 83.6\%$ ,  $V_3 = 86.6\%$  et  $V_4 = 86.4\%$ . Étant donné que tous ont violé les seuils requis pour violer l'inégalité de Bell respective (71%, 77% et 81.7% pour  $d = 2, 3$  et 4), nous avons démontré l'enchèvement des états à deux photons ainsi générés (voir la Figure 3-a,b,c). La tomographie quantique a été utilisée pour reconstruire la matrice de densité d'états quantiques mesurées, puis pour en extraire la fidélité, c'est-à-dire un paramètre fournissant l'accord entre les états idéaux et expérimentaux. Une fidélité supérieure à 50% signifie un bon enchèvement entre les deux états. Puisque nous avons extrait des mesures de fidélité égales à  $F_2 = 88.5\%$ ,  $F_3 = 80.9\%$  et  $F_4 = 76.6\%$  respectivement pour le cas  $d = 2, 3$  et 4, nous avons démontré la bonne qualité des états quantiques générés (voir la Figure 3-d,e,f).

La tâche spécifique accomplie au cours de cette thèse et dans le cadre du travail décrit ci-dessus consistait à dériver théoriquement les mesures nécessaires (c'est-à-dire, les projections) pour mesurer l'interférence et la tomographie quantiques. Les résultats décrits dans cette section sont expliqués en détail au Chapitre 4 de cette thèse et ont été publiés dans la Référence [6] de cette thèse.

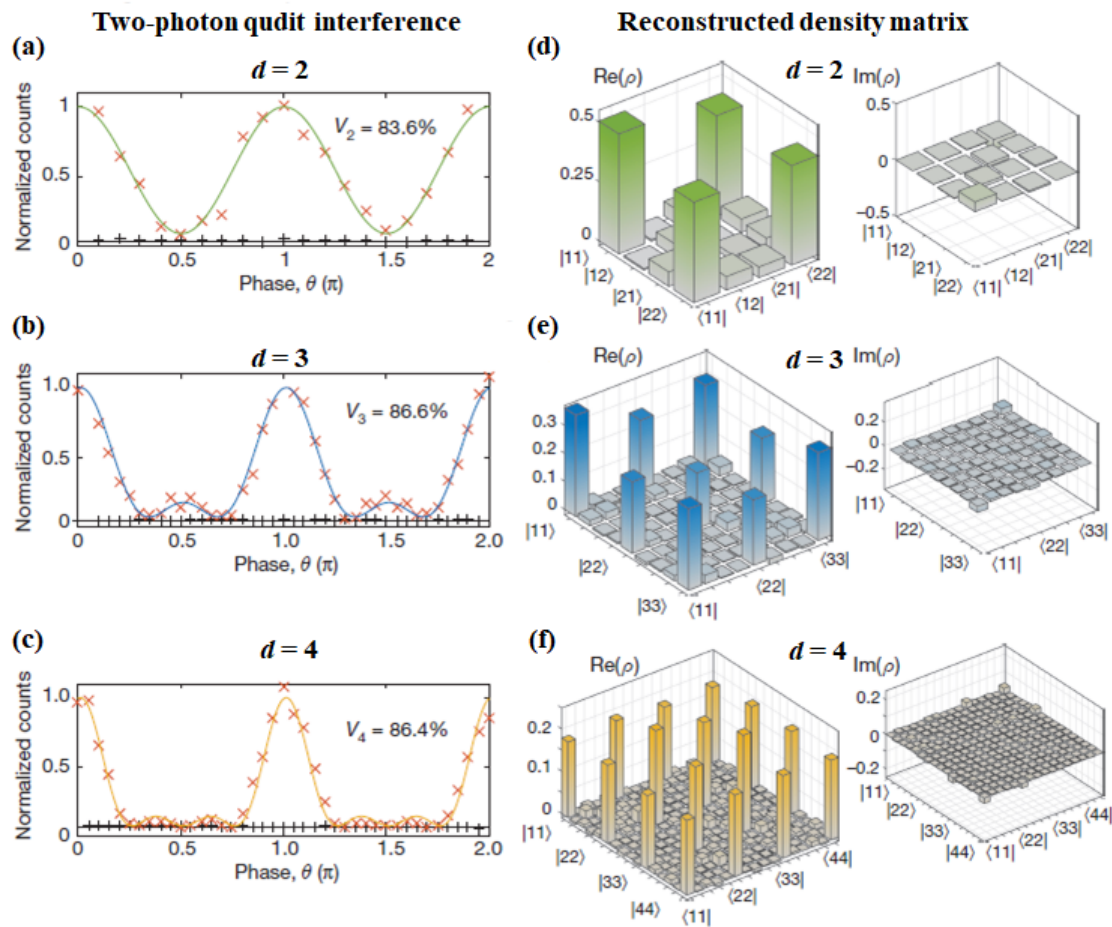


**Figure 3** – Violation de l'inégalité de Bell et tomographie quantique d'états enchevêtrés en fréquence. Diagrammes d'interférence quantiques obtenus pour (a)  $d = 2$ , (b)  $d = 3$  et (c)  $d = 4$  en projetant les états à deux photons sur une superposition de  $d$  modes de fréquence. Des visibilités brutes (sans soustraction de fond) de 83.6%, 86.6% et 86.4% ont été extraites des diagrammes d'interférence. Celles-ci dépassent les visibilités de 71%, 77% et 81.7%, nécessaires pour violer l'inégalité de Bell respectivement pour  $d = 2, 3$  et  $4$ , démontrant ainsi l'enchevêtrement des états à deux photons générés. Matrice de densité mesurée des états qudit reconstruits par tomographie quantique pour (d)  $d = 2$ , (e)  $d = 3$  et (f)  $d = 4$ . Des fidélités de 88.5%, 80.9% et 76.6% ont été obtenues respectivement pour  $d = 2, 3$  et  $4$ , démontrant ainsi un très bon accord entre l'état maximale enchevêtré et l'état mesuré. [6]

## Réalisation et caractérisation de l'enchevêtrement d'un état « cluster » de photons à trois niveaux et à quatre parties

Sur la base des résultats présentés ci-dessus, un autre objectif de recherche important a été atteint : la génération d'états « cluster » multipartites et multidimensionnels, ainsi que leur utilisation pour démontrer la preuve du concept d'informatique quantique multidimensionnel à sens unique (ou unidirectionnelle « one-way quantum computing »). Les

états cluster sont une classe de systèmes multipartites dont l'enchevêtrement a des propriétés uniques : connectivité maximale et persistance la plus élevée de l'enchevêtrement. La première propriété implique que toute paire de qubits / qudits d'un état cluster peut être projetée dans un état maximalelement enchevêtré en effectuant des mesures projectives sur les paires restantes de l'état cluster. La deuxième propriété implique que le nombre de mesures nécessaires pour détruire l'enchevêtrement d'un état cluster est plus grand que pour les autres états enchevêtrés (ayant un nombre égal de parties). Ces deux propriétés rendent les états cluster particulièrement prometteurs pour la réalisation du calcul quantique "unidirectionnel" (ou basé sur la mesure). Un ordinateur unidirectionnel utilise un état cluster en tant que ressource physique pour le calcul. Le calcul est effectué à travers de simples projections sur l'état cluster. Dans la littérature, la réalisation expérimentale d'états cluster de photons discrets est limitée aux qubits.

Dans cette thèse, en utilisant une plate-forme optique intégrée similaire à celle décrite ci-dessus, nous avons généré pour la première fois un état cluster quadripartite de deux photons à trois niveaux (c'est-à-dire un « qutrit »), voir la Figure 4. La raison pour laquelle le système doit être considéré comme quadripartite est que nous avons considéré deux degrés de liberté par photon, le temps et la fréquence (en particulier, les intervalles de temps et de fréquences, c'est-à-dire « time-bins » et « frequency-bins »), chacun étant caractérisé par trois niveaux (modes) quantiques :  $|1\rangle$ ,  $|2\rangle$ ,  $|3\rangle$  pour le temps et  $|a\rangle$ ,  $|b\rangle$ ,  $|c\rangle$  pour la fréquence. Bien que le temps et la fréquence soient en réalité le même degré de liberté (l'une est la transformation de Fourier de l'autre), si le produit entre les modes temporels et spectrales est supérieur à la limite d'Einstein-Podolsky-Rosen pour les corrélations quantiques (qui est égal à 1), ils doivent être considérés comme indépendants et peuvent donc être traités comme des degrés de liberté différents. Dans l'expérience décrite ici, cette condition était largement satisfaite : les modes temporel et spectral ont été générés avec une séparation respective égale à 24 ns et 200 GHz, de sorte que le produit temps-fréquence était de 4,800  $\gg$  1. Ce résultat nous a permis de générer deux types distincts d'enchevêtrement, un en temps et un en fréquence. Au vu de ces considérations, il est clair que le système doit être considéré comme quadripartite : les deux degrés de liberté par photon constituent les parties du système, tandis que les deux photons (signal et idler) représentent les "porteurs" des parties.

La réalisation de l'état cluster susmentionné a nécessité deux étapes : la génération

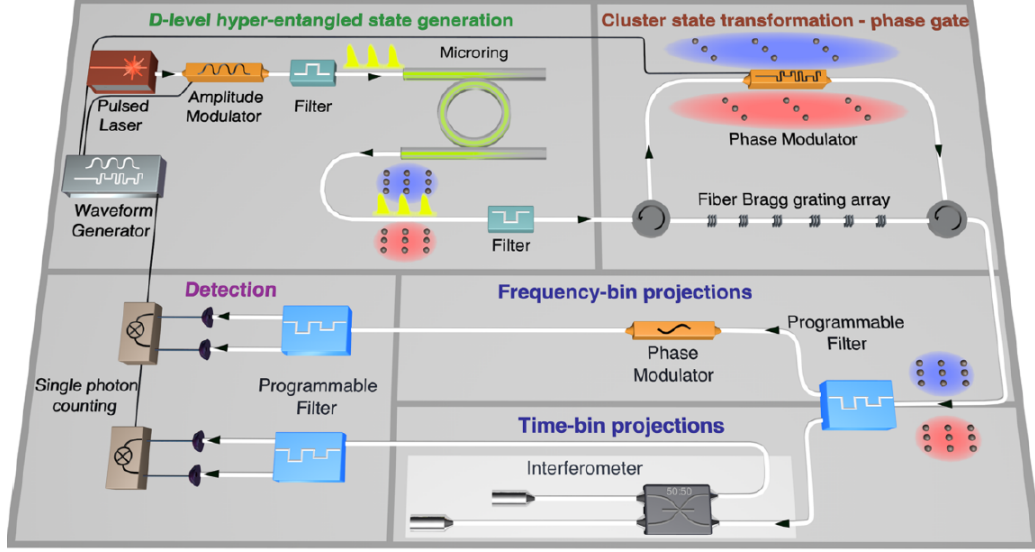


**Figure 4** – Configuration expérimentale pour la génération d'états cluster à d niveau et pour les mesures effectuées. Trois impulsions optiques excitent une fréquence de résonance du micro-résonateur non linéaire, où signal et idler (marqués respectivement en rouge et bleu) sont générés via SFWM. Étant dans une superposition de trois modes en temps et trois modes en fréquence (indiqués par des puces), les photons sont dans un état hyper-enchevêtré. L'accès individuel aux amplitudes et aux phases de cet état a été réalisé à travers une nouvelle porte à phase contrôlée consistant en un ensemble de réseaux de Bragg sur fibre. Un modulateur de phase électro-optique a été utilisé pour changer la phase des différents termes de l'état hyper-enchevêtré afin de produire l'état cluster à d niveaux. Un filtre programmable a été utilisé pour envoyer l'état cluster en deux configurations différentes pour l'analyse : 1) projections en fréquence à travers un modulateur de phase électro-optique, et 2) projection en temps via un interféromètre déséquilibré. Les photons ont ensuite été séparés par des filtres et mesurés avec des détecteurs à photon unique. [7]

d'un état simultanément enchevêtré (« hyper-enchevêtré ») en temps et en fréquence,  $|\Psi_{\text{Hyper}}\rangle$ , et donc la transformation de celui-ci en un cluster  $|\Psi_{\text{Cluster}}\rangle$ . À cette fin, nous avons tout d'abord déduit analytiquement la forme explicite de la fonction d'onde de l'état cluster  $|\Psi_{\text{Cluster}}\rangle$  qui est (sauf pour un facteur de normalisation égal à  $1/3$ ) :

$$\begin{aligned}
|\Psi_{\text{Cluster}}\rangle &= |1_s, 1_i, a_s, a_i\rangle + |1_s, 1_i, b_s, b_i\rangle + |1_s, 1_i, c_s, c_i\rangle \\
&+ |2_s, 2_i, a_s, a_i\rangle + e^{i2\pi/3} |2_s, 2_i, b_s, b_i\rangle + e^{-i2\pi/3} |2_s, 2_i, c_s, c_i\rangle \\
&+ |3_s, 3_i, a_s, a_i\rangle + e^{-i2\pi/3} |3_s, 3_i, b_s, b_i\rangle + e^{i2\pi/3} |3_s, 3_i, c_s, c_i\rangle,
\end{aligned}$$

où 's' et 'i' désignent le signal et l'idler, respectivement. D'un point de vue expérimental, il n'est pas possible de générer cette fonction d'onde directement à travers les sources de photons. Au contraire, il est possible de générer des états-produit hyper-enchevêtrés et aussi séparables. Dans notre cas spécifique, l'état-produit a été généré en excitant trois

modes de fréquence de la microcavité avec trois impulsions « mode-locked » ; la fonction d'onde associée à cet état-produit est :

$$\begin{aligned}
|\Psi_{\text{Hyper}}\rangle &= (|1_s, 1_i\rangle + |2_s, 2_i\rangle + |3_s, 3_i\rangle) \otimes (|a_s, a_i\rangle + |b_s, b_i\rangle + |c_s, c_i\rangle) \\
&= |1_s, 1_i, a_s, a_i\rangle + |1_s, 1_i, b_s, b_i\rangle + |1_s, 1_i, c_s, c_i\rangle \\
&+ |2_s, 2_i, a_s, a_i\rangle + |2_s, 2_i, b_s, b_i\rangle + |2_s, 2_i, c_s, c_i\rangle \\
&+ |3_s, 3_i, a_s, a_i\rangle + |3_s, 3_i, b_s, b_i\rangle + |3_s, 3_i, c_s, c_i\rangle.
\end{aligned}$$

En comparant  $|\Psi_{\text{Hyper}}\rangle$  et  $|\Psi_{\text{Cluster}}\rangle$ , il est possible constater que les deux états diffèrent par les facteurs de phase :  $|\Psi_{\text{Hyper}}\rangle$  peut donc être transformé en  $|\Psi_{\text{Cluster}}\rangle$  en y introduisant les phases appropriées. Expérimentalement, nous avons introduit ces phases avec une « porte de phase contrôlée » construite sur des composants de fibre (Figure 5).

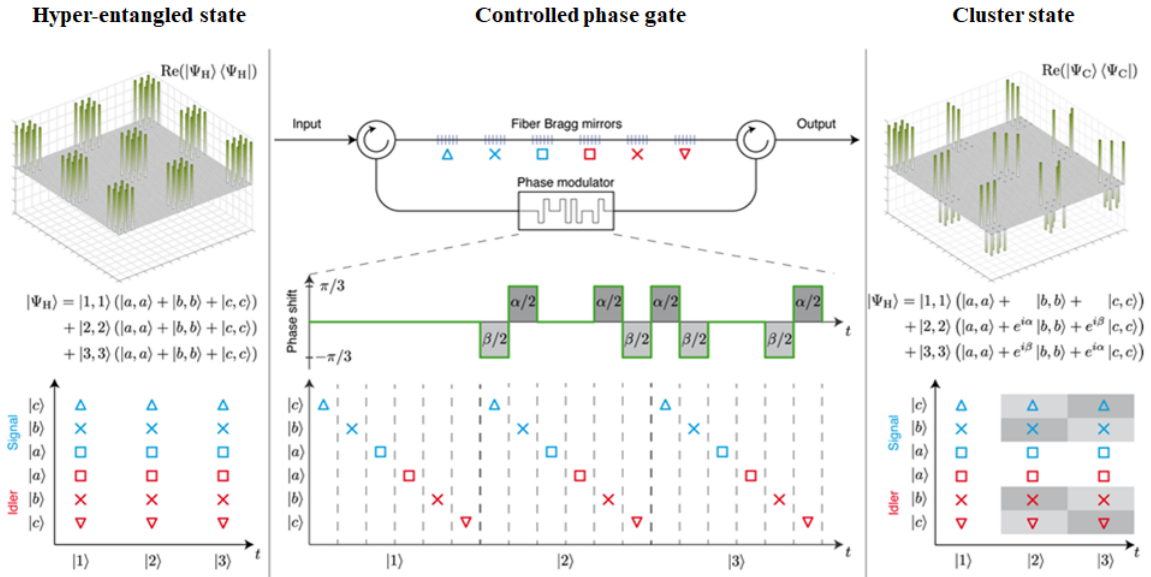


**Figure 5** – Génération d'états de cluster avec une porte de phase contrôlée. L'état à deux photons hyper-enchevêtrés est composé simultanément de trois modes temporels  $|1\rangle, |2\rangle, |3\rangle$  et de trois modes de fréquence  $|a\rangle, |b\rangle, |c\rangle$  pour chaque photon (la partie réelle de la matrice de densité associée à l'état hyper-enchevêtré est représentée dans le panneau en haut à gauche). Une porte de phase contrôlée donne accès à chaque terme de l'état en dispersant temporairement les modes de fréquence individuels dans différentes fenêtres temporelles à travers un réseau de miroirs de Bragg sur fibres (voir panneau central). Un modulateur électro-optique a été utilisé pour changer la phase de chaque terme de l'état, ici par  $\alpha/2$  et  $\beta/2$ . Les photons entrent ensuite dans le réseau de fibres de Bragg à partir de l'autre extrémité, de sorte que la correspondance fréquence-temps soit inversée de manière cohérente. En choisissant les phases  $\alpha = 2\pi/3$  et  $\beta = -2\pi/3$ , l'état hyper-enchevêtré est transformé en un état cluster à trois niveaux (la partie réelle de la matrice de densité est affichée dans le panneau en haut à droite). [7]

Les composants principaux de la porte à phase contrôlée étaient : un réseaux de six

miroirs de Bragg fibré et un modulateur de phase électro-optique. Le réseau avait la fonction précise de répartir temporellement les modes de fréquence individuels dans différentes fenêtres temporelles, de manière à avoir accès à chaque terme de la fonction d'onde. Le modulateur de phase électro-optique a été donc utilisée pour modifier convenablement la phase de chaque terme. À partir des matrices de densité (reconstruites analytiquement via Matlab) de  $|\Psi_{\text{Hyper}}\rangle$  et  $|\Psi_{\text{Cluster}}\rangle$  (Figure 5), nous pouvons observer la différence entre la structure des deux fonctions d'onde.  $|\Psi_{\text{Hyper}}\rangle$  est séparable,  $|\Psi_{\text{Cluster}}\rangle$  ne l'est pas et présente, en particulier, un enchevêtrement défini comme « véritable multipartite ».

Cela signifie que les projections sur une base temporelle de paires de qutrits provoquent l'effondrement des paires restantes dans des états bipartites qui sont maximalelement enchevêtrés en fréquence et qui sont orthogonaux (et vice versa). C'est précisément le principe de fonctionnement du traitement quantique unidirectionnel, qui a été démontré ici pour la première fois de son histoire pour les systèmes multidimensionnels. L'orthogonalité et l'enchevêtrement des états bipartites restantes ont été validés par des mesures d'interférence quantique : la visibilité extraite des chiffres d'interférence a violé l'inégalité de Bell pour les systèmes à trois niveaux, confirmant ainsi l'enchevêtrement bipartite, à savoir enchevêtrement de Bell (Figure 6).

Le véritable enchevêtrement quadripartite de l'état cluster créé ici a été confirmé en obtenant un opérateur quantique spécifique (appelé « témoin d'enchevêtrement »  $\mathcal{W}$ , expliqué en détail dans la section suivante) et en déterminant sa valeur d'attente. Sur la base de ce qui a été démontré dans la littérature pour les états cluster de qubits, nous avons théoriquement dérivé le premier témoin d'enchevêtrement pour les états cluster de qutrits et avons ensuite fourni les opérations nécessaires pour mesurer expérimentalement sa valeur d'attente, dont l'expression mathématique est :

$$\langle \mathcal{W}^{(\Psi_{\text{Cluster}})} \rangle = \frac{5}{3} \text{Re} \left( \langle \mathbb{I}_1 \mathbb{I}_2 Z_3 Z_4^\dagger \rangle + \langle Z_1^\dagger Z_2 \mathbb{I}_3 \mathbb{I}_4 \rangle + \langle \mathbb{I}_1 Z_2 X_3 X_4 \rangle + \langle X_1 X_2 Z_3 \mathbb{I}_4 \rangle \right. \\ \left. + \langle Z_1 \mathbb{I}_2 X_3 X_4 \rangle + \langle Z_1^\dagger Z_2^\dagger X_3 X_4 \rangle + \langle X_1 X_2 \mathbb{I}_3 Z_4 \rangle + \langle X_1 X_2 Z_3^\dagger Z_4^\dagger \rangle \right).$$

Dans cette expression,  $Re$  dénote la partie réelle de la valeur d'attente. En particulier, alors que chacun des huit termes entre parenthèses peut prendre une valeur complexe, la valeur totale d'attente de l'opérateur témoin doit être un nombre réel (puisque le témoin d'enchevêtrement est une observable physique qui doit être mesuré expérimentalement).  $\mathbb{I}$  représente la matrice d'identité,  $Z$  et  $X$  sont les matrices de Pauli généralisées (dans ce cas, des matrices  $3 \times 3$ ), où  $\dagger$  indique la transposition conjuguée de chaque matrice. Les

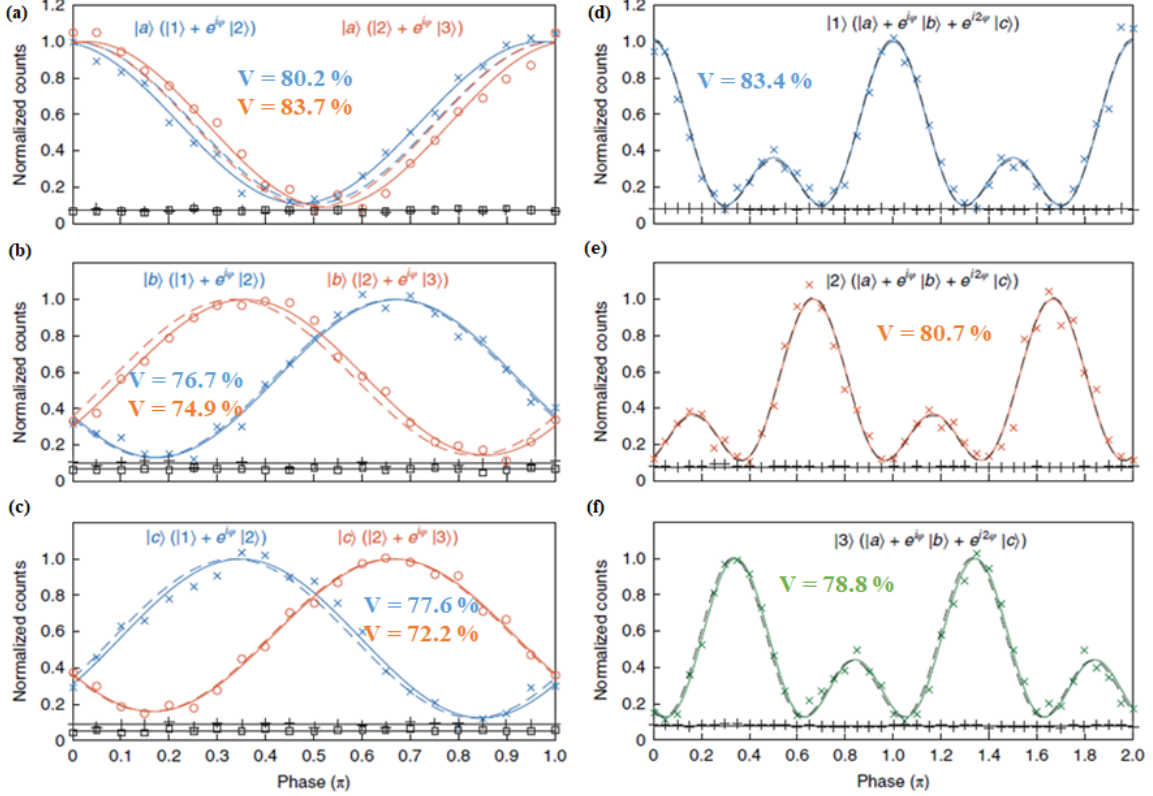


**Figure 6** – Interférence quantique et visibilité mesurées pour des états enchevêtrés bipartites et orthogonaux obtenues en réalisant des projections temporelles **(a-c)** et spectrales **(d-f)** sur l'état cluster. [7]

indices 1, 2, 3 et 4 font référence au qudit sur lequel chaque matrice agit. L'expression mathématique de chaque matrice est

$$Z = \begin{pmatrix} 1 & 0 & 0 \\ 0 & e^{i2\pi/3} & 0 \\ 0 & 0 & e^{-i2\pi/3} \end{pmatrix}, \quad Z^\dagger = \begin{pmatrix} 1 & 0 & 0 \\ 0 & e^{-i2\pi/3} & 0 \\ 0 & 0 & e^{i2\pi/3} \end{pmatrix}$$

$$X = \begin{pmatrix} 0 & 0 & 1 \\ 1 & 0 & 0 \\ 0 & 1 & 0 \end{pmatrix}, \quad \mathbb{I} = \begin{pmatrix} 1 & 0 & 0 \\ 0 & 1 & 0 \\ 0 & 0 & 1 \end{pmatrix}.$$

En mesurant les matrices de Pauli généralisées par des mesures projectives (voir la Figure 7), nous avons déterminé une valeur d'attente  $\langle \mathcal{W}^{(\Psi_{\text{Cluster}})} \rangle = -0.28 \pm 0.04$ . Cette valeur, étant négative, elle a confirmé le véritable enchevêtrement quadripartite du cluster que nous avons construit. Mesurer  $\langle \mathcal{W}^{(\Psi_{\text{Cluster}})} \rangle$  a nécessité un total de 648 mesures projectives (81 mesures pour chacun des huit termes de l'expression ci-dessus), théoriquement calculées une par une. Expérimentalement, les qutrits 1 et 2 ont été mesurés

sur la base des modes temporels, les qutrits 3 et 4 ont été mesurés sur la base des modes spectraux. Plus précisément, les matrices  $Z$  et  $\mathbb{I}$  ont été mesurées dans la base de calcul (c.-à-d.  $\{|1\rangle, |2\rangle, |3\rangle\}$  pour le temps et  $\{|a\rangle, |b\rangle, |c\rangle\}$  pour la fréquence), tandis que la matrice  $X$  a été mesurée par une combinaison linéaire de ceux-ci (c.-à-d.  $\{|t1\rangle, |t2\rangle, |t3\rangle\}$  pour le temps et  $\{|fa\rangle, |fb\rangle, |fc\rangle\}$  pour la fréquence). Les mesures de  $\{|1\rangle, |2\rangle, |3\rangle\}$  et de  $\{|a\rangle, |b\rangle, |c\rangle\}$  ont été effectuées respectivement par détection de photons et par filtres de phase. Les mesures relatives à  $\{|t1\rangle, |t2\rangle, |t3\rangle\}$  et à  $\{|fa\rangle, |fb\rangle, |fc\rangle\}$  ont été effectuées respectivement à travers un interféromètre à deux bras de Michelson non équilibré et un modulateur de phase électro-optique.

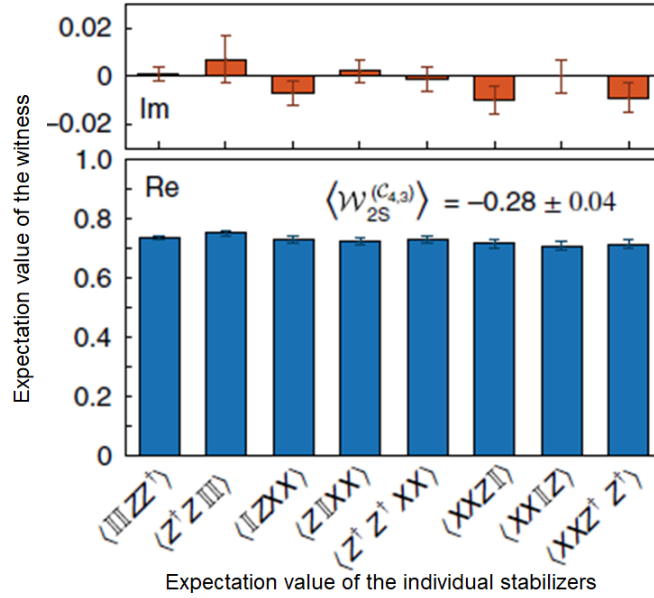


**Figure 7** – Mesure du témoin d’enchèvement. Partie réelle (barres bleues) et imaginaire (barres rouges) des valeurs d’attente mesurées pour chaque terme composant le témoin d’enchèvement de l’état cluster. La valeur d’attente pour chaque terme peut être complexe en raison des propriétés non-hermitiennes des matrices de Pauli généralisées; cependant, seules les huit parties réelles contribuent à la valeur d’attente du témoin d’enchèvement, qui a une valeur négative (réelle) égale à  $-0.28 \pm 0.04$ . [7]

La tâche spécifique accomplie au cours de cette thèse dans le cadre du travail décrit ci-dessus consistait à dériver théoriquement l’expression de la fonction d’onde de l’état cluster, ainsi que la structure mathématique de l’opérateur « entanglement witness », sa valeur d’attente, et ensuite les mesures nécessaires à son évaluation. Enfin, toutes les mesures de projection nécessaires pour mesurer l’interférence quantique ont été théoriquement dérivées. Les résultats décrits dans cette section sont expliqués en détail au chapitre

6 de cette thèse et ont été publiés dans la Référence [7] de cette thèse.

## Témoin d'enchèvement universel multipartite et à $d$ niveaux

Parallèlement à ces travaux théoriques et expérimentaux, nous avons élaboré une étude sur le témoin d'enchèvement. Cette étude a été de nature exclusivement théorique, mais peut être appliquée expérimentalement. Le témoin d'enchèvement (« entanglement witness ») est un opérateur qui permet de définir les propriétés et l'enchèvement d'un état généré expérimentalement sans recourir à des techniques de tomographie compliquées, impossibles à obtenir dans le cas de systèmes multidimensionnels et / ou multipartites. Pour certains systèmes quantiques, y compris les états cluster, il est en fait possible d'exprimer le témoin à travers de stabilisateurs qui, formés par des matrices de Pauli, peuvent être mesurés par de simples mesures projectives sur les différentes parties qui composent le système quantique. Cette caractéristique rend le témoin relativement facile à mesurer. Une valeur d'attente négative du témoin d'enchèvement implique que l'état généré est en accord avec l'état idéal et présente donc un enchèvement multipartite « véritable » (dans le cas spécifique des états cluster, la valeur d'attente du témoin calculé sur un état idéal est égale à -1). Le formalisme à la base du témoin ainsi formé a été formulé pour la première fois pour les systèmes de qubits par G. Toth et O. Guehne (*Physical Review A* **72**, 022340 (2005)), mais, avant les résultats présentés ici, il n'a jamais été étendu aux qutrits. Ici, nous avons développé une approche universellement valable qui nous permet d'obtenir des témoins d'enchèvement expérimentalement optimales, qui sont capables d'identifier la présence et l'enchèvement éventuel de tout état quantique arbitrairement complexe. Une caractéristique principale des opérateurs ainsi obtenus est qu'ils sont relativement faciles à mesurer d'un point de vue expérimental, c'est-à-dire qu'ils nécessitent peu d'instruments de mesure et sont faciles à mettre en œuvre. Ces caractéristiques différencient les témoins d'enchèvement obtenus ici de ceux connus dans la littérature qui, au contraire, en se basant sur des contraintes mathématiques rigoureuses, sont impossibles à mesurer expérimentalement. Une autre caractéristique qui distingue un témoin d'enchèvement expérimentalement optimal  $\mathcal{W}_{\text{exp}}^{\text{opt}}$  d'un témoin théoriquement optimal est la résistance au bruit expérimental (bruit blanc). Par résistance au bruit, on entend le seuil de bruit expérimental au-delà duquel un témoin d'enchèvement n'est plus capable de déterminer la présence ou l'absence d'enchèvement dans un système (en d'autres

termes, la limite au-delà de laquelle la valeur d'attente du témoin n'est pas plus négatif). Un témoin théoriquement optimal  $\mathcal{W}_{\text{theor}}^{\text{opt}}$  a un seuil de bruit très élevé, mais sa mesure nécessite néanmoins des techniques presque impossibles ou cependant assez difficiles à reproduire expérimentalement. En revanche,  $\mathcal{W}_{\text{exp}}^{\text{opt}}$  est facilement mesurable, mais son seuil de résistance au bruit est nettement inférieur. En considérant le graphique de la Figure 8, l'objectif de l'approche est de déterminer un témoin d'enchèvement expérimental qui maximise la confiance statistique (le paramètre  $\sigma$  dans la Figure 8) avec laquelle une valeur d'attente négative peut être mesurée. Lorsque cette condition de maximisation est atteinte, on parle de témoin d'enchèvement expérimentalement optimal.

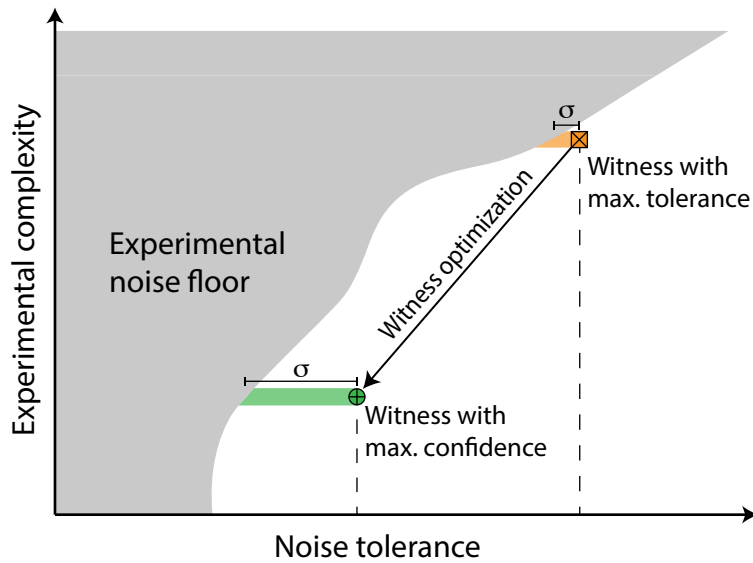


**Figure 8** – Complexité des paramètres de mesure vs tolérance au bruit du témoin d'enchèvement. Le bruit expérimental de fond (zone grise) introduit par les paramètres de mesure augmente avec l'augmentation de la complexité de la mesure. Un témoin d'enchèvement théoriquement optimal (carré orange) a la tolérance au bruit la plus élevée, mais exige des mesures complexes et souvent irréalisables expérimentalement. Au contraire, un témoin d'enchèvement expérimentalement optimal (cercle vert) nécessite une complexité de mesure réduite, mais présente une tolérance au bruit inférieure à celle du témoin d'enchèvement théoriquement optimal. Le but est de maximiser  $\sigma$  (zone ombrée verte ou orange) qui représente la confiance statistique avec laquelle une valeur d'attente négative du témoin d'enchèvement est mesurée (c'est-à-dire,  $\sigma$  est la distance entre le bruit de fond et la tolérance au bruit du témoin d'enchèvement). [5]

L'expression analytique du témoin d'enchèvement obtenu ici, dans sa forme la plus générale, est la suivante :

$$\mathcal{W}_{\text{exp}}^{\text{opt}} = \frac{1}{1 - \alpha} [(\alpha + \lambda_{\text{max}}) \cdot \mathbb{I} - \mathcal{W}_{\text{meas}}],$$

où  $\alpha = 1/d$  ( $d$  est le nombre de niveaux par part du système quantique),  $\lambda_{\max}$  est un nombre scalaire et  $\mathcal{W}_{\text{meas}}$  est un opérateur qui contient tous les termes nécessaires à la détermination du témoin d’enchèvement et qui est facilement mesurable expérimentalement.  $\mathcal{W}_{\text{meas}}$  s’oppose donc à un autre opérateur,  $\Theta$ , qui forme aussi le témoin et nécessite au contraire des techniques de mesure impossibles à reproduire expérimentalement. Le terme  $\lambda_{\max}$  représente précisément la valeur maximale d’attente que l’opérateur peut assumer et qui va remplacer  $\Theta$ . La technique d’expression du témoin en fonction de  $\lambda_{\max}$  et de  $\mathcal{W}_{\text{meas}}$  tout en conservant les propriétés mathématiques de cet opérateur, est à la base de la méthode dérivée. De l’expression générique de  $\mathcal{W}_{\text{exp}}^{\text{opt}}$ , nous avons obtenu la forme explicite du témoin d’enchèvement spécifiquement désigné pour déterminer la présence et le véritable enchèvement d’états cluster multipartites et multidimensionnels. Ce témoin est :

$$\mathcal{W}_{\text{exp}}^{\text{opt}}(\text{cluster}) = \frac{d+1}{d-1}\mathbb{I} - \frac{d}{d-1} \left\{ \prod_{\text{odd } k} \frac{1}{d} \sum_{l=1}^d \mathcal{S}_k^{(l)} + \prod_{\text{even } k} \frac{1}{d} \sum_{l=1}^d \mathcal{S}_k^{(l)} \right\},$$

où  $\mathcal{S}_k^{(l)}$  représente les stabilisateurs qui composent le témoin (le sommet ( $l$ ) indique la puissance de l’opérateur et l’indice  $k$  fait référence aux parties (qudits) qui composent le système). Dans ce cas,  $\mathcal{W}_{\text{meas}}$  a été construit en utilisant des stabilisateurs.  $\mathcal{W}_{\text{exp}}^{\text{opt}}(\text{cluster})$  nécessite donc deux sets de mesures (une pour  $X$  et une pour  $Z$ ).

Dans cette thèse, nous avons aussi montré qu’il était possible d’adapter  $\mathcal{W}_{\text{exp}}^{\text{opt}}$  aux restrictions expérimentales spécifiques ainsi qu’aux instruments de mesure disponibles. On prend l’exemple d’un état de deux photons à trois niveaux temporels (trois « timebins ») qui sont enchévêtrés entre eux :  $|\psi\rangle = 1/\sqrt{3}(|1,1\rangle + |2,2\rangle + |3,3\rangle)$ . Le témoin d’enchèvement capable d’identifier la présence et l’enchèvement de  $|\psi\rangle$  contient les matrices de Pauli tridimensionnelles, et y compris la matrice  $X$ . La mesure de cette matrice nécessite des projections simultanées sur une superposition de trois intervalles de temps ( $|1\rangle, |2\rangle, |3\rangle$ ), et donc d’un interféromètre de Michelson à trois bras. Cependant, il est particulièrement difficile de mettre en œuvre cet instrument en laboratoire car il nécessite des techniques de stabilisation et de manipulation complexes. Au contraire, le seul instrument disponible est un interféromètre de Michelson à deux bras, stable et facilement contrôlable. Un interféromètre ainsi fabriqué permet de réaliser des projections uniquement sur deux niveaux à la fois au lieu de trois, comme le demande la matrice  $X$ . L’approche formulée ici nous permet de trouver un témoin d’enchèvement capable

d'identifier la présence d'enchevêtrement dans le système à trois niveaux malgré la restriction expérimentale permettant de faire des projections sur deux niveaux à la fois. Avec notre approche, les stabilisateurs sont remplacés par des matrices de projection particulières, à savoir les matrices de Gell-Mann, qui permettent en particulier de projeter un état à trois niveaux par rapport à deux d'entre eux à la fois. En particulier, le témoin spécifiquement créé pour identifier la présence et l'enchevêtrement de  $|\psi\rangle$  et adapté aux restrictions expérimentales prend la forme

$$\mathcal{W}_{\text{adapted}} = \frac{5}{3}\mathbb{I} - (Z^\dagger Z + Z Z^\dagger) - (X_{0,1}X_{0,1} + X_{0,2}X_{0,2} + X_{1,2}X_{1,2}),$$

où

$$Z = \begin{pmatrix} 1 & 0 & 0 \\ 0 & e^{i2\pi/3} & 0 \\ 0 & 0 & e^{-i2\pi/3} \end{pmatrix}, \quad Z^\dagger = \begin{pmatrix} 1 & 0 & 0 \\ 0 & e^{-i2\pi/3} & 0 \\ 0 & 0 & e^{i2\pi/3} \end{pmatrix}$$

$$X_{0,1} = \begin{pmatrix} 0 & 1 & 0 \\ 1 & 0 & 0 \\ 0 & 0 & 0 \end{pmatrix}, \quad X_{0,2} = \begin{pmatrix} 0 & 0 & 1 \\ 0 & 0 & 0 \\ 1 & 0 & 0 \end{pmatrix}, \quad X_{1,2} = \begin{pmatrix} 0 & 0 & 0 \\ 0 & 0 & 1 \\ 0 & 1 & 0 \end{pmatrix},$$

sont les matrices  $Z$  de Pauli, sa transposée conjuguée, et enfin  $X_{0,1}$ ,  $X_{0,2}$ , et  $X_{1,2}$  sont trois des huit matrices de Gell-Mann.

Enfin, nous avons utilisé  $\mathcal{W}_{\text{exp}}^{\text{opt}}(\text{cluster})$  pour étudier la résistance au bruit blanc d'états cluster multipartites et multidimensionnels, qui est

$$\varepsilon_{\text{th}} = \begin{cases} \left[ \frac{2d}{d-1} \left( 1 - \frac{1}{d^{N/2}} \right) \right]^{-1}, & \text{even } N \\ \left[ \frac{2d}{d-1} \left( 1 - \frac{1}{2d^{(N+1)/2}} - \frac{1}{2d^{(N-1)/2}} \right) \right]^{-1}, & \text{odd } N. \end{cases}$$

À partir de cette expression, on peut observer que la résistance d'un état cluster au bruit blanc augmente avec l'augmentation du nombre de niveaux par partie, tandis qu'elle diminue avec l'augmentation du nombre de parties. C'est la première fois qu'un tel comportement est validé pour des systèmes multipartites multidimensionnels. De plus, nous avons montré que, pour un même état quantique, différentes restrictions expérimentales conduisent à des témoins d'enchevêtrement expérimentalement optimaux différents et aussi à des sensibilités différentes pour le même type de bruit.

Le travail théorique expliqué dans cette section a été une partie cruciale et fondamentale des études de doctorat qui ont été réalisées et présentées ici. Tous ces résultats ont été validés et confirmés par une analyse théorique très rigoureuse qui a précédé les simulations numériques et les expériences. Les résultats décrits dans cette section sont expliqués en détail au Chapitre 5 de cette thèse et ont été publiés dans la Référence [5] de cette thèse.

Les démonstrations expérimentales susmentionnées ont été entièrement obtenues sur une plate-forme optique intégrée (« on-chip »), tandis que les états générés ont été manipulés en utilisant des composants de fibres compatibles avec les infrastructures de télécommunication disponibles dans le commerce. Au vu de cet aspect, les résultats présentés dans cette thèse sont en phase avec les dernières avancées technologiques qui visent à réduire autant que possible la taille et le coût des plates-formes utilisés.

Les études de recherche effectuées au cours de ce projet de doctorat sont principalement de nature théorique et se sont révélés essentiels à la fois pour la réalisation expérimentale des états enchevêtrés susmentionnés, ainsi que pour effectuer les mesures nécessaires à la caractérisation de leur enchevêtrement.

Pour comprendre pleinement le formalisme et les outils que nous avons utilisés pendant ce projet de doctorat, cette thèse est organisée comme suit. Le Chapitre 1 présente une introduction à la mécanique quantique et contient le formalisme utilisé pour décrire et analyser les états quantiques, ainsi que le concept de mesure d'un état quantique. Le Chapitre 2 se concentre sur le phénomène d'enchevêtrement. En particulier, nous décrivons ce phénomène dans tous ses aspects fondamentaux et présentons en détail deux types d'états enchevêtrés, qui ont un rôle clé dans cette thèse : les états de Bell et les états hyper-enchevêtrés. Au Chapitre 3, nous présentons la classe d'états sur laquelle cette thèse se concentre principalement : les états cluster. Ensuite, nous présentons comment l'opérateur témoin d'enchevêtrement est connu dans la littérature, décrivant comment utiliser cet opérateur pour déterminer et confirmer la présence d'un véritable enchevêtrement multipartite des états cluster à deux niveaux (qubits). Enfin, dans les Chapitres 4, 5 et 6, nous rapportons la nouveauté : en particulier, nous présentons en détail l'étude et les résultats obtenus au cours de ce doctorat de recherche.

# Abstract

Microscopic systems such as elementary particles, atoms, and molecules, can be comprehensively described only by quantum mechanics, which thus plays a crucial role for a better understanding of fundamental physics. A very important phenomenon that only occurs in quantum mechanics is entanglement, which describes non-classical correlations between microscopic systems. These correlations exist independently of the physical distance between them, as well as independently of the basis in which these are measured. Specifically, this is the aspect that makes entanglement a purely quantum phenomenon. The importance of quantum mechanics however goes much beyond fundamental physics, since quantum phenomena potentially allow us to solve complex issues associated with currently available technologies. For example, quantum mechanics and entanglement can allow for faster and more powerful computing and information processing, as well as guarantee fully secure communications. Complex entangled states are specifically required for these tasks, and many efforts have been spent towards their experimental realization.

However, a full exploitation of entanglement necessitates a deep understanding of this phenomenon, as well as a complete characterization of entangled states. This still represents an open issue, especially in the case of quantum systems which are characterized by a large number of parties (i.e., the physical components - or units - forming a quantum system) and/or a high dimensionality. To date, a technique that enables the entanglement characterization of any arbitrarily complex quantum state in an experimentally feasible manner has not been developed yet. Moreover, realizing complex states in practical, scalable, and low-cost platforms, as demanded by modern technology, is still a big milestone to achieve.

Motivated by the importance as well as by the crucial role of entanglement, we oriented our research interests towards the realization of complex quantum systems, as well as towards the derivation of a universal approach capable of characterizing their entan-

glement with a minimal experimental effort. Experimental feasibility is indeed at the basis of entanglement application for modern technology.

Towards this goal, we first explored quantum systems that we could use as a basis for the realization of complex entangled states, i.e. consisting of multiple parties and levels (or dimensions). This investigation led us to the first ever generation of high-dimensional frequency-entangled photon pairs on-chip. We further coherently manipulated these states in order to characterize their dimensionality through Schmidt mode decomposition, as well as their entanglement via quantum interference measurements and Bell inequality violations. The quantum state analysis pursued here provided us the basis for developing a universal approach for entanglement characterization.

In this research work, we theoretically derived a universal entanglement witness that allows us to detect the presence of any arbitrarily complex pure quantum state, as well as of its eventual entanglement. We provided a technique that permits us to customize the witness (still preserving its mathematical properties) based on specific experimental restrictions and available measurement settings, in such a way to make the witness measurement experimentally feasible. Such a feature bridges the theoretical work pursued in this thesis and the experiments presented here. We explicitly derived a witness which is capable of detecting the presence of high-dimensional multipartite cluster states, and used this operator to test the robustness of these states toward noise.

In connection to this, we present the first ever realization of a four-partite three-level cluster state by making use of two photons that are simultaneously entangled (i.e. hyper-entangled) in time and in frequency. Cluster states are a class of multipartite systems with unique entanglement properties which make them crucial to realize so-called ‘one-way’ quantum computers. We confirmed the genuine multipartite entanglement of the generated cluster state by making use of the developed witness. We finally implemented two-partite projection measurements on the cluster state both in time and in frequency, thus demonstrating proof-of-principle high-dimensional one-way quantum processing. While cluster states have been already realized in quantum optical platforms for two-level systems, their extension to multiple levels (i.e. more dimensions) has never been explored prior to this work. The fundamental importance as well as the potential applications of cluster states in quantum technology, motivated us towards the investigation and the exploitation of these states in higher dimensions.

The realizations demonstrated here were achieved in an integrated photonic platform, while quantum state manipulations were implemented by making use of fiber-based components that are compatible with off-the-shelf telecommunication infrastructures. In view of this, the results presented here are extremely timely with the latest technology advancements, which aim at reducing the size and the cost of platforms as much as possible.

The work that has been specifically accomplished in the context of this research line and that is the main subject of this thesis has a theoretical footprint. In particular, the pursued studies have been focused on deriving a theoretical, yet experimentally-oriented, formalism enabling the entanglement characterization of complex (i.e. multipartite and/or high-dimensional) photon states. More specifically, such a theoretical work was crucial for the experimental realization of entangled photon states, and to perform the quantum measurements necessary for their entanglement characterization. One of the main tasks described in this thesis was indeed to theoretically provide all the measurements needed for quantum state analysis in such a way that these could be reproduced and implemented in an experimentally feasible manner.

In order to fully understand the formalism and the tools that we exploited in this research work, this thesis is organized as follows. Chapter 1 is an introduction to quantum mechanics. It contains the formalism that we used to describe quantum states, as well as the operations implemented on them. Chapter 2 is about the entanglement phenomenon. Here, we present classes of entangled states that are crucial for this research work. These are the so-called Bell states and hyper-entangled states. In Chapter 3 we introduce cluster states and witness operators. From the literature, we provide a description of how witnesses can be used to detect entanglement of two-level cluster states. Finally, Chapters 4, 5, and 6 report the investigation and results accomplished in this research work, with a main focus on the theoretical framework, in line with the theory work that has been accomplished during the PhD studies and that is the main subject of this thesis.

# Sommario

La meccanica quantistica è la sola branca della fisica in grado di descrivere le proprietà e la dinamica dei sistemi microscopici, quali particelle elementari, atomi e molecole, ragione per cui essa gioca un ruolo cruciale per una maggiore comprensione della fisica fondamentale. Un concetto basilare della meccanica quantistica e che è privo di qualsiasi analogo classico è il fenomeno dell'entanglement, il quale descrive correlazioni tra due o più sistemi microscopici. Queste correlazioni persistono indipendentemente sia dalla distanza fisica che li separa sia dalla base rispetto alla quale tali sistemi vengono misurati. È proprio quest'ultimo aspetto a rendere l'entanglement un fenomeno di natura esclusivamente quantistica. L'importanza della meccanica quantistica va tuttavia ben al di là della comprensione della fisica fondamentale. In particolare, i fenomeni quantistici possono svolgere un ruolo chiave sia per lo sviluppo di nuove tecnologie sia per superare le capacità e i limiti delle tecnologie che sono attualmente disponibili. Ad esempio, certi fenomeni quantistici permettono di realizzare computer (chiamati appunto computer quantistici) con potenza ed efficacia di calcolo di gran lunga superiori al loro analogo classico e che sono inoltre capaci di immagazzinare e processare una maggiore quantità di dati. Oppure, l'entanglement fra due o più sistemi permette di comunicare in totale sicurezza. L'introduzione dei principi e dei fenomeni della meccanica quantistica nell'ambito delle tecnologie richiede l'utilizzo di stati entangled complessi. Per questo motivo, la comunità scientifica si è impegnata parecchio negli ultimi decenni nella realizzazione sperimentale di questi ultimi.

Tuttavia, un appropriato utilizzo dell'entanglement in tutti i suoi aspetti richiede una piena comprensione di tale fenomeno, nonché la capacità di caratterizzare *in toto* qualsiasi stato entangled. Ciò rimane tuttora una questione aperta, soprattutto nel caso di stati quantistici complessi caratterizzati da un numero elevato di parti e/o di livelli (cioè multipartiti e/o multidimensionali). Ad oggi, non esiste un approccio universale in

grado di studiare e caratterizzare l'entanglement di un sistema quantistico qualsivoglia complesso. In più, la realizzazione di stati entangled complessi su piattaforme pratiche, riducibili in scala e a basso costo, come richiesto dalle tecnologie moderne, rimane ancora un grande obiettivo da raggiungere.

Motivati dall'importanza e dal ruolo cruciale dell'entanglement, abbiamo rivolto la nostra attività di ricerca alla realizzazione di stati entangled complessi, così come alla teorizzazione di un approccio universalmente valido e in grado di caratterizzare in pieno l'entanglement di questi. Un obiettivo importante che ci siamo prefissati nella derivazione di tale approccio era che questo permettesse di caratterizzare l'entanglement attraverso misure da effettuare con il minore sforzo sperimentale possibile. La fattibilità di un esperimento è infatti una condizione basilare per poter applicare l'entanglement nella tecnologia moderna.

Al fine di raggiungere tali obiettivi, abbiamo innanzitutto esplorato degli stati quantistici che abbiamo poi potuto usare come base per realizzare stati entangled complessi (costituiti cioè da più parti e da più livelli, o dimensioni). Questo studio ci ha condotti a realizzare per la prima volta in assoluto su una piattaforma integrata (“on-chip”) coppie di fotoni multidimensionali ed entangled in frequenza. Abbiamo inoltre manipolato e processato in maniera coerente i suddetti stati al fine di caratterizzarne la dimensionalità (tramite la decomposizione in modi di Schmidt) e l'entanglement (tramite interferenza quantistica, violazione delle disuguaglianze di Bell e tomografia quantistica). Tale analisi ci ha fornito le basi per derivare l'approccio universale sopra menzionato.

Nella presente attività di ricerca, abbiamo sviluppato un metodo teorico per derivare un operatore di entanglement witness universale in grado di individuare la presenza di stati quantistici puri qualsivoglia complessi e di determinarne l'eventuale entanglement. Abbiamo inoltre formulato una tecnica che permette di adattare e/o modificare il witness (pur mantendendone inalterate le proprietà matematiche) in base a specifiche restrizioni sperimentali e/o alla strumentazione disponibile in laboratorio, in modo tale da renderne la misura sperimentalmente fattibile. Questa caratteristica fa da tramite fra il lavoro teorico riportato in questa tesi e gli esperimenti presentati nella stessa. Infine, partendo dall'espressione più generale del witness, ne abbiamo formulato uno specificamente designato per individuare la presenza e l'entanglement di stati cluster multipartiti e multidimensionali. Questo particolare witness è stato quindi utilizzato per esaminare

la robustezza di tali stati cluster rispetto al rumore sperimentale (rumore bianco, nello specifico).

In relazione a questo risultato, abbiamo dimostrato per la prima volta in assoluto un cluster state di fotoni quadri-partito a tre livelli (qutrit), nel quale cioè ognuna delle quattro parti è caratterizzata da tre livelli quantizzati. Lo stato cluster è stato realizzato facendo uso di due fotoni aventi entanglement simultaneo (hyper-entanglement) in tempo e frequenza. La genuinità dell'entanglement multipartito del cluster state è stata dimostrata tramite l'operatore witness da noi stessi derivato. I cluster states formano una classe di sistemi multipartiti il cui entanglement gode di proprietà uniche che rendono questi stati cruciali per la realizzazione dei cosiddetti "one-way" quantum computers. Facendo misure di proiezione in tempo e in frequenza sullo stato cluster, abbiamo dimostrato la prima prova di concetto in assoluto di one-way quantum processing a più dimensioni. Se da un lato i cluster states sono già stati dimostrati in letteratura facendo uso di fotoni a due livelli (qubits), la loro estensione a fotoni a più livelli (qudits) non era mai stata dimostrata prima del lavoro di ricerca descritto in questa tesi. L'importanza dei cluster states per la fisica fondamentale e le loro potenziali applicazioni nella tecnologia quantistica sono fra le motivazioni principali che ci hanno spinto a studiare questi stati e ad estenderli a dimensioni superiore a due.

I fotoni di cui sopra sono stati generati su una piattaforma integrata ("on-chip") e sono stati interamente manipolati e processati tramite componenti in fibra compatibili con le infrastrutture standard utilizzate per le telecomunicazioni. Tenendo conto di questo importante aspetto, i risultati riportati in questa tesi si mostrano al passo con gli ultimi avanzamenti della tecnologia, la quale mira a ridurre il più possibile le dimensioni e i costi dei dispositivi di cui fa uso.

Il lavoro compiuto durante questa fase di ricerca è di natura prevalentemente teorica e si è dimostrato cruciale non solo per la realizzazione sperimentale dei suddetti stati quantistici, ma anche per capire quali fossero le misure necessarie da effettuare per caratterizzarne l'entanglement.

Affinché il lettore possa comprendere a pieno il formalismo e gli strumenti utilizzati durante il lavoro di dottorato, la tesi è organizzata come segue. Il Capitolo 1 presenta un'introduzione alla meccanica quantistica e contiene il formalismo usato per descrivere, misurare e analizzare un qualsiasi stato quantistico. In particolare, viene spiegato nel

dettaglio il concetto di misura in meccanica quantistica. Il Capitolo 2 è incentrato sul fenomeno dell'entanglement, il quale viene descritto in ogni suo aspetto fondamentale. Nello specifico, il capitolo si sofferma su due categorie di stati entangled che assumono un ruolo chiave in questo lavoro di ricerca: gli stati di Bell e gli stati hyper-entangled. Nel Capitolo 3 vengono introdotti e spiegati in ogni loro proprietà gli stati quantistici su cui si focalizza principalmente la tesi: i cluster states. Viene quindi presentato l'operatore entanglement witness (per come noto in letteratura), e si descrive come usarlo per determinare e confermare la presenza di entanglement genuino multipartito di cluster states a due livelli (qubits). Infine, nei Capitoli 4, 5 e 6 viene riportata la novelty, e vengono descritti in dettaglio lo studio e i risultati ottenuti durante l'attività svolta nel dottorato di ricerca.

# Chapter 1

## Introduction to quantum mechanics

### 1.1 Fundamentals of quantum mechanics

At the macroscopic scale, nature can be well described by classical mechanics. The fundamental principle of classical physics is that physical variables (also known as ‘degrees of freedom’, namely DOF) such as position  $x$  and momentum  $p$  of a body possess a well-defined value, which can be measured with a finite precision. In case of many-body systems (e.g. ensembles of several particles, like gases), identifying and tracing each unit becomes extremely arduous or even impossible. In this case, statistics is used, which describes the dynamic of many-particle systems in terms of probability distributions (for example, the Maxwell-Boltzmann statistics describes the velocity distribution of the particles composing a gas). Statistics can thus be interpreted as a tool to describe those physical variables of a system that cannot be known exactly, even though they possess a well-defined value. In this sense, classical mechanics is based on determinism, while the concept of uncertainty can be seen as ‘ignorance’ with respect to an otherwise well-defined situation.

When inspecting nature at an atomic scale (for example, atoms or elementary particles such as electrons), it can be realized that classical mechanics fails to describe physical phenomena properly. Microscopic systems can be fully explained only by quantum mechanics that relies on principles that are completely different and revolutionary compared to those of classical physics. Quantum mechanics is a relatively ‘new’ branch of the physics, since its fundamentals were formulated at the beginning of 1900 by a number of physicists, such as Max Planck, Albert Einstein, Niels Bohr, Louis de Broglie, Max

Born, Paul Dirac, Werner Heisenberg, Wolfgang Pauli, Erwin Schrödinger, and Richard Feynman.

A fundamental of quantum physics that does not occur in classical mechanics' descriptions is the *uncertainty principle*, which was formulated by Werner Heisenberg in 1927 [1–3]. It states that the position  $x$  and the momentum  $p$  of a particle (as well as any other physical variable, such as energy) cannot be known at the same time with the same exact precision. The uncertainty principle can be summarized by the inequality  $\Delta x \cdot \Delta p \geq \hbar/2$ , where  $\Delta x$  and  $\Delta p$  are the uncertainties related to measure the position and the momentum of a particle, respectively, while  $\hbar = 1.05457 \times 10^{-34}$  J · s is Planck's constant. From a physical perspective, the inequality means that, the more precisely the position of a particle is determined, the less precisely its momentum can be measured. In this sense, determinism does not and cannot exist in quantum mechanics. On the contrary, it is necessary to describe microscopic systems in terms of the probability of possessing a given value of a physical variable. For such a description, the so-called wave function (alternatively, density function or wave packet)  $\Psi(x, t)$  is used, which usually depends on space and time and embeds all the accessible information than can be known about a quantum system. According to the Born statistical interpretation of the wave function, this gives the probability amplitude of finding the particle at position  $x$ , at time  $t$ . More precisely [2],

$$|\Psi(x, t)|^2 dx = \left\{ \begin{array}{l} \text{probability of finding the particle} \\ \text{between } x \text{ and } x + dx, \text{ at time } t \end{array} \right\} \quad (1.1.1)$$

where  $|\Psi(x, t)|^2$  is the probability density. This concept can be extended to any DOF: the wave function gives the probability amplitude of finding a particle in a certain quantum state, at time  $t$ . Since the particle has to be *somewhere*, or has to be found in a state anyway, the integral of  $|\Psi(x, t)|^2$  must be normalized, i.e.

$$\int_{-\infty}^{\infty} |\Psi(x, t)|^2 dx = 1. \quad (1.1.2)$$

otherwise, the statistical interpretation would be nonsense [2].

Quantum mechanics takes its name from a concept that is intrinsic to such a branch. In classical mechanics, a physical quantity (e.g., the energy, the momentum) can vary continuously over a range of possible values. The quantum counterpart of that quantity is bounded instead to assume certain specific values, while the in-between values are

forbidden. The minimum separation (i.e., the ‘gap’) between two consecutive values is the “quantum” step and is proportional to  $\hbar$ . In that sense, the non-classical physical variable is defined as ‘quantized’.

Another basic concept that is exclusive for quantum mechanics is *superposition*, which relies on the property that a non-classical unit can be, at the same time, in a combination of two distinct quantum states of the same physical variable. The concept of superposition can be explained by considering, for example, energy. Classically, a particle can have either the energy  $\varepsilon_1$  or the energy  $\varepsilon_2$ . According to quantum mechanics, the particle can possess both  $\varepsilon_1$  and  $\varepsilon_2$ , while it is not possible to determine which one until the energy is measured. In particular, as it will be clarified in section 1.3, detecting the energy of the particle forces it to ‘collapse’ in the energy that is measured. In this sense, a measurement results in the so-called ‘collapse of the wave function’. This is obviously in contrast with classical physics, according to which a particle possesses a specific, defined, and finite physical variable prior to and independent of any measurement.

Another important concept of quantum mechanics is the *wave-particle duality*. Any quantum entity can behave and can be described as either a particle or a wave. For example, at a quantum scale, the electromagnetic radiation, i.e. the light, behaves like a particle, which is called photon (see section 1.6).

## 1.2 Formalism of quantum mechanics

### 1.2.1 Dirac’s notation

The description as well as the characterization of the novel quantum states presented in this thesis (i.e. high-dimensional frequency-entangled Bell and multipartite cluster states) have been pursued by making use of the so-called Dirac’s approach, which was introduced by Paul Dirac [1, 3]. Making use of the ‘bra-ket’ notation, this approach is very useful to describe quantum systems. The Dirac formalism consists of describing quantum states in a complex vector space, known as Hilbert space  $\mathcal{H}^d$ , where  $d$  denotes the number of physical components within that space (or, equivalently, the single-state dimensionality). In this section, the bra-ket notation will be described in all the features that can be useful to better understand the mathematical formalism used in this thesis.

A state vector in the space  $\mathcal{H}^d$  is known as ‘ket’ and is denoted by

$$|\alpha\rangle = \begin{pmatrix} a_1 \\ \vdots \\ a_d \end{pmatrix}, \quad (1.2.1)$$

where  $\alpha$  represents the physical variable and  $a_1, \dots, a_d$  its components (scalar numbers, usually complex). The ket contains complete information about the system; everything that one is allowed to ask and to know about the quantum system is contained within the ket. Multiplying a ket  $|\alpha\rangle$  by a (complex) number  $\alpha$  results in another ket, i.e.  $\alpha|\alpha\rangle$ . For any ket  $|\alpha\rangle$ , its complex conjugate (i.e., the dual) always exists and is called ‘bra’. This is defined as  $\langle\alpha| \equiv (|\alpha\rangle)^\dagger = (a_1 \cdots a_d)$ , where  $\dagger$  denotes the conjugate transpose, while  $*$  stands for the complex conjugate. The bra which is dual to  $\alpha|\alpha\rangle$  is  $\alpha^* \langle\alpha|$ , not  $\alpha \langle\alpha|$ .

Three important products can be defined between kets and bras: the scalar (or inner), the tensor, and the outer products. These three products have been widely used in the research work presented here in order to define, characterize, and measure the wave function of the realized quantum states. For this reason, it is necessary to introduce these products to the reader at this stage.

**Scalar (or inner) product.** Given a bra  $\langle\beta|$  and a ket  $|\alpha\rangle$ , the scalar product is defined as

$$\langle\beta|\alpha\rangle = (b_1^* \cdots b_d^*) \cdot \begin{pmatrix} a_1 \\ \vdots \\ a_d \end{pmatrix} \quad (1.2.2)$$

which results in a scalar number (usually complex), similarly to the scalar product between two vectors in the Euclidean space. Two fundamental postulates characterize the inner product. First,  $\langle\beta|\alpha\rangle = \langle\alpha|\beta\rangle^*$ ; second,  $\langle\alpha|\alpha\rangle \geq 0$ , with the equality holding only if  $|\alpha\rangle$  is a vanishing ket (i.e. with only zero components). Two quantum states  $|\alpha\rangle$  and  $|\beta\rangle$  are orthogonal if  $\langle\beta|\alpha\rangle = 0$ .

**Tensor product.** This product is crucial to understand quantum systems which are formed by two or more parties (for example, the Bell and cluster states demonstrated here). Suppose there are two different Hilbert spaces, namely  $V$  and  $W$ , having both dimensionality  $d$ . Their tensor product is written as  $V \otimes W$  and results in a new,  $d \times d$ -dimensional Hilbert space. The vectors composing the space  $V \otimes W$  are of the form  $|v\rangle \otimes |w\rangle$ , with  $|v\rangle \in V$  and  $|w\rangle \in W$ . For simplicity, the abbreviated notations

$|v\rangle|w\rangle$  or  $|v,w\rangle$  will be used throughout this thesis instead of  $|v\rangle \otimes |w\rangle$ .

**Outer product.** The outer product between a  $d$ -dimensional ket  $|\alpha\rangle$  and a bra  $\langle\beta|$  of same dimension results in a matrix of the form

$$|\alpha\rangle\langle\beta| = \begin{pmatrix} a_1 \\ \vdots \\ a_d \end{pmatrix} \cdot (b_1^* \cdots b_d^*) = \begin{pmatrix} a_1 b_1^* & \cdots & a_1 b_d^* \\ \vdots & \ddots & \vdots \\ a_d b_1^* & \cdots & a_d b_d^* \end{pmatrix} \quad (1.2.3)$$

The outer product has been exploited in this thesis in order to express the density matrix (defined in section 1.4) of the quantum states derived here.

## 1.2.2 Observables, operators, and matrices

Any physical quantity can be measured, that is, it can be observed. For this reason, a measurable quantity is called ‘observable’. As a postulate of quantum mechanics, any measurement has an operator that is associated to it. This operator, usually denoted by a capital letter, e.g.  $O$ , is represented with a matrix, and thus with an outer product of the form  $O = |\alpha\rangle\langle\beta|$ . In quantum mechanics, an operator acts on a ket in a similar manner as a matrix acts on a vector in linear algebra. The action is denoted as  $O \cdot (|v\rangle) = O|v\rangle$  and allows us to define a set of eigenvalues and eigenstates (or eigenkets) for the operator  $O$  with respect to the quantum state  $|v\rangle$ . Specifically, given an observable  $O$ , the eigenkets of  $O$  with respect to  $|v\rangle$  are defined as the vectors  $|v_1\rangle, |v_2\rangle, \dots, |v_d\rangle$  satisfying the eigenvalue equations

$$O|v_1\rangle = \lambda_1|v_1\rangle, \quad O|v_2\rangle = \lambda_2|v_2\rangle, \quad \dots, \quad O|v_d\rangle = \lambda_d|v_d\rangle, \quad (1.2.4)$$

where  $\lambda_1, \lambda_2, \dots, \lambda_d$  are the eigenvalues and  $|v_1\rangle, |v_2\rangle, \dots, |v_d\rangle$  are the eigenstates. A similar set of equations can be written for the Hermitian conjugate of  $O$  (i.e.  $O^\dagger = |\beta\rangle\langle\alpha|$ ) with respect to the bra  $\langle v|$  as

$$\langle v_1|O^\dagger = \lambda_1^*\langle v_1|, \quad \langle v_2|O^\dagger = \lambda_2^*\langle v_2|, \quad \dots, \quad \langle v_d|O^\dagger = \lambda_d^*\langle v_d|. \quad (1.2.5)$$

An operator  $H$  is defined Hermitian if  $H = H^\dagger$  and is characterized by a very important property which is defined by following theorem [2]:

*The eigenvalues of a Hermitian operator  $H$  are real; the eigenkets of  $H$  corresponding to different eigenvalues are orthogonal.*

Together with uniqueness, the first part of the theorem leads to the basic concept that all observable (measurable) properties of a quantum system must be represented by Hermitian operators. Since the eigenvalues of an operator are the outcomes of its measurement and since only real variables can be experimentally determined, the operator describing a physical quantity must be Hermitian. The second part of the theorem defines a basis of orthogonal states (i.e. the so-called eigenbasis) which span and fully describe the Hilbert space of a given quantum state. Considering again the tensor product defined at the end of subsection 1.2.1, if  $|i\rangle$  and  $|j\rangle$  are orthonormal basis for the Hilbert spaces  $V$  and  $W$ , respectively, then any state of the form  $|i\rangle \otimes |j\rangle$  is a basis for  $V \otimes W$  [4].

The matrix representing a Hermitian operator can be always expressed in the basis of its eigenstates. This operation is known as diagonalization [4]. One of the main scopes of this research work was to characterize the entanglement of a high dimensional multipartite optical cluster state. As it will be shown in chapter 6, this task required to measure specific physical observables of the quantum state (time and frequency). These measurements could be accomplished solely through novel high dimensional quantum operators that we developed in this research work and that were capable of detecting physical observables. Therefore, the analytical proof that such operators were Hermitian was a crucial step in order to proceed with quantum state analysis and measurements. This proof is provided in Appendix I [5].

### 1.3 Measurements in quantum mechanics

Deriving and measuring quantum operators was one of the main scopes of this research work. In particular, all the measurements that we could perform and that were necessary for Bell inequality violations [6, 7], quantum state tomography [6], and witness detection [7], are the so-called ‘projection measurements’ [4]. It is thus worth to describe the concept of measurement in quantum mechanics (already outlined in section 1.1, though), as well as the concept of expectation value, which is strictly connected to projections.

In [3], Paul Dirac states: “A measurement always causes the system to jump into an eigenstate of the dynamical variable that is being measured”. To explain this statement,

suppose that, before measuring an observable  $M$ , the wave function  $|\psi\rangle$  representing the quantum system is in a superposition of the set of the eigenstates  $\{|m\rangle\}$  of  $M$  [1]:

$$|\psi\rangle = \sum_{m=1}^d c_m |m\rangle, \quad (1.3.1)$$

where  $c_m$  are complex numbers such that  $\sum_m |c_m|^2 = 1$ . When the system is measured through a projection, it causes the collapse of the system into one of the eigenstates  $|m\rangle$  (which is unknown prior to the measurement) as

$$|\psi\rangle \xrightarrow{\text{M measurement}} |m\rangle. \quad (1.3.2)$$

The coefficients  $c_m$  denote the probability amplitude that, after the measurement, the quantum state collapses into a specific state  $|m\rangle$ . Chosen a measurement setting  $\{|m\rangle\}$ , the probability of projecting the quantum state  $|\psi\rangle$  into  $|m\rangle$  is defined as the absolute square of the scalar product between the wave function and the measurement setting, i.e.

$$\text{Probability of } m = |\langle m|\psi\rangle|^2. \quad (1.3.3)$$

According to the Dirac notation, this probability can be expressed in a more convenient way as [5]

$$\begin{aligned} \text{Probability of } m &= |\langle m|\psi\rangle|^2 = \langle m|\psi\rangle \langle m|\psi\rangle^* = \langle m|\psi\rangle \langle \psi|m\rangle \\ &= \langle \psi|m\rangle \langle m|\psi\rangle = \langle \psi|M|\psi\rangle = \langle M\rangle, \end{aligned} \quad (1.3.4)$$

where  $\langle M\rangle$  is defined as the expectation value of the operator  $M = |m\rangle\langle m|$  with respect to the state  $|\psi\rangle$  and the outcome  $m$ . It follows that measuring an observable  $M$  via projections performed in the  $M$  eigenbasis  $\{|m\rangle\}$  is equivalent to measuring the expectation value of that observable.

The projection measurements that we derived theoretically and performed experimentally in this research work allowed us to obtain probabilities such as Eq. (1.3.4). Specifically, the measurement outcomes that are necessary for quantum experiment tasks take the form of probabilities Eq. (1.3.4). This aspect will be clear to the reader in chapter 4 and chapter 6, where the measurements accomplished here are described in detail.

The relation between the probability of a measurement outcome and the expectation value of an observable shows an important concept in quantum mechanics: the expectation value of any quantum operator can only be measured in its eigenbasis [4, 5]. In this

work we measured the expectation value of the witness by expressing all the matrices composing it in the diagonal form and measuring them in their respective eigenbasis.

More in general, a projector can be defined as follows. Assume  $W$  is a  $k$ -dimensional subspace of the  $d$ -dimensional space  $V$ , where the dimensionality of  $W$  is different with respect to the dimensionality of  $V$ . It is possible to construct an orthonormal basis  $\{|1\rangle, \dots, |d\rangle\}$  for  $V$  such that  $\{|1\rangle, \dots, |k\rangle\}$  is an orthonormal basis for  $W$ . By definition,

$$P \equiv \sum_{i=1}^k |i\rangle\langle i| \quad (1.3.5)$$

is the projector into the sub-space  $W$ . Such a definition is independent on the orthonormal basis  $\{|1\rangle, \dots, |k\rangle\}$  used for  $W$  [4]. The projector is a Hermitian operator, having thus real eigenvalues and satisfying the conditions  $P = P^\dagger$  and  $P^2 = P$ .

## 1.4 Density matrix

An approach that is particularly useful to describe quantum systems consisting of two or multiple parties (i.e., its physical components, or units), relies on the so-called density matrix  $\rho$ , which provides all information about a quantum state [4]. Experimentally, the density matrix of a realized quantum state can be constructed via the so-called quantum state tomography technique [8] which allows us to compare the realized state with the ideal target (see section 2.6). Here, in order to characterize the high-dimensional frequency-entangled states demonstrated in [6], we made use of the density matrix formalism and validated the quality of the generated state via quantum state tomography (see subsection 4.2.3).

The density matrix enables us to distinguish ‘pure’ from ‘mixed’ states. A quantum system is in a pure state if its wave function  $|\psi\rangle$  is known exactly. Such a system is isolated from the environment, with which it does not interact [9]. In this case the density operator is simply given by  $\rho = |\psi\rangle\langle\psi|$  [4]. Otherwise,  $\rho$  is in a mixed state. Specifically, this happens in the case of open quantum systems interacting with the environment, as well as in the presence of classical noise [9]. The quantum system is thus given by a combination of states  $|\psi_i\rangle$ , each having a probability  $p_i$ , and the density matrix results in  $\rho = \sum_{i=1}^d p_i |\psi_i\rangle\langle\psi_i|$ . Pure and mixed states obey the conditions  $Tr(\rho^2) = 1$  and  $Tr(\rho^2) < 1$ , respectively, where  $Tr()$  denotes the trace of the matrix (resulting in a number). The novel Bell and cluster states demonstrated here are both pure states.

Furthermore, the approach presented in this thesis to derive universal witnesses assumes that the quantum system under analysis is in a pure state and can be thus expressed as  $\rho = |\psi\rangle\langle\psi|$  [5].

A crucial relation exists between the expectation value of an observable and the density matrix of the quantum state that is measured by that observable. Assume that  $\rho$  is expressed in the orthonormal basis  $\{|i\rangle\}$  that coincides with the basis in which the operator  $M$  is measured. It can be found that [4]

$$\langle M \rangle = \langle \psi | M | \psi \rangle = \sum_i \langle i | M | \psi \rangle \langle \psi | i \rangle = \text{Tr}(M |\psi\rangle\langle\psi|) = \text{Tr}(M\rho) \quad (1.4.1)$$

In order to determine the noise tolerance of the novel witness operators as well as of the realized cluster states, we made use of the relation expressed in Eq. (1.4.1). Specifically, the use of this relation will be clear to the reader in subsection 5.2.1 [5, 7].

## 1.5 Qubits and qudits

Quantum mechanics is important not only for a better understanding of fundamental physics, but also for modern technology applications. For example, a quantum system can be used to process, encode, and store information, as well as for quantum computing [4]. For example, we made use of the here demonstrated  $d$ -level cluster states to implement proof-of-principle high-dimensional one-way quantum processing [7] (see introduction of chapter 3 and section 6.4). The possibility of using quantum states for these tasks leads to introduce the concepts of ‘qubit’ and ‘qudit’. Since the novel Bell [6] and cluster [7] states demonstrated here are both qudit systems, it is important to define these two concepts, as well as the differences between qubits and qudits. Explaining these differences will contribute to understand the motivation that induced us to consider high dimensional systems for the research studies pursued here.

In order to introduce, first, the concept of qubit, and then of qudit, it is necessary to consider two tasks that are at the basis of computers. These are information processing and storing. Classical (ordinary) computers perform these tasks by making use of ‘bits’; a bit can be seen as a piece of information that, using a binary-digit language, can exist, at a time, either in the state 0 or in the state 1. On the other hand, quantum computers can process and store information by exploiting the concept of superposition introduced in section 1.1. Information can thus exist both in the states  $|0\rangle$  and  $|1\rangle$  at the same time,

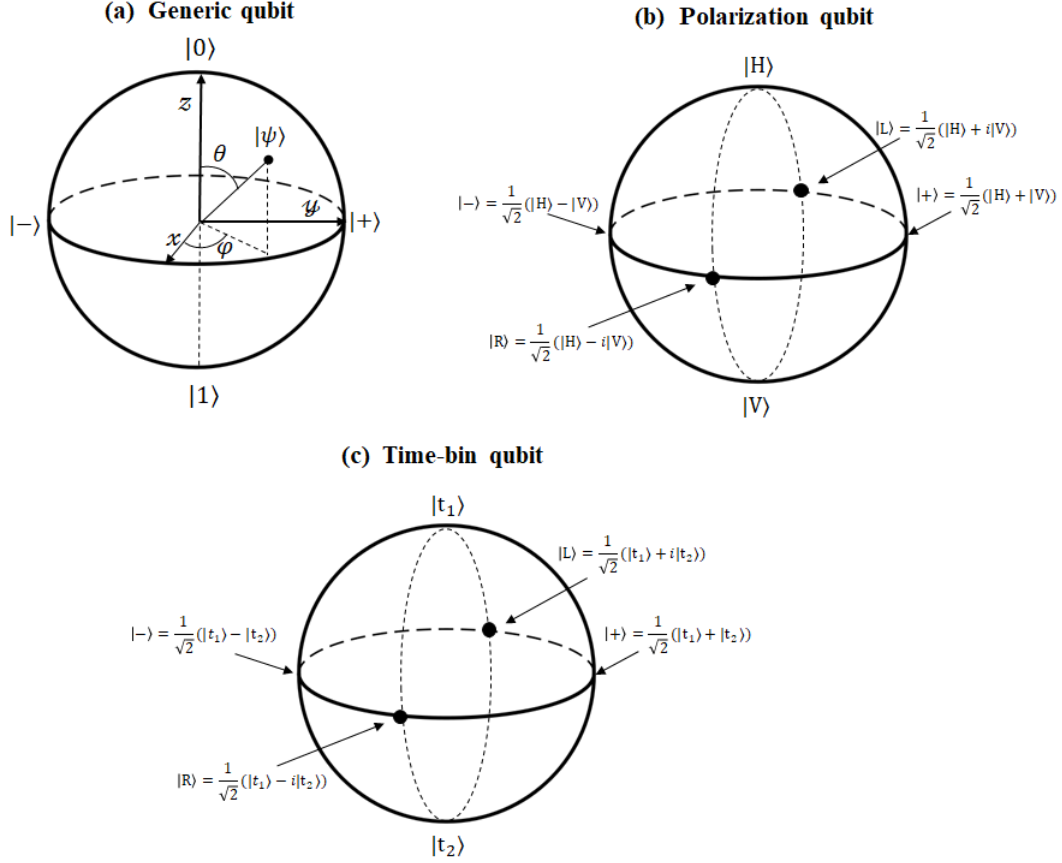


**Figure 1.1** – Representation of a qubit state in the Bloch sphere. **(a)** Representation of a generic two-level quantum state  $|\psi\rangle$  spanning the points (e.g. the two poles  $|0\rangle$  and  $|1\rangle$ ) as well as the angles  $\theta$  and  $\varphi$  of the Bloch sphere. **(b-c)** Physical representation of the Bloch sphere for **(b)** polarization and **(c)** time-bin qubits.

i.e. in a two-level (or two-dimensional) system. This concept is expressed as ‘quantum bit’ or ‘qubit’, and the superposition of the two bits can be written as

$$|\psi\rangle = a_0 |0\rangle + a_1 |1\rangle. \quad (1.5.1)$$

The coefficients  $a_0$  and  $a_1$  are complex numbers that give the probability amplitude that the system is found in one of the two states  $|0\rangle$  and  $|1\rangle$ , respectively, and that satisfy the normalization condition  $|a_0|^2 + |a_1|^2 = 1$ . In a vector notation, the kets  $|0\rangle$  and  $|1\rangle$  form the so-called ‘computational basis’ of the Hilbert space of  $|\psi\rangle$  and are defined as

$$|0\rangle = \begin{pmatrix} 1 \\ 0 \end{pmatrix}, \quad |1\rangle = \begin{pmatrix} 0 \\ 1 \end{pmatrix}. \quad (1.5.2)$$

Qubits can be easily described by making use of a geometric representation. Consider a so-called Bloch sphere, where  $|0\rangle$  is the north pole and  $|1\rangle$  the south pole, while  $\theta$  and  $\varphi$

are the polar and azimuthal angles, respectively (see Figure 1.1-a). A generic qubit state within this sphere can be written as

$$|\psi\rangle = \cos\left(\frac{\theta}{2}\right)|0\rangle + e^{i\phi}\sin\left(\frac{\theta}{2}\right)|1\rangle \quad (1.5.3)$$

and, in contrast with a classical state, it can span any direction of the Bloch sphere at the same time. Since quantum computers make use of superposition systems like  $|\psi\rangle$ , they can process and store a higher amount of information compared to their classical counterparts that instead operate by using single states (bits) at a time.

The amount of information that quantum computers can process and store, can be significantly increased by making use of  $d$ -level (i.e. high-dimensional, with  $d > 2$ ) systems, also known as ‘qudits’ [10]. A generic qudit state  $|\psi\rangle$  is defined as the superposition

$$|\psi\rangle = \sum_{i=0}^{d-1} a_i |i\rangle, \quad (1.5.4)$$

where  $d$  denotes the number of levels (or the single-state dimensionality), and the coefficients  $a_i$ , satisfying the condition  $\sum_{i=0}^{d-1} |a_i|^2 = 1$ , denote the probability for the system  $|\psi\rangle$  to be found in one of the states  $|i\rangle$ . The computational basis  $\{|i\rangle\}$  is represented in a vector notation as

$$|0\rangle = \begin{pmatrix} 1 \\ 0 \\ \vdots \\ 0 \end{pmatrix}, \quad |1\rangle = \begin{pmatrix} 0 \\ 1 \\ \vdots \\ 0 \end{pmatrix}, \quad \dots, \quad |d-1\rangle = \begin{pmatrix} 0 \\ 0 \\ \vdots \\ 1 \end{pmatrix}. \quad (1.5.5)$$

Qudits exhibit several advantageous properties over qubits. For example, they can be used to increase the sensitivity of quantum imaging schemes [11], to improve the robustness and the key-rate of quantum communication protocols [12], as well as to achieve more efficient and error-tolerant quantum computation [10]. Furthermore, compared to qubits, qudit systems are more tolerant to noise emerging from, e.g., experimental conditions and measurement settings [5–7, 13]. In this work, we validated this property both for the high-dimensional Bell states (chapter 4) and for the multipartite cluster states (chapter 5 and chapter 6). Specifically, we present a novel result which affirms that, also for multipartite systems, qudits are more tolerant to noise than qubits [5, 7] (see subsection 5.2.1 and subsection 6.3.3).

In a two-level state, the Hilbert space dimensionality is given by  $2^N$ , where  $N$  denotes the number of parties, whereas, in a  $d$ -level system, the Hilbert space size is given by

$d^N$ . Therefore, while increasing the Hilbert space size of qubit systems is bound by the number of parties, in case of qudits, the single state dimensionality  $d$  can also be leveraged for that purpose.

Qudits can be implemented physically by making use of several quantum systems. In this work, we accomplished this task by exploiting the quantum states of lights, i.e. photons, which have been used here to realize high-dimensional Bell [6] and cluster [7] states.

## 1.6 Quantum states of light: photons

Photons play a central role in the development of modern technology, which owes its origin to quantum optics that is both a fundamental scientific subject and a testing ground for quantum information science. In this section, some photons' features will be outlined that are useful to understand why they are widely used in both the literature and here in this work.

Photons are massless particles that travel, in the vacuum, at the constant velocity  $c = 2.99792458 \times 10^8$  m/s while carrying information (in analogy with the electromagnetic radiation). Although massless, photons possess an intrinsic energy due to their non-vanishing momentum defined as  $p = \hbar k$ , where  $\hbar$  is the Planck constant introduced in section 1.1 and  $k = 1/\lambda$ , with  $\lambda$  being the photon's wavelength. The intrinsic photon energy is thus given by  $E_p = \hbar\nu$ , where  $\nu = c/\lambda$  is the frequency of the photon [14–16].

Photons exhibit several features that make them particularly suitable for the development of new technologies based on photonic platforms. First, they possess many external as well as internal degrees of freedom. External DOFs include, for example, the spatial position (i.e. the location that a photon can occupy at a time), the path traveled by a photon in, e.g., a waveguide or optical fiber, and so forth. Internal degrees of freedom include, for example, polarization [16] (which is equivalent to the direction of the electromagnetic field oscillation), orbital angular momentum [17] (OAM, i.e. the quantum equivalent of the orientation of classical light in space), the generation time (or, equivalently, the arrival time of a photon to a detector), also known as time-bin [12, 18, 19], and the frequency, known also as frequency-bin [6, 20].

Photons are chargeless particles which do not interact with each other (in contrast

to, e.g., electrons). Furthermore, they may weakly interact with the environment, which makes them highly robust towards perturbations which the latter may cause.

Finally, photons exhibit a long coherence time. This means that, in contrast with other quantum systems, they are affected by decoherence only if exposed to different environments that lead to different noise contributions (for example, when they travel through distinct propagating channels). Due to this property, photons can propagate over long distances (several hundreds [21–23] or even few thousands [24] of kilometers) and can be used thus for, e.g., quantum communication protocols and telecommunications, since their transmission is also compatible with established fiber-based infrastructures [6, 19, 23].

Long before their exploitation for quantum technologies, photons have been widely used for fundamental physics experiments, aimed to better explore quantum phenomena such as entanglement (see chapter 2). Early experiments have been performed mainly in free space by making use of polarization [25, 26], optical path [27], and OAM [25] modes. Over the years, the development of quantum technologies, as well as the widespread use of fiber-based telecommunication infrastructures, have led to exploit other robust and fiber-compatible DOFs, such as time [18, 19, 28] and frequency [6, 20]. Benefitting from new technology advancements, in this work we exploited frequency for realizing high-dimensional Bell states [6], as well as both time and frequency for demonstrating cluster states [7].

## 1.7 The Pauli matrices

A very important class of Hermitian operators is formed by the four  $2 \times 2$  Pauli matrices  $\sigma_i$ , with  $i = 0, x, y, z$  [4]. These matrices are extremely useful for fundamental physics and experiments, since they can be used to measure physical observables such as polarization [29–31]. They further play a crucial role in quantum computation and information science, since they allow the implementation of many quantum operations such as quantum state rotations [4]. In the standard two-level computational basis  $\{|0\rangle, |1\rangle\}$ ,

the Pauli matrices are

$$\begin{aligned}\sigma_0 \equiv \mathbb{I} &= \begin{pmatrix} 1 & 0 \\ 0 & 1 \end{pmatrix}, & \sigma_x &= \begin{pmatrix} 0 & 1 \\ 1 & 0 \end{pmatrix}, \\ \sigma_y &= \begin{pmatrix} 0 & -i \\ i & 0 \end{pmatrix}, & \sigma_z &= \begin{pmatrix} 1 & 0 \\ 0 & -1 \end{pmatrix},\end{aligned}\tag{1.7.1}$$

or, equivalently,

$$\begin{aligned}\sigma_0 &= |0\rangle\langle 0| + |1\rangle\langle 1| \\ \sigma_x &= |0\rangle\langle 1| + |1\rangle\langle 0| \\ \sigma_y &= -i(|0\rangle\langle 1| - |1\rangle\langle 0|) \\ \sigma_z &= |0\rangle\langle 0| - |1\rangle\langle 1|.\end{aligned}\tag{1.7.2}$$

Together with the Hermitian property, i.e.  $\sigma_i^\dagger = \sigma_i$ , Pauli's matrices exhibit many important features. Their square results in the identity matrix, i.e.  $\sigma_{0,x,y,z}^2 = \mathbb{I}$ , while  $\sigma_{x,y,z}$  are traceless, i.e.  $Tr(\sigma_{x,y,z}) = 0$ , and have determinant equal to  $-1$ , i.e.  $\det(\sigma_{x,y,z}) = -1$ .

The Pauli operators  $\sigma_{x,y,z}$  do not commute and satisfy the commutation rules [32]

$$\begin{aligned}[\sigma_x, \sigma_y] &= 2i\sigma_z, \\ [\sigma_y, \sigma_z] &= 2i\sigma_x, \\ [\sigma_z, \sigma_x] &= 2i\sigma_y, \\ [\sigma_i, \sigma_i] &= 0 \quad \forall i.\end{aligned}\tag{1.7.3}$$

The Pauli matrices  $\sigma_{x,y,z}$  have all eigenvalues  $\pm 1$ , but they have different eigenstates. In particular, the eigenvalue equations associated to the Pauli matrices are:

$$\begin{aligned}\sigma_0 |0\rangle &= |0\rangle & \sigma_0 |1\rangle &= |1\rangle \\ \sigma_x |+\rangle &= |+\rangle & \sigma_x |-\rangle &= -|-\rangle \\ \sigma_y |L\rangle &= |L\rangle & \sigma_y |R\rangle &= -|R\rangle \\ \sigma_z |0\rangle &= |0\rangle & \sigma_z |1\rangle &= -|1\rangle,\end{aligned}\tag{1.7.4}$$

with  $|\pm\rangle = 1/\sqrt{2}(|0\rangle \pm |1\rangle)$ ,  $|L\rangle = 1/\sqrt{2}(|0\rangle + i|1\rangle)$ , and  $|R\rangle = 1/\sqrt{2}(|0\rangle - i|1\rangle)$ . According to these equations, all the Pauli matrices, expressed in their respective eigenbasis,

become diagonal:

$$\begin{aligned}
\sigma_0 &= |0\rangle\langle 0| + |1\rangle\langle 1| \\
\sigma_x &= |+\rangle\langle +| - |-\rangle\langle -| \\
\sigma_y &= |L\rangle\langle L| - |R\rangle\langle R| \\
\sigma_z &= |0\rangle\langle 0| - |1\rangle\langle 1|.
\end{aligned} \tag{1.7.5}$$

Expressing the Pauli matrices in their eigenbasis is not only a crucial condition for their measurement, but also emphasizes that they can be measured by means of projections (see section 1.3). For example, assume we want to measure the expectation value of  $\sigma_x$ ; this can be possible by only expressing this matrix as  $\sigma_x = |+\rangle\langle +| - |-\rangle\langle -|$ . With this in mind, the expectation value of  $\sigma_x$  with respect to a generic quantum state  $|\psi\rangle$  is [5]

$$\langle \sigma_x \rangle = \langle \psi | \sigma_x | \psi \rangle = \langle \psi | + \rangle \langle + | \psi \rangle - \langle \psi | - \rangle \langle - | \psi \rangle = |\langle + | \psi \rangle|^2 - |\langle - | \psi \rangle|^2. \tag{1.7.6}$$

From the expression above, it can be seen that  $\sigma_x$  can be measured by means of several single-party projections that are summed up. In particular, two measurements are needed here. One projects the quantum state onto  $|+\rangle$ , and the other projects  $|\psi\rangle$  onto  $|-\rangle$ . A similar argument holds for  $\sigma_0$ ,  $\sigma_z$ , and  $\sigma_y$ , for which the two projection settings are  $\{|0\rangle, |1\rangle\}$  and  $\{|L\rangle, |R\rangle\}$ , respectively. Measuring the Pauli matrices with only two projection settings is at the basis of the witness (i.e. a quantum operator, the detailed definition and description of which are provided in section 3.3) that has been developed in the literature, as well as of the witness derived here, in order to measure cluster states of qubits [33] (subsection 3.3.1) and qudits [5] (chapter 5), respectively.

Another matrix that is important to introduce is the  $2 \times 2$  Hadamard matrix [4]

$$H = \frac{1}{\sqrt{2}} \begin{pmatrix} 1 & 1 \\ 1 & -1 \end{pmatrix}, \tag{1.7.7}$$

which is unitary ( $H^\dagger H = H H^\dagger = \mathbb{I}$ ) and Hermitian ( $H^\dagger = H = H^{-1}$ ). The action of the Hadamard matrix on the computational basis as well as in a superposition, results in a basis change. Specifically [4]:

$$\begin{aligned}
H |0\rangle &= \frac{1}{\sqrt{2}} (|0\rangle + |1\rangle) \equiv |+\rangle, \\
H |1\rangle &= \frac{1}{\sqrt{2}} (|0\rangle - |1\rangle) \equiv |-\rangle, \\
H |+\rangle &\equiv H \frac{1}{\sqrt{2}} (|0\rangle + |1\rangle) = |0\rangle, \\
H |-\rangle &\equiv H \frac{1}{\sqrt{2}} (|0\rangle - |1\rangle) = |1\rangle.
\end{aligned} \tag{1.7.8}$$

Finally, the Hadamard matrix allows us to transform a Pauli matrix into another Pauli matrix as:

$$\begin{aligned}
\sigma_x &= H\sigma_zH^\dagger \\
\sigma_z &= H\sigma_xH^\dagger \\
\sigma_y &= -H\sigma_yH^\dagger.
\end{aligned}
\tag{1.7.9}$$

## 1.8 The generalized Pauli matrices

The high-dimensional ( $d \times d$ ) Pauli matrices are the generalization of the  $2 \times 2$  Pauli matrices for  $d$ -level quantum systems and observables. However, they exhibit very different properties with respect to their two-level counterparts. First of all, only an extension of  $\sigma_0$ ,  $\sigma_x$ , and  $\sigma_z$  can be defined directly. Specifically [34]:

$$\Sigma_0 \equiv \mathbb{I}_d = \begin{pmatrix} 1 & 0 & 0 & \cdots & 0 \\ 0 & 1 & 0 & \cdots & 0 \\ 0 & 0 & 1 & \cdots & 0 \\ \vdots & \vdots & \vdots & \ddots & \vdots \\ 0 & 0 & 0 & \cdots & 1 \end{pmatrix}
\tag{1.8.1}$$

$$\Sigma_x \equiv X = \begin{pmatrix} 0 & 0 & 0 & \cdots & 0 & 1 \\ 1 & 0 & 0 & \cdots & 0 & 0 \\ 0 & 1 & 0 & \cdots & 0 & 0 \\ 0 & 0 & 1 & \cdots & 0 & 0 \\ \vdots & \vdots & \vdots & \ddots & \vdots & \vdots \\ 0 & 0 & 0 & \cdots & 1 & 0 \end{pmatrix}
\tag{1.8.2}$$

$$\Sigma_z \equiv Z = \begin{pmatrix} 1 & 0 & 0 & \cdots & 0 \\ 0 & \omega & 0 & \cdots & 0 \\ 0 & 0 & \omega^2 & \cdots & 0 \\ \vdots & \vdots & \vdots & \ddots & \vdots \\ 0 & 0 & 0 & \cdots & \omega^{d-1} \end{pmatrix}.
\tag{1.8.3}$$

Here,  $\omega = e^{i2\pi/d}$  is the root of unity, which satisfies the property  $1 + \omega + \omega^2 + \cdots + \omega^{d-1} = 0$ .

The product of the generalized Pauli matrices results in

$$\Sigma_z \cdot \Sigma_x = \omega \Sigma_x \cdot \Sigma_z \begin{pmatrix} 0 & 0 & 0 & \cdots & 0 & 1 \\ \omega & 0 & 0 & \cdots & 0 & 0 \\ 0 & \omega^2 & 0 & \cdots & 0 & 0 \\ 0 & 0 & \omega^3 & \cdots & 0 & 0 \\ \vdots & \vdots & \vdots & \ddots & \vdots & \vdots \\ 0 & 0 & 0 & \cdots & \omega^{d-1} & 0 \end{pmatrix} = \Sigma_y. \quad (1.8.4)$$

The resulting matrix is denoted as  $\Sigma_y$  because, in the two-level case, it reduces to  $\sigma_y$ . The set of all the products  $\{\Sigma_x^k \cdot \Sigma_x^{k'}\}_{k,k'=0}^{d-1}$  forms the so-called Pauli group  $\mathcal{P}$  [35]. This group is complete, orthonormal, but not Hermitian, since the generalized Pauli matrices, in contrast with the two-level counterpart, are not Hermitian, i.e.  $\Sigma_{x,z}^\dagger \neq \Sigma_{x,z}$ .

It can be seen that, in analogy with the property  $\sigma_i^2 = \mathbb{I}$ , the relations

$$\Sigma_x^d = \Sigma_z^d = \mathbb{I}_d \quad (1.8.5)$$

hold. Furthermore, each generalized Pauli matrix is connected to its transpose conjugate as

$$\begin{aligned} (\Sigma_z^n)^\dagger &= \Sigma_z^{d-n} \\ (\Sigma_x^n)^\dagger &= \Sigma_x^{d-n} \end{aligned} \quad (1.8.6)$$

where  $n = 1, \dots, d$ . As a consequence, the eigenvalues of  $\Sigma_{x,z}^{d-n}$  (or, equivalently,  $\Sigma_{x,z}^\dagger$ ) are the complex conjugates of the eigenvalues of  $\Sigma_{x,z}^n$  (i.e.  $\Sigma_{x,z}$ ), and vice versa.

The eigenvalue equations defining eigenvalues and eigenstates of  $\Sigma_x$  and  $\Sigma_z$  are given by

$$\begin{aligned} (\Sigma_z)^n &= \omega^{n \cdot k} |k\rangle \\ (\Sigma_x)^n &= \omega^{k \cdot (d-n)} |x_k\rangle, \end{aligned} \quad (1.8.7)$$

with  $k = 0, \dots, d-1$ . The eigenbasis of  $\Sigma_z$  is thus the computational basis  $\{|k\rangle\}_{k=0}^{d-1}$ , while the eigenbasis of  $\Sigma_x$  consists of a linear combination of it, specifically  $\{|x_j\rangle\}_{j=0}^{d-1}$ , with  $|x_j\rangle = 1/\sqrt{d} \sum_{k=0}^{d-1} \omega^{j \cdot k} |k\rangle$ .

According to the eigenvalue equations, the generalized Pauli matrices can be written both in their respective diagonal form as:

$$\begin{aligned} \Sigma_z &= \sum_{k=0}^{d-1} \omega^k |k\rangle \langle k| \\ \Sigma_x &= \sum_{k=0}^{d-1} \omega^{d-k} |x_k\rangle \langle x_k|. \end{aligned} \quad (1.8.8)$$

In analogy with the two-dimensional case, the generalized Pauli matrices can be measured through projections, provided that these are expressed in their respective eigenbasis. As it will be described in detail in chapter 6, in order to determine the expectation value of the novel witness operator, we measured the  $3 \times 3$ -dimensional  $\Sigma_z$  and  $\Sigma_x$  matrices, as well as their transpose conjugates [5, 7] (see subsection 6.3.1).

Similarly to the two-level case, a high-dimensional counterpart of the Hadamard matrix, i.e. the Walsh-Hadamard matrix  $W$ , can be defined. This is unitary, i.e.  $W^\dagger W = WW^\dagger = \mathbb{I}_d$ , where  $W^\dagger = W^{-1}$ , but not Hermitian ( $W^\dagger \neq W$ ). The Walsh-Hadamard matrix  $W$  and its transpose conjugate read respectively:

$$W = \frac{1}{\sqrt{d}} \begin{pmatrix} 1 & 1 & 1 & \dots & 1 \\ 1 & \omega^{d-1} & \omega^{2(d-1)} & \dots & \omega^{(d-1)(d-1)} \\ 1 & \omega^{d-2} & \omega^{2(d-2)} & \dots & \omega^{(d-1)(d-2)} \\ \vdots & \vdots & \vdots & \ddots & \vdots \\ 1 & \omega^2 & \omega^4 & \dots & \omega^{2(d-1)} \\ 1 & \omega & \omega^2 & \dots & \omega^{n-1} \end{pmatrix}, \quad (1.8.9)$$

and

$$W^\dagger = \frac{1}{\sqrt{d}} \begin{pmatrix} 1 & 1 & 1 & \dots & 1 \\ 1 & \omega & \omega^2 & \dots & \omega^{n-1} \\ 1 & \omega^2 & \omega^4 & \dots & \omega^{2(d-1)} \\ \vdots & \vdots & \vdots & \ddots & \vdots \\ 1 & \omega^{d-2} & \omega^{2(d-2)} & \dots & \omega^{(d-1)(d-2)} \\ 1 & \omega^{d-1} & \omega^{2(d-1)} & \dots & \omega^{(d-1)(d-1)} \end{pmatrix}. \quad (1.8.10)$$

The matrix  $W$  allows for a basis change as

$$\begin{aligned} W |k\rangle &= |x_k\rangle, \\ W |x_k\rangle &= |k\rangle, \end{aligned} \quad (1.8.11)$$

with  $k = 0, \dots, d-1$ , as well as to convert a generalized Pauli matrix into another generalized Pauli matrix:

$$\begin{aligned} \Sigma_x &= W \Sigma_z W^\dagger & \Sigma_x^\dagger &= W \Sigma_z^\dagger W^\dagger \\ \Sigma_z &= W \Sigma_x^\dagger W^\dagger & \Sigma_z^\dagger &= W \Sigma_x W^\dagger. \end{aligned} \quad (1.8.12)$$

As it will be described in more detail in chapter 6, we made use of these transformations in order to derive the stabilizers (i.e. quantum operators that are defined and described

in detail in section 3.2 of this thesis) and thus the witness operators for the demonstrated four-partite three-level cluster state [7].

# Chapter 2

## Entanglement

“The best possible knowledge of the whole [entangled state] does not include the best possible knowledge of its parts.”

Erwin Schrödinger, *Naturwissenschaften*, 1935. [36]

In this chapter the phenomenon of entanglement will be explained in all the facets that are useful to understand the quantum states which have been investigated and derived in this work. High-dimensional Bell and cluster states are both entangled systems, even though they exhibit different types of entanglement. For this reason we recurred to two different analyses in order to define the entanglement properties of these two states. Dedicating a whole chapter to entanglement as well as to different types of entangled states is thus crucial for the reader to understand the features of the here derived quantum states.

### 2.1 The concept of entanglement

The term ‘entanglement’ [37–39] originates from the German word “Verschänkung” that literally means “folding the arms” and that the physicist E. Schrödinger attributed to a correlation of quantum nature [36]. Over the decades, the concept of entanglement has changed its facets: while in the early years of quantum mechanics it was considered a ‘mystery’ [40], today entanglement is recognized as an essential resource in quantum information science [37], playing a fundamental role in many tasks such as quantum computation [41], communication [42, 43], teleportation [21], cryptography [25, 44], error correction [45], and dense coding [46].

As an overview of the different standpoints about entanglement, some statements from physicists that have investigated this phenomenon are reported here (unless it is indicated explicitly, the statements are not quotations) [37].

Entanglement is . . .

- a correlation that is stronger than any classical correlation. [John S. Bell]
- a correlation that contradicts the theory of elements of reality. [David Mermin]
- “a trick that quantum magicians use to produce phenomena that cannot be imitated by classical magicians.” [Asher Peres]
- a resource that enables quantum teleportation. [Charles H. Bennett]
- a global structure of the wave function that allows for faster algorithms. [Peter Shor]
- a tool for secure communication. [Artur Ekert]

In spite of the crucial role of entanglement, the mathematical structure of this phenomenon is not fully understood yet, and there is neither a general theory nor a formal definition for it [37]. In order to overcome this issue, lots of effort has been spent on the theoretical investigation of entanglement, as well as on the experimental realization of entangled systems. These attempts have led to promising progresses towards reaching a general theory of entanglement, as well as a complete characterization of this phenomenon [37–39, 47].

Interpreted by Erwin Schrödinger as the “essence of quantum physics” [36], entanglement is a purely non-classical phenomenon that affects those quantum systems consisting of two or more parties and that originates from the fact that a quantum entity (e.g., a particle) can be in a superposition of two or multiple quantum states.

The simplest possible scenario to explain entanglement is a bipartite pure quantum system  $S$  made of two parties, namely  $A$  and  $B$ . The extension to multiple parties will be discussed in section 2.5. Suppose that  $A$  and  $B$  belong to two different Hilbert spaces, i.e.  $\mathcal{H}_A$  and  $\mathcal{H}_B$ , each of them spanned by a basis  $\{|i_A\rangle\}$  and  $\{|j_B\rangle\}$ , respectively, that can assume any dimensionality  $d$ . Assume the systems  $A$  and  $B$  are prepared independently in the quantum states  $|\psi_A\rangle$  and  $|\psi_B\rangle$ , respectively, as well as they do not undergo any interaction. In this case, the wave function of the whole quantum system  $S$  (i.e.  $|\psi_S\rangle$ )

is described by the tensor product  $|\psi_S\rangle = |\psi_A\rangle \otimes |\psi_B\rangle$ . The two subsystems A and B are completely independent and can be fully described by their respective wave functions  $|\psi_A\rangle$  and  $|\psi_B\rangle$ . Any manipulation (e.g. a measurement) of A, has neither influence nor effects on B (and vice versa). The quantum system S is separable. Any bipartite system which is separable is not entangled.

Suppose now that systems A and B undergo some interactions. In this case, the whole system is not separable, and it is impossible to write  $|\psi_S\rangle$  as a tensor product of  $|\psi_A\rangle$  and  $|\psi_B\rangle$ , i.e.  $|\psi_S\rangle \neq |\psi_A\rangle \otimes |\psi_B\rangle$ . This notation means that all accessible information about A cannot be obtained by just measuring A, but measurements on B are also needed. The quantum state  $|\psi_S\rangle$  contains information about both A and B separately, as well as about correlations between their measurements. A and B are thus entangled [32]. The wave function of a generic bipartite pure entangled state is given by

$$|\psi_S\rangle = \sum_{i,j=0}^{d-1} \alpha_{i,j} |i_A\rangle \otimes |j_B\rangle, \quad (2.1.1)$$

where  $\alpha_{ij}$  are the (joint) probability amplitudes that the entangled system, after a measurement on A or B, collapses into a certain quantum state. From the expression of the wave function  $|\psi_S\rangle$ , it can be seen that the two parties composing the entangled system S are both in a superposition of quantum states, i.e.  $|i_A\rangle$  and  $|j_B\rangle$ , while it is impossible to know, prior to the measurement, the quantum state in which the system will collapse.

Despite of a physical (e.g. spatial) separation between A and B, measuring a subsystem (e.g. A) immediately effects the other subsystem (e.g. B), even though no operation is performed on it. The quantum state in which B collapses can be determined, with certainty, from the measurement outcome of A (and vice versa), as there is indeed no ambiguity about this outcome. However, the aspect that makes entanglement a purely quantum phenomenon is that it persists independently of the basis in which the measurement is performed (i.e. the computational basis or a linear combination of it). Otherwise, the correlations can be described classically (that is, in terms of classical probabilities). Although not reported here, this aspect can be demonstrated by means of the density matrix of the entangled system that, in analogy with any other observable, is expressed in the basis used for the measurement (see section 1.3).

At first glance, entanglement seems to contradict the uncertainty principle introduced in section 1.1. Suppose to have an energy-time entangled state, both the energy of the

subsystem A and the arrival time of B can be measured with a finite precision. However, since they are entangled, these two measured quantities can be known at the same time with a higher precision than the limit imposed by the uncertainty principle. This apparent paradox can be however addressed through practical considerations. Physical observables are always determined by experimental measurement settings that can only provide a finite precision, since their measurement outcomes always possess an error. This prevents to have a ‘certain’ knowledge about the measured observable.

## 2.2 The Bell states

Introducing the Bell states is crucial for the reader to understand the fundamental results behind the research work presented in this thesis. In chapter 4 we will indeed report the demonstration of the first ever high-dimensional frequency-entangled photon pairs having the form of Bell states. In chapter 6 we will further show that projecting high-dimensional four-partite cluster states results into different and orthogonal Bell states.

Bell states took their name from the physicist John S. Bell who investigated these systems for the first time in 1964 [48]. Four Bell states can be defined, which form a class of pure bipartite states exhibiting maximally entanglement. Perhaps, the Bell states are the most important and exploited entangled states, since many entanglement applications, such as quantum communication [42, 43] or teleportation [21], rely on the ability to perform Bell measurements [49] (see subsection 2.2.1). They also form a basis for two-partite entangled states of both qubit [32] and qudit [6, 13, 49–51] systems. Specifically, any pure bipartite entangled state can be generated from Bell states by means of *local operations and classical communications* (LOCC) that typically enable us to prepare a quantum state, as well as to create and/or transform an entangled state [4, 52]. *Local operations* (LO) comprise all quantum state manipulations that are allowed by the laws of quantum mechanics (e.g., projection measurements) and that are restricted to the individual parties composing the system. Manipulations that require an interaction between the subsystems cannot be considered local operations. The result of a (local) measurement on one subsystem (e.g. Alice) can be transmitted via *classical communication* (CC) to a receiver (e.g. Bob), who is ready to perform in turn a local operation on ‘his’ subsystem. When A and B are entangled, such a measurement can be conditioned on the result of

the local measurement on A [52].

### 2.2.1 Two-level (qubit) Bell states

Consider a bipartite entangled system  $S$  composed of two-level subsystems A and B. The Hilbert space of the whole system is spanned by the basis  $\{|0_A, 0_B\rangle, |0_A, 1_B\rangle, |1_A, 0_B\rangle, |1_A, 1_B\rangle\}$ . Such a basis can represent any physical variable (e.g. polarization, time, frequency, energy, etc.). The dimensionality of the whole system Hilbert space  $\mathcal{H}_S$  is  $d^N = 2^2 = 4$ , where  $d = 2$  denotes the number of levels per single party, and  $N = 2$  the number of parties. In such a basis, the four Bell states are [32]:

$$\begin{aligned} |\Phi^\pm\rangle &= \frac{1}{\sqrt{2}} (|0_A\rangle |0_B\rangle \pm |1_A\rangle |1_B\rangle) \\ |\Psi^\pm\rangle &= \frac{1}{\sqrt{2}} (|0_A\rangle |1_B\rangle \pm |1_A\rangle |0_B\rangle). \end{aligned} \tag{2.2.1}$$

Let us give the Bell state a physical facet. For that purpose, we consider a two-photon system which is entangled in polarization. Replacing the qubits 0 and 1 with horizontal  $|H\rangle$  and vertical  $|V\rangle$  polarization, respectively, the four Bell states become

$$\begin{aligned} |\Phi^\pm\rangle_{\text{photon}} &= \frac{1}{\sqrt{2}} (|H_A\rangle |H_B\rangle \pm |V_A\rangle |V_B\rangle) \\ |\Psi^\pm\rangle_{\text{photon}} &= \frac{1}{\sqrt{2}} (|H_A\rangle |V_B\rangle \pm |V_A\rangle |H_B\rangle). \end{aligned} \tag{2.2.2}$$

Once the generic definition of Bell states has been introduced, it is opportune to outline their features. To that purpose, consider the two-photon state  $|\Phi^+\rangle_{\text{photon}}$  and assume it is generated by a source of entangled photons (see subsection 2.2.3), as shown in Figure 2.1. Each photon is generated in the quantum superposition  $1/\sqrt{2}(|H_{A(B)}\rangle + |V_{A(B)}\rangle)$ . The photons are then transmitted far apart through two different free-space channels. Two observers, namely A(lice) and B(ob), thus prepare two independent measurement settings per each, so that they can perform projections on photons A and B, respectively. Suppose that only Alice accomplishes this task. For that purpose, she uses a basis spanning the Bloch sphere of photon A (see Figure 1.1-b). This basis can be, for example,  $\{|H_A\rangle, |V_A\rangle, |+_A\rangle, |-_A\rangle\}$  or  $\{|H_A\rangle, |V_A\rangle, |R_A\rangle, |L_A\rangle\}$ , where  $|\pm\rangle = 1/\sqrt{2}(|H\rangle \pm |V\rangle)$  and  $|L/R\rangle = 1/\sqrt{2}(|H\rangle \pm i|V\rangle)$ , and can be realized experimentally with a polarizer, which is capable of rotating polarization. Independently of the measurement setting chosen by Alice, detecting the polarization of photon A immediately affects that of photon B, which collapses in the same polarization as A. For example, if a measurement causes

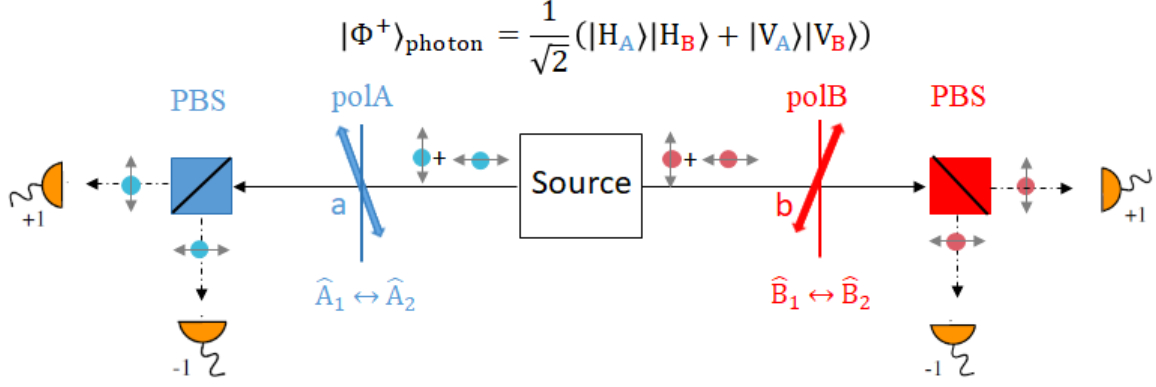


**Figure 2.1** – Bell-type experiment. A source creates two photons in an entangled state (e.g.  $|\Phi^+\rangle_{\text{photon}}$ ). The photons are transmitted far apart through two different propagating channels for quantum state analysis. Two observers, i.e. (A)lice and (B)ob, prepare for that purpose two independent measurement settings (denoted by  $\hat{A}_{1,2}$  and  $\hat{B}_{1,2}$ ) consisting of a polarizer (i.e. polA and polB). This is used to rotate the basis in which Alice and Bob perform their measurements, which is a necessary condition to prove photon entanglement and thus violate the Bell inequality (see section 2.3). Finally, the photons enter polarizing beam splitters (PBS), where the horizontal polarization ( $\leftrightarrow$ ) is reflected, while the vertical polarization ( $\updownarrow$ ) is transmitted. The subsequent detection of the photons at either one of the two detectors yields the distinct values  $\pm 1$ . Coincident measurements between the outcomes are then used for quantum interference.

the collapse of A in the state, e.g.  $|H_A\rangle$ , the same measurement determines the collapse of B into  $|H_B\rangle$ .

Consider now another scenario related to the same experiment. Assume that both Alice and Bob perform independently projection measurements on photons A and B, respectively. Each observer can perform local projections with respect to any polarization component. They finally communicate via a classical channel (e.g. telephone) to compare the outcomes of their respective measurements. As a direct consequence of the maximum entanglement of  $|\Phi^+\rangle_{\text{photon}}$ , Alice and Bob will always find the same result (e.g.  $|H_A\rangle$  and  $|H_B\rangle$ ) with equal probability (i.e.  $1/2$ ) [32].

## 2.2.2 Multi-level (qudit) Bell states

The high-dimensional Bell states are a direct extension of two-level Bell states to qudits. The subsystems A and B composing the whole system S have now dimensionality  $d_A$  and  $d_B$ , respectively, while the Hilbert space of the entangled system is spanned by the basis  $\{|i_A, j_B\rangle\}$  with  $i_A = 0_A, \dots, d_A - 1$  and  $j_B = 0_B, \dots, d_B - 1$ .

The most generic form of a high-dimensional Bell states is [51, 53]

$$|\Psi_{\text{Bell}}\rangle = \frac{1}{\sqrt{d}} \sum_{k=0}^{d-1} e^{i\frac{2\pi}{d}n\cdot k} |k_A\rangle |k \oplus m_B\rangle, \quad (2.2.3)$$

where  $\{|k\rangle\}_{k=0}^{d-1}$  denotes the computational basis and  $k \oplus m \equiv (k + m) \pmod{d}$  (with  $n, m = 0, 1, \dots$  being integer numbers). It can be seen that, for  $d = 2$ ,  $|\Psi_{\text{Bell}}\rangle$  reduces to two-dimensional states  $|\Psi^\pm\rangle$  and  $|\Phi^\pm\rangle$ .

As an example of a physical system being in a high-dimensional Bell states, the case of two frequency-entangled photons can be considered [6]. Denoting the frequency modes as  $|a_i\rangle$ , the Bell state is given by

$$|\Psi_{\text{freq}}\rangle = \sum_{i=0}^{d-1} c_{a_i} |a_i\rangle_A |a_i\rangle_B, \quad (2.2.4)$$

where  $c_{a_i}$  is a complex probability amplitude satisfying the condition  $\sum_i |c_{a_i}|^2 = 1$ .

### 2.2.3 Generating Bell states: SPDC and SFWM

Two main processes can be used to generate experimentally photon pairs in a Bell state [54]. One is the spontaneous parametric down-conversion (SPDC) [29, 55–57], the other is the spontaneous four-wave mixing (SFWM) [6, 7, 19, 54, 58–61]. These processes are the quantum counterparts of classical difference-frequency generation and four-wave mixing (FWM), respectively [54]. The process that we exploited here to generate frequency-entangled Bell states [6], as well as time- and frequency-entangled cluster states [7] is the SFWM occurring within a microring optical resonator.

SPDC and SFWM are nonlinear phenomena, occurring within a  $\chi^{(2)}$  and a  $\chi^{(3)}$  medium, respectively. A second-order nonlinear medium that can be used as a source for SPDC can be  $\chi^{(2)}$  crystals (e.g. BBO [62–64], or KTP [65]), as well as waveguides made of, e.g., lithium niobate [66–68]. Third-order nonlinear materials that are mainly used as sources for SFWM are silicon-based integrated chips [69, 70] and microring resonators [71–74]. Recently, Hydex-based microring resonators have been exploited as a SFWM source of single and entangled photons [19, 75, 76]. The novel entangled states demonstrated here have been generated by making use of a high-Q Hydex microring resonator [6, 7]. This material – similar to silicon nitride – is characterized by a high nonlinearity and a very high Q factor (235,000 in [6, 7], but it can also reach a value  $> 10^6$  [54]) which enables SFWM enhancement. While the nonlinear optical properties characteristics of

$\chi^{(2)}$  and a  $\chi^{(3)}$  media are out of the scope of this work, we focus here on describing the quantum aspect of the two processes allowing for the generation of single and entangled photons.

**SPDC.** In this phenomenon, a photon from an intense pump laser having frequency  $\omega_p$  is annihilated within a  $\chi^{(2)}$  crystal to generate two daughter photons, namely signal ( $s$ ) and idler ( $i$ ), having frequency  $\omega_s$  and  $\omega_i$ , respectively. It can be demonstrated that the seed fields are provided by vacuum fluctuations: only the virtual signal and idler pairs satisfying energy and momentum conservation are efficiently transformed into real photons [54]. Due the energy ( $\hbar\omega$ ) and momentum ( $\hbar\mathbf{k}$ ) conservation of the SPDC phenomenon, the conditions

$$\hbar\omega_p = \hbar\omega_s + \hbar\omega_i \quad (2.2.5)$$

and

$$\hbar\mathbf{k}_p = \hbar\mathbf{k}_s + \hbar\mathbf{k}_i. \quad (2.2.6)$$

must be simultaneously satisfied.

Furthermore, energy conservation requires the signal and idler to be generated at frequencies that are symmetrically located with respect to half of the frequency of the pump field, i.e.  $\omega_s = \omega_p/2 + \Delta\Omega$  and  $\omega_i = \omega_p/2 - \Delta\Omega$ , where  $\Delta\Omega$  is the frequency shift with respect to the degenerate process [54].

**SFWM.** In this phenomenon, two pump photons having frequencies  $\omega_{p_1}$  and  $\omega_{p_2}$  are annihilated within a  $\chi^{(3)}$  medium to generate signal and idler photons with frequency  $\omega_s$  and  $\omega_i$ , respectively. In that case, the energy and momentum conservation conditions require that

$$\hbar\omega_{p_1} + \hbar\omega_{p_2} = \hbar\omega_s + \hbar\omega_i. \quad (2.2.7)$$

and

$$\hbar\mathbf{k}_{p_1} + \hbar\mathbf{k}_{p_2} = \hbar\mathbf{k}_s + \hbar\mathbf{k}_i, \quad (2.2.8)$$

respectively. For simplicity, as well as according to the generation scheme used in this work, we assume that the SFWM is degenerate, i.e.  $\omega_{p_1} = \omega_{p_2} = \omega_p$ . In this case, the conditions for energy and momentum conservation become

$$\hbar\omega_{2p} = \hbar\omega_s + \hbar\omega_i \quad (2.2.9)$$

and

$$\hbar\mathbf{k}_{2p} = \hbar\mathbf{k}_s + \hbar\mathbf{k}_i, \quad (2.2.10)$$

respectively. Moreover, in contrast with the SPDC, energy conservation requires that the frequencies of signal and idler photons must be symmetrically distributed around the pump frequency as  $\omega_s = \omega_p + \Delta\Omega$  and  $\omega_i = \omega_p - \Delta\Omega$ , respectively.

More in general, both SPDC and SFWM sources can be used to generate maximally entangled (i.e. Bell) states in a variety of degrees of freedom, such as polarization [67, 69], time [12, 19], frequency [6, 20, 77], OAM [17], and so forth, depending on the configuration of the conversion process.

In SPDC, as well as in SFWM, the combination of vacuum fluctuations and conservation laws is at the core of the entanglement between signal and idler. However, the necessary condition to achieve entanglement is that both signal and idler have to be generated in a superposition of at least two quantum states (i.e. modes), e.g. horizontal and vertical polarizations, early and late time-bin generation, and so forth.

As an example of how to generate entangled photon pairs in nonlinear media, we here consider the realization of time-bin entanglement [18, 19].

Time-bin entanglement is a discrete form of energy-time entanglement, that is between the energy and the arrival time of two photons [18]. This can be obtained by discretizing the time in which the photon is generated (or, equivalently, at which it arrives at the detector) into time slots. Time-bin entanglement can be demonstrated by pumping a third-order nonlinear microcavity (here, the microring resonator) with multiple (phase-locked) pulses delayed each by  $\Delta t$  (see Figure 2.2). Without loss of generality, let us consider the generation of a qubit entangled state: the delay between two optical pulses can be created through a two-arm unbalanced (i.e. Mach-Zehnder) interferometer, as depicted in Figure 2.2 [19]. Assume that a single-photon pulse enters the interferometer. Here, the pulse splits into two separated pulses, one each per interferometer arm. Moreover, since the length of the two arms differs by a phase  $\varphi$ , the two pulses will be delayed each other by a  $\Delta t$  which is proportional to  $\varphi$ . As long as the duration of the single-photon pulse is shorter than length difference between the two arms, the interferometer output consists of two well-separated pulses. Naming  $t_1$  and  $t_2$  the earlier and later pulse, respectively, the resulting single-photon double pulse will be in the quantum superposition [18]

$$|\psi\rangle_{\text{out}} = a_{t_1} |t_1\rangle + a_{t_2} |t_2\rangle. \quad (2.2.11)$$

Assume now that  $|\psi\rangle_{\text{out}}$  enters the SFWM source, i.e. the microring resonator, from which

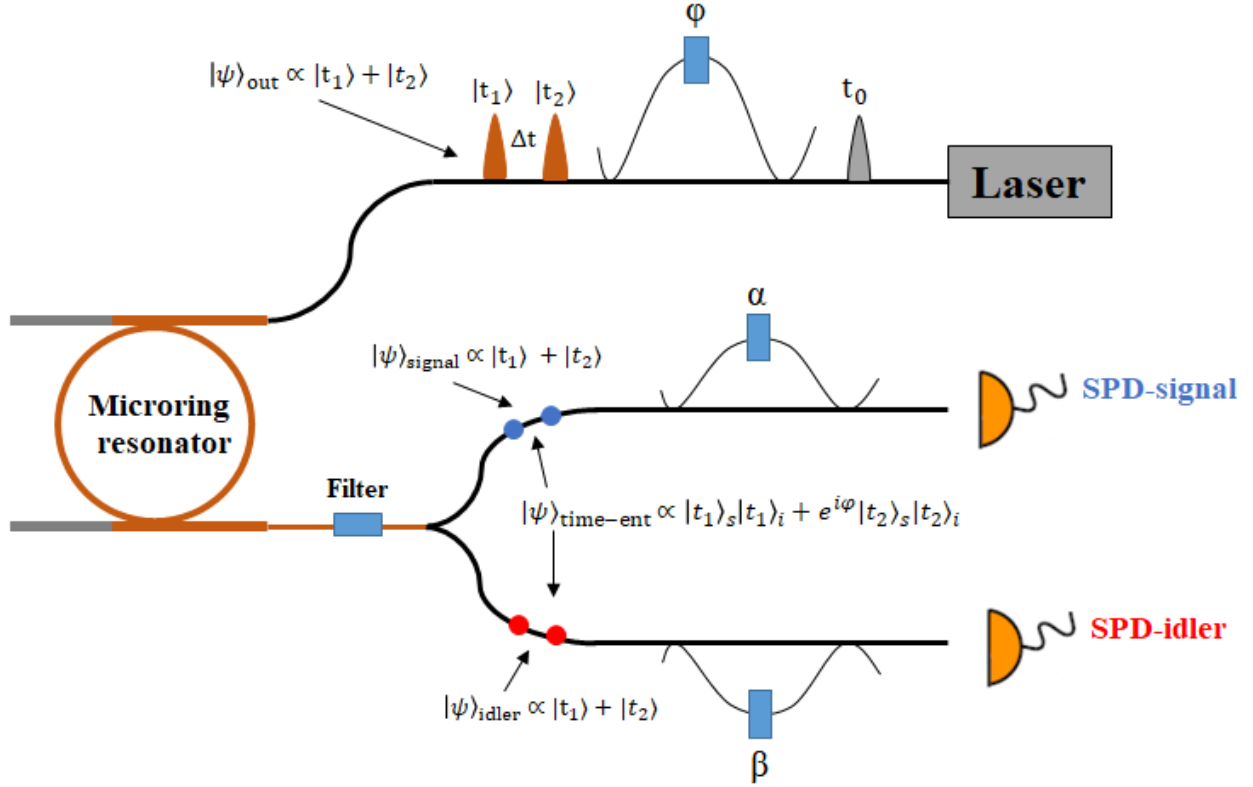


**Figure 2.2** – Generation of time-bin entanglement. A single-photon pulse generated through a (pulsed) laser enters an unbalanced interferometer, where the two arm length differs by a phase  $\varphi$ . The interferometer output thus consists of a single-photon double pulse which is in a quantum superposition of the earlier ( $|t_1\rangle$ ) and the later ( $|t_2\rangle$ ) pulse. The two pulses, delayed by a  $\Delta t \propto \varphi$ , then enters a nonlinear microring resonator, where the signal and the idler photons (violet and red bullets, respectively) are generated through spontaneous four-wave mixing. Due to the quantum superposition of the input state, the two photons are generated in a time-bin entangled state of the form  $|\psi\rangle_{\text{time-ent}} \propto |t_1\rangle_s |t_1\rangle_i + e^{i\varphi} |t_2\rangle_s |t_2\rangle_i$ . In order to perform quantum state analysis (e.g. entanglement verification via quantum interference measurements), the entangled pair is spectrally filtered and each photon is routed in an interferometer with temporal delay proportional to  $\varphi$ . To perform entanglement analysis, it is necessary to change the phases  $\alpha$  and  $\beta$  between the two interferometers (e.g. via variable phase filters), in analogy with polarization rotations. Each photon is finally detected by means of a single photon detector (SPD) in order to get coincidence measurements.

signal and idler are generated. Since the input pump photon is in a quantum superposition of two temporal slots, the two daughter photons are created each in a superposition of  $|t_1\rangle$  and  $|t_2\rangle$ , while, prior to any quantum measurement on the two photons, the time at which they are generated remains undefined. The quantum superposition, as well as the lack of knowledge about the generation time, is responsible for generating signal and

idler in a time-bin entangled state, which reads

$$|\psi\rangle_{\text{time-ent}} = a_{t_1} |t_1\rangle_s |t_1\rangle_i + a_{t_2} |t_2\rangle_s |t_2\rangle_i. \quad (2.2.12)$$

When  $|\psi\rangle_{\text{time-ent}}$  is generated such that  $|a_{t_1}|^2 = |a_{t_2}|^2 = 1/2$ , then it results in the maximally entangled Bell state

$$|\psi\rangle_{\text{time-ent}} = \frac{1}{\sqrt{2}} (|t_1\rangle_s |t_1\rangle_i + |t_2\rangle_s |t_2\rangle_i). \quad (2.2.13)$$

## 2.3 Bell's inequality and Quantum Interference

At a first glance, entanglement seems to contradict the principles of both locality and realism. The former states that information cannot travel faster than light. The latter affirms that the physical properties of any system cannot depend on the measurement. This is because measurements on a single party of an entangled system have effects on the other party which are immediate independently of any spatial distance between them (see section 2.1). This apparent contradiction has been a matter of debate since 1935, when A. Einstein, B. Podolsky and N. Rosen (EPR) argued the so-called ‘EPR paradox’ in [40]. Here, they state: “In quantum mechanics in the case of two physical quantities described by non-commuting operators, the knowledge of one precludes the knowledge of the other. Then either (1) the description of reality given by the wave function in quantum mechanics is not complete or (2) these two quantities cannot have simultaneous reality. Consideration of the problem of making predictions concerning a system on the basis of measurements made on another subsystem that had previously interacted with it, leads to the result that if (1) is false then (2) is also false. One is thus led to conclude that the description of reality as given by a wave function is not complete.”

The essence of the EPR paradox is that quantum mechanics, as based on the wave function to describe physical reality, could not be a complete theory. Rather, it should be completed with additional variables, called ‘hidden variables’ [48, 78], restoring causality and locality principles [78, 79]. For example, let us consider again the Bell state  $|\Phi^+\rangle_{\text{photon}}$  in Eq. (2.2.2). According to the EPR interpretation, the observed correlation between the photons’ polarizations occurs as if their values were actually determined by some ‘hidden’ variables that have been chosen locally by a virtual Charles at the moment of the state preparation and immediately before the photons were separated apart (this,

unbeknownst to both Alice and Bob). The choice of Charles can be seen as if he assigned a polarization to a photon according to the outcome of a classic dice tossing (e.g. vertical polarization for 1, 2, or 3 and horizontal for 4, 5, or 6) [32].

In 1964, John S. Bell formulated the Bell theorem which ruled out the hidden variable theory as a quantum mechanical description of physical reality [48]. The essence of this theorem is that quantum mechanics is actually incompatible with either locality or realism principles. More precisely, under the assumption of both locality and realism, the correlations in the measurement outcomes of two distant observers must necessarily obey an inequality, which is the so-called ‘Bell inequality’ [6, 7, 13, 19, 78–80]. It establishes a correspondence between ‘non-classical’ correlations (i.e. those not obeying to local realism and that thus cannot be described by classical random variables) and entanglement. In particular, the Bell inequality determines a threshold value: if the result of measurement outcomes is below the threshold, then the inequality is not violated and the correlations can be explained through classical probabilities. Otherwise, the inequality is violated, the correlations are purely quantum and no classical interpretation of them is either allowed or possible.

Different forms of the Bell inequality exist. The most widely used in experiments is the expression that was formulated by Clauser, Horne, Shimony, and Holt (CHSH) in 1969 [81]. The CHSH inequality has been derived for dichotomic observables, i.e. those variables that have a measurement outcome which can take only two values, i.e.  $+1$  and  $-1$  (for example, polarization and spin). The origin of the CHSH Bell inequality can be explained by considering the Bell-type experiment of Figure 2.1. The first step is deriving a Bell operator and then a Bell inequality to violate. For that purpose, the two observers Alice and Bob have to use at least two measurement settings per each (i.e.  $A_1, A_2$  and  $B_1, B_2$ , respectively). The settings  $A_{1,2}$  must be independent of each other, as well as of  $B_{1,2}$  (and vice versa). A requirement for both  $A_{1,2}$  and  $B_{1,2}$  is to locally perform non-destructive measurements. This means that they have to project or change the quantum state locally without detecting it. For polarization-measurements, the settings  $A_{1,2}$  and  $B_{1,2}$  can be implemented by using polarizers (polA and polB in Figure 2.1), which allows polarization rotation without detecting it. Since entanglement persists independently of the basis used for the measurement, rotating the measurement basis reveals crucial to demonstrate that the correlations are not classical and thus violate the Bell inequality.

Then, the photons pass a polarizing beam splitter (PBS) which reflects and transmits horizontal and vertical polarization components, respectively. Finally, the photons are detected at either one of the two detectors that yield the distinct values  $\pm 1$  for vertical and horizontal polarizations, respectively. At this stage, coincidence measurements of the two detected photons can be performed [52].

The described measurement setting allows us to define the Bell operator

$$B_{\text{CHSH}} = A_1 \otimes B_1 + A_1 \otimes B_2 + A_2 \otimes B_1 - A_2 \otimes B_2, \quad (2.3.1)$$

where  $A_j$  and  $B_k$  are Hermitian operators representing the measurement settings (i.e. the observables). In order to obey nonlocality, the Bell operator must violate the CHSH inequality [52, 81]:

$$|B_{\text{CHSH}}| = |\langle A_1 \otimes B_1 \rangle + \langle A_1 \otimes B_2 \rangle + \langle A_2 \otimes B_1 \rangle - \langle A_2 \otimes B_2 \rangle| \leq 2. \quad (2.3.2)$$

The formal derivation of Eq. (2.3.2) is reported in Appendix A.

When the experimental conditions satisfying Eq. (2.3.2) are violated, the nonlocality of the realized quantum state is demonstrated. Furthermore, for the two-partite quantum states that are generated through SPDC and SFWM, the violation of this inequality can be exploited as a proof to confirm entanglement. In this specific case, nonlocality of quantum states can be used as a synonym of entanglement. However, more in general, the Bell inequality cannot be used as a test for entanglement, since there exist some entangled states that do not violate the Bell inequality [52, 82].

The quantum states that maximally violate the CHSH inequality are the Bell states. The maximal violation occurs when the expectation value of the Bell operator reaches the value  $2\sqrt{2}$  of Eq. (A.0.3) which can be achieved by making use of a specific measurement settings  $A_j, B_k$ . Let us consider two configurations in which the maximal violation can be obtained, one is for polarization-entanglement, the other for time-bin entanglement.

For polarization-entanglement, the Bell inequality in Eq. (2.3.2) can be rewritten as [54]

$$S \equiv |E(a, b) - E(a, b')| + |E(a', b) + E(a', b')| \leq 2, \quad (2.3.3)$$

where  $a \equiv A_1$ ,  $a' \equiv A_2$  and  $b \equiv B_1$ ,  $b' \equiv B_2$  are the measurement settings used by Alice and Bob in the Bell-type experiment of Figure 2.1. These settings correspond to the angles of the polarizers polA and polB in front of the detectors, respectively. The terms

of the form  $E(a, b)$  are defined as

$$E(a, b) = \frac{cc(a, b) + cc(a + 90^\circ, b + 90^\circ) - cc(a, b + 90^\circ) - cc(a + 90^\circ, b)}{cc(a, b) + cc(a + 90^\circ, b + 90^\circ) + cc(a, b + 90^\circ) + cc(a + 90^\circ, b)} \quad (2.3.4)$$

with  $cc(a, b)$  being the number of coincidences obtained by setting polarizers for the signal and for the idler to  $a$  and  $b$ , respectively. It can be seen that the angles leading to a maximal violation of the CHSH inequality are  $a = 0^\circ$ ,  $a' = 45^\circ$ ,  $b = 22.5^\circ$ , and  $b' = 67.5^\circ$ .

To demonstrate energy-time entanglement, a different Bell inequality can be exploited, which was derived by Franson in [82]. However, when energy-time entanglement is considered in its discrete form, which is the time bin, this can be considered formally equivalent to polarization-entanglement. For this reason, a Bell inequality such as that of Eq. (2.3.3) can be equivalently used for demonstrating nonlocality and time-bin entanglement. The measurement setting needed to obtain the Bell operator  $S$  of Eq. (2.3.4) consists of two unbalanced interferometers (one for the signal and one for the idler), both with variable phase shifters (see Figure 2.2). This allows us to change the phase between the two arms of the same interferometer, as well as the phase between the two interferometers. In analogy with polarizers, the two interferometers change the basis for the measurement while not destroying the photon state. For a time-bin entangled state of the form  $|\psi\rangle_{\text{time-ent}}$  (see Eq. (2.2.12)), the maximal violation of the CHSH inequality is obtained when the phases between the signal and idler interferometers are set as are  $a = \pi/4$ ,  $a' = -\pi/4$ ,  $b = 0$ , and  $b' = \pi/2$  [54, 83].

From a practical perspective, it is more convenient to determine a Bell inequality through quantum interference measurement rather than through its direct measure. Lying at the heart of linear quantum optics, quantum interference, at its basic level, describes the interaction of two indistinguishable photons entering the same device, such as a beam splitter or an interferometer, depending on the degree of freedom that is considered (polarization and time-bin, respectively).

Determining a Bell inequality through its direct measure requires at least  $d^{2N}$  measurements ( $2^{2 \times 2} = 16$ , in case of a two-photon two-level entangled state), as well as the use of an optimal angle or phase settings for polarization or time-bin entanglement, respectively. This is because it is necessary to project signal and idler into the states  $|\psi\rangle_s = \sin(\alpha) |t_1\rangle + \cos(\alpha) |t_2\rangle$  and  $|\psi\rangle_i = \sin(\beta) |t_1\rangle + \cos(\beta) |t_2\rangle$ , respectively, as well as

to vary each angle/phase for four possible optimal values [32, 54].

Quantum interference does not require to optimize angle/phase settings and necessitates less measurements with respect to a direct measure of the Bell inequality. In particular, considering the experimental setting of Figure 2.2, it is sufficient to project either the signal or the idler photon into the state  $|\psi\rangle_{s,i} = |t_1\rangle + e^{i\varphi}|t_2\rangle$ , while varying the pump interferometer phase  $\varphi$ . Finally, from the coincidence counts between signal and idler, quantum interference can be measured. This is expected to take the form  $1 - V(\alpha + \beta - 2\varphi)$ , where  $\alpha$  and  $\beta$  are the phases of the signal and idler interferometer, respectively. The term  $V$  denotes the visibility, which is typically defined in terms of the observed maximum and minimum intensity in an interference pattern as  $V = I_{\max} - I_{\min}/I_{\max} + I_{\min}$ . In quantum mechanics the visibility that is measured from quantum interference is related to the expectation value of the Bell operator as  $\langle B_{\text{CHSH}} \rangle_{QM} = 2\sqrt{2} * V$  (see Appendix A). This relation allows us to verify the Bell inequality violation if the condition  $V > 1/\sqrt{2} \simeq 0.707$  (for the two-level case) is satisfied.

### 2.3.1 High-dimensional Bell inequalities

Bell inequalities have been formulated also for bipartite  $d$ -level systems. In this section, we report the class of Bell's inequalities that were derived by Collins *et al.* in [13] and that we used in this research work for entanglement verification [6]. We further used the Bell inequality in order to demonstrate that projecting a four-partite three-level cluster state resulted into orthogonal two-partite entangled systems [7].

The approach used by Collins *et al.* is described in detail in Appendix B, while the threshold values to be considered for Bell inequality violation are only reported here. Given an entangled state of the form

$$|\psi\rangle = \frac{1}{\sqrt{d}} \sum_{j=0}^{d-1} |j\rangle_A \otimes |j\rangle_B, \quad (2.3.5)$$

and denoting with  $p$  the noise level (i.e. the probability that such a state is affected by noise, see subsection 3.3.2 and subsection 5.2.1), the Bell parameter  $I_d$  is certainly violated if (see Appendix B)

$$p > \frac{2}{I_d(QM)} = p_d^{\min}, \quad (2.3.6)$$

where  $p_d^{\min}$  is the noise sensitivity threshold [13]. The explicit expressions of this thresh-

olds for  $d = 2, 3, 4$ , and  $d \rightarrow \infty$  are given by

$$p_{d=2}^{\min} = \frac{1}{\sqrt{2}} \simeq 0.7071 \quad (2.3.7a)$$

$$p_{d=3}^{\min} = \frac{6\sqrt{3} - 9}{2} \simeq 0.69615 \quad (2.3.7b)$$

$$p_{d=4}^{\min} = \frac{3}{\sqrt{2} + \sqrt{10 - \sqrt{2}}} \simeq 0.69055 \quad (2.3.7c)$$

$$p_{d \rightarrow \infty}^{\min} = \frac{\pi^2}{16 \times \textit{Catalan}} \simeq 0.67344, \quad (2.3.7d)$$

where  $\textit{Catalan} \cong 0.9159$  is the Catalan constant. From the values reported in Eqs. (2.3.7a - 2.3.7d), it can be seen that two-partite  $d$ -level systems are more noise tolerant than their two-level counterparts [13]. Moreover, the noise tolerance increases as the quantum state dimensionality  $d$  increases. In [6], we experimentally validated this concept for the realized high-dimensional Bell states (see subsection 4.2.2), while in [5] we demonstrated analytically that this behavior is also valid for multipartite cluster states (see subsection 5.2.1).

## 2.4 Schmidt mode decomposition

Any pure bipartite quantum state can be expressed in a very useful form, called ‘Schmidt decomposition’ [4, 84, 85], that allows us to define its entanglement properties, as well as to quantify the amount of entanglement. For this reason, the Schmidt decomposition has been largely used in the literature for defining bipartite systems [4, 85–88]. Introducing the Schmidt decomposition is noteworthy here, since it has been used in this research work in order to validate the dimensionality of the generated frequency-entangled photon pairs [6] (see subsection 4.2.1), as well as to derive the explicit expression of the witness for high dimensional multipartite cluster states (see section 5.2) [5].

Assume that the density matrix of a pure bipartite state  $|\psi_S\rangle$  is given by  $\rho_S = \rho_{AB} = |\psi_S\rangle\langle\psi_S|$ , where A and B denote the two parties composing the system S. Both A and B always possess a set of orthonormal states  $\{|i_A\rangle\}$  and  $\{|i_B\rangle\}$ , respectively, such that the whole wave function  $|\psi_S\rangle$  can be written in the so-called Schmidt form [84]

$$|\psi_S\rangle = \sum_{i=0}^{d-1} \lambda_i |i_A\rangle |i_B\rangle. \quad (2.4.1)$$

Here,  $\lambda_i$  are non-negative real number satisfying the condition  $\sum_{i=0}^{d-1} |\lambda_i|^2 = 1$  and are known as Schmidt coefficients [4, 84].

In order to understand how information about the quantum state  $|\psi_S\rangle$  can be extracted from the Schmidt decomposition, it is necessary to analyze the Schmidt coefficients. To that purpose, the concept of reduced density matrix has to be introduced, which is indispensable in the analysis of composite quantum systems [4]. Given the density matrix of the whole system S, i.e.  $\rho_S = \rho_{AB}$ , the reduced density matrix of the system A with respect to the system B is defined as [84]

$$\rho_A \equiv Tr_B(\rho_{AB}) = \sum_{i=0}^{d-1} \langle i_B | \rho_{AB} | i_B \rangle, \quad (2.4.2)$$

where  $Tr_B()$  defines the partial trace over the system B [85]. It is important not to confuse the partial trace with the standard trace of a matrix, simply denoted as  $Tr()$ . The simple trace is given by a number, while the partial trace is an operator and is given by a matrix. The partial trace is also known as ‘mapping operator’, since it can be experimentally performed by projecting the quantum state S into an orthonormal basis  $\{|i_B\rangle\}$  of the system B.

It can be demonstrated that the Schmidt coefficients  $\lambda_i$  of Eq. (2.4.1) are the eigenvalues of the reduced density matrices  $\rho_A = \sum_{i=0}^{d-1} \lambda_i^2 |i_A\rangle\langle i_A|$  and  $\rho_B = \sum_{i=0}^{d-1} \lambda_i^2 |i_B\rangle\langle i_B|$ , which share thus a common set of eigenvalues and eigenstates [84]. The Schmidt coefficients do provide the dimensionality, as well as the entanglement properties, of any pure bipartite quantum state  $|\psi_S\rangle$ . In particular, by means of the Schmidt coefficients, the following quantities can be obtained.

- The *Schmidt number*, defined as [52]

$$K = \frac{1}{\sum_{i=0}^{d-1} \lambda_i^2} = \frac{1}{Tr_B(\rho_{AB}^2)}, \quad (2.4.3)$$

quantifies the number of single states (for example, the individual frequency modes [6]) in the Schmidt decomposition. It ranges from one for separable (unentangled) states to  $d$ , corresponding to the dimensionality of each subsystem. In this sense, the Schmidt number provides the quantum state dimensionality. The value  $d$  is specifically obtained for maximally entangled state. When a Schmidt number proximal to  $d$  (as an error has to be associated to it) is experimentally determined, the realization of a  $d_A \times d_B$ -dimensional system is confirmed, where  $d_A$  and  $d_B$  are the dimensionalities of subsystems A and B, respectively [6].

- The *Schmidt rank*  $s$ , which provides the number of non-vanishing Schmidt coefficients  $\lambda_i$ . It ranges from one for separable states to  $d$  for maximally entangled

states [52], and thus allows us to estimate whether a quantum state exhibits entanglement or not.

- The *concurrence*, defined as [52]

$$C(|\Psi\rangle) = \sqrt{\frac{d}{d-1} \left(1 - \sum_{j=0}^{d-1} \lambda_j^2\right)} \quad (2.4.4)$$

- Finally, the Schmidt coefficients can be used to express the *entanglement entropy* (or *entanglement of formation*) [52, 85] that enables us to quantify the amount of entanglement (i.e., it is an entanglement monotone [52]). This quantity is defined as

$$E(|\psi\rangle) = S(\rho_{A(B)}) = - \sum_{i=0}^{d-1} \lambda_i \log_d \lambda_i = -Tr \left( \rho_{A(B)} \log_d \left( \rho_{A(B)} \right) \right), \quad (2.4.5)$$

and can be obtained through the spectral decomposition (i.e. the diagonalization) of  $\rho_{A(B)} = \sum_i \lambda_i^2 |i_{A(B)}\rangle \langle i_{A(B)}|$ .

## 2.5 Multipartite entangled states

Extending the approaches to characterize entanglement of bipartite systems to multipartite states is not straightforward, while these are limited to very restricted cases. For example, a Schmidt mode decomposition for multipartite quantum states is currently limited to three-partite systems [89]. Another example is the Bell inequality. Thus far, the so-called Mermin inequality is the only expression that has been derived to investigate and validate the nonlocality of multipartite systems. However, the Mermin inequality can be used just for few classes of entangled states. Specifically, this is limited to Greenberger-Horne-Zeilinger states (defined in subsection 2.5.1) and four-partite cluster states (defined in chapter 3). Furthermore, this inequality can be applied only to qubits [90–93]. More in general, a complete characterization of multipartite entanglement is still an open issue, and many attempts have been pursued towards this purpose from both a theoretical and an experimental perspective [38, 39, 47, 52, 94–96].

The novel cluster states demonstrated here form a class of multipartite states with very peculiar entanglement properties. In order to properly investigate and validate these (both theoretically and experimentally), it was necessary to explore new venues which were alternative to those mentioned above. We thus chose witness operators in order to

accomplish our research goal. The motivation of this specific choice will be clear in the following chapters where we first introduce the definition and the generic properties of witness operators (section 3.3, subsection 3.3.1), and then introduce the approach that we used to derive novel witnesses (chapter 5) [5].

In the current section, we provide the definition, as well as examples of multipartite entangled states, that are useful for the reader in order to understand the properties of the cluster states realized in this work.

Consider a quantum system  $S$  that is composed of  $N$  parties, namely  $A, B, C, \dots, N$ , each described by its respective wave function  $|\psi_A\rangle, |\psi_B\rangle, |\psi_C\rangle, \dots, |\psi_N\rangle$ . If all accessible information about each party is contained in its wave function, then the quantum system  $S$  is fully separable, while the associated wave function can be written as the tensor product of the individual parties as  $|\psi_S\rangle = |\psi_A\rangle \otimes |\psi_B\rangle \otimes |\psi_C\rangle \otimes \dots \otimes |\psi_N\rangle$ . A measurement performed on each subsystem has effects on none of the others. If a measurement of one party has effects at least on another party, the system  $S$  is then entangled and  $|\psi_S\rangle \neq |\psi_A\rangle \otimes |\psi_B\rangle \otimes |\psi_C\rangle \otimes \dots \otimes |\psi_N\rangle$ .

Two different scenarios can occur. First, the entanglement exists only between some subsystems. In this case, the whole quantum state is considered as separable, and the degree of separability is determined by the number of parties that are entangled. Second scenario: all the parties share entanglement and the quantum state results overall inseparable (see Figure 2.3. In this case, the system  $S$  exhibits genuine multipartite entanglement, which is a very important resource for quantum secure communication. For example, it enables us to protect a shared secret against eavesdropping or unfaithful parties [97]. Separable and inseparable multipartite quantum states form a convex set, which is represented in Figure 2.3 of this thesis. Cluster states [98] are a class of genuine multipartite entangled systems (see chapter 3). We validate the genuine four-partite entanglement of the here demonstrated cluster state by deriving a novel operator specifically designed for that purpose (i.e. the high dimensional witness) [5, 7].

While for bipartite systems, a unique class of entangled states exists, i.e. the class of Bell states, for multipartite systems there are several and inequivalent classes of multipartite entangled states [89, 99, 100]. For example, in the case of  $N = 3$  parties, an important representative class is given by the Greenberger-Horner-Zeilinger (GHZ) states [101], which took the name from the physicists (i.e. D.M. Greenberger, M.A. Horner, and

A. Zeilinger) that formulated them in 1990.

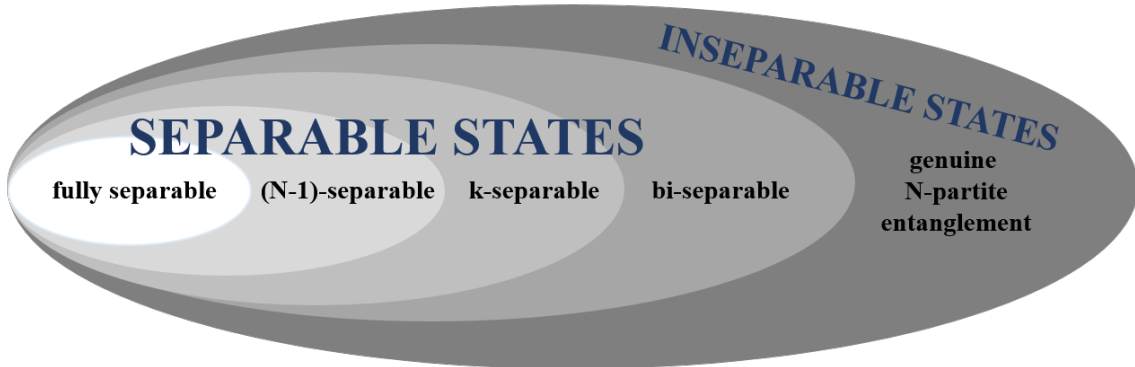


**Figure 2.3** – There are different degrees of separability in a multipartite quantum state, which are determined by the number of subsystems that share entanglement. Specifically, in fully separable states, no party shares entanglement. In  $(N-1)$ -separable states, all but one parties are entangled. In  $k$ -separable states, only  $k < N - 1$  parties share entanglement. Bi-separable quantum states consists of two macro subsystems: the entanglement is shared only between the parties composing the same subsystem, while there is no entanglement between the two macro subsystems. The hyper-entangled states of Eqs. (2.5.2) and (6.2.1) are examples of bi-separable states. Finally, genuine multipartite (or  $N$ -partite) entangled states are overall inseparable, i.e. all the parties composing them share entanglement.

### 2.5.1 Greenberger-Horne-Zeilinger (GHZ) states

GHZ states [101] are introduced here with the main scope of comparing them with cluster states. In particular, it will be shown (see section 3.1 and section 3.4) that for  $N = 3$  parties, cluster states are (locally) equivalent to GHZ states, while for  $N > 3$  there is no equivalence either between GHZ and cluster states or between cluster states and any other entangled system. Such an equivalence is valid independently of the quantum state dimensionality.

GHZ states are maximally entangled states with, at least, a number of parties equal to three. The most generic expression of their wave function is given by [101]

$$|\text{GHZ}\rangle_{N,d} = \frac{1}{\sqrt{d}} \sum_{i=0}^{d-1} \bigotimes_{n=1}^N |i\rangle_n, \quad (2.5.1)$$

where the index  $n$  runs over the number of parties. A feature of GHZ states is that, tracing out (i.e. detecting) one party of the system, results in an unentangled state, since the remaining parties collapse into a fully mixed state (which is separable). This feature is one of the most important differences between GHZ and cluster states, and it will be

described in detail in chapter 3 and section 6.1. In order to compare GHZ and cluster states, some specific examples of GHZ wave functions are reported in Appendix C.

## 2.5.2 Hyper-entangled states

Hyper-entangled states [102] are multipartite quantum systems that are simultaneously entangled in two or more independent physical variables such as, in case of photons, polarization, optical path, linear or orbital angular momentum [31, 57, 103]. Experimentally, this means that it is possible to access each degree of freedom individually and independently.

A hyper-entangled state can be considered as a multipartite system, even though it is composed by just two particles (e.g. photons) [7, 57, 103, 104]. Specifically, each degree of freedom represents an independent party, while the particles can be seen as the ‘carriers’ of the parties. Hyper-entanglement enables the access to a Hilbert space which has equal or even larger size with respect to the Hilbert space that can be accessed through entanglement in a single degree of freedom. For example, consider two photons that are hyper-entangled in polarization and linear momentum. Each photon is seen as a carrier of two parties, one defined by the polarization and one by the linear momentum. This leads to a total number of four parties, which results in a Hilbert space size equal to  $2^4 = 16$ . A system which is formed by four photons that are entangled in a single degree of freedom (e.g. polarization), has a Hilbert space size equal to  $4^2 = 16$ , as well.

Using a reduced number of photons by exploiting the concept of hyper-entanglement has several advantages with respect to using multiple photons. For example, the optical platform necessary to implement a few (e.g. two) photon system results significantly less complex and more scalable than a platform required for multiple photons. Furthermore, using a few photons provides benefits in terms of detection rates [7]: since the probability of detecting photons scales as  $p^N$ , where  $0 < p < 1$ , it is clear that, the higher the number of particles, the lower the detection rate.

In light of these considerations, hyper-entanglement is a promising resource for quantum information processing [57, 105] and can find many applications in quantum communication protocols, such as remote entangled state preparation [106] and quantum super dense coding [107]. This has led to an intensive investigation of this phenomenon, and many hyper-entangled states have been demonstrated thus far by making use of the

same generation techniques that are used to generate entangled photons (i.e. SPDC and SFWM, see subsection 2.2.3). Specifically, hyper-entanglement has been widely used in a relatively recent literature in order to experimentally realize four-partite cluster states of qubits with just two photons [55, 57].

A two-photon hyper-entangled state is typically realized from the product of two Bell states, each exhibiting entanglement in a different degree of freedom. For example, let us consider the product of the two states  $|\Phi^-\rangle_{\text{photon}} = \frac{1}{\sqrt{2}}(|H_A\rangle|H_B\rangle - |V_A\rangle|V_B\rangle)$  and  $|\Psi^+\rangle_{\text{photon}} = \frac{1}{\sqrt{2}}(|r_A\rangle|l_B\rangle + |l_A\rangle|r_B\rangle)$ , exhibiting entanglement in polarization and linear momentum, respectively ( $r$  and  $l$  denote the right and left photon paths). This results in the hyper-entangled state [57]

$$|\Xi_{\text{Hyper}}\rangle = |\Phi^-\rangle_{\text{photon}} \otimes |\Psi^+\rangle_{\text{photon}} \quad (2.5.2)$$

$$\frac{1}{\sqrt{2}}(|H_A\rangle|H_B\rangle - |V_A\rangle|V_B\rangle) \otimes \frac{1}{\sqrt{2}}(|r_A\rangle|l_B\rangle + |l_A\rangle|r_B\rangle).$$

A state of this form is overall separable (specifically, it is bi-separable, see Figure 2.3), i.e. it does not exhibit genuine multipartite entanglement.

The concept of hyper-entanglement has been exploited already in the literature for qubit systems by making use of degrees of freedom that are intrinsically different (e.g. polarization and linear momentum). However, hyper-entanglement has never been explored thus far either in higher dimension or by making use of the same type of entanglement. In the research work pursued in this thesis, we generated a four-partite three-level cluster states by making use of just two photons. To this end, we exploited for the first time ever the concept of hyper-entanglement in higher dimension as well as the same type of entanglement, i.e. time- and frequency-entanglement. These are actually two discrete forms of energy-time entanglement (see chapter 6) [7].

## 2.6 Quantum state tomography

The density matrix  $\rho$  of a given quantum state provides all accessible information about it (e.g. if it is bipartite or multipartite, pure or mixed, entangled or separable, and so forth). Reconstructing the density matrix of a realized quantum state is thus crucial in order to access information on it, as well as to validate that the demonstrated system is close to the ideal target. This task is particularly important when the target to realize is an entangled state. In this case, the measured density matrix enables us to

determine the quality of entanglement of the generated state [108]. A technique allowing the reconstruction of  $\rho$  is the so-called ‘quantum state tomography’ (QST), which has been introduced for qubits in [8] and then extended to qudits in [109]. From QST, it is also possible to quantify entanglement through entanglement monotones such as concurrence, entanglement of formation, linear and von Neumann entropy [52]. Measuring these quantities necessitates indeed a complete knowledge about the density matrix of the quantum state under analysis.

A detailed description of this technique is important here for two main reasons. First, qudit QST has been exploited to validate that the developed high-dimensional frequency-entangled two-photon states were generated close to ideal Bell states [6]. Second, describing the measurements needed for QST is necessary to understand why we could not apply it to characterize the entanglement of high-dimensional cluster states, as well as why it was necessary to develop a different approach towards this end [5, 7].

Quantum state tomography has been introduced for the first time for polarization-entangled photons [8], it can be extended however to any entangled photon degree of freedom, such as time [19, 108] and frequency [6]. In order to reconstruct the full density matrix, qubit QST requires at least a complete set of  $2^{2N}$  projection measurements that have to be performed in a basis spanning the Bloch sphere of the whole system (see section 1.5 and Figure 1.1-b,c). Qudit QST requires instead at least  $d^{2N}$  projections, which is a large number of measurements.

In order to describe the formalism necessary to reconstruct the density matrix of a quantum state, in Appendix D we report the simple case of a frequency-entangled state of two qubit photons. The generalization to multiple qubits and qudits can be found in detail in [8] and [109], respectively.

The density matrix  $\rho$  which is associated to a given physical system has to be Hermitian, as well as positive-definite. The last property means that, given an eigenstate  $|\psi\rangle$  of a positive-definite matrix  $\rho$ , the condition  $\langle\psi|\rho|\psi\rangle > 0$  must be satisfied  $\forall |\psi\rangle$ . However, a density matrix that is reconstructed through quantum state tomography is not typically either Hermitian or positive-definite. This issue can be experimentally addressed by considering the so-called ‘maximum-likelihood estimation’ approach [8], which consists in determining the measured density matrix that “most likely” approximates the physically realistic density matrix. This approach relies on three steps, which are (i)

generating an expression that represents the physical density matrix, *(ii)* introducing a ‘likelihood function’ that quantifies how good the physical density matrix is with respect to the experimental data, and *(iii)* finding the optimal data set for which the likelihood function has its maximum value. These steps are described in detail in Appendix D. In this work, the positivity of the density matrices of the generated high-dimensional frequency-entangled two-photon states that were reconstructed through quantum state tomography was ensured by making use of the maximum-likelihood estimation approach (see subsection 4.2.3).

From quantum state tomography it is finally possible to extract an important quantity that is used to validate the quality of a measured quantum state and how much it is close to the ideal target. This quantity is the so-called ‘fidelity’  $F$  [4, 8, 19] that can be defined as the overlap between the ideal and the reconstructed (measured) density matrix  $\rho_{\text{th}}$  and  $\rho_{\text{exp}}$ , respectively. In formula, the fidelity is

$$F(\rho_{\text{th}}, \rho_{\text{exp}}) = \left[ \text{Tr} (\sqrt{\rho_{\text{th}} \rho_{\text{exp}} \rho_{\text{th}}})^{1/2} \right]^2 \quad (2.6.1)$$

and ranges from 0 to 1 (i.e.  $0 \leq F \leq 1$ ). A zero-fidelity means that there is no overlap (i.e., agreement) between  $\rho_{\text{th}}$  and  $\rho_{\text{exp}}$ , while a fidelity equal to 1 (or, equivalently, 100%) signifies that the two density matrices are identical. While it is experimentally impossible to extract a maximal fidelity, the more  $F$  approaches 1, the closer the measured quantum state is to the ideal target. In view of this, a fidelity higher than 0.5 (i.e., 50% which can thus be considered a threshold value) already testifies a good overlap between  $\rho_{\text{th}}$  and  $\rho_{\text{exp}}$  [4]. A necessary condition to extract the fidelity from a tomography-reconstructed density matrix is ensuring its positivity, which means that the fidelity has to be evaluated from the optimized maximum likelihood function representing the physical (theoretical) density matrix (see Appendix D).

In this work we made use of the quantum state fidelity in order to validate the quality of the generated frequency-entangled photon pairs [6]. Specifically, we showed that all the extracted fidelity values largely exceeded 50%, thus confirming a good agreement between measured and ideal density matrices (see chapter 4).

# Chapter 3

## Cluster states

A main result of the pursued research work is the demonstration of a  $d$ -level multipartite optical cluster state, as well as the characterization of its entanglement through the development of a universal witness operator [5, 7]. Two-level cluster states [98] have been deeply investigated in the literature and have been demonstrated in several optical quantum platforms. In particular, such states have been realized by making of both two- [30, 31, 57] and multi- [29, 110–112] photon states that are entangled in degrees of freedom such as polarization, space, linear and orbital angular momentum. Together with the experimental realization, the characterization of two-level photon cluster state entanglement has been already accomplished by means of specific operators which have been measured via linear optics techniques [30, 33, 57, 113]. On the other hand,  $d$ -level cluster states have been investigated only theoretically [114], while neither experimental realizations nor entanglement characterization have been demonstrated thus far.

In [7] we demonstrate the first ever realization of a  $d$ -level multipartite cluster state, specifically, a four-partite three-level cluster state. To this end, we made use of a two-photon state generated in an integrated optical platform. Such an achievement is reported in chapter 6 of this thesis. We further characterized the entanglement of the novel cluster state through a specific operator (i.e. a witness) that has been derived theoretically in [5]. The derivation is presented in chapter 5 of this thesis. In the current chapter, we introduce the generic properties of cluster states of both qubit [98] and qudit [114] systems. Such a description will provide the reader the tools to fully understand the properties as well as the importance of the novel cluster state demonstrated in this research work.

Cluster states are a class of genuine multipartite entangled states (see section 2.5)

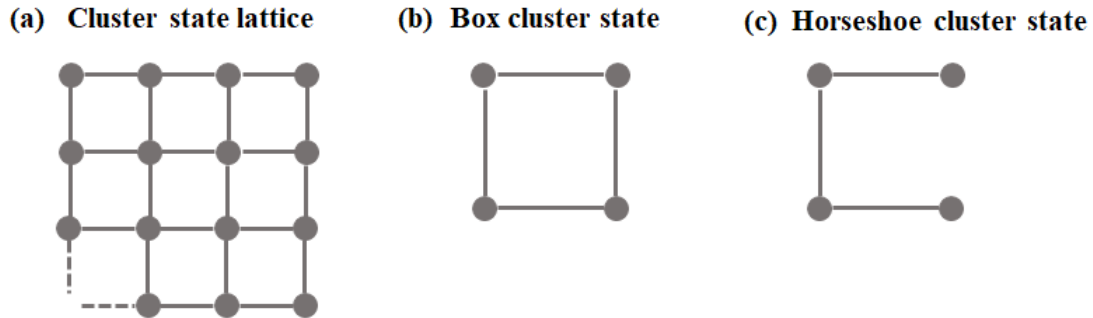


**Figure 3.1** – Different cluster state structures. **(a)** Most generic representation of a cluster state, consisting of nodes, which represent the qubits, and interconnecting lines, which represent the entanglement between the qubits. **(b)** Box and **(c)** Horseshoe cluster states. By means of single-qubit unitary operations, it is possible to convert a lattice structure into another one while maintaining the same type and amount of entanglement.

that were introduced by H. J. Briegel and R. Raussendorf for qubit systems [98] and that were then extended to qudits [114]. From a physical perspective, cluster states are defined as ensemble of qubits located at sites  $a \in \mathbb{Z}^d$  of a  $d$ -dimensional lattice associated to an Euclidean (i.e. a coordinate) space (with  $d = 1, 2, 3$ ) [98]. In order to give rise to a cluster state, these qubits need to undergo interactions that create entanglement between them and that are given by the Hamiltonian  $H_{\text{int}} = -1/4 \sum_{a,a'} \hbar g(t) f(a - a') \sigma_z^{(a)} \sigma_z^{(a')}$ . The indices  $a, a'$  run over all occupied sites of the lattice,  $g(t)$  is the coupling strength, while  $f(a - a')$  specifies the interaction range. Finally,  $\sigma_z$  is the Pauli matrix defined in section 1.7, where the superscripts  $(a)$  and  $(a')$  denote the qubit on which the operator acts [98]. A cluster state system is usually depicted as a lattice (see Figure 3.1-a): the nodes represents the qubits, while the interconnecting lines symbolize the entanglement between them [110, 115]. Following approaches reported in existing literature [98], only cluster states that exhibit interaction between the next neighbors have been considered and analyzed in this work.

A cluster state where only connected qubits interact can be realized by first preparing a large number of physical qubits each in the superposition state  $|+\rangle = 1/\sqrt{2}(|0\rangle + |1\rangle)$ . The qubits then undergo interactions with their nearest (connected) neighbors through, e.g. controlled-phase (C-Phase) gate operations of the form  $|j\rangle |k\rangle \rightarrow (-1)^{jk} |j\rangle |k\rangle$  (with  $j, k \in 0, 1$ ). These operations effectively generate the entanglement between the qubits. A cluster state can assume different lattice structures, which are determined by the specific qubits that are entangled through the C-Phase gate [110]. For example, a cluster state

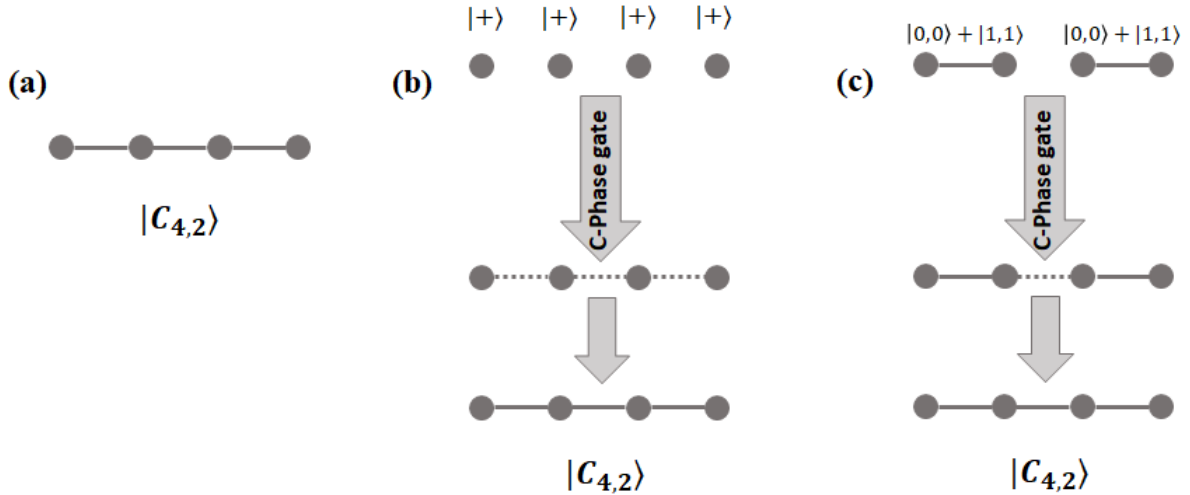


**Figure 3.2** – (a) Chain representing the four-qubit linear cluster state. (b) Experimental way to create the linear cluster state: the four qubits are initially prepared each in the state  $|+\rangle$  and then a C-phase operation is applied between them. (c) An alternative way to experimentally generate the cluster state, starting from two different entangled qubit pairs and then entangling them by means of a single C-Phase gate operation.

can take the form of a box (Figure 3.1-b), or of a horseshoe (Figure 3.1-c). When qubits undergo interactions just in a one-dimensional lattice (i.e. in a chain), the cluster state assumes a linear form (Figure 3.2-a). Figure 3.2-b,c reports a schematic picture of how a four-partite qubit linear cluster state can be implemented by recurring to C-Phase gate operations [115]. The lattice structure of a given cluster state with defined  $N$  and  $d$  can always be converted into another structure by applying unitary operations on the single qubits. Since local unitary operations do not affect entanglement [116], the resulting state is still a cluster state, which is equivalent to the previous one and exhibits the same type of genuine multipartite entanglement.

In this thesis, only linear cluster states will be considered. The four-partite three-level cluster state that we demonstrated was specifically derived by applying single-qubit unitary operations to the corresponding linear form. The reader can find details about this transformation in chapter 6 for the novel cluster state, and in Appendix E for the two-level counterpart.

Due to the described interactions between qubits, cluster states acquire two unique properties, which distinguish them from any other entangled system. These are the *maximal connectedness* (that is, any pair of the cluster state can be projected into a maximally entangled state through local projection measurements on the remaining par-

ties) and *highest persistency of entanglement* (that is, a cluster state requires a maximal number of projection measurements to fully destroy its entanglement). Specifically,  $\lfloor N/2 \rfloor$  projections are needed for that purpose, where  $\lfloor \cdot \rfloor$  denotes the integer part [7, 98, 114]. According to these properties, cluster states can be used as an entanglement resource. For example, Bell and GHZ states can be generated from cluster states by just implementing local operations on cluster states [4, 98].

Furthermore, it can be seen that two- and three-partite cluster states are locally equivalent to Bell and GHZ states, respectively, while cluster states with a number of parties  $N \geq 4$  form a different class which is non-equivalent to any other quantum state [7, 98]. Explicit examples of this property are reported in section 3.1 and section 3.4 for the two- and the  $d$ -level cases, respectively.

Perhaps, the most important application of cluster states is that they can be used as a physical resource for the so-called ‘one-way’ (or ‘measurement-based’) quantum computers, which were introduced for the first time in [41] and that have been already experimentally implemented by making use of two-level cluster state [30, 31, 110]. In the work presented in this thesis we present the first ever demonstration of high-dimensional one-way quantum processing implemented on a three-level cluster state [7] (see section 6.4).

In [41], R. Raussendorf and H. J. Briegel proposed a model of a scalable quantum computer, where the whole computational resource is provided initially in the physical form of a cluster state. Information is then encoded into the cluster, processed, and finally read out by means of projection measurements on the individual parties of the cluster state. Since the actual computation consists of a sequence of local projections, the measurements effectively drive the whole computation (for this reason, they are called ‘measurement-based’ quantum computers). The attribute ‘one-way’ originates from the fact that the computational resource (i.e. the cluster state) can be used only once, since its entanglement is destroyed by the performed projection measurements [41, 117].

One-way operations can be accomplished by means of two basic local projections: those in the computational basis  $\{|0\rangle_j, |1\rangle_j\}$  and those in the superpositions  $B_j(\alpha) = \{|\pm\alpha\rangle_j, |\pm\alpha\rangle_j\}$ , given that  $|\pm\alpha\rangle_j = 1/\sqrt{2}(|0\rangle_j + e^{i\alpha}|1\rangle_j)$ , where  $\alpha$  is a real number and  $j$  denotes the qubit. Operations in the computational basis are considered ‘disentangling operations’, since these remove the physical qubit  $j$  and leave a smaller cluster state. In a one-way quantum computer, the operations in superposition basis are those responsible

for the actual quantum information processing. Projections with respect to the basis  $B_j(\alpha)$  can be accomplished through single-qubit rotations such as  $R_z(\alpha) = \exp(-i\alpha\sigma_z/2)$  [110].

Any quantum operation can be performed by the correct choice of  $B_j(\alpha)$  on a sufficiently large cluster state, while the type of computing to be implemented is typically determined by the cluster state structure [110]. In this sense, quantum computation based on cluster states is universal [41, 117]. However, the implementation of one-way computation is still a theoretical open issue. In particular, the scalability under realistic noise conditions required for fault-tolerant one-way quantum computation is still challenging to address. Even though a noise threshold has been already estimated [118], there is no definite answer to the question whether quantum computation based on cluster states is less or more sensitive to noise compared to the standard model [110].

One-way quantum computers rely on a complex entangled state (the cluster state) as a resource, while they make use of very simple projection measurements for the actual computation. Since it is based on projections, one-way quantum computing provides probabilistic outcomes. For example, let us define the outcomes of a measurement on a physical qubit  $j$  as 0 and 1 for  $|+\alpha\rangle_j$  and  $|-\alpha\rangle_j$ , respectively. When the outcome 0 is found, then the computation proceeds as desired. However, when the outcome 1 is found, a well-defined error is introduced, which is called ‘Pauli error’, as it is caused by the measurement of the Pauli matrices. In order to compensate for these known errors, it is necessary to implement a feedforward process, that is, the output of a measurement is used to control the next measurement, and so forth [119, 120].

One-way quantum computers differ from linear quantum computers by many aspects. For example, the latter make use of a simple quantum state as a source that can be used several times since it is not measured. However, the performed operations are based on several and complex quantum logic gates and circuits, which makes them unsuitable for scalable platforms [119–121]. Finally, due to this type of operations, linear quantum computers provide deterministic outcomes.

After a generic description of the physical properties of cluster states, it is necessary to introduce their wave function for both qubit and qudit states. This will allow the reader to understand from a theoretical as well as an experimental perspective the structure of the novel cluster state demonstrated here.

### 3.1 Two-level (qubit) cluster states

The quantum wave function of a generic  $N$ -partite two-level linear cluster state  $|\phi_{N,2}\rangle$  is given by [98]

$$|\phi_{N,2}\rangle = \frac{1}{2^{N/2}} \bigotimes_{a=1}^N \left[ |0\rangle_a + |1\rangle_a (\sigma_z)^{(a+1)} \right], \quad (3.1.1)$$

with the action of the Pauli matrix  $\sigma_z$  defined as  $\sigma_z |s\rangle = (-1)^s |s\rangle$  ( $s \in \{0, 1\}$ ) (see section 1.7). The superscript  $(a+1)$  denotes the qubit on which  $\sigma_z$  acts. A linear cluster state  $|\phi_{N,2}\rangle$  consists of  $2^N$  terms. By means of appropriate unitary operations on the single qubits,  $|\phi_{N,2}\rangle$  can be transformed into a compact form  $|C_{N,2}\rangle$ . This state can have up to  $2^{N/2}$  or  $2^{(N-1)/2}$  terms for even and odd number of parties  $N$ , respectively. This transformation is described in Appendix E for the cases of  $N = 2, 3$ , and 4 parties, with the scope of comparing cluster states with Bell and GHZ states.

### 3.2 Stabilizer formalism for qubit cluster states

Even though they are expressed in their compact form, cluster states exhibit a very complex wave function. It thus necessary to use an alternate and easier approach to investigate these states from both a theoretical and an experimental perspective. This approach is provided by the so-called ‘stabilizer formalism’ [33], which has been used to describe cluster states of both qubits [33] and qudits [114]. In the pursued research work we made use of the stabilizers formalism developed for qudits in order to derive the presented entanglement witness operator for  $d$ -level cluster states [5, 7] (see chapter 5 and chapter 6). Motivated by the crucial role that stabilizers have played in this research work, a detailed description of the stabilizer formalism for qubit [33] and qudit [114] cluster states is necessary here.

An observable  $\mathcal{S}_k$  is a stabilizing operator for a quantum state  $|\psi\rangle$  when its action on that specific state keeps the whole wave function unchanged. Eventually, a stabilizer can change the quantum state  $|\psi\rangle$  by a global phase factor (more precisely,  $e^{i\pi} = -1$ ), which does not modify the overall state, though. A stabilizer for the state  $|\psi\rangle$  is thus denoted as  $\mathcal{S}_k^{(\psi)}$ , and satisfies the eigenvalue equation [33]

$$\mathcal{S}_k^{(\psi)} |\psi\rangle = |\psi\rangle, \quad (3.2.1)$$

where  $k = 1, \dots, N$  runs over the number of qubits composing the system<sup>1</sup>.

A peculiar property of stabilizers is that they can be expressed as products of the Pauli matrices  $\sigma_{0,x,y,z}$ . This implies that they can be measured through single-qubit projections [5, 7, 113]. This feature is particularly advantageous in quantum information science, since, in any quantum information experiment, an arbitrary projection on a single party is regarded as an ‘easy’ operation, while joint measurements may be difficult to carry out [5] (a detailed description and examples about easy and difficult operations is provided in section 5.3 of this thesis).

The stabilizer formalism can be defined for a variety of entangled states, such as GHZ and cluster states [33]. Only the latter case is considered here. The set of  $N$  stabilizing eigenvalue equations satisfied by a linear  $N$ -qubit cluster state  $|\phi_{N,2}\rangle$  are

$$\mathcal{S}_k^{(\phi_{N,2})} |\phi_{N,2}\rangle = |\phi_{N,2}\rangle, \quad (3.2.2)$$

provided that [33]

$$\begin{aligned} \mathcal{S}_1^{(\phi_{N,2})} &:= \sigma_x^{(1)} \sigma_z^{(2)}, \\ \mathcal{S}_k^{(\phi_{N,2})} &:= \sigma_z^{(k-1)} \sigma_x^{(k)} \sigma_z^{(k+1)}, \quad k = 2, 3, \dots, N-1 \\ \mathcal{S}_N^{(\phi_{N,2})} &:= \sigma_z^{(N-1)} \sigma_x^{(N)}. \end{aligned} \quad (3.2.3)$$

The superscript of the Pauli matrices denotes the qubits on which they act, while the identity  $\sigma_0$  acting on the missing qubits is omitted for simplicity. The eigenvalue equations in Eq. (3.2.2) allow us to determine the set of  $N$  ‘main stabilizers’  $\{\mathcal{S}_1^{(\phi_{N,2})}, \dots, \mathcal{S}_N^{(\phi_{N,2})}\}$ . This generates in turn a stabilizer group  $\mathcal{S}$ , which is given by all the distinct  $2^N$  products of the main stabilizers (together with the identity  $\mathbb{I}$ ) [122]. Since the Pauli matrices are Hermitian, the stabilizer group is Abelian (i.e. commutative).

Furthermore, the  $N$  main stabilizers can be used to construct the density matrix of the cluster state  $\rho_{N,2} = |\phi_{N,2}\rangle\langle\phi_{N,2}|$  as [5, 33]

$$\rho_{N,2} = \prod_{k=1}^N \frac{\mathcal{S}_k^{(\phi_{N,2})} + \mathbb{I}}{2}. \quad (3.2.4)$$

This shows that a given cluster state  $|\phi_{N,2}\rangle$  is uniquely defined by its  $N$  main stabilizers  $\mathcal{S}_k^{(\phi_{N,2})}$ . Two cluster states having same  $N$  but a different wave function (for example, a

---

1. Taking into account that a stabilizer can change the wave function by an overall factor  $e^{i\pi}$ , the eigenvalue equation should be more precisely written as  $\mathcal{S}_k^{(\psi)} |\psi\rangle = \pm |\psi\rangle$ . In the context of this thesis, the notation of Ref.[33] will be adopted, where the phase factor is missing.

linear  $|\phi_{N,2}\rangle$  and a compact  $|C_{N,2}\rangle$  cluster state) possess a different set of main stabilizers, even though they are locally equivalent. As an example, we report in Appendix E the list of the four main stabilizers of four-qubit linear and compact cluster states.

### 3.3 Entanglement witness

As it has been seen in section 2.6, quantum state tomography requires a large number of measurements (specifically,  $d^{2N}$ ). In addition, these measurements can be very intricate to perform experimentally, especially for high dimensional and/or multipartite quantum systems. For example, quantum state tomography can necessitate multiple projections to be performed at the same time on a  $d$ -level system, which is typically a very unfeasible task from an experimental point of view (see section 5.3). For this reason, characterizing entanglement through QST techniques may become extremely arduous, while it is necessary to accomplish this task in a way as easy and accessible as possible despite of the quantum state complexity. Witness operators based on the stabilizer formalism have been derived towards this purpose [33]. Particularly relevant in this work is the entanglement characterization of cluster states via stabilizer witnesses.

Witness operators have been investigated for the first time by A. Peres and P. Horodecki [37–39], while the name “entanglement witnesses” has been attributed later by B. Terhal due to the capability of these operators to distinguish separable from entangled states [47].

A witness  $\mathcal{W}$  is a Hermitian operator that is used in experiments to determine whether a realized quantum state is close to the ideal targeted state and/or whether it is entangled or not. In their definition, a distinction between witnesses for bipartite and multipartite systems has to be considered.

A witness for a bipartite quantum state is defined by the following theorem [37, 39, 123–125]:

*A bipartite density matrix  $\rho \in \mathcal{H}_A \otimes \mathcal{H}_B$  of a generic pure quantum state is entangled if and only if there exists a Hermitian matrix  $\mathcal{W} = \mathcal{W}^\dagger$ , called entanglement witness, such that*

$$\text{Tr}(\mathcal{W}\rho) < 0, \tag{3.3.1}$$

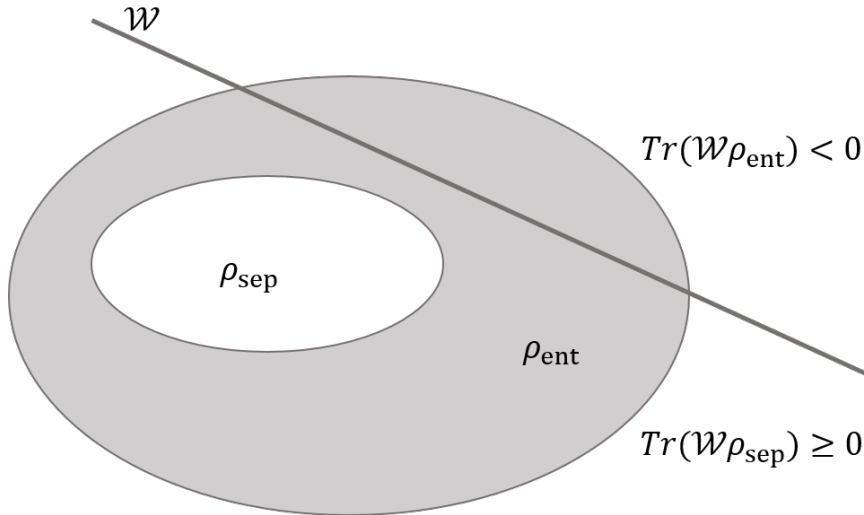


**Figure 3.3** – Geometric representation of the witness. The convex set of bipartite states is divided into two different sets by a line, which represents a hyperplane corresponding to the entanglement witness  $\mathcal{W}$ . All states located to the left of the hyperplane or belonging to it (incl. all separable states) provide non-negative witness expectation value, i.e.,  $Tr(\mathcal{W}\rho_{\text{sep}}) \geq 0$ , while those located to the right are entangled states detected by the witness and thus provide a negative expectation value, i.e.  $Tr(\mathcal{W}\rho_{\text{ent}}) < 0$ .

and

$$Tr(\mathcal{W}\rho_{\text{sep}}) \geq 0 \tag{3.3.2}$$

for any separable state  $\rho_{\text{sep}}$ .

This theorem assesses that a witness does exist for any entangled state and, if a negative expectation value is measured, the immediate conclusion is that the state cannot be separable [47]. Since for bipartite systems non-separability is equivalent to entanglement (see section 2.1), it follows that, for any bipartite entangled state, there always exists a witness capable of its detection. In contrast with entanglement monotones, such as concurrence or entanglement entropy [52], a witness enables entanglement detection but not quantification.

The existence of a witness originates from geometrical considerations. The convex set of bipartite systems consists of two subsets: one containing all separable states, and the other containing all states which are not separable (see Figure 3.3). An entanglement witness defines a hyperplane (the straight line of Figure 3.3) that separates these two subsets. All states located to the left of the hyperplane, or belonging to it, are separable and result in a non-negative witness expectation value. Those states located to the right of the hyperplane are entangled; these are detected by  $\mathcal{W}$ , which results in a negative

expectation value [38].

The case of multipartite systems is much different than the bipartite case. Since distinct classes of multipartite entangled states exist (section 2.5), a witness can be used for both detecting the presence of entanglement and for distinguishing such different classes [116]. In particular, every multipartite entangled state has a witness that is specifically designed for its detection [5]. The definition of witnesses for multipartite system follows:

*A multipartite witness  $\mathcal{W}$  is an observable having a zero or positive expectation value for all separable states, and a negative one for some entangled states [39, 124, 125], i.e.*

$$\text{Tr}(\mathcal{W}\rho) \begin{cases} \geq 0 & \text{for all separable states} \\ < 0 & \text{for some entangled states.} \end{cases} \quad (3.3.3)$$

According to this definition, measuring a non-negative expectation value only provides information that the tested state is not close to the target, while it can still belong to another class of entangled states. In this sense, the provided result is typically ambiguous and does not indicate either the presence or the absence of entanglement.

Let us consider the example of a witness  $\mathcal{W}_{\text{GHZ}}$  constructed to detect states belonging to the class of GHZ states [116]. The following condition exists:

$$\begin{aligned} \text{Tr}(\mathcal{W}_{\text{GHZ}}\rho) < 0 &\Rightarrow \rho \text{ is in the GHZ class} \\ \text{Tr}(\mathcal{W}_{\text{GHZ}}\rho) \geq 0 &\Rightarrow \rho \text{ is not detected.} \end{aligned} \quad (3.3.4)$$

It follows that  $\text{Tr}(\mathcal{W}_{\text{GHZ}}\rho) \geq 0$  for all the systems which are fully separable, biseparable, as well as have not a GHZ-entanglement.

### 3.3.1 Entanglement witness for qubit cluster states

A witness operator has typically a complex mathematical structure. Therefore, determining its expectation value may require the knowledge of the density matrix  $\rho = |\psi\rangle\langle\psi|$ . In this sense, even though a witness exists when  $|\psi\rangle$  is entangled, the detection of this operator through a sequence of measurements on  $\rho$  can be a difficult task [47].

The recent investigation and experimental realization of complex quantum systems such as GHZ and cluster states have intensified the need for deriving witnesses which are

capable of their detection, and straightforward to measure at the same time. This goal has been partially achieved by G. Toth and O. Gühne for specific important classes of qubit states such as GHZ and cluster states [33]. Specifically, G. Toth and O. Gühne exploited the stabilizer formalism in order to derive ‘optimal stabilizer witnesses’ which were experimentally feasible to measure. Two main reasons have led to use stabilizers. First, these operators can be expressed as products of Pauli matrices, which means, they can be measured by means of single-qubit projections (section 3.2). Second, both stabilizers and multipartite witnesses are unique for a given quantum state.

In order to derive a witness which is experimentally feasible and which can be defined as ‘optimal’, two criteria have to be considered and addressed [33]. First, the noise that can be tolerated by a witness has to be as high as possible. Second, the experimental effort required to measure the expectation value of the witness has to be as low as possible. The noise which is typically considered to establish the optimality of a witness is the white noise, as the most common in experimental scenarios [33, 80, 113, 126–128]. In this regards, the reader is referred to subsection 5.2.1, where the effects of white noise on a quantum system, in particular on  $d$ -level multipartite cluster states, are described in detail.

The optimal stabilizer witness that has been derived in [33] for two-level cluster states is now reported. The stabilizer approach used for its derivation will be crucial to understand the method used in this work to derive the novel universal entanglement witness [5].

The optimal stabilizer witness capable of detecting genuine multipartite entanglement close to an ideal cluster state  $|\phi_{N,2}\rangle$  is given by [33]

$$\mathcal{W}_{\text{opt}}^{(\phi_{N,2})} := 3\mathbb{I} - 2 \left( \prod_{\text{odd } k} \frac{\mathcal{S}_k + \mathbb{I}}{2} + \prod_{\text{even } k} \frac{\mathcal{S}_k + \mathbb{I}}{2} \right). \quad (3.3.5)$$

For the ideal state  $|\phi_{N,2}\rangle$ , the expectation value of such a witness is equal to -1, i.e.  $\langle \mathcal{W}_{\text{opt}}^{(\phi_{N,2})} \rangle = \text{Tr}(\mathcal{W}_{\text{opt}}^{(\phi_{N,2})} \rho_{N,2}) = -1$ , where  $\rho_{N,2} = |\phi_{N,2}\rangle\langle\phi_{N,2}|$ . Experimentally, a negative expectation value already provides a necessary and sufficient condition to demonstrate that a realized quantum system exhibits genuine entanglement close to the ideal cluster state.

In the witness expression  $\mathcal{W}_{\text{opt}}^{(\phi_{N,2})}$ , the stabilizers  $\mathcal{S}_k$  are classified as ‘odd’ and ‘even’ by the index  $k$  defining the qubits on which the Pauli matrices act [33]. Odd stabilizers include the measurements in which only  $\sigma_x$  (and not  $\sigma_z$ ) is applied to odd qubits.

Similarly, even stabilizers include the measurements where even qubits are transformed only by  $\sigma_x$  (but not by  $\sigma_z$ ). This classification can be seen explicitly from the eigenvalue equations Eqs. (3.2.3) of section 3.2, as well as from the explicit form of the four main stabilizers of the cluster state  $|\phi_{4,2}\rangle$  (see Eqs. (E.0.11) of Appendix E).

From an experimental perspective, an advantageous property of the witness  $\mathcal{W}_{\text{opt}}^{(\phi_{N,2})}$  is that it can be measured through just two measurement settings, defined by  $\{\sigma_x^{(1)}, \sigma_z^{(2)}, \sigma_x^{(3)}, \sigma_z^{(4)}, \dots\}$  and  $\{\sigma_z^{(1)}, \sigma_x^{(2)}, \sigma_z^{(3)}, \sigma_x^{(4)}, \dots\}$  [33]. The two settings include the Pauli matrices needed for measuring odd and even stabilizers, respectively. Since any quantum operator has to be measured in its eigenbasis, determining  $\sigma_x$  and  $\sigma_z$  (and thus the witness) requires projections on the two settings  $\{|+\rangle, |-\rangle\}$  and  $\{|0\rangle, |1\rangle\}$ , respectively (see section 1.7).

In complete analogy with what has been assessed for stabilizers, the entanglement witness for a compact cluster state  $\mathcal{W}_{\text{opt}}^{(C_{N,2})}$  will have a different expression with respect to the witness for the linear cluster state. This is because the stabilizers composing them will be different. The expression of  $\mathcal{W}_{\text{opt}}^{(C_{N,2})}$  can be obtained from Eq. (3.3.1) by applying the same unitary operations that are used to convert the cluster state, as well as the stabilizers, from the linear to the compact form.

### 3.3.2 Noise tolerance of qubit cluster states

From an experimental perspective, it is always impossible to reproduce exactly an ideal state  $\rho = |\Psi\rangle\langle\Psi|$ . This is because many factors can influence an experiment, such as white noise, fluctuations, environmental perturbations, and so forth. White noise is mainly due to the experimental conditions, as well as to the measurement settings that are used, for example, for quantum state generation, detection, and analysis (i.e. sources, filters, fibers, detectors, phase modulators, etc.). When noise affects a pure entangled state, it adds some mixture to its density matrix, thus modifying the entanglement properties. Testing the robustness of any pure entangled state towards noise is thus crucial to determine the threshold at which the state becomes a non-entangled mixture and/or can be still considered close to the target state. An entanglement witness can be used to test such a robustness [5, 33].

In this section, we report the noise tolerance of two-level cluster states with respect to the optimal witness of Eq. (3.3.5) as demonstrated in [33]. This threshold will turn

out to be useful when we present the noise tolerance of  $d$ -level cluster states which has been derived in [5] and which is reported in subsection 5.2.1. We will consider indeed the two expressions in order to compare the noise robustness of two- and  $d$ -level cluster states from both theoretical and experimental perspectives (see also subsection 6.3.3).

When affected by white noise, the density matrix of a pure two-level quantum state  $\rho = |\Psi\rangle\langle\Psi|$  is modified as [33]

$$\rho_{\text{noise}} = \varepsilon_{\text{noise}} \frac{\mathbb{I}}{2^N} + (1 - \varepsilon_{\text{noise}}) |\Psi\rangle\langle\Psi|, \quad (3.3.6)$$

where  $0 \leq \varepsilon_{\text{noise}} \leq 1$  is the probability that the quantum state is affected by noise. In case of cluster states, the witness  $\mathcal{W}_{\text{opt}}^{(\phi_{N,2})}$  of Eq. (3.3.5) can still detect  $\rho_{\text{noise}}$  as a genuine multipartite entangled state close to the ideal cluster state  $|\phi_{N,2}\rangle$  provided that [33]

$$\varepsilon_{\text{noise}} < \begin{cases} \left(4 - \frac{4}{2^{N/2}}\right)^{-1}, & \text{even } N \\ \left[4 - 2\left(\frac{1}{2^{(N+1)/2}} + \frac{1}{2^{(N-1)/2}}\right)\right]^{-1}, & \text{odd } N. \end{cases} \quad (3.3.7)$$

In subsection 5.2.1 we provide the analytical demonstration of this expression for the case of  $d$ -level cluster states, as well as show that, for  $d = 2$ , the two expressions coincide [5].

From this expression, it can be seen that, in the limit  $N \rightarrow \infty$ , the tolerated noise reaches the minimum value  $\varepsilon_{\text{noise}} = 0.25$ , which means that, for any number of qubits  $N > 2$ , at least 25% of noise is tolerated. Furthermore, it can be noticed that the higher the number of qubits, the lower the tolerated noise [33]. For example, a four-qubit cluster state tolerates up to 33% noise, while the thresholds for five- and six-partite cluster states are 30.7% and 28.6%, respectively.

### 3.4 Multi-level (qudit) cluster states

We now introduce the wave function, as well as the stabilizer formalism, of  $d$ -level cluster states that have been derived in [114]. This introduction will be essential for the reader to understand the formalism that we have used in this thesis to demonstrate high dimensional cluster states and validate their entanglement properties [5, 7].

The wave function of a qudit linear cluster state  $|\phi_{N,d}\rangle$  is given by [5, 114]

$$|\phi_{N,d}\rangle = \frac{1}{d^{N/2}} \bigotimes_{a=1}^N \left( \sum_{k=0}^{d-1} |k\rangle_a Z_{a+1}^k \right), \quad (3.4.1)$$

where  $Z$  is the generalized Pauli matrix (introduced in section 1.8), the action of which is defined as  $Z_a |k\rangle_a = \omega^k |k\rangle_a$ , with  $\omega = e^{i2\pi/d}$ .

For an even number of parties, a  $d$ -level linear cluster state consists of  $d^N$  terms. In complete analogy with the two-level case, it can be transformed, by means of opportune unitary operations on the individual qudits, into a compact form  $|C_{N,2}\rangle$  which has  $d^{N/2}$  terms. Similarly, for an odd number of parties, the linear cluster state containing  $d^{(N+1)/2}$  terms can be transformed into a compact form having  $d^{(N-1)/2}$  terms.

In the case of  $N = 2$  and 3 parties, high dimensional cluster states are locally equivalent to Bell and GHZ states, respectively. This equivalence is shown section 6.1 and Appendix G for the specific case of  $d = 3$  levels, i.e. a ‘qutrit’. We consider such a dimensionality according to the fact that the cluster state investigated and demonstrated here is a three-level system [7].

### 3.4.1 Stabilizer formalism for qudit cluster states

In analogy with the qubit case,  $d$ -level cluster states can be defined and described in terms of stabilizers [114]. However, in contrast with the two-level case, the stabilizer formalism has never been explored in the literature in order to derive high-dimensional entanglement witnesses. The research work presented in this thesis has accomplished this task for the first time ever [5, 7].

The need for developing a stabilizer formalism for high-dimensional cluster states originates from the fact that the wave function of these states assumes a very complex form, which is very arduous to investigate and analyze both theoretically and experimentally. As it can be seen from the examples provided in Appendix G (which are the simplest states, though), such a complexity is mainly due to several terms and phase factors which a cluster state possesses.

According to the definition of a stabilizing operator provided in Eqs. (3.2.2) and (3.2.3), the set of  $N$  stabilizing eigenvalue equations satisfied by a linear cluster state  $|\phi_{N,d}\rangle$  are [5, 114]

$$\mathcal{S}_k^{(\phi_{N,d})} |\phi_{N,d}\rangle = |\phi_{N,d}\rangle, \quad (3.4.2)$$

provided that

$$\mathcal{S}_k^{(\phi_{N,d})} = X_a \bigotimes_{b \in \mathcal{N}(a)} Z_b \quad (3.4.3)$$

where

$$\mathcal{N}(a) = \begin{cases} \{2\}, & a = 1 \\ \{N - 1\}, & a = N \\ \{a - 1, a + 1\}, & a \notin \{1, N\} \end{cases} \quad (3.4.4)$$

denotes the neighbors of the  $a$ -th qudit, while  $X \equiv \Sigma_x$  and  $Z \equiv \Sigma_z$  are the generalized Pauli matrices (see section 1.8). The index  $k$  runs over the number of parties  $N$ , thus defining the  $N$  ‘main’ stabilizers.

Stabilizers (and thus the eigenvalue equations) for compact cluster states can be obtained by applying the unitary operations that are used to convert  $|\phi_{N,d}\rangle$  into  $|C_{N,d}\rangle$ , to the Pauli matrices acting on the qudits that have been transformed [5].

All the distinct products of the main stabilizers, as well as of their transpose conjugates (as they are not Hermitian, see Appendix I), give rise to a set of  $d^N$  stabilizers forming the stabilizer group  $\mathcal{S}$ . In contrast with the two-dimensional case, such a group is not commutative (i.e. it is not Abelian), rather, it is a Pauli group  $\mathcal{P}$ . A Pauli group typically contains both an operator (e.g. a generalized Pauli matrix, a stabilizer) and its transpose conjugate, together with the identity matrix [35].

Finally, the set of  $d^N$  stabilizers allow us to express the density matrix of a given cluster state as [5]

$$\rho_{N,d} = \frac{1}{d^N} \sum_{n=1}^{d^N} \mathcal{S}_n. \quad (3.4.5)$$

In this sense, stabilizers can be used to uniquely define cluster states. In chapter 5 and chapter 6 this property will be shown explicitly for a four-partite qutrit cluster state, while, at the same time, we will show that this expression can be further simplified by making use of the  $N$  main stabilizers only [5, 7].

As it can be seen from the properties outlined in this section, high dimensional stabilizers are not a mere extension of the two-dimensional counterparts, as they exhibit different features (for example, they are not Hermitian). This is a direct consequence of the fact that these are composed of the generalized Pauli matrices. High dimensional stabilizers assume thus a very complex structure, which can be very difficult to measure, requiring  $d$ -level projections that may result very intricate to reproduce experimentally. This is among the main aspects that has prevented the exploitation of high dimensional stabilizers for deriving witness operators thus far. In the research work pursued here, we addressed this issue, and developed an approach that allows us to select those stabilizers

that are more feasible to experimentally reproduce and measure. A detailed description on how this goal has been achieved is reported in chapter 5 [5].

# Chapter 4

## High-dimensional frequency-entangled photon pairs

In this chapter we provide the theoretical basis for the analysis of high-dimensional photon states, as well as for their entanglement characterization. The theoretical study pursued here allowed the experimental realization and coherent control of  $d$ -level frequency-entangled photon pairs [6]. These states were realized specifically ‘on chip’, which means in an integrated optical platform (see section 4.1), while they were manipulated by making use of fiber-based components which are compatible with established telecommunication systems. The coherent control of the realized quantum states consisted of operations that were performed to validate the dimensionality (through Schmidt mode decomposition, see subsection 4.2.1), as well as the entanglement through quantum interference (subsection 4.2.2) and quantum state tomography (subsection 4.2.3) measurements. The specific task that has been accomplished in the work of this thesis was to theoretically derive the measurement settings necessary to accomplish this task. Specifically, these were provided in the form of probability amplitudes (see Eq. (1.3.4)), according to the measurements that we could implement in the laboratory.

Most importantly, the generation and analysis of high-dimensional frequency-entangled two-photon states provided us the prerequisites that were necessary for both the theoretical investigation and the experimental realization of  $d$ -level cluster states [7] (see chapter 6). These states were demonstrated specifically starting from a quantum system which exhibited entanglement in both time and frequency. In this sense the here introduced frequency-entangled states can be seen as the basis in which we could realize

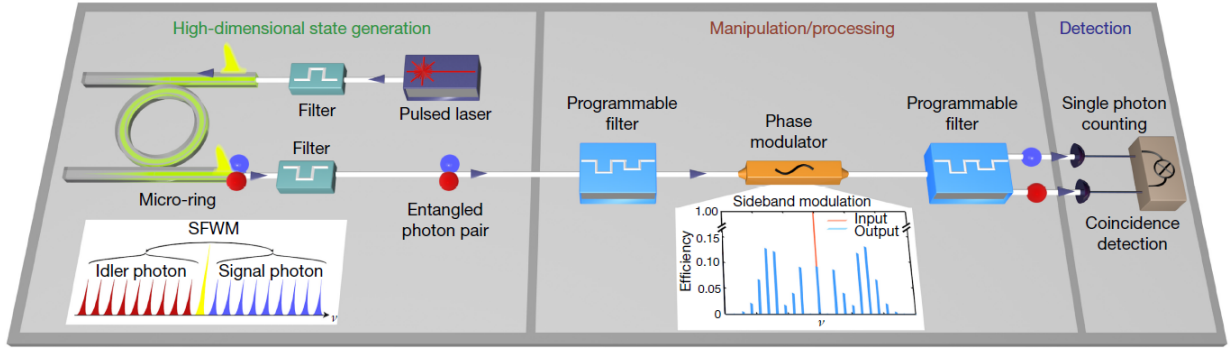


**Figure 4.1** – Experimental setup for high-dimensional quantum state generation and control. A passively mode-locked laser was coupled into the integrated microring resonator after being spectrally filtered to precisely excite a single resonance. SFWM (see left inset) led to the generation of photon pairs (signal and idler) spectrally symmetric to the excitation and in a quantum superposition of the frequency modes defined by the resonances. Programmable filters and a modulator were used for manipulating the state (the right inset shows frequency sideband generation by the modulator as a function of frequency  $\nu$ ), before the signal and idler photons were detected by two single photon counters. [6]

the targeted two-photon cluster state.

The results presented in this chapter finally validate that the frequency domain [20, 129, 130] offers a unique framework for generating qudit states on a photonic chip, as well as for manipulating them in a single spatial mode.

## 4.1 Generation of frequency-entanglement

The scheme that was used here to generate two-photon frequency-entanglement is reported in Figure 4.1. It exploited the SFWM phenomenon (subsection 2.2.3) occurring within an integrated nonlinear microring resonator fabricated from a high refractive index material comprised of silica ( $\text{SiO}_2$ , refractive index  $n = 1.7$ ) and Hydrex glass (see Figure 4.2) [75, 131]. The microring (having a radius  $\sim 48 \mu\text{m}$ ) was vertically coupled to two bus waveguides (cross-section  $1.45 \times 1.5 \mu\text{m}$ , which is the same as the ring), thus forming a four-port configuration (i.e., in, through, drop, and add). The microring, here operating at both the transverse electric (TE) and magnetic (TM) polarization modes, was characterized by a free spectral range (FSR, that is, the spectral separation between adjacent resonance modes) of 200 GHz, and by a Q-factor of 235,000 [19]. The input and output waveguides of the microring (as well as any other setup component) were connected to polarization-maintaining single-mode optical fibers. In particular, the mi-

croving waveguides (order of magnitude of  $\mu\text{m}$ ) were pigtailed (by our collaborators) to the optical fibers (order of magnitude of  $\text{mm}$ ) through the use of mode converters, in such a way to obtain a low-loss (i.e.,  $<1.5$  dB per facet) chip-to-fiber coupling [76].

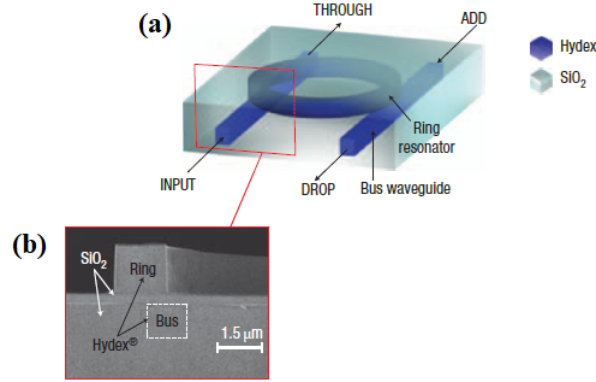


**Figure 4.2** – Material and structure of the microring resonator. **(a)** Four-port microring resonator made of  $\text{SiO}_2$  and Hydex glass. **(b)** SEM image of the cross-section of the microring. acquired before depositing the upper  $\text{SiO}_2$  cladding. The microring radius is about  $48 \mu\text{m}$ , while its cross-section (which is the same as that of the waveguides) is  $1.45 \times 1.5 \mu\text{m}$ . Adapted from [131]

In the described experiment, a single resonance of the microring was excited through a spectrally filtered mode-locked laser at a wavelength of about  $1,550 \text{ nm}$ . The pump pulse duration and the repetition rate were  $570 \text{ ps}$  and  $16.8 \text{ MHz}$ , respectively, while the pulse energy was  $3,600 \text{ mJ}$ .

The excitation of a single microring resonance resulted in the generation of correlated photon pairs (i.e. (s)ignal and (i)idler) that were spectrally symmetric to the excitation field and that covered multiple resonances. Following the microring excitation, the pump was filtered out with a high-isolation bandstop frequency filter (Lightwave2020, extinction ratio  $> 90 \text{ dB}$ ) [76], such that the two photons could be sent in the manipulation/detection schemes (see 4.2.4). The operation bandwidth of the filter was from  $1,527.4 \text{ nm}$  to  $1,567.5 \text{ nm}$ , which allowed us to manipulate ten signal and ten idler resonance pairs (see 4.2.1). More precisely, the frequency range of the signal was  $1,527.4 \text{ nm} - 1,550 \text{ nm}$ , while the idler frequency range was  $1,550 \text{ nm} - 1,567.5 \text{ nm}$  (being  $1,550 \text{ nm}$  the pump wavelength).

In the experimental scheme used here, the signal and idler photons were generated over a spectrum of quantum frequency combs (QFCs), that is, light sources with a broad spectrum of equally-spaced frequency modes [6, 19, 61, 132]. This way, the two photons were generated each in a superposition of multiple frequency modes. Such a superpo-

sition, together with the energy conservation of SFWM, allowed the generation of high dimensional frequency-entanglement. The realized two-photon states can be described by the wave function

$$|\Psi_{\text{two-ph}}\rangle = \sum_{k=0}^{d-1} c_k |k\rangle_s |k\rangle_i, \quad (4.1.1)$$

where  $\sum_k |c_k|^2 = 1$ . The quantum states  $|k\rangle_s$  and  $|k\rangle_i$  represent the frequency modes of the signal and the idler, respectively, while  $d$  is the single-state dimensionality. The described setup allowed for the generation of photon pairs where each photon reached a frequency-dimensionality  $d = 10$ . This resulted in the realization of a two-photon state having a  $10 \times 10$ -dimensional Hilbert space.

In section 4.2, we report the details about the theoretical and experimental analysis that have been pursued to characterize the realized quantum states [6].

## 4.2 Quantum state analysis

### 4.2.1 State dimensionality through Schmidt mode decomposition

In section 2.4 we reported the Schmidt mode decomposition as a tool to verify, through the Schmidt number, the dimensionality of any pure two-partite quantum system. Here, in order to demonstrate that the generated two-photon states reached a  $10 \times 10$  dimensionality, we made use of the Schmidt mode decomposition and evaluated experimentally the Schmidt number of the system. Verifying the dimensionality of single photons was also necessary in the prospective of the generation of a multipartite  $d$ -level cluster state. The projection measurements that were accomplished on this state resulted in the realization of high-dimensional two-partite entangled states, the dimensionality of which can be determined via the Schmidt mode decomposition. In particular, it can be demonstrated [113] that any bipartite subset that is extracted from a multipartite system (for example, a cluster state), has a maximal Schmidt coefficient equal to  $1/\sqrt{d}$ . This was a crucial point towards the derivation of the universal multipartite witnesses demonstrated in [5], and it will be described in detail in subsection 5.3.1.

In the frequency domain, the Schmidt mode decomposition of Eq. (2.4.1) of a two-

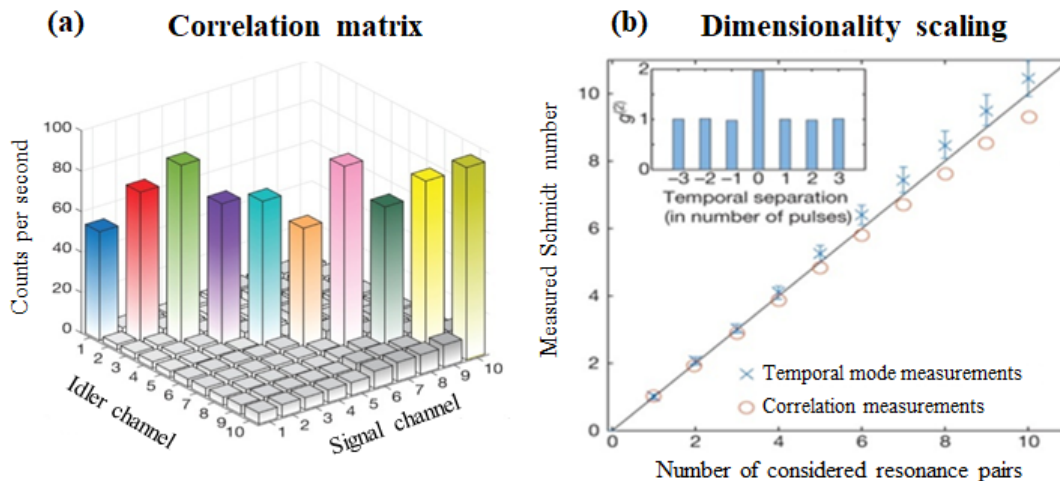


**Figure 4.3** – Characterization of the quantum state dimensionality. **(a)** Measured JSI of the high-dimensional quantum state, showing photon coincidences only at symmetric mode pairs (that is, on the diagonal of the matrix) and revealing a frequency correlation. **(b)** Schmidt number as a function of the considered resonance pairs, symmetric to the excitation frequency, with the upper bound (blue crosses) obtained from the second-order coherence, and lower bound (red circles) calculated from the correlation matrix. The inset in (b) shows the measured second-order coherence function of a single photon emitted at one specific resonance with a maximum of  $1.92 \pm 0.03$ , corresponding to  $1.086 \pm 0.03$  effective modes. [6]

photon entangled state can be rewritten as

$$\mathcal{F}(\omega_s, \omega_i) = \sum_{n=1}^d \sqrt{\lambda_n} \psi_n(\omega_s) \phi_n(\omega_i), \quad (4.2.1)$$

where  $\mathcal{F}(\omega_s, \omega_i)$  is the joint spectral amplitude (JSA) [87], and  $\lambda_n$  are the Schmidt coefficients (defined in section 2.4), while  $\psi_n(\omega_s)$  and  $\phi_n(\omega_i)$  are the wave functions of signal and idler, respectively, with  $\omega_s$  and  $\omega_i$  being their respective frequencies. In the JSA expression, the Schmidt number  $K = \left(\sum_{n=1}^d \lambda_n^2\right)^{-1}$  represents the lowest amount of relevant orthogonal frequency modes of the system [86].

From an experimental point of view, determining  $K$  directly from the JSA is very challenging, since its measurement would need the full phase information of the quantum state [86]. For this reason, the Schmidt number was extracted here by making use of a different and experimentally easier approach. Specifically, we determined a lower and an upper bound for  $K$  (i.e.  $K_{\text{low}}$  and  $K_{\text{up}}$ , respectively) such that, from their comparison, we could validate the dimensionality of the realized frequency-entangled states [6].

In order to estimate the lower bound  $K_{\text{low}}$ , we made use of the joint spectral intensity (JSI) [88] that is defined as  $|\mathcal{F}(\omega_s, \omega_i)|^2$  and can be measured by performing spectrally

resolved coincidence measurements. The JSI is therefore the correlation matrix (see Figure 4.3-a). In order to get the minimum number of orthogonal modes (which means,  $K_{\text{low}}$ ), the relation  $\mathcal{F}(\omega_s, \omega_i) \approx \sqrt{|\mathcal{F}(\omega_s, \omega_i)|^2}$  can be used, which however results in a loss of phase information (which is not necessary for determining  $K_{\text{low}}$ , though) [88]. The Schmidt eigenvalues needed for  $K_{\text{low}}$  estimation were hence extracted from the correlation matrix  $\sqrt{|\mathcal{F}(\omega_s, \omega_i)|^2}$  by performing the singular value decomposition. This is indeed the equivalent of the Schmidt mode decomposition of a two-partite state (section 2.4), but applied to its measured density matrix.

Operationally, the coincidence measurements were accomplished by routing different signal and idler frequency modes to two single photon detectors and by finally counting photon coincidences for all sets of mode combinations. The dead time of the single-photon detectors was approximately 100-200 ns, while the dark count rate and the channel detection jitter (with respect to the common sync clock) were  $\sim 1$  kHz and  $\sim 80$  ps, respectively. The integration time significantly varied depending on the measurement to be performed (e.g., an hour for ‘fast’ measurements such as the correlation measurements described in this section, or 2-3 days for ‘long’ measurements such as those necessary for quantum state tomography and interference, see subsection 4.2.2, subsection 4.2.3, and subsection 4.2.4).

As it can be seen from Figure 4.3-a, the photon coincidences were measured only for those mode combinations that were spectrally symmetric to the excitation field, which is a characteristic of frequency-entangled states. From the singular value decomposition of the correlation matrix, we extracted the lower bound for the Schmidt number, which was found to be  $K_{\text{low}} = 9.4$ . The ten modes symmetric to the resonance of the microring could be selected and manipulated individually through a commercially available telecommunications programmable filter having an operational bandwidth of 1,527.4 nm to 1,567.5 nm (see section 4.1). The use of such a filter could be possible due to the large FSR of the microring (200 GHz).

In order to estimate the upper bound  $K_{\text{up}}$ , we made use of the second-order signal-idler coherence function  $g_{s,i}^{(2)}(t)$  in the time domain. The setup used to measure the coherence function consisted of a programmable filter (used to adjust the number of the considered photon pairs resonances), a 50:50 beam splitter, and two single-photon detectors (see Figure 4.1).

The second-order coherence function  $g^{(2)}(\tau)$  typically provides the degree of correlations between the number of photons detected in the range defined by the times  $t$  and  $t + \tau$ . A very important value is  $g^{(2)}(\tau = 0)$ , which gives information about how often two photons are detected at the same time. Three different scenarios may occur. First,  $g^{(2)}(\tau = 0) = 0$ : photons arrive in pairs at zero time delay, but independently at long time delays. This is known as *photon bunching*. Second,  $g^{(2)}(\tau = 0) = 1$ : the detection events are uncorrelated and photons arrive randomly at the two detectors. In this case, *coherent light* is observed. Third,  $g^{(2)}(\tau = 0) < 0$ : this is the opposite of photon bunching and is known as *photon antibunching*. The photons tend to arrive evenly spaced in time, the probability of obtaining coincident photons in a time interval is less than for coherent light [15, 16].

The time-domain second-order coherence function of a quantum state is directly correlated to the number of effective modes  $N_{\text{eff}}$  within the system [133]. Assuming that these modes have equal amplitudes, the maximum of  $g_{s,s}^{(2)}$  is directly related to  $N_{\text{eff}}$  as

$$g_{s,s}^{(2)}(t = 0) = 1 + \frac{1}{N_{\text{eff}}}, \quad (4.2.2)$$

where subscript ‘s,s’ refers to ‘signal-signal’ correlations. If a state is measured in a single mode (i.e.,  $g_{s,s}^{(2)}(t = 0) = 2$ ), the state is pure [134]. If the signal and the idler are measured both in a single mode, then the two-photon state is fully separable and it is not entangled.

The generation of a pure quantum state is strictly related to the pump configuration that is used to excite the photon pairs. If the excitation bandwidth is equal to the signal and idler bandwidth, then the state is generated with highly pure frequency modes [135]. In the experiment presented here, this purity condition could be achieved by pumping the microring resonator with a broadband pulsed laser that has been spectrally filtered to excite only a single resonance. Specifically, this resonance acted as an additional spectral filter, ensuring a match between the input pulse and the full resonance bandwidth. This way, each photon of the signal-idler pairs was expected to be emitted at one specific resonance.

By selecting individually ten resonances for both signal and idler, we validated that the resonance of each photon was in a highly pure quantum state (see Figure 4.3-b). The  $g_{s,i}^{(2)}$  function (inset of Figure 4.3) was normalized with respect to the background level (equal to 1), which was determined by considering the ratio between  $g_{s,i}^{(2)}$  and the cross-correlation

level at larger pulse separations. As a consequence of the high purity of each photon resonance, the whole two-photon state, defined over a pair of single resonances that were symmetric to the excitation frequency, has a Schmidt number that is approximately equal to one. In this experiment, we considered the Schmidt number of ten selected resonance pairs. From the sum of these, we obtained the upper bound of the Schmidt number, which was  $K_{\text{up}} = 10.45 \pm 0.53$  (see Figure 4.3).

Since the lower and upper bound  $K_{\text{low}}$  and  $K_{\text{up}}$  coincided within the error bar, we could conclude that the number of relevant orthogonal modes was ten, which means that each photon was generated in a 10-dimensional frequency state. Finally, the measured Schmidt modes validated that each of the generated photon pairs simultaneously spanned multiple highly pure frequency modes. This allowed us to conclude that high-dimensional frequency-entangled states of the form of Eq. (4.1.1) were generated.

Realizing Bell-like states with highly pure single modes is a crucial requirement in quantum information processing [136]. In section 3.1, section 3.4, as well as in Appendix E and Appendix G, we further showed that it is possible to transform Bell states into two-partite cluster states (and vice versa) by means of opportune local unitary operations. For example, Bell states are equivalent to two-partite linear cluster states when the Hadamard operator is applied to the second qudit (see section 1.8). In this sense, the high dimensional two-photon states demonstrated in [6] can be used as a basis to implement gate and measurement-based quantum operations.

Determining the dimensionality as well as the purity of the frequency modes of a two-photon state is not sufficient to validate and characterize its entanglement. This can be accomplished by extracting the visibility and the quantum state fidelity from quantum interference (section 2.3) and quantum state tomography (section 2.6), respectively. To this end, it was necessary to project the realized quantum states into a single, as well as in superpositions of frequency modes. The specific measurements that were first derived theoretically, and then implemented experimentally, are discussed in the next two sections.

## 4.2.2 Quantum interference measurement

The projection measurements that were allowed by the available measurement setting (see subsection 4.2.4) take the form

$$|\psi_{\text{proj}}\rangle = \sum_{k=0}^{d-1} \alpha_k e^{i\varphi_k} |\bar{k} + k\rangle, \quad (4.2.3)$$

where  $\bar{k}$  denotes the spectral mode selected for the projection, while  $\alpha_k$  and  $\varphi_k$  are the amplitudes and phases that can be chosen arbitrarily for each photon, respectively.

Since the amplitudes  $c_k$  of Eq. (4.1.1) were measured here to be very similar to each other, we could assume that the generated high dimensional frequency-entangled states can be approximated as

$$\sum_{k=1}^d c_k |k\rangle_s |k\rangle_i \approx \frac{1}{\sqrt{d}} \sum_{k=1}^d |k\rangle_s |k\rangle_i = |\Psi_{\text{Bell}}\rangle, \quad (4.2.4)$$

which means, they were generated in a Bell form. We confirmed this assumption by using quantum interference and Bell inequalities' violation (see subsection 2.3.1) [13].

According to the measurements allowed by the used manipulation scheme, we chose to perform projections of the form

$$|\psi_{\text{proj}}\rangle = \frac{1}{\sqrt{d}} \sum_{k=0}^{d-1} e^{ik\theta} |\bar{k} + k\rangle, \quad (4.2.5)$$

where  $\theta$  denotes the phase difference between signal and idler. The projections of Eq. (4.2.5) enabled us to measure quantum interference (in the coincidence counts) as a function of  $\theta$ . Specifically, the two-photon states were projected into

$$|\Psi_{\text{proj}}\rangle = \frac{1}{d} \left( \sum_{k=0}^{d-1} e^{ik\theta} |\bar{k} + k\rangle_s \right) \left( \sum_{k=0}^{d-1} e^{ik\theta} |\bar{k} + k\rangle_i \right), \quad (4.2.6)$$

for  $d = 2, 3$ , and  $4$ , where the subscripts 's' and 'i' stand for signal and idler, respectively. These projections were experimentally accomplished by mixing the modes  $|k\rangle$ ,  $|k+1\rangle$ ,  $|k+2\rangle$ , and  $|k+3\rangle$  through the manipulation setup described in subsection 4.2.4 [6].

The specific task that was accomplished in this thesis was the derivation of the explicit form of all the projection measurements enclosed in Eq. (4.2.5). These are reported in Appendix H.

Making use of the derived projections, the quantum interference patterns were mea-

sured through the following probability amplitudes

$$\begin{aligned}
& |\langle \Psi_{\text{proj},d=2}(\theta) | \Psi_{\text{Bell},d=2} \rangle|^2 \\
& |\langle \Psi_{\text{proj},d=3}(\theta) | \Psi_{\text{Bell},d=3} \rangle|^2 \\
& |\langle \Psi_{\text{proj},d=4}(\theta) | \Psi_{\text{Bell},d=4} \rangle|^2.
\end{aligned} \tag{4.2.7}$$

The expected quantum interference signal  $C_d(\theta)$  for  $d = 2, 3,$  and  $4$  is given by

$$\begin{aligned}
C_{d=2}(\theta) &= 1 + \varepsilon_2 \cos 2\theta, \\
C_{d=3}(\theta) &= 3 + 2\varepsilon_3 (2 \cos 2\theta + 4 \cos 4\theta), \\
C_{d=4}(\theta) &= 4 + 2\varepsilon_4 (3 \cos 2\theta + 2 \cos 4\theta + \cos 6\theta),
\end{aligned} \tag{4.2.8}$$

respectively. The coefficients  $\varepsilon_d \equiv \varepsilon_{\text{noise}}$  are the probabilities that the entangled state is affected by noise and originate from the white noise model (see subsection 3.3.2 and subsection 5.2.1).

The measured quantum interference signals are reported in Figure 4.4-a,b,c for the cases  $d = 2, 3,$  and  $4,$  respectively. These were then used to extract the respective visibility  $V_d$  which resulted<sup>1</sup> [6]

$$\begin{aligned}
V_2 &= 83.6\% \\
V_3 &= 86.6\% \\
V_4 &= 86.4\%.
\end{aligned} \tag{4.2.9}$$

The visibility is typically related to the noise probability  $\varepsilon_d$  as [6]:

$$\begin{aligned}
V_2 &= \varepsilon_2 \\
V_3 &= \frac{3\varepsilon_3}{2 + \varepsilon_3} \\
V_4 &= \frac{4\varepsilon_4}{2 + \varepsilon_4}.
\end{aligned} \tag{4.2.10}$$

We considered the values  $p_d^{\text{min}}$  reported in Eqs. (2.3.7a)-(2.3.7c) (which however express the probability that the entangled state is not affected by noise), in order to relate the measured visibilities with the noise tolerated by the generated frequency-entangled states. We further used the visibilities for Bell inequality violations. In order to violate the high

---

1. The visibilities have been extracted from their respective quantum interference pattern by changing the phase  $\theta$  and measuring the variation in the coincidence counts, which are however normalized to 1 here. For this reason, the error bar associated to each visibility value is not reported, while such an error is given by the square root of the number of counts.

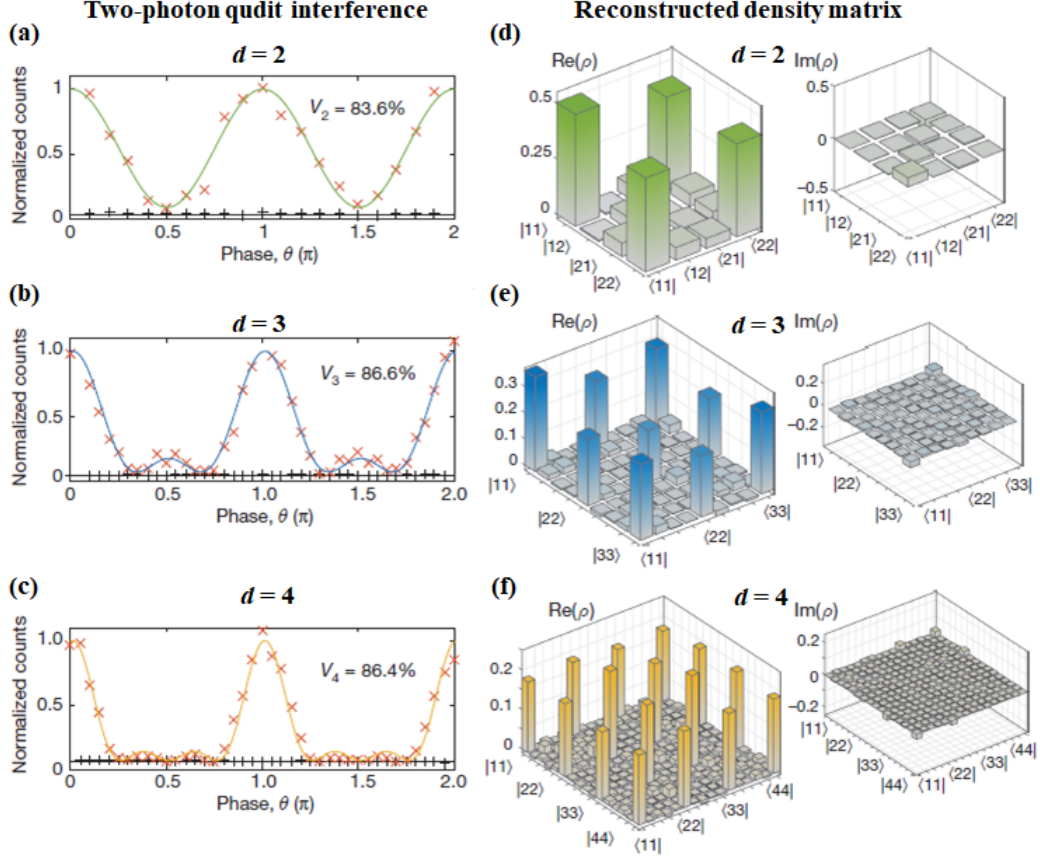


**Figure 4.4** – Bell inequality violation and quantum state tomography of frequency-entangled states. Quantum interference patterns for (a)  $d = 2$ , (b)  $d = 3$ , and (c)  $d = 4$ , which have been obtained by projecting the two-photon states on a superposition of  $d$  frequency modes. Raw visibilities (without background subtraction) of 83.6%, 86.6% and 86.4% were extracted from the interference patterns. These exceeded the visibilities of 71%, 77% and 81.7%, required to violate the Bell inequality for  $d = 2, 3$  and  $4$ , respectively, thus demonstrating the entanglement of the generated two-photon states. Measured density matrix of the qudit states reconstructed through quantum state tomography for (d)  $d = 2$ , (e)  $d = 3$  and (f)  $d = 4$ . Fidelities of 88.5%, 80.9%, and 76.6% were obtained for  $d = 2, 3$ , and  $4$ , respectively, thus demonstrating very good agreement between the measured and the expected maximally entangled states. [6]

dimensional Bell inequalities for  $d = 2, 3$ , and  $4$ , the following conditions must be satisfied [13]:

$$\begin{aligned}
 \frac{1}{\sqrt{2}} &\approx 0.7071 < V_2 \\
 \frac{3(6\sqrt{3} - 9)}{6\sqrt{3} - 5} &\approx 0.7746 < V_3 \\
 \frac{6}{3 + \sqrt{10 - \sqrt{2}}} &\approx 0.8170 < V_4.
 \end{aligned} \tag{4.2.11}$$

A comparison between Eqs. (4.2.11) and (4.2.9) immediately shows that the visibil-

ities all violate their respective Bell inequality. This confirmed that the demonstrated frequency-entangled photon pairs were generated in high dimensional Bell states<sup>2</sup> [6].

The visibilities reported in Eqs. (4.2.9) allow us to do further considerations about high dimensional quantum states. We can observe that the visibility increases as the single-state dimensionality increases. According to the relation between noise and visibility, we thus conclude that quantum state with higher dimensionality are more robust to noise with respect to lower-dimensional states. This conclusion is a further experimental confirmation of what has been demonstrated in [13] and that is reported in subsection 2.3.1 of this thesis: two-partite  $d$ -level quantum states are more noise tolerant than their two-level counterpart. In [5, 7] we demonstrated this concept also for multipartite systems from both a theoretical and an experimental perspective, respectively (see subsection 5.2.1 and subsection 6.3.3).

### 4.2.3 Quantum state tomography

In order to perform qudit quantum state tomography and verify the quality of the generated entangled states, we made use of the same type of  $d$ -level projections that were used for quantum interference (see subsection 4.2.2). However, the number of made projections was significantly increased, as a minimum of  $d^{2N}$  measurements is needed for full quantum state tomography (see section 2.6).

The density matrices of the generated two-photon states were reconstructed for the dimensionalities  $d = 2, 3$ , and  $4$ . This required performing  $2^{2 \times 2} = 16$ ,  $3^{2 \times 2} = 81$ , and  $4^{2 \times 2} = 256$  projection measurements, respectively. The projections that were used for quantum state tomography and that were theoretically derived here are reported in Appendix H. The measured density matrices, reconstructed by following a similar approach as that reported in Appendix D, are depicted in Figure 4.4-d,e,f, for  $d = 2, 3$ , and  $4$ , respectively. In order to ensure the positivity of the matrices reconstructed through quantum state tomography, we estimated the maximum likelihood function by

---

2. In order to measure quantum interference and extract the visibility, coincidence counts are needed that are collected by means of single-photon detectors (see section 2.3 and subsection 4.2.4). In principle, the detection rate of single-photon detectors can be influenced by other photons' properties (e.g., polarization, momentum), which cannot obviously be avoided. However, as long as these properties are not experimentally manipulated (through, e.g., wave plates), we can assume they do not influence the detection rate.

following the procedure described in [8] (more precisely, its extension to qudits [109]), which is reported in section 2.6 and Appendix D of this thesis. According to this approach, the numerical optimization of the maximum likelihood function was performed here by making use of a MATLAB code that had been written prior to the starting of this PhD studies and that was utilized for optimizing the maximum likelihood function in [19]. The experimental data  $n_\nu$  (see Appendix D) that were used as input for the optimization are the measured coincidence counts. Acquiring these experimental data and using them to launch the MATLAB simulations for maximum likelihood estimation was not part of the theoretical work that has been specifically accomplished for the purpose of this PhD thesis.

Finally, From Eq. (2.6.1) of section 2.6 we further estimated the fidelity  $F$  of the generated two-photon states. Specifically, the measured fidelities resulted in  $F_{d=2} = 88.5\%$ ,  $F_{d=3} = 80.9\%$ , and  $F_{d=4} = 76.6\%$ . By observing these values, it can be seen that the quantum state fidelity decreases as the single-state dimensionality  $d$  increases. The reason of such a behavior can be fully understood in subsection 4.2.4, in which we introduce the experimental scheme that was used to perform the frequency projections.

It is worth to remind that, while a fidelity of one describes a perfect overlap between the ideal and the measured states, an overlap  $>50\%$  is already a sufficient condition to testify the good quality of a generated quantum state (see section 2.6). Since here the lowest fidelity is  $76.6\%$  (much higher than  $50\%$ ), the here realized two-photon states all exhibit a good overlap with the ideal maximally entangled Bell states for the respective dimensions  $d = 2, 3$ , and  $4$ .

#### 4.2.4 Experimental scheme for quantum state manipulation

The  $d$ -level projections described in subsection 4.2.2 and subsection 4.2.3 necessitated precise, coherent, and non-probabilistic (i.e., preserving the density matrix of the quantum state) operations and control over the individual frequency qudits. Furthermore, it is highly desirable that these operations can have access to multiple modes by making use of a minimum number of components. This is because of the applications that high dimensional states may have for quantum information processing.

In this context, the frequency domain is particularly suitable, since it is possible to address multiple frequency components in a single spatial mode (for example, a standard

telecom fiber). This addressing could be achieved practically by means of ultrafast signal processing, state-of-the-art, yet established radio-frequency and telecommunication technologies [137]. Such technologies can be exploited for quantum state manipulation, e.g., for implementing fundamental optical gate operations (e.g. phase gates), as well as high dimensional frequency mixing (i.e. ‘beam splitting’ in the frequency domain).

In this work, we exploited fiber-based technologies in order to coherently control the frequency-entangled states and hence to perform  $d$ -level projections in the spectral domain. These projections could be implemented via phase shift and frequency mixing, which were realized by using two programmable phase filters and an electro-optic modulator, respectively (see Figure 4.1) [6].

While we could in principle generate two-photon states with up to  $d = 10$  dimensionality per single photon, the coherent state manipulation was possible, with the current setup, up to  $d = 4$ . As it will be discussed later in this section, this limitation was mainly due to the electro-optic modulation techniques used for quantum state processing.

The detailed description of the manipulation scheme is reported in Figure 4.5. Such a scheme can be viewed as the operating principle of the ‘Manipulation/processing’ panel of Figure 4.1. The first programmable filter (PF1) was used to impose an arbitrary spectral amplitude and phase mask on the generated two-photon state  $|\Psi_{\text{two-ph}}\rangle$ . This action is denoted operationally as  $A_{\text{PF1}}|\Psi_{\text{two-ph}}\rangle$ , where  $A_{\text{PF1}}$  is operator representing the action of PF1 (see Figure 4.5-b). The so-transformed state  $A_{\text{PF1}}|\Psi_{\text{two-ph}}\rangle$  was then sent to the electro-optic phase modulator (Mod), which was driven by a radio-frequency synthesizer [138, 139]. The action of the modulator on the input state  $|\Psi_{\text{two-ph}}\rangle$  is denoted as  $A_{\text{Mod}}A_{\text{PF1}}|\Psi_{\text{two-ph}}\rangle$ .

In the case of a single frequency mode input, the phase modulation nonlinearly creates sidebands: here, the amplitudes and spectral spacing can be controlled via modulation voltage and radio frequency, respectively. If an integer multiple of such a sidebands spacing matches the free spectral range of the microring resonator, the mixing of optical signals in neighbouring resonances takes place. This process is governed by a linear,

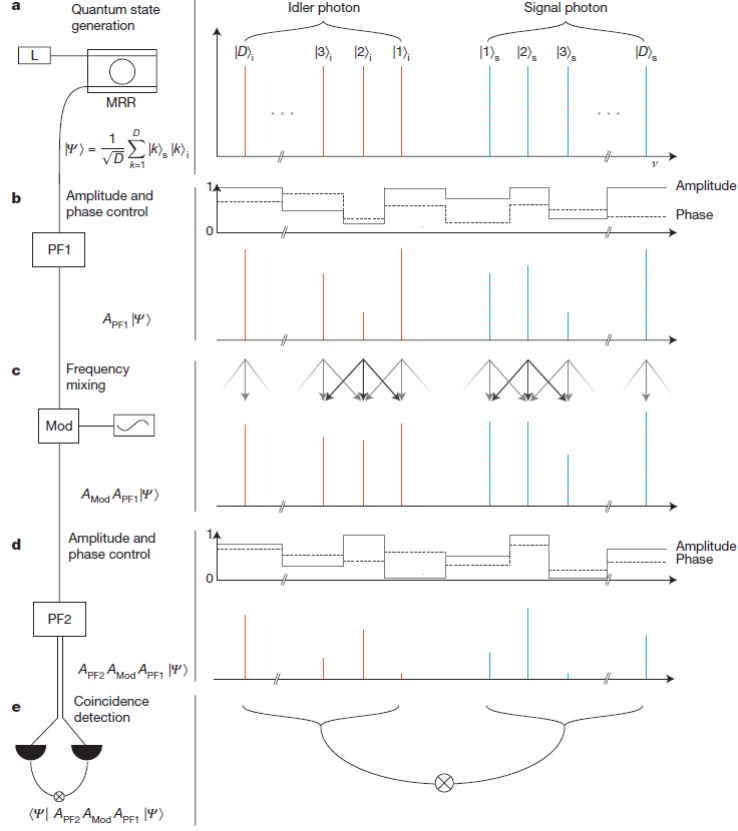


**Figure 4.5** – Experimental implementation of coherent control. **(a)** The initial states  $|\Psi\rangle$  were generated through the microring resonator (MRR). **(b)** Using a programmable filter (PF1), any arbitrary spectral phase and amplitude mask can be imposed on the quantum states for manipulation. **(c)** An electro-optic modulator (Mod) was used to coherently mix different frequency components of the high-dimensional states. **(d)** A second programmable filter (PF2) can impose an amplitude and phase mask and route the signal and idler to two different paths. **(e)** The photons were then detected using single photon counters and timing electronics. This step, together with the previous adjustable coherent control, allows the implementation of adaptable projection measurements. [6]

unitary, and time-dependent operator<sup>3</sup>, which, in the time-domain, has the form

$$T(t) = e^{iV_m k \sin(2\pi\nu_m t + \phi_m)}. \quad (4.2.12)$$

Here,  $t$  denotes the time,  $V_m$  is the voltage amplitude of the radio-frequency tone,  $k$  is the electro-optical coefficient of the phase modulator,  $\nu_m$  is the radio frequency, and  $\phi_m$  is the initial phase. Due to its intrinsic time-periodicity, this operator can be expressed

3. The operator in Eq. (4.2.12) can generate very wide bands. However, this does not represent a problem for the equipment used here, as the frequency modulation that we performed remains in the operator range unit. More precisely, we performed a maximal frequency modulation of 300 GHz, which is  $\sim 2$  nm.

as an infinite trigonometric series:

$$T(t) = \sum_{n=-\infty}^{\infty} a_n e^{i2n\pi\nu_m t}. \quad (4.2.13)$$

In this expression,  $a_n$  denotes the coefficient of the sidebands, and is determined by the Jacobi–Anger expansion as

$$a_n = J_n(V_m k) e^{in\phi_m}. \quad (4.2.14)$$

Here,  $J_n(V_m k)$  is the  $n$ -order Bessel function of the first kind, evaluated at  $V_m k$ . The amplitude of the sidebands is determined by Bessel coefficients. This means that, for a given input optical signal, the phase-modulated output is described by a series of harmonic functions, the weight of which is given by the Bessel coefficients. Each frequency mode is split into a series of modulation products (frequency modes) that are spectrally spaced by multiples of the driving frequency  $\nu_m$ . The achievable modulation bandwidth depends on both  $\nu_m$  and  $V_m$ . Therefore, as long as a sufficiently high value of voltage  $V_m$  is supplied, a low driving frequency  $\nu_m$  can generate modulation products at high frequencies.

The quantum mechanical operator that describe the frequency-mixing action and that transform an input state into an output state is defined as [140, 141]:

$$A_{\text{Mod}}^{\{s,i\}} = \sum_{\bar{k}=0}^{d-1} \sum_{\bar{l}=0}^{d-1} c_{\{s,i\},\bar{k}-\bar{l}}^{\text{Mod}} |\bar{l}\rangle \langle \bar{k}|. \quad (4.2.15)$$

The mixing coefficients are related to the sideband modulation terms by  $c_{\{s,i\},x}^{\text{Mod}} = a_{x \cdot p}$ , where  $p$  is a natural number such that  $p \cdot \nu_m$  matches the FSR of the microring resonator. At this stage, it is possible to explain the equivalence between the projection state  $|\Psi_{\text{proj}}\rangle$  of Eq. (4.2.6) and the experimental realization formulated through the operation  $A_{\text{PF1}}|\Psi_{\text{two-ph}}\rangle$ . Eq. (4.2.6) projects both signal and idler photons into a quantum superposition of frequency modes  $|k\rangle$ , each of them having a precise phase factor  $e^{ik\theta}$ . In order to properly reproduce such a projection experimentally, it is thus necessary to apply a phase to the individual frequency modes as well as to shift a given frequency mode from  $|\bar{k}\rangle$  to  $|\bar{k} + k\rangle$ . The action of applying a phase is described experimentally by the operator  $A_{\text{PF1}}$  (i.e., the first programmable phase filter), while the action of mode shifting can experimentally be accomplished by means of a frequency-mixing to be performed through the electro-optic phase modulator. The operator describing the EOM action (denoted as  $A_{\text{Mod}}$ ) is thus nothing but a scattering operator [140, 141]. Therefore, applying first  $A_{\text{PF1}}$  and then  $A_{\text{mod}}$  on the two-photon state  $|\Psi_{\text{two-ph}}\rangle$  experimentally reproduce the two-photon state projection of Eq. (4.2.6).

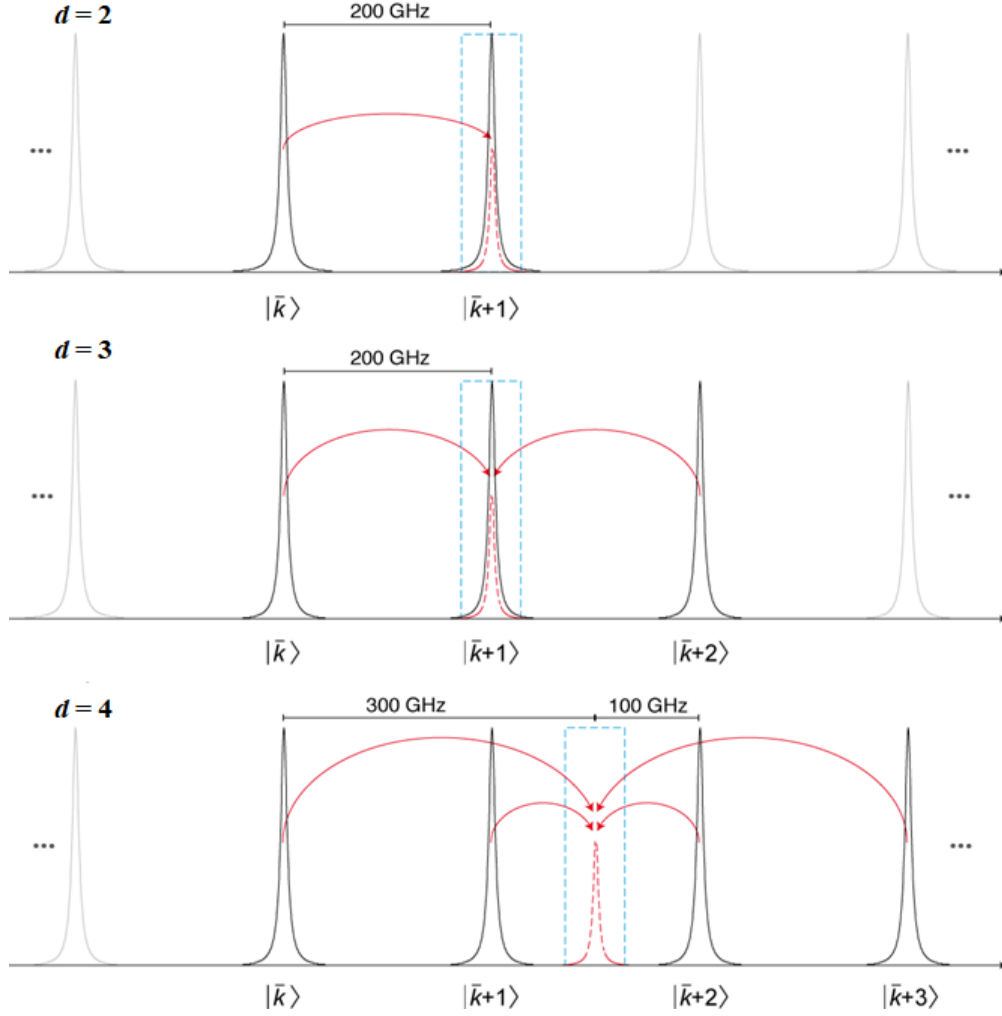


**Figure 4.6** – Coherent mixing of multiple frequency modes.  $d$  modes  $|\bar{k}\rangle$  are spectrally selected (solid black line) and mixed (red arrows) by means of an electro-optic phase modulator. The frequency mode where all components overlap (red dashed line) is then selected via a narrow spectral filter (blue dashed window). For  $d = 2$  and  $3$ , a frequency shift of 200 GHz (equal to the FSR) is implemented, whereas for  $d = 4$  two different frequency shifts of 100 GHz and 300 GHz are enforced. In all cases, this is achieved through sideband generation. Note that for  $d = 4$ , and in contrast to  $d = 2$  and  $3$ , the final frequency mode does not overlap with any microcavity resonance. [6]

In the experiment performed here,  $\text{FSR} = 200 \text{ GHz}$ , while  $\nu_m \approx 33.3 \text{ GHz}$ . By making use of a sine-wave radio-frequency signal, for the  $d = 2$  and  $3$  cases, 11% of the power was transferred to each of the  $\pm 200 \text{ GHz}$  modes, while 8% of the power remained (unmodulated) in the fundamental frequency (see Figure 4.6). This resulted in a resonance mode to be mixed with its two first-neighbors. In case of  $d = 4$ , only 4% of the power was transferred to both  $\pm 100 \text{ GHz}$  and  $\pm 300 \text{ GHz}$  modulation sidebands, which led to a mixing of four resonances in a vacuum mode (see Figure 4.6). The rest of the power

was lost to other modulation sidebands, not required for the targeted mixing process. Due to the loss of power caused by the frequency modulation, we were limited to manipulate the quantum states up to  $d = 4$ . Since the modulator has a sideband spacing of 33.3 GHz while the mode spacing between  $|k\rangle$  and  $|k + 1\rangle$  is 200 GHz, most of the energy goes to frequency modes in between  $|k\rangle$  and  $|k + 1\rangle$ . However, by post-selection, the modes out of the selected  $|\bar{k}\rangle$  were considered losses, which are unavoidable in an experiment. In view of this, we could not consider the experimental operator  $A_{\text{Mod}}$  unitary. The losses and the slight imbalance in the power distribution can be compensated by making use of more complex modulation functions (e.g. the functions produced by arbitrary waveform generators). Furthermore, with a higher-bandwidth electro-optic modulation schemes [142] or/and by decreasing the FSR of the microring resonator [142, 143], it is potentially possible to mix a larger number of frequency modes. These can also enable the direct interference between signal and idler.

Finally, after the frequency mixing stage, a second programmable filter (PF2) was used to select different individual components of the manipulated state through a second amplitude mask. This action is represented as  $A_{\text{PF2}}A_{\text{Mod}}A_{\text{PF1}}|\Psi_{\text{two-ph}}\rangle$ ). PF2 was further used to route the signal and the idler to two separate single-photon detectors for coincidence measurements, which were necessary for retrieving quantum interference patterns. The coincidence counts are operationally represented as  $\langle\Psi_{\text{two-ph}}|A_{\text{PF2}}A_{\text{Mod}}A_{\text{PF1}}|\Psi_{\text{two-ph}}\rangle$  (see Figure 4.5-e), which indeed provided numbers (counts).

We have now the necessary instruments to understand why the quantum state fidelity decreases with an increasing number of levels. Such a behavior is due to the efficiency of the electro-optic phase modulator in the frequency conversion and mixing. From the projections listed in Eqs. (H.0.2) and (H.0.3) of Appendix H, it can be seen that, as  $d$  increases, a higher number of frequency components and phase terms are involved. This would require a more intricate control of phase shifts and frequency mixing from the electro-optic phase modulator, which results in a reduced efficiency. This in turn affects the quantum state fidelity, since its estimation relies on  $d$ -level projections.

The efficiency of the phase modulator affects also the coincidence to accidental ratio (CAR), which is defined as the ratio between correlated events and the system noise (i.e. accidental events). In a way, CAR is the quantum equivalent of the classical signal-to-noise ratio. CAR decreases as the conversion efficiency lowers down, which means that,

compared to noisy events, less coincident counts are detected.

# Chapter 5

## Universal multipartite $d$ -level entanglement witness

In subsection 3.3.1 we introduced the so-called optimal stabilizer witness that allows us to detect the presence of genuine multipartite entanglement of two-level cluster states [33]. The experimental feasibility with which this witness can be measured, as well as its high noise tolerance (see subsection 3.3.1 and Appendix F), have led to its exploitation in many quantum optical platforms in order to confirm the experimental realization of four- [29–31, 57, 111, 112], six- [144, 145], and eight- [146] qubit photon cluster states. Performing the two-level projections with respect to the basis of  $\sigma_z$  and  $\sigma_x$ , as required by the stabilizer witness, is quite straightforward from an experimental perspective for almost any two-level observable. For example, in the case of polarization,  $\sigma_z$  can be measured through polarizing beam splitters, while  $\sigma_x$  can be measured by combining wave plates with polarizers [30, 57]. In the case of time-bin,  $\sigma_z$ -projections can be performed simply via photo-detection, while  $\sigma_x$  can be measured by making use of unbalanced two-arm interferometers [18, 19] (see section 5.3).

While stabilizer witnesses are well established for two-level systems, an extension to either  $d$ -level cluster states or to other complex quantum systems have never been derived yet. This is mainly because implementing  $d$ -level projections to measure high dimensional stabilizers (subsection 3.4.1) is very challenging from an experimental point of view. The complexity of the projections can be further increased by the observable that is measured. For example,  $d$ -level projections in the time domain are much more difficult to perform compared to the two-level counterparts. Another example concerning the

issue of performing  $d$ -level projection was seen in subsection 4.2.4, where we showed that the efficiency of the electro-optic phase modulator for frequency mixing decreases as the number of required projections increases. A detailed discussion about the classification of measurements in ‘easy’ and ‘difficult’ to implement is reported in subsection 5.3.1. The challenging implementation of  $d$ -level projections, as well as the experimental losses they add, have significantly hampered the derivation of entanglement witnesses based on the high dimensional stabilizer formalism.

The latest advancement in the generation of complex entangled states, as well as the applications they may have for quantum information science, have increased the need to derive efficient and universal methods that are capable of the detection and characterization of these states, as well as of their entanglement. Ideally, these approaches should accomplish this task by requiring measurements that are experimentally feasible and have a robust noise tolerance, in complete analogy with the witness derived in [33]. It is thus clear that these techniques cannot rely, e.g. on quantum state tomography, which requires at least  $d^{2N}$  projection measurements (see section 2.6) that are often intricate to reproduce. For example, for the four-partite three-level cluster state that we demonstrated here [7], full quantum state tomography necessitates a minimum of  $3^{(2 \times 4)} = 6561$  projections both in time and in frequency, which would involve several mixing of time and frequency modes, thus further introducing several dB losses (see subsection 5.3.1).

A main goal of this research project was the realization of a four-partite three-level cluster state. This also required the detection and validation of the genuine multipartite entanglement of such a state. In this context, the specific task that has been accomplished in this work was to derive a method capable of detecting multipartite entanglement of high-dimensional cluster states in an experimentally feasible, yet noise resistant, manner. To this end, we considered a theoretical approach similar to that developed in [33] for qubit cluster states (subsection 3.3.1), and we extended it to higher dimensions. This led to the derivation of an entanglement witness in the high-dimensional stabilizer formalism specifically designed for detecting four-partite three-level cluster states, as well as any multipartite  $d$ -level cluster state, by means of just two measurement settings (i.e. those of the generalized Pauli matrices  $X$  and  $Z$ ) [5]. We exploited the derived witness to also investigate the robustness of  $d$ -level cluster states towards white noise (see

subsection 5.2.1) [5].

Furthermore, motivated by the importance as well as the applications of other complex entangled systems, we used our technique to derive experimentally optimal universal witnesses that are capable of detecting the presence of any pure complex quantum state, as well as of its entanglement, in an experimentally feasible manner. Our approach further allows us to customize these witnesses towards experimental restrictions and/or specific measurement settings that are available in an experiment (see section 5.3). This customization allowed us to address the challenge of implementing the  $d$ -level projections required to measure stabilizers.

## 5.1 Approach for the witness derivation

The starting point of our approach is a standard witness that is used to detect the presence of a generic pure multipartite quantum state  $|\psi\rangle$  and those states close to it [113]. This is labeled as ‘theoretical optimal’ (see below), and it is given by

$$\mathcal{W}_{\text{theor}}^{\text{opt}} = \frac{1}{1 - \alpha} (\alpha \cdot \mathbb{I} - \rho), \quad (5.1.1)$$

where  $\mathbb{I}$  is the identity operator,  $\rho = |\psi\rangle\langle\psi|$ , and  $\alpha$  is a coefficient that has to be chosen in such a way that all separable systems result in a non-negative expectation value of the witness (see section 3.3). The detailed method for determining  $\alpha$  is presented in [113] (see also section 5.2 of this thesis). The witness of Eq. (5.1.1) is normalized such that its expectation value for the ideal state  $|\psi\rangle$  is minus one.

The witness  $\mathcal{W}_{\text{theor}}^{\text{opt}}$  is optimal from a theoretical perspective; it exhibits mathematical compactness, it relies on tight bounds, as well as it provides the highest selectivity (that is, the highest noise tolerance). Furthermore,  $\mathcal{W}_{\text{theor}}^{\text{opt}}$  presents symmetry properties that are similar to those of the quantum state  $|\psi\rangle$  which the witness detects. However, determining the witness of Eq. (5.1.1) is almost impossible from an experimental perspective, since it requires measurements that, according to the previous observations, are highly intricate and difficult to implement, especially when the complexity of the quantum state (i.e. the number of parties and/or the dimensionality) increases. For example, it would necessitate quantum state tomography in order to determine  $\rho$  [8, 94, 109, 147].

The approach presented here is based on a judicious modification and simplification of the theoretical optimal witness  $\mathcal{W}_{\text{theor}}^{\text{opt}}$  which is finalized to make it straightforward to

measure. In particular, it should allow us to confirm the generation of a targeted quantum state by making use of projection measurements that are significantly lowered in number as well as in complexity, and that require the least possible experimental components. In light of this goal, we first introduce an operator  $\mathcal{W}_{\text{meas}}$  which contains those measurement settings that are easy to implement in the practice (i.e. these are reduced in number and complexity), as well as the operator  $\Theta = \mathcal{W}_{\text{meas}} - \rho$  which includes instead all the measurements that are challenging to implement (e.g., those necessary for full quantum state tomography). The only restriction for the operators  $\mathcal{W}_{\text{meas}}$  and  $\Theta$  is that they must be Hermitian, since only physical observables can be measured (see section 1.3). A part from this restriction, any arbitrary  $\mathcal{W}_{\text{meas}}$  can be chosen. The witness of Eq. (5.1.1) thus becomes:

$$\mathcal{W} = \frac{1}{1 - \alpha} (\alpha \cdot \mathbb{I} - \mathcal{W}_{\text{meas}} + \Theta). \quad (5.1.2)$$

The goal is now to replace the  $\Theta$  operator within Eq. (5.1.2) with a scalar number (i.e. its eigenvalue) that keeps the bounds of the witness unchanged, while avoiding the need for measuring  $\Theta$ . It is important to emphasize that we are allowed to introduce as well as to replace  $\Theta$  by the only fact that our approach relies on entanglement detection via operators rather than on entanglement quantification via monotones.

This scalar number is here determined by considering the worst possible measurement outcome, (i.e. the largest eigenvalue of  $\Theta$ , namely  $\lambda_{\text{max}}(\Theta)$ ), which results in the maximal expectation value of  $\Theta$  for any probed quantum state. This concept can be summarized in the inequality

$$\langle \Theta \rangle \leq \lambda_{\text{max}}(\Theta) = \langle \lambda_{\text{max}}(\Theta) \cdot \mathbb{I} \rangle, \quad (5.1.3)$$

Replacing  $\Theta$  in Eq. (5.1.2) with  $\lambda_{\text{max}}(\Theta) \cdot \mathbb{I}$  thus leads to the most generic expression of a witness that we label here as ‘experimentally optimized’ and that reads

$$\mathcal{W}_{\text{exp}}^{\text{opt}} = \frac{1}{1 - \alpha} [(\alpha + \lambda_{\text{max}}) \cdot \mathbb{I} - \mathcal{W}_{\text{meas}}]. \quad (5.1.4)$$

The witness  $\mathcal{W}_{\text{exp}}^{\text{opt}}$  allows us to detect the presence and, eventually, the entanglement of any pure quantum state for which Eq. (5.1.1) is a witness.

Referring to Figure 5.1, we now discuss the differences between the witnesses  $\mathcal{W}_{\text{theor}}^{\text{opt}}$  and  $\mathcal{W}_{\text{exp}}^{\text{opt}}$ . This will clarify why the witness of Eq. (5.1.4) can be defined as experimentally optimal, as well as what the final goal is in the derivation of this operator. Figure 5.1 depicts the experimental complexity of the measurement settings needed to detect a

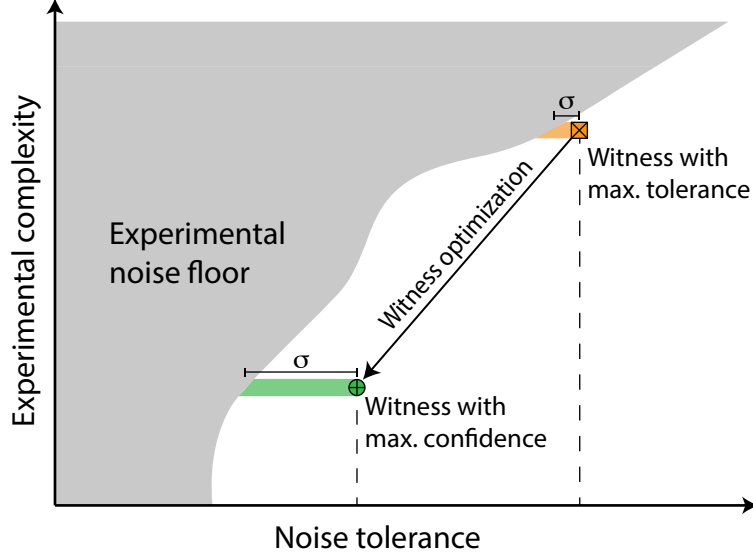


**Figure 5.1** – Complexity of the measurement settings vs noise tolerance of the witness. The experimental noise floor (gray area) introduced by the measurement settings increases with the measurement complexity. A theoretically optimal witness (orange square) has the highest noise tolerance, but it demands intricate and often unfeasible measurements. An experimentally optimal witness (green circle) requires reduced measurement complexity, but has a lower noise tolerance. The goal is to maximize  $\sigma$  (the shaded green or orange area) representing the measurement confidence (i.e. the distance between the noise floor and the witness noise tolerance). [5]

witness versus the noise tolerance of the witness. The theoretically optimal witness (orange square) can be clearly distinguished from the experimentally optimal witness (green circle). Any measurement setting that is used for witness detection introduces an experimental noise floor (the gray area) which typically grows as the complexity of the measurement setup increases. The dependency of the experimental noise on the measurement complexity is mainly due to the fact that a witness usually comprises many measurements. In this scenario, the theoretical optimal witness  $\mathcal{W}_{\text{theor}}^{\text{opt}}$ , due to its large mathematical bounds, provides the maximum tolerance towards the experimental noise floor. However, this comes at the price of very intricate and complex measurements that are required by  $\mathcal{W}_{\text{theor}}^{\text{opt}}$  for quantum state detection. As a consequence, the experimental noise floor rises and it is very likely that actually measuring such a witness is not possible in the practice. On the other hand, when the measurements (and in turn the related errors) are lowered in both number and complexity, the witness bound (which means, its noise tolerance) decreases, while the experimental noise floor reduces at the same time. An experimental optimal witness is typically characterized by these features.

As a generic consideration, measuring a negative expectation value of a witness with high statistical confidence already provides a necessary and sufficient condition to confirm the generation of a targeted quantum state. In the best-case scenario, an experimentally optimal witness should provide the maximal statistical confidence with which its expectation value is measured.

A goal of this approach is to determine a witness providing a compromise between the noise sensitivity and the experimental feasibility. In particular, the aim is maximizing the measurement confidence with which a negative expectation of the witness is measured. Referring to Figure 5.1, this quantity is represented by  $\sigma$ , which is the shaded green or orange area of the figure. Specifically, the measurement confidence is given by the distance between the experimental noise floor and the noise tolerance of the witness: an experimentally optimal witness, as well as a witness that is optimized according to the measurement settings (see section 5.3), provides the maximum separation between these experimental noise floor and noise robustness. This task can be accomplished by properly choosing the measurement setting required to determine the operator  $\mathcal{W}_{\text{meas}}$  in Eq. (5.1.4).

## 5.2 Entanglement witness for multipartite $d$ -level cluster states with two measurement settings

In order to derive a witness capable of detecting  $d$ -level multipartite cluster states as well as addressing the goal stated in the previous section, we explicitly constructed the operator  $\mathcal{W}_{\text{meas}}$  by making use of high dimensional stabilizers (see subsection 3.4.1).

The first step to derive this witness is determining the coefficient  $\alpha$  in Eq. (5.1.1). This is defined as the overlap between genuine multipartite entangled states  $|\psi\rangle$  and biseparable states  $|\phi\rangle$ , i.e.

$$\alpha = \max_{|\phi\rangle \in B} |\langle \phi | \psi \rangle|^2, \quad (5.2.1)$$

where  $B$  denotes the set of biparable states [113]. Determining  $\alpha$  is typically a difficult task, however a simple method based on the Schmidt decomposition can be found [113]. In this work, we estimate  $\alpha$  by also using the property of maximal connectedness of cluster states (see chapter 3): it is possible to project any subset of qudits of a cluster state into maximally entangled bipartite states by only performing local operations on the

remaining qudits [98]. In light of this property, the maximal Schmidt coefficient of any bipartite sub-system that is extracted by the initial cluster state is equal to  $1/\sqrt{d}$  [113]. In the case of multipartite cluster states, this implies that the overlapping coefficient results in  $\alpha = 1/d$ . In view of this, the witness operator of Eq. 5.1.1 becomes

$$\mathcal{W}_{\text{theor}}^{\text{opt}} = \frac{d}{d-1} \left( \frac{1}{d} \cdot \mathbb{I} - \rho_{N,d} \right), \quad (5.2.2)$$

where  $\rho_{N,d}$  denotes the density matrix of the cluster state, which is not convenient to measure, though. As reported in Eq. (3.4.5) of subsection 3.4.1,  $\rho_{N,d}$  can be expressed through the full set of its  $d^N$  stabilizers as

$$\rho_{N,d} = \frac{1}{d^N} \sum_{k=1}^{d^N} \mathcal{S}_k. \quad (5.2.3)$$

We demonstrate that the expression of Eq. (5.2.3) can be further simplified by just using the  $N$  main stabilizers (together with their transpose conjugate) of the cluster state (defined in subsection 3.4.1). We thus write  $\rho_{N,d}$  as

$$\rho_{N,d} = \prod_{k=1}^N \frac{1}{d} \sum_{l=1}^d \mathcal{S}_k^{(l)}, \quad (5.2.4)$$

where  $(l)$  denotes the power degree of the stabilizer. In Eq. (5.2.4) we also uphold the convention that, due to the properties of the generalized Pauli matrices,  $\mathcal{S}_k^{(d)} = \mathbb{I}$ , independently of the label  $k$ .

Among the stabilizers composing Eq. (5.2.4), we can conveniently choose a subset of those stabilizers consisting of only two independent measurement settings, which can be determined by considering only even and odd main stabilizers (that are defined in subsection 3.3.1 and in Appendix E for the two-level case, as well as later in this section for the  $d$ -level case). We thus include such operators in the expression of  $\mathcal{W}_{\text{meas}}$ , which results in

$$\mathcal{W}_{\text{meas}} = \prod_{\text{odd } k} \frac{1}{d} \sum_{l=1}^d \mathcal{S}_k^{(l)} + \prod_{\text{even } k} \frac{1}{d} \sum_{l=1}^d \mathcal{S}_k^{(l)}. \quad (5.2.5)$$

Bearing in mind that the operator  $\Theta$  to be replaced is given by  $\Theta = \mathcal{W}_{\text{meas}} - \rho_{N,d}$ , and combining Eqs. (5.2.4) and (5.2.5), we obtain:

$$\Theta = \prod_{\text{odd } k} \frac{1}{d} \sum_{l=1}^d \mathcal{S}_k^{(l)} + \prod_{\text{even } k} \frac{1}{d} \sum_{l=1}^d \mathcal{S}_k^{(l)} - \prod_{k=1}^N \frac{1}{d} \sum_{l=1}^d \mathcal{S}_k^{(l)}. \quad (5.2.6)$$

By exploiting the properties of the stabilizers, we analytically demonstrated that the maximum eigenvalue of  $\Theta$  is 1 for any  $N$  and  $d$ , i.e.  $\langle \Theta \rangle \leq \lambda_{\text{max}} = 1$  (see Appendix I).

We are thus allowed to replace  $\Theta$  (and thus  $\lambda_{\max}$ ) with 1 in Eq. (5.1.4). The analytic proof that we provide allowed us to estimate numerically the maximal eigenvalue of  $\Theta$  in the practical examples considered in section 5.3.

Finally, according to Eq. (5.2.5) and considering that  $\alpha = 1/d$ , we obtain the final expression

$$\mathcal{W}_{\text{exp}}^{\text{opt}} = \frac{d+1}{d-1}\mathbb{I} - \frac{d}{d-1} \left\{ \prod_{\text{odd } k} \frac{1}{d} \sum_{l=1}^d \mathcal{S}_k^{(l)} + \prod_{\text{even } k} \frac{1}{d} \sum_{l=1}^d \mathcal{S}_k^{(l)} \right\}. \quad (5.2.7)$$

The witness in Eq. (5.2.7) is the explicit form of the operator in Eq. (5.1.4) for multipartite  $d$ -level cluster states. In analogy with the two-level case, the witness consists of just two measurement settings, which are defined by the sets  $\{X^{(1)}, Z^{(2)}, X^{(3)}, Z^{(4)}, \dots\}$  and  $\{Z^{(1)}, X^{(2)}, Z^{(3)}, X^{(4)}, \dots\}$ . The former setting includes the generalized Pauli matrices needed to measure the odd stabilizers of Eq. (5.2.7), while the latter setting contains the matrices necessary to measure even stabilizers. Due to their non-Hermitian property, the two measurement settings can also include the transpose conjugate of the generalized Pauli matrices.

As an explicit example, let us consider the entanglement witness of the two-partite qutrit linear cluster state defined in Eq. (G.0.1) of Appendix G. From Eq. (5.2.7), this witness results in

$$\mathcal{W}_{\text{exp}}^{\text{opt}}(\phi_{2,3}) = \mathbb{I} - \frac{1}{2} \left( X_1 Z_2 + X_1^\dagger Z_2^\dagger + Z_1 X_2 + Z_1^\dagger X_2^\dagger \right). \quad (5.2.8)$$

As it can be seen, odd stabilizers (i.e.  $X_1 Z_2$  and  $X_1^\dagger Z_2^\dagger$ ) include the measurements where odd qudits are transformed only by  $X$  (or  $X^\dagger$ ) but not  $Z$  (or  $Z^\dagger$ ). Similarly, even stabilizers (i.e.  $Z_1 X_2$  and  $Z_1^\dagger X_2^\dagger$ ) include the measurements where even qudits are transformed only by  $X$  (or  $X^\dagger$ ) but not by  $Z$  (or  $Z^\dagger$ ).

The witness in Eq. (5.2.7) can be considered as containing just two measurement settings since its detection necessitates just two types of projections: those on the eigenbasis of  $X$  (or  $X^\dagger$ ) and those on the eigenbasis of  $Z$  (or  $Z^\dagger$ ), in analogy with the two-level case (see subsection 3.3.1), where the Pauli matrices are Hermitian and thus they coincide with the respective transpose conjugate. The reader is referred to subsection 6.3.1 for the details about the generalized Pauli matrices  $X$ ,  $Z$ ,  $X^\dagger$ , and  $Z^\dagger$  as well as their eigenvalues.

Finally, it can be seen that, in case of  $d = 2$ ,  $\mathcal{W}_{\text{exp}}^{\text{opt}}$  of Eq. (5.2.7) reduces to the optimal stabilizer witness for qubit cluster states of Eq. 3.3.5 [33].

### 5.2.1 Noise tolerance of multipartite d-level cluster states

We made use of the witness of Eq. (5.2.7) to investigate the tolerance of high-dimensional cluster states towards white noise [5]. While, in principle, our approach can be applied to any type of noise affecting experiments, we considered white noise for our analysis because it is the most relevant and exploited in many theoretical and experimental scenarios as reasonably modeling experimental noise contributions [33, 80, 113, 126, 128].

When white noise affects a pure entangled state, it adds some mixture to the density matrix, thus modifying the entanglement properties of it. Testing the robustness of pure entangled states to noise is thus crucial to determine the threshold at which the state becomes a non-entangled mixture. In the specific case of a  $d$ -level cluster state  $|C_{N,d}\rangle$ , white noise modifies the density matrix  $\rho_{N,d} = |C_{N,d}\rangle\langle C_{N,d}|$  as [5]

$$\rho_{\text{noise}} = \varepsilon_{\text{noise}} \frac{\mathbb{I}}{d^N} + (1 - \varepsilon_{\text{noise}}) |C_{N,d}\rangle\langle C_{N,d}|, \quad (5.2.9)$$

where  $0 \leq \varepsilon_{\text{noise}} \leq 1$  is the amount of noise added, that is, the percentage of introduced mixture. For simplicity, just the compact cluster is considered here, while the demonstration can be also extended to the linear form, as well as to any pure state. The necessary and sufficient for the witness  $\mathcal{W}_{\text{exp}}^{\text{opt}}$  to still detect entanglement and/or the presence of the probed quantum state is that  $\text{Tr}(\mathcal{W}_{\text{exp}}^{\text{opt}}\rho_{\text{noise}}) < 0$ . From Eq. (5.2.9), we obtain

$$\text{Tr} \left\{ \mathcal{W}_{\text{exp}}^{\text{opt}} \left[ \varepsilon_{\text{noise}} \frac{\mathbb{I}}{d^N} + |C_{N,d}\rangle\langle C_{N,d}| - \varepsilon_{\text{noise}} |C_{N,d}\rangle\langle C_{N,d}| \right] \right\} < 0. \quad (5.2.10)$$

Extracting all the terms within the inequality leads to the expression

$$\varepsilon \left( d^{-N} \text{Tr}(\mathcal{W}_{\text{exp}}^{\text{opt}}) - \langle C_{N,d} | \mathcal{W}_{\text{exp}}^{\text{opt}} | C_{N,d} \rangle \right) + \langle C_{N,d} | \mathcal{W}_{\text{exp}}^{\text{opt}} | C_{N,d} \rangle < 0. \quad (5.2.11)$$

This gives the condition

$$\varepsilon_{\text{noise}} < \varepsilon_{\text{th}} := \frac{-\langle C_{N,d} | \mathcal{W}_{\text{exp}}^{\text{opt}} | C_{N,d} \rangle}{d^{-N} \text{Tr}(\mathcal{W}_{\text{exp}}^{\text{opt}}) - \langle C_{N,d} | \mathcal{W}_{\text{exp}}^{\text{opt}} | C_{N,d} \rangle}. \quad (5.2.12)$$

The value  $\varepsilon_{\text{th}}$  is defined as the maximum noise up to which the witness can still detect entanglement and/or the target state. From Eq. (5.2.12), since the witness  $\mathcal{W}_{\text{exp}}^{\text{opt}}$  is normalized as  $\langle C_{N,d} | \mathcal{W}_{\text{exp}}^{\text{opt}} | C_{N,d} \rangle = -1$ , we can notice that the tolerated noise strictly depends on the term  $d^{-N} \text{Tr}(\mathcal{W}_{\text{exp}}^{\text{opt}})$ , and thus on the trace of the witness operator. Through an analytical, as well as a numerical analysis for different values of  $N$  and  $d$ ,

we investigated such a dependence and derived a generic expression for  $Tr(\mathcal{W}_{\text{exp}}^{\text{opt}})$ . As it was expected, this relies in turn on both the dimensionality  $d$  and on the number of parties  $N$  of the quantum state as:

$$Tr(\mathcal{W}_{\text{exp}}^{\text{opt}}) = \begin{cases} \left[ \frac{2d}{d-1} \left( \frac{d+1}{2d} - \frac{1}{d^{N/2}} \right) \right] \cdot d^N, & \text{even } N \\ \left[ \frac{d}{d-1} \left( \frac{d+1}{d} - \frac{1}{d^{(N+1)/2}} - \frac{1}{d^{(N-1)/2}} \right) \right] \cdot d^N, & \text{odd } N. \end{cases} \quad (5.2.13)$$

Combining Eqs. (5.2.12) and (5.2.13) leads to the generic expression of the noise threshold tolerated by qudit cluster states with respect to the witness of Eq. (5.2.7):

$$\varepsilon_{\text{th}} = \begin{cases} \left[ \frac{2d}{d-1} \left( 1 - \frac{1}{d^{N/2}} \right) \right]^{-1}, & \text{even } N \\ \left[ \frac{2d}{d-1} \left( 1 - \frac{1}{2d^{(N+1)/2}} - \frac{1}{2d^{(N-1)/2}} \right) \right]^{-1}, & \text{odd } N. \end{cases} \quad (5.2.14)$$

In the two-level case ( $d = 2$ ), the expression of Eq. (5.2.14) reduces to the known noise threshold derived for qubit cluster states in [33] (see subsection 3.3.2 of this thesis).

We can make some important observations by looking into Eq. (5.2.14). First, we demonstrate that, the higher the dimensionality of a quantum state, the stronger the noise tolerance. This, in complete analogy with bipartite systems [6, 13] (see subsection 2.3.1), while the extension to multipartite quantum systems has never been considered prior to this work. Second, given a number of parties  $N$ , the noise tolerance of high-dimensional cluster states increases indeed with  $d$ , reaching a maximum of  $\varepsilon_{\text{th}} \rightarrow 0.5$  for  $d \rightarrow \infty$ . The same threshold is also reached by two-partite cluster states, independently of their dimensionality  $d$ . This shows that bipartite systems (i.e. Bell-type states) are more robust to noise with respect to any complex entangled system. Such a robustness has led to widely exploit Bell states for several applications in quantum communications. Relying on the transmission of a quantum state over long distances [21, 23, 24], it is clear that quantum communications necessitate quantum states that are highly resistant to noise as well as environmental perturbations. The expression of Eq. (5.2.14) further shows that, given the single-state dimensionality  $d$ , the noise tolerance is lowered by a growing number of parties  $N$ . Finally, we demonstrate for the first time that different cluster states with the same Hilbert-space sizes have different noise tolerances: the higher the dimension, the higher the resistance. For example, cluster states with  $N = 8$ ,  $d = 2$

and  $N = 4$ ,  $d = 4$  have equal Hilbert-space sizes (i.e.  $2^8 = 4^4 = 256$ , respectively), but distinct noise tolerances, i.e.  $\varepsilon_{\text{th}} = 0.2667$  and  $\varepsilon_{\text{th}} = 0.4$  (which is 1.5 times higher), respectively. This is a direct consequence of the fact that qudits become more robust to noise as their dimensionality increases.

In analogy with the geometric description of the witness provided in section 3.3, let us now explain through geometrical considerations why higher dimensional entanglement is more robust than lower dimensional entanglement. For that purpose, we now consider Figure 5.2, which shows the convex set  $\mathcal{S}$  of multipartite states, formed by the subsets of separable ( $\mathcal{S}_{\text{sep}}$ ) and inseparable (i.e., entangled,  $\mathcal{S}_{\text{ent}}$ ) states [148]. The volume of the whole set  $\mathcal{S}$  is given by the volume of the two subsets as  $\mathcal{S} = \mathcal{S}_{\text{sep}} \cdot \mathcal{S}_{\text{ent}}$ . Since  $\mathcal{S}$  must keep the same volume, if  $\mathcal{S}_{\text{sep}}$  decreases, the volume of the subset  $\mathcal{S}_{\text{ent}}$  occupied by the entangled states then increases (and vice versa). It can be demonstrated that the volume of separable states  $\mathcal{S}_{\text{sep}}$  decreases as the single-state dimensionality  $d$  increases [148]. The immediate consequence is that  $\mathcal{S}_{\text{ent}}$  grows in volume. Figure 5.2 also relates the convex set of separable and entangled states with the witness (see also section 3.3). It is clear that, if  $\mathcal{S}_{\text{ent}}$  becomes larger, it is more likely that the witness (i.e. the hyperplane separating  $\mathcal{S}_{\text{sep}}$  and  $\mathcal{S}_{\text{ent}}$ ) covers such a subset. This means that the witness can detect the presence of entanglement with higher probability (which means, with higher statistical confidence). In this sense, an increasing single-state dimensionality results in a higher noise tolerance of entangled states with respect to the witness.

In the work described here, the type of noise that has been considered to test the robustness of both the witness and cluster states demonstrated here is white noise. As mentioned throughout this thesis, the main reason of such a choice is that white noise is the most common in experimental scenarios and is mainly due to the measurement settings used for quantum state manipulation (e.g., filtering) and/or detection. However, other noise contributions rising from different setup components can also be interesting as well as useful to consider. For instance, an interesting scenario to investigate is the effects of Raman scattering in the sample on the entanglement witness as well as on  $d$ -level cluster states. In contrast with white noise, Raman scattering stems from the quantum state source, which is, in the specific case of the work presented in this thesis, the microring resonator. As it can be seen from Figure 4.3, Raman noise mainly affects the symmetry of the generated frequency modes; the farther they are from the central pump frequency,

the more asymmetric they become. From a theoretical point of view, this means that the Raman noise contribution increases as the quantum state dimensionality grows. For this reason, while Raman scattering may result negligible for two-level quantum states, it can have significant impact on  $d$ -level quantum systems and thus on their density matrix. As a direct consequence, the robustness of the high-dimensional entanglement witness demonstrated in this thesis would be affected by Raman scattering; specifically, the noise tolerance would decrease as the number of levels increases. This is completely in contrast with the scenario occurring in the case of white noise. It can be interesting thus to investigate how the noise threshold that can be tolerated by high-dimensional quantum states and witness depends on the number of levels, as well as to investigate how such a threshold may differ from that reported in Eq. (5.2.1). It can also be interesting to consider a scenario including both noise contributions, i.e. those due to the quantum state source (e.g. Raman scattering caused by the microring resonator) and to the manipulation scheme (the white noise caused by, e.g., filters and detectors), as well as to investigate whether the two noises can be somehow compensated. In practice, the noise contribution that is worth to investigate and analyze mainly and strongly depends on the type of experimental setup, quantum state, and degrees of freedom considered. Finally, by exploiting the approach demonstrated here to customize a witness according to the measurement setting (see section 5.3), we can extend and improve it in such a way that can enable witness customization towards the experimentally available quantum state source.

In the case of the three-level cluster state demonstrated in this thesis, analyzing the effects of Raman scattering on the quantum state or on the measured witness was not necessary. This is because, as can be seen in detail in chapter 6, we considered only three frequency modes per photon, where the Raman effects can still be considered negligible (see Figure 4.3). On the other hand, in the hypothetical experimental scenario in which higher dimensional cluster states are generated, it may become necessary and crucial to investigate Raman scattering noise and derive a properly customized witness.

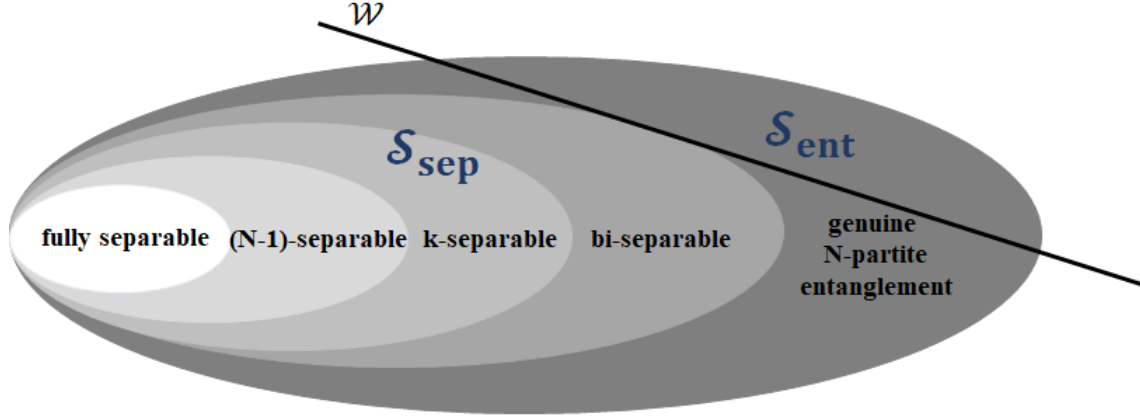


**Figure 5.2** – The volume  $\mathcal{S}$  of the convex set of separable ( $\mathcal{S}_{\text{sep}}$ ) and inseparable (i.e., entangled,  $\mathcal{S}_{\text{ent}}$ ) states is given by  $\mathcal{S} = \mathcal{S}_{\text{sep}} \cdot \mathcal{S}_{\text{ent}}$ . The volume of  $\mathcal{S}_{\text{ent}}$  increases as the single-state dimensionality  $d$  grows. As a consequence, the volume of  $\mathcal{S}_{\text{sep}}$  decreases. If  $\mathcal{S}_{\text{ent}}$  becomes larger, it is more likely that the witness (i.e. the hyperplane separating  $\mathcal{S}_{\text{ent}}$  and  $\mathcal{S}_{\text{sep}}$ ) covers such a subset, thus detecting entanglement with a much higher probability.

## 5.3 Tailoring the witness to realistic measurement settings

### 5.3.1 Application to optical cluster states given some measurement restrictions

Many realistic scenarios occur that can hamper significantly the capability of measuring a witness of the form of Eq. (5.1.4). The approach described in section 5.1 allows us to customize the witness  $\mathcal{W}_{\text{exp}}^{\text{opt}}$  of Eq. (5.1.4) according to the specific restrictions that can affect the experiment. In principle, any experimental scenario as well as quantum system can be considered for this customization, for example, photonic or solid-state (e.g. trapped ions, cold atoms) platforms. Without loss of generality, we consider here the specific case of a four-partite three-level optical cluster state  $|C_{4,3}\rangle$  in the time and frequency frameworks. We report this particular example as we are motivated by the experimental realization of such a state in [7] (see chapter 6 of this thesis).

While the detailed description of this cluster state, as well as of its stabilizers, is provided in section 6.1 and subsection 6.3.1, respectively, we consider here only those aspects that are relevant to understand how the witness measurement can be conditioned by experimental restrictions. The wave function of such a mentioned cluster state is given

by

$$\begin{aligned}
|C_{4,3}\rangle = & \frac{1}{3} \left[ |0_{t1}, 0_{t2}\rangle (|0_{f1}, 0_{f2}\rangle + |1_{f1}, 1_{f2}\rangle + |2_{f1}, 2_{f2}\rangle) \right. \\
& + |1_{t1}, 1_{t2}\rangle \left( |0_{f1}, 0_{f2}\rangle + e^{i2\pi/3} |1_{f1}, 1_{f2}\rangle + e^{-i2\pi/3} |2_{f1}, 2_{f2}\rangle \right) \\
& \left. + |2_{t1}, 2_{t2}\rangle \left( |0_{f1}, 0_{f2}\rangle + e^{-i2\pi/3} |1_{f1}, 1_{f2}\rangle + e^{i2\pi/3} |2_{f1}, 2_{f2}\rangle \right) \right],
\end{aligned} \tag{5.3.1}$$

where  $t1$  and  $t2$  denote the time-entangled qutrits 1 and 2, while  $f1$  and  $f2$  denote the frequency-entangled qutrits 3 and 4 (see section 6.1).

Let us assume that we want to validate the genuine four-partite entanglement of  $|C_{4,3}\rangle$ , which is a task that can be accomplished through a witness operator of the form of Eq. (5.2.7). From that expression, it can be seen that measuring  $\mathcal{W}_{\text{exp}}^{\text{opt}}$  requires the use of the four main stabilizers of the four-partite cluster state. These are (the order of matrices correspond to the qutrits they act on, subsection 6.3.1):

$$\begin{aligned}
\mathcal{S}_1 &= Z^\dagger Z \text{III}, & \mathcal{S}_2 &= X X Z \text{II}, \\
\mathcal{S}_3 &= \text{II} Z X X, & \mathcal{S}_4 &= \text{III} Z Z^\dagger,
\end{aligned} \tag{5.3.2}$$

where  $Z = |0\rangle\langle 0| + e^{i2\pi/3}|1\rangle\langle 1| + e^{-i2\pi/3}|2\rangle\langle 2|$  and  $X = |x_0\rangle\langle x_0| + e^{-i2\pi/3}|x_1\rangle\langle x_1| + e^{i2\pi/3}|x_2\rangle\langle x_2|$  are the generalized Pauli matrices as expressed in their respective eigenbasis, which are  $\{|0\rangle, |1\rangle, |2\rangle\}$  and  $\{|x_n\rangle = \frac{1}{\sqrt{3}} \sum_{j=0}^2 e^{i2n\pi/3} |j\rangle\}$ , with  $n = 0, 1, 2$ , respectively (see Eq. (G.0.4) of Appendix G). The complete set of  $3^4 = 81$  stabilizers that uniquely define the cluster state  $|C_{4,3}\rangle$  can be extracted from the main stabilizers of Eq. (5.3.2) as well as their transpose conjugates  $\mathcal{S}_1^\dagger, \mathcal{S}_2^\dagger, \mathcal{S}_3^\dagger$ , and  $\mathcal{S}_4^\dagger$ . We here derived analytically all the 81 distinct stabilizers, which are listed in Appendix J.

In order to construct the witness of Eq. (5.2.7), we could use in principle any of the 81 stabilizers. However, suppose that some experimental restrictions exist which avoid to arbitrarily choose any of these stabilizers. This in turn impose restriction in the witness measurement. In particular, let us assume that that projecting all four qutrits at the same time is not experimentally feasible, and that it is only possible to project either qutrits 1 and 2 (or 3 and 4) into superposition states. Considering the 81 operators in Appendix J, this means that it is not possible to simultaneously project all the qutrits in the eigenbasis of  $X$ ,  $Z$ ,  $Y = XZ$ , and  $V = XZ^\dagger$ . Rather, if qutrits 1 and 2 (or 3 and 4) were projected on the eigenbasis of  $X$ ,  $Y$ , or  $V$ , the other qutrits had to be projected on the eigenbasis of  $Z$ . Furthermore, since a measurement in the  $X$ -,  $Y$ -, or  $V$ -basis typically coincides with a significant experimental complexity and losses, it is

highly desirable to perform such measurements on just a few qudits at a time. In the specific case of a three-dimensional Hilbert space, the matrices  $X$  and  $Z$  are reported in subsection 6.3.1, while  $Y$  and  $V$  are given by

$$Y = \begin{pmatrix} 0 & 0 & e^{-i2\pi/3} \\ 1 & 0 & 0 \\ 0 & e^{i2\pi/3} & 0 \end{pmatrix}, \quad V = \begin{pmatrix} 0 & 0 & e^{i2\pi/3} \\ 1 & 0 & 0 \\ 0 & e^{-i2\pi/3} & 0 \end{pmatrix}. \quad (5.3.3)$$

The eigenvectors of  $X$  and  $Z$  can be found in Appendix G, while the eigenvectors of  $Y$  and  $V$  are

$$\begin{aligned} |y_0\rangle &= \frac{1}{\sqrt{3}} \left( e^{i2\pi/3} |0\rangle + |1\rangle + |2\rangle \right) \\ |y_1\rangle &= \frac{1}{\sqrt{3}} \left( |0\rangle + e^{i2\pi/3} |1\rangle + |2\rangle \right) \\ |y_2\rangle &= \frac{1}{\sqrt{3}} \left( |0\rangle + |1\rangle + e^{i2\pi/3} |2\rangle \right) \end{aligned} \quad (5.3.4)$$

and

$$\begin{aligned} |v_0\rangle &= \frac{1}{\sqrt{3}} \left( e^{-i2\pi/3} |0\rangle + |1\rangle + |2\rangle \right) \\ |v_1\rangle &= \frac{1}{\sqrt{3}} \left( |0\rangle + e^{-i2\pi/3} |1\rangle + |2\rangle \right) \\ |v_2\rangle &= \frac{1}{\sqrt{3}} \left( |0\rangle + |1\rangle + e^{-i2\pi/3} |2\rangle \right) \end{aligned} \quad (5.3.5)$$

respectively.

Assuming that the measurements are performed in the time and frequency domains leads the following observations.  $\mathcal{S}_1$  and  $\mathcal{S}_4$  only contain the identity  $\mathbb{I}$  and  $Z$ , which result experimentally easy to measure both in time and in frequency. This is because  $\mathbb{I}$  and  $Z$  necessitate only projections in the computational basis. In the time-domain, these measurements consist in determining the arrival time of the photon, which is feasible as long as the detector has sufficient temporal resolution. In the frequency-domain,  $\mathbb{I}$  and  $Z$  measurements only necessitate optical filtering/diffraction, which results a feasible task as long as the frequency separation is accessible. Furthermore,  $\mathbb{I}$ - and  $Z$ -measurements have a very low noise floor. For example, filtering components typically add an error of around 1 to 2 dB, depending on the filter type [7]. In order to measure the stabilizer  $\mathcal{S}_2$ , time bins have to be projected into the  $X$ - basis (i.e. in the  $|x_j\rangle$  states), while the frequency bins are measured in the  $Z$ - and  $\mathbb{I}$ -basis. Measuring  $X$  necessitates a stable optical interferometer, which already adds a significant experimental complexity, as well as a medium amount of optical loss (typically, around 5 dB). Vice versa, the stabilizer

$\mathcal{S}_3$  demands time and frequency measurements in the computational basis and in the  $X$ -basis, respectively. Projecting frequencies in the  $X$ -basis requires the shifting of the photon frequencies, which can be implemented, for example, by imprinting a spectral phase shift followed by electro-optic modulation [6, 7] (see subsection 4.2.4). This however is highly complex to carry out and also adds significant losses (around 20 dB). Finally, measuring stabilizers like  $\mathcal{S}_2 \cdot \mathcal{S}_3 = e^{-i2\pi/3}XY YX$  requires even to perform projections with an interferometer and frequency shifter at the same time, i.e. an unfeasible with current available technology.

Since each stabilizer contributes equally to the entanglement witness (see Eq. (5.2.7)), it is thus convenient to consider only those operators that can be measured with a reduced experimental complexity and that add low losses. In the specific example considered here, the restriction for the measurement would be to use either the interferometer or the frequency shifter, but not both at the same time.

With this in mind, among the 81 stabilizers listed in Appendix J, only  $M = 20$  of them, together with their transposed conjugates, can be considered for a feasible measurement. These are:

$\mathcal{S}_1 = Z^\dagger Z \text{III}$	$\mathcal{S}_{11} = \text{I}ZYV$
$\mathcal{S}_2 = XXZ\text{II}$	$\mathcal{S}_{12} = VYZ^\dagger Z^\dagger$
$\mathcal{S}_3 = \text{I}ZXX$	$\mathcal{S}_{13} = VY\text{I}Z$
$\mathcal{S}_4 = \text{III}ZZ^\dagger$	$\mathcal{S}_{14} = VYZ\text{II}$
$\mathcal{S}_5 = Z^\dagger Z^\dagger XX$	$\mathcal{S}_{15} = Z^\dagger Z^\dagger VY$
$\mathcal{S}_6 = Z\text{I}XX$	$\mathcal{S}_{16} = Z\text{I}VY$
$\mathcal{S}_7 = XXZ^\dagger Z^\dagger$	$\mathcal{S}_{17} = \text{I}ZVY$
$\mathcal{S}_8 = XX\text{I}Z$	$\mathcal{S}_{18} = YVZ^\dagger Z^\dagger$
$\mathcal{S}_9 = Z^\dagger Z^\dagger YV$	$\mathcal{S}_{19} = YV\text{I}Z$
$\mathcal{S}_{10} = Z\text{I}YV$	$\mathcal{S}_{20} = YVZ\text{II}$

By making use of the technique described in section 5.1, these 20 stabilizers can be exploited to derive an experimentally-optimized witness which is customized to the discussed experimental restrictions.

The first step is constructing the operator  $\mathcal{W}_{\text{meas}}$ , which contains all the feasible

measurement settings that are provided by the 20 stabilizers:

$$\mathcal{W}_{\text{meas}} = \frac{1}{27} \sum_{k=1}^{20} (\mathcal{S}_k + \mathcal{S}_k^\dagger). \quad (5.3.6)$$

Then, we define the operator  $\Theta$  to be replaced with its largest eigenvalue:

$$\Theta = \frac{1}{27} \sum_{k=1}^{20} (\mathcal{S}_k + \mathcal{S}_k^\dagger) - \frac{1}{81} \sum_{k=1}^{81} \mathcal{S}_k. \quad (5.3.7)$$

We numerically estimated the largest eigenvalue of  $\Theta$ , which resulted in  $\lambda_{\text{max}}(\Theta) = 13/27$ . Replacing  $\lambda_{\text{max}}(\Theta)$  in Eq. (5.1.4) and bearing in mind that  $\alpha = 1/3$ , the final expression of the customized witness can finally be obtained [5]:

$$\mathcal{W}_{\text{exp}}^{\text{cust}} = \frac{11}{9} - \frac{1}{18} \sum_{k=1}^{20} (\mathcal{S}_k + \mathcal{S}_k^\dagger). \quad (5.3.8)$$

We further estimated the tolerance of  $\mathcal{W}_{\text{exp}}^{\text{cust}}$  towards white noise, which resulted in  $\varepsilon_{\text{th}} = 0.45$ . This value is 20% higher than the threshold of the witness  $\mathcal{W}_{\text{exp}}^{\text{opt}}$  of Eq. (5.2.7) (i.e.,  $\varepsilon_{\text{th}} = 0.375$ ). The stronger tolerance is justified by the fact that the witness has been customized with respect to very specific experimental conditions. This brings us to conclude that different experimental restrictions lead to different optimal witnesses (and noise sensitivities) for the same given quantum state.

### 5.3.2 Detecting multi-level entanglement via two-level projections

We have shown that this novel method allows us to select any subset of stabilizers that is feasible to measure. However, different scenarios occur where stabilizers cannot be measured in any case. Since a stabilizer operator is described by a  $d \times d$  matrix, its measurement necessitates  $d$ -level projections. If the available measurement setting does not enable us to perform such projections, but only projections on a lower number of levels, then it is not possible to measure the stabilizer. In that case, the stabilizer must be replaced with another operator, which has to be still easy to measure and that permits the construction of an entanglement witness. Our approach allows us to accomplish this task, since enabling us to construct almost any arbitrary and practically feasible operator that can be used in lieu of stabilizers.

Without loss of generality, let us consider a two-photon three-level quantum state, which is entangled in time [18, 19, 28]. In the computational basis  $\{|0\rangle, |1\rangle, |2\rangle\}$ , this state

reads  $|\psi\rangle = 1/\sqrt{3}(|0,0\rangle + |1,1\rangle + |2,2\rangle)$ . Let us suppose that the available measurement setting allows us to perform only two-level projections. In this case, the presence of  $|\psi\rangle$  cannot be detected through stabilizers, since the measurement of them would require three-level projections to be implemented through a three-arm interferometer [149], which is extremely challenging to stabilize, though. The only available measurement setting is instead a stable two-arm interferometer [7, 19] that enables us to perform measurements only on a two-level basis. In this context, it means that projections into a superposition of just two time bins at a time are allowed [7, 150]. This restriction signifies that it is possible to measure the diagonal elements of the quantum state, but not its off-diagonal elements. In other words, only measurements in the basis of  $Z$  and  $\mathbb{I}$ , but not of  $X$ ,  $V$ , and  $Y$ , can be implemented. The goal is thus constructing a witness that can be measured exclusively through two-level projections.

Towards this end, we make use of the developed approach (section 5.1). Let us first start from the witness of Eq. (5.1.1). Since, in that case  $\alpha = 1/3$ , such a witness results in:

$$\mathcal{W}_{\text{theor}}^{\text{opt}} = \frac{\mathbb{I}}{2} - \frac{3}{2}|\psi\rangle\langle\psi|. \quad (5.3.9)$$

The two main stabilizers of the state  $|\psi\rangle$  are  $\mathcal{S}_1 = XX$  and  $\mathcal{S}_2 = ZZ^\dagger$ . We use the two operators, as well as their transpose conjugate, to derive the set of  $3^2 = 9$  stabilizers uniquely defining the density matrix  $\rho = |\psi\rangle\langle\psi|$ . According to Eq. (5.2.4), such a matrix reads

$$\rho = \frac{1}{9} \left( \mathbb{III} + ZZ^\dagger + Z^\dagger Z + XX + X^\dagger X^\dagger + VY + V^\dagger Y^\dagger + YV + Y^\dagger V^\dagger \right). \quad (5.3.10)$$

Replacing  $\rho$  in  $\mathcal{W}_{\text{theor}}^{\text{opt}}$  leads to the expression

$$\mathcal{W}_{\text{theor}}^{\text{opt}} = \frac{\mathbb{I}}{2} - \frac{1}{6} \left( \mathbb{III} + ZZ^\dagger + Z^\dagger Z + XX + X^\dagger X^\dagger + VY + V^\dagger Y^\dagger + YV + Y^\dagger V^\dagger \right). \quad (5.3.11)$$

We now introduce the operator  $\Phi = \frac{1}{6} (XX + X^\dagger X^\dagger + VY + V^\dagger Y^\dagger + YV + Y^\dagger V^\dagger)$  in which we enclose the part of the witness that cannot be directly measured due to the experimental restrictions. The witness of Eq. (5.3.11) thus becomes

$$\mathcal{W}_{\text{theor}}^{\text{opt}} = \frac{\mathbb{I}}{3} - \frac{1}{6} (ZZ^\dagger + Z^\dagger Z) - \Phi. \quad (5.3.12)$$

In order to construct a different witness that does not include the measurement of  $\Phi$ , we introduce the two-dimensional projection operators  $X_{0,1}$ ,  $X_{0,2}$ , and  $X_{1,2}$ . These are

comparable to the partial trace operators (see section 2.4) [85], where the subscripts label the subparts of the system with respect to which the projection is performed. The action of these operators is to project on two-level superpositions of only two modes at a time, while removing the third mode. This corresponds to the action of a two-arm interferometer on a three-level time-bin state. In the computational basis  $\{|0\rangle, |1\rangle, |2\rangle\}$ , the two-dimensional projectors result in

$$X_{0,1} = \begin{pmatrix} 0 & 1 & 0 \\ 1 & 0 & 0 \\ 0 & 0 & 0 \end{pmatrix}, \quad X_{0,2} = \begin{pmatrix} 0 & 0 & 1 \\ 0 & 0 & 0 \\ 1 & 0 & 0 \end{pmatrix}, \quad X_{1,2} = \begin{pmatrix} 0 & 0 & 0 \\ 0 & 0 & 1 \\ 0 & 1 & 0 \end{pmatrix}, \quad (5.3.13)$$

and are identical to three out of the eight Gell-Mann matrices (i.e. a generalization of the Pauli matrices for the groups SU(2) and SU(3)) [151]. Any matrix belonging to the SU(3) group can be expressed as a linear combination of the Gell-Mann matrices. In light of the properties of the Gell-Mann matrices, as well as of their analogy with the two-dimensional projectors defined in Eq. (5.3.13), we are allowed to make use of these operators to replace stabilizers. We can proceed then with the derivation of the witness by following the procedure of section 5.1.

We first construct an operator that has significant overlap with the non-zero elements of  $\Phi$ . Such an operator is formed by  $\mathcal{W}_{\text{meas}}$  and  $\Theta$ , which read

$$\mathcal{W}_{\text{meas}} = \frac{1}{6} (Z^\dagger Z + Z Z^\dagger) + \frac{1}{2} (X_{0,1} X_{0,1} + X_{0,2} X_{0,2} + X_{1,2} X_{1,2}) \quad (5.3.14)$$

and

$$\Theta = \frac{1}{2} (X_{0,1} X_{0,1} + X_{0,2} X_{0,2} + X_{1,2} X_{1,2}) - \frac{1}{6} (X X + V Y + Y V + X^\dagger X^\dagger + V^\dagger Y^\dagger + Y^\dagger V^\dagger), \quad (5.3.15)$$

respectively. The largest eigenvalue of  $\Theta$  was evaluated numerically to be equal to 1. Therefore, by replacing  $\lambda_{\text{max}}(\Theta) = 1$  into Eq. (5.1.4) and by inserting Eq. (5.3.14), we obtain the (normalized) experimentally-customized witness

$$\mathcal{W}_{\text{exp}}^{\text{cust}} = \frac{5}{3} \mathbb{I} - (Z^\dagger Z + Z Z^\dagger) - (X_{0,1} X_{0,1} + X_{0,2} X_{0,2} + X_{1,2} X_{1,2}). \quad (5.3.16)$$

We finally analyzed the noise sensitivity of the witness in Eq. (5.3.16). Specifically, the noise tolerance results in  $\varepsilon_{\text{th}} = 0.375$ , which is around 33% lower than that of the witness in Eq. (5.2.7) (which is  $\varepsilon_{\text{th}} = 0.5$ ). The higher noise sensitivity of the customized witness of Eq. (5.3.16) with respect to the experimentally optimal one is compensated by the fact

that  $\mathcal{W}_{\text{exp}}^{\text{cust}}$ , in contrast with  $\mathcal{W}_{\text{exp}}^{\text{opt}}$  allows us to detect and to perform projections on a  $d$ -level quantum state through measurement settings which can only access a lower number of levels. Furthermore, the measurement settings needed for such a witness detection are significantly simplified (i.e. a two-arm vs. a three-arm interferometer is needed) and reduced in number. Specifically, each term composing the witness requires 39 projections instead of the 81 projections required for detecting the witness of Eq. (5.2.7).

# Chapter 6

## Demonstration of a four-partite three-level photon cluster state

The experimental realization of a four-partite three-level (qutrit) cluster state in an optical platform, the entanglement detection of this state through a witness operator, as well as the proof-of-concept high-dimensional one-way quantum processing, will all be presented in this chapter [7]. These achievements could be obtained in light of the theoretical investigation of the entanglement properties of high-dimensional cluster states that have been pursued in this research work. The results presented in this chapter are a specific application of the theory shown in chapter 5 [5] to a photonic platform in the time and frequency domains [7].

### 6.1 Wave function of a four-partite three-level cluster state

In order to realize experimentally a high-dimensional cluster state, it was necessary to investigate from a theoretical perspective its wave function. To that purpose, we exploited the formalism for qudit cluster states presented in section 3.4.

The first step was to analyze a four-partite three-level linear cluster state  $|\phi_{4,3}\rangle$  and developing its wave function in the most generic form, which means without taking into account either the physical particles of the system or the degrees of freedom. As derived from Eq. (3.4.1) and by expressing it in the computational basis  $\{|0\rangle, |1\rangle, |2\rangle\}$ , the wave

function of the linear cluster state results in

$$\begin{aligned}
|\phi_{4,3}\rangle = \frac{1}{3} & \left( |x_0\rangle_1 |0\rangle_2 |0\rangle_3 |x_0\rangle_4 + |x_0\rangle_1 |0\rangle_2 |1\rangle_3 |x_1\rangle_4 + |x_0\rangle_1 |0\rangle_2 |2\rangle_3 |x_2\rangle_4 \right. \\
& + |x_1\rangle_1 |1\rangle_2 |0\rangle_3 |x_0\rangle_4 + \omega |x_1\rangle_1 |1\rangle_2 |1\rangle_3 |x_1\rangle_4 + \omega^2 |x_1\rangle_1 |1\rangle_2 |2\rangle_3 |x_2\rangle_4 \\
& \left. + |x_2\rangle_1 |2\rangle_2 |0\rangle_3 |x_0\rangle_4 + \omega^2 |x_2\rangle_1 |2\rangle_2 |1\rangle_3 |x_1\rangle_4 + \omega |x_2\rangle_1 |2\rangle_2 |2\rangle_3 |x_2\rangle_4 \right). \tag{6.1.1}
\end{aligned}$$

As also defined in Appendix G,  $\omega = e^{i2\pi/3}$ ,  $\omega^2 = e^{i4\pi/3} = e^{-i2\pi/3}$ , while

$$\begin{aligned}
|x_0\rangle &= \frac{1}{\sqrt{3}} (|0\rangle + |1\rangle + |2\rangle) \\
|x_1\rangle &= \frac{1}{\sqrt{3}} (|0\rangle + \omega |1\rangle + \omega^2 |2\rangle) \\
|x_2\rangle &= \frac{1}{\sqrt{3}} (|0\rangle + \omega^2 |1\rangle + \omega |2\rangle). \tag{6.1.2}
\end{aligned}$$

The state  $|\phi_{4,3}\rangle$  consists of  $3^4 = 81$  components, while it can be transformed by means of single-qudit unitary operations, into a compact cluster state  $|C_{4,3}\rangle$  which has  $3^{4/2} = 9$  terms and still maintains the same entanglement as its linear counterpart (see the introduction of chapter 3). Here, the task was to derive the compact cluster state in such a way that it could be then realized in the available quantum optical platform.

A specific goal towards this end was obtaining a wave function which exhibits some symmetries that are similar (yet extended to  $d = 3$  levels) to those of the two-level cluster state  $|C_{4,2}\rangle$  of Eq. (E.0.10). We found that this goal could be achieved by applying to  $|\phi_{4,3}\rangle$  the same type of unitary operations that are used to convert  $|\phi_{4,2}\rangle$  into  $|C_{4,2}\rangle$ . In particular, we transformed the linear cluster state  $|\phi_{4,3}\rangle$  into the compact form  $|C_{4,3}\rangle$  by applying the  $3 \times 3$  Walsh-Hadamard matrix  $W$  to qutrits 1 and 4, and the  $3 \times 3$  identity operator to qutrits 2 and 3. These two matrices are defined in Eqs. (G.0.5) of Appendix G.

From these considerations, the compact cluster state obtained as  $W_1 \otimes \mathbb{I}_2 \otimes \mathbb{I}_3 \otimes W_4 |\phi_{4,3}\rangle = |C_{4,3}\rangle$  results in [5, 7]

$$\begin{aligned}
|C_{4,3}\rangle = \frac{1}{3} & \left( |0_1, 0_2, 0_3, 0_4\rangle + |0_1, 0_2, 1_3, 1_4\rangle + |0_1, 0_2, 2_3, 2_4\rangle \right. \\
& + |1_1, 1_2, 0_3, 0_4\rangle + e^{i2\pi/3} |1_1, 1_2, 1_3, 1_4\rangle + e^{-i2\pi/3} |1_1, 1_2, 2_3, 2_4\rangle \\
& \left. + |2_1, 2_2, 0_3, 0_4\rangle + e^{-i2\pi/3} |2_1, 2_2, 1_3, 1_4\rangle + e^{i2\pi/3} |2_1, 2_2, 2_3, 2_4\rangle \right). \tag{6.1.3}
\end{aligned}$$

It can be seen that this wave function exhibits a form that is symmetric with respect to the components as well as the phases of the quantum state. In addition, in the

case of  $d = 2$  levels, the cluster state  $|C_{4,3}\rangle$  reduces to  $|C_{4,2}\rangle$  of Eq. (E.0.10), where  $\omega = e^{i2\pi/d} = e^{i2\pi/2} = -1$  and the level  $|2\rangle$  is missing. This result agrees with the theoretical predictions stated above.

We can observe that both  $|\phi_{4,3}\rangle$  and  $|C_{4,3}\rangle$  have the same Hilbert space size  $3^4 = 81$ , and that exhibit maximal connectedness, as well as a persistency of entanglement equal to  $\lfloor 4/2 \rfloor = 2$ . These two properties are missing instead in the four-partite qutrit GHZ state  $|\text{GHZ}_{4,3}\rangle$  defined in Eq. (C.0.4) of Appendix C. This confirms that, for a number of parties  $N \geq 4$ , cluster states are not equivalent to either GHZ or any other class of entangled states. The maximal connectedness of the cluster state in Eq. (6.1.3) was exploited here to demonstrate proof-of-principle high dimensional one-way quantum operations (see section 6.4).

## 6.2 Cluster state realization

The potential applications of cluster states to quantum computing, together with the several advantages of using photons (see section 1.6), led to a significant effort towards the realization of cluster states in optical quantum platforms [29–31, 57, 145, 146]. However, the generation of photon cluster states is currently limited to qubits, while their extension to higher dimension has never been explored thus far prior to this work [7].

In the introduction of chapter 3, it has been described briefly how to create a linear cluster state by means of interactions between next neighbor qubits via controlled-phase gate operations [115]. However, a realization based on interactions is extremely difficult in an optical platform, due to the fact that photons do not mutually interact (see section 1.6). For this reason, an alternate and feasible approach has been considered to generate cluster states with photons. This technique specifically relies on combining two Bell states (subsection 2.2.1), which are then entangled via a single C-Phase gate operation between selected qubits (typically a few) [115]. In Figure 3.2 a schematic representation of such a technique is reported for the specific case of a four-partite qubit cluster state [115].

Two approaches exist to generate a cluster state from the product of two Bell states. The first relies on making use of multiple (e.g. four) photons that are entangled in a single degree of freedom (for example, polarization) [29, 146]. In this case, two photon pairs are

generated into two distinct Bell states which are then entangled to form the cluster. The other approach relies on using a few photons (e.g. two) that exhibit entanglement in two distinct and independent degrees of freedom, such as polarization and linear momentum [30, 31, 57, 145]. This approach exploits the concept of hyper-entanglement (see subsection 2.5.2), where a single photon pair is generated simultaneously in two Bell states (one per degree of freedom).

By recurring either to multiple or to a few photons, cluster states have been demonstrated mainly in free space (e.g. in [57]) and, more recently, in waveguides [152] by making use of the polarization, space, paths, linear and orbital angular momentum degrees of freedom. In [153], the realization of photon cluster states in optical fibers was also proposed by exploiting time-bin entanglement.

In this work, we demonstrate the first four-partite three-level optical cluster state. To that purpose, we exploited the hyper-entanglement between time and frequency of two photons that are generated through SFWM in a nonlinear microcavity. This is the first time ever that the concept of hyper-entanglement is extended to high-dimensional states, as well as to time-bin and frequency-bin entanglement, which are two discrete forms of the same energy-time entanglement [7]. In the following section, we provide the details about the realization and the features of such hyper-entangled state.

### 6.2.1 Time- and frequency-bin hyper-entanglement

Past realizations of hyper-entangled photons have been accomplished by exploiting combinations of degrees of freedom which are intrinsically different and are thus represented by commuting observables, such as polarization, space, linear and orbital momentum. The reader can find the formal definition of commuting observable in Appendix A. Operationally, this means that each degree of freedom can be accessed individually and independently. For example, linear momentum can be measured through thin glass plates acting as phase shifters, while polarization can be accessed with half- and quarter-wave plates (shifting polarization direction by  $\pi$  and  $\pi/2$ , respectively) together with polarizing beam splitters [57].

The here presented hyper-entangled state has been realized by making use of time and frequency, which are intrinsically the same degree of freedom (since one is the Fourier transform of the other) and are thus represented by two non-commuting observables. In

particular, this state consists of just a qutrit photon pair: the time and frequency modes of each photon are considered as two separated parties, each of them being in a qutrit state. A legitimate question thus arises: *Why can such a state not be considered as a two-partite nine-level system?*

From a mathematical point of view, a two-partite nine-level and a four-partite three-level system have the same Hilbert space size, i.e.  $9^2 = 81$  and  $3^4 = 81$ , respectively. The same Hilbert space dimensionality can thus give rise to two different representations of the same quantum system. However, the physical property of the underlying quantum system, as well as by the accessible operations that are used for the state manipulation, determine which of the two representation has to be chosen.

Two-partite  $d$ -level representations require operations that allow for level changes of the same observable (for example, shifting and/or mixing frequency modes). The two-photon states demonstrated in [6] and reported in chapter 4 are an example of this representation. Although the levels of that same observable could be potentially divided into distinct subsystems, operations on one of them are usually not independent from the other subsystems. Multipartite  $d$ -level representations require instead unitary operations that can be performed on each subsystem independently of the others (for example, projection measurements on the eigenbasis of a single subsystem).

The hyper-entanglement between two (or more) degrees of freedom does enable a fully independent control on the individual subsystems. For this reason, hyper-entangled states can be considered as multipartite systems [7, 102].

In the case of commuting observables, it is straightforward to understand that degrees of freedom which are intrinsically different can be accessed independently of each other. A different scenario occurs when non-commuting observables, such as time and frequency, are considered. At a first glance, it seems that any operation on time cannot be performed independently of frequency, and vice versa. A deeper investigation shows that this is possible, though, provided that specific constraints are considered.

The temporal and frequency observables in energy-time entanglement typically form Einstein-Podolsky-Rosen quantum correlations (which means, nonlocal correlations, see section 2.3) [82]. When the product between the time and the frequency modes is much larger than the EPR limit (equal to one), then the two observables result in two commuting operators, thus allowing us to generate hyper-entanglement. In this work, in order

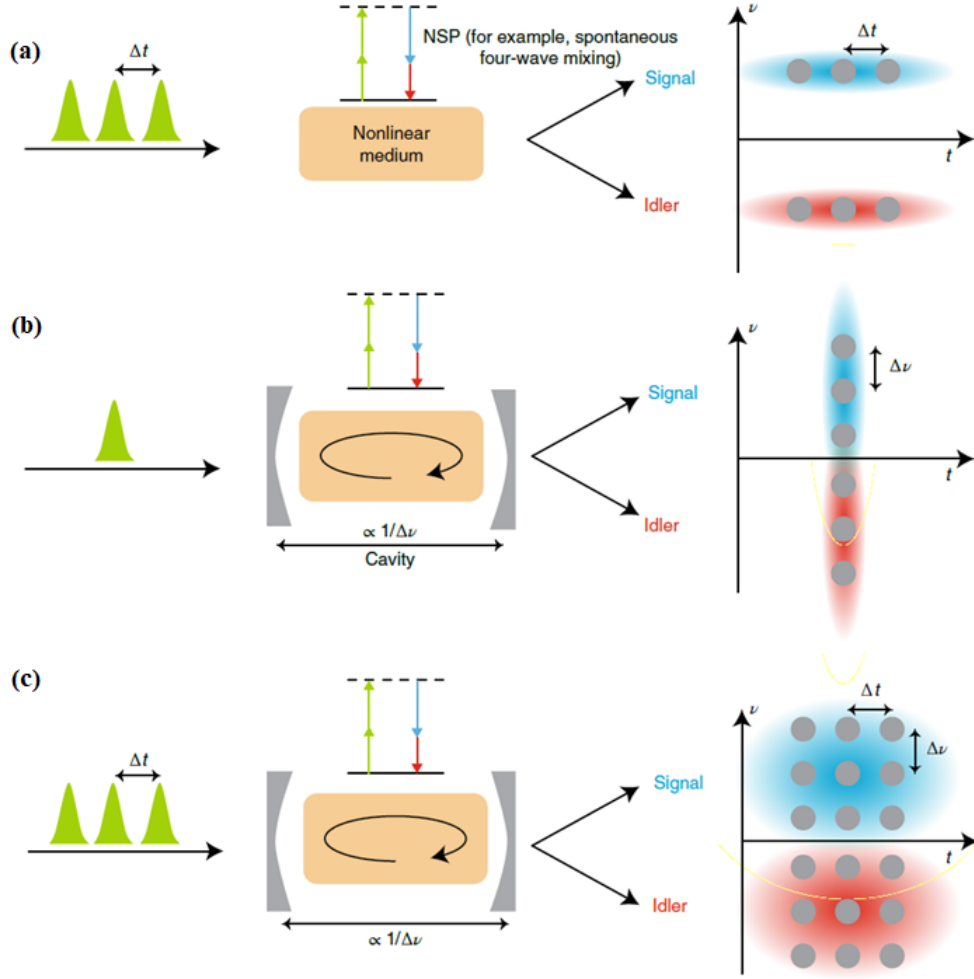


**Figure 6.1** – Scheme for the generation of time-frequency hyper-entanglement. **(a)** An optical pulse train (here, composed of three pulses) excites a nonlinear medium, where photon pairs (signal and idler) are generated through a nonlinear spontaneous process (NSP, here four-wave mixing) in a superposition of three time modes, given by the number of pulses. This results in a three-level time-bin entangled two-photon state. **(b)** A single pulse excites a nonlinear medium placed inside a cavity (composed by two semi-reflective mirrors), where photon pairs are created over a broad bandwidth in a superposition of three spectral modes, given by the number of selected cavity resonances per photon. This leads to a three-level frequency-bin entangled state. **(c)** Merging the concepts of (a) and (b), an optical pulse train excites a nonlinear cavity, thus generating a photon pair which is simultaneously entangled in time and frequency (i.e. a three-level hyper-entangled two-photon state). [7]

to treat time and frequency as independent observables, we needed to generate time and frequency modes in such a way that the EPR limited was exceeded. As it will be shown later in this section, the time-frequency product was  $4,800 \gg 1$ , which allowed us to claim the generation of hyper-entanglement [7].

As discussed in subsection 2.2.3, time-bin entanglement can be generated through

exciting a spontaneous parametric process in an optical nonlinear medium with multiple phase-locked pulses (see Figure 6.1-a). Frequency-bin entanglement can be realized by placing this nonlinear medium within an optical resonator, where the emission bandwidth covers multiple cavity resonances (see Figure 6.1-b). Here, we merged these two generation schemes; we excited a microring resonator with an optical train consisting of three pulses and generated through SFWM a photon pair with an emission bandwidth covering three resonances of the cavity. This way, signal and idler photons resulted entangled simultaneously in time and frequency, i.e. they resulted in a four-partite three-level hyper-entangled state (see Figure 6.1-c). Naming the time and frequency modes as  $|1\rangle$ ,  $|2\rangle$ ,  $|3\rangle$  and  $|a\rangle$ ,  $|b\rangle$ ,  $|c\rangle$ , respectively, the photon pair is generated in the two Bell-like states  $|\Psi\rangle_{\text{time}} = |1_s, 1_i\rangle + |2_s, 2_i\rangle + |3_s, 3_i\rangle$  and  $|\Psi\rangle_{\text{freq}} = |a_s, a_i\rangle + |b_s, b_i\rangle + |c_s, c_i\rangle$  at the same time.

The four-qutrit cluster state  $|C_{4,3}\rangle$  was realized then by entangling the product state  $|\Psi\rangle_{\text{time}} \otimes |\Psi\rangle_{\text{freq}}$  through a controlled phase gate [7].

The research work that has been pursued in this thesis is mainly theoretical. However, it is important to give the reader a brief description of the experimental setup used to generate the hyper-entangled state (see Figure 6.2) [7].

The triple phase-locked pulses were generated by using a carrier-envelope phase stabilized mode-locked laser (Menlo Systems Inc.) operating at a repetition rate of 250 MHz (which means, a 4 ns pulse separation). The phase frequency of the carrier envelope (i.e., the offset between the optical phase and the maximum of the wave envelope of a pulse) was locked to  $250/6 = 41.667$  MHz. Then, an electro-optic intensity modulator, driven by an arbitrary waveform generator, was used to temporally gate the three pulses that were separated by 24 ns (that is, taking each 6th from the initial pulse train). The set of pulses was repeated at a rate 10 MHz (which means, every 100 ns). The triple pulses were then spectrally filtered, amplified, and coupled into the same microring resonator as in section 4.1 [54, 59, 75]) at the resonance wavelength of 1,555.93 nm. The average pump power coupled through the chip was 2.4 mW (as it was measured at the drop port). After the microring resonator, the excitation field was removed using a high-isolation (150 dB) notch filter. The generated time- and frequency-entangled photon pair was finally coupled into the controlled phase gate, where it was manipulated to realize the cluster state. From the description of the generation scheme, it can be seen that the product

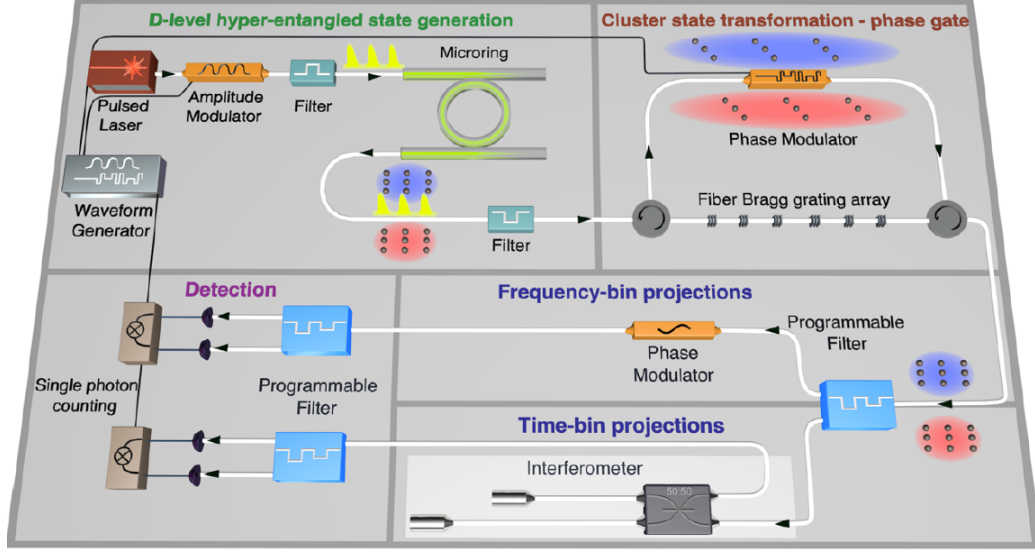


**Figure 6.2** – Experimental setup for generation of d-level cluster-states and for measurement-based quantum operations. Three optical pulses excite a resonance frequency of the nonlinear microring resonator, where signal and idler (marked respectively in red and blue) are generated via SFWM. Being in a superposition of three time and three frequency modes (indicated by bullets), the photons are in a hyper-entangled state. The individual access to amplitudes and phases of this state were achieved through a novel controlled phase gate consisting of a fiber Bragg grating array allowing for frequency-to-time mapping. A phase modulator was used to change the phase of the different state terms to produce d-level cluster states. A programmable filter was used to send the cluster state into two different analysis setups: 1) frequency-bin projections through an electro-optic phase modulator, and 2) time-bin projections via an imbalanced interferometer. The photons were then separated by filters and measured with single-photon detectors. [7]

between time-mode separation (i.e.  $\Delta t = 24$  ns) and frequency-mode separation (i.e.  $\Delta\nu = 200$  GHz) was  $\Delta t\Delta\nu = 4,800 \gg 1$ .

The generated hyper-entangled state  $|\Psi\rangle_{\text{time}} \otimes |\Psi\rangle_{\text{freq}}$  thus results in the wave function [7]

$$\begin{aligned}
|\Psi_{\text{Hyper}}\rangle &= (|1_s, 1_i\rangle + |2_s, 2_i\rangle + |3_s, 3_i\rangle) \otimes (|a_s, a_i\rangle + |b_s, b_i\rangle + |c_s, c_i\rangle) \\
&= |1_s, 1_i, a_s, a_i\rangle + |1_s, 1_i, b_s, b_i\rangle + |1_s, 1_i, c_s, c_i\rangle \\
&\quad + |2_s, 2_i, a_s, a_i\rangle + |2_s, 2_i, b_s, b_i\rangle + |2_s, 2_i, c_s, c_i\rangle \\
&\quad + |3_s, 3_i, a_s, a_i\rangle + |3_s, 3_i, b_s, b_i\rangle + |3_s, 3_i, c_s, c_i\rangle.
\end{aligned} \tag{6.2.1}$$

The physical qudits are encoded here as:  $|0_1\rangle \rightarrow |1_s\rangle$ ,  $|0_2\rangle \rightarrow |1_i\rangle$ ,  $|0_3\rangle \rightarrow |a_s\rangle$ ,  $|0_4\rangle \rightarrow |a_i\rangle$ ,  $|1_1\rangle \rightarrow |2_s\rangle$ ,  $|1_2\rangle \rightarrow |2_i\rangle$ ,  $|1_3\rangle \rightarrow |b_s\rangle$ ,  $|1_4\rangle \rightarrow |b_i\rangle$ ,  $|2_1\rangle \rightarrow |3_s\rangle$ ,  $|2_2\rangle \rightarrow |3_i\rangle$ ,  $|2_3\rangle \rightarrow |c_s\rangle$ ,  $|2_4\rangle \rightarrow |c_i\rangle$ . This means that, for both signal and idler photons, qutrits 1 and 2

are physically encoded in the time, while qutrits 3 and 4 are physically encoded in the frequency. The wave function  $|\Psi_{\text{Hyper}}\rangle$  exhibits a form which is symmetric with respect to the quantum state components. Such a symmetry was crucial here, since we exploited it in order to transform the entangled state  $|\Psi_{\text{Hyper}}\rangle$  into the target cluster state  $|C_{4,3}\rangle$ .

The product state  $|\Psi_{\text{hyper}}\rangle$  is still bi-separable (see Figure 2.3), which means that there is no entanglement between the time and the frequency modes of signal and idler. Specifically, any (non-destructive) projection measurement on the time-bin entangled state  $|\Psi\rangle_{\text{time}}$  does not affect the frequency-bin entangled sub-state  $|\Psi\rangle_{\text{freq}}$  (and vice versa). Comparing the separable state  $|\Psi_{\text{Hyper}}\rangle$  with the compact cluster state  $|C_{4,3}\rangle$  of Eq. (6.1.3), it can be noticed that they have a very similar form, since the terms of their respective wave functions are the same. However,  $|\Psi_{\text{Hyper}}\rangle$  and  $|C_{4,3}\rangle$  differ by the phase factors  $\alpha = 2\pi/3$  in front of  $|2_s, 2_i, b_s, b_i\rangle$  and  $|3_s, 3_i, c_s, c_i\rangle$ , as well as  $\beta = -2\pi/3$  in front of  $|2_s, 2_i, c_s, c_i\rangle$  and  $|3_s, 3_i, b_s, b_i\rangle$ . Therefore, the product state  $|\Psi_{\text{Hyper}}\rangle$  necessitates a judicious modification of specific phase terms in order to be converted into the cluster state  $|C_{4,3}\rangle$ . This required having the access to the individual terms of  $|\Psi_{\text{Hyper}}\rangle$  while preserving coherence. Such a specific task was accomplished through developing a (fiber-based) controlled phase gate that allowed us to manipulate individually time and frequency modes.

## 6.2.2 Controlled phase gate for the cluster state realization

The key components of developed controlled-phase gate are described in this section, as well as depicted in the middle panel of Figure 6.3 [7].

The bi-separable state  $|\Psi_{\text{Hyper}}\rangle$  was sent as input of the C-Phase gate through a circulator. In order to have access to its individual terms, a frequency-to-time mapping was necessary, that is, the individual frequency modes were temporally dispersed into different time slots. Such a frequency-to-time mapping could be achieved via a custom-made Fiber Bragg Grating (FBG) array. This consists of six independent FBGs that were matched to the photon wavelengths (i.e. 1,551.08, 1,552.70, 1,554.31, 1,557.55, 1,559.17 and 1,560.80 nm) and that were spatially separated in the fiber such that a temporal delay of 3.96 ns between adjacent frequency modes was achieved. The FBGs were apodized using a squared cosine function that has been implemented by means of moving a Talbot phase mask with a piezo actuator [154].

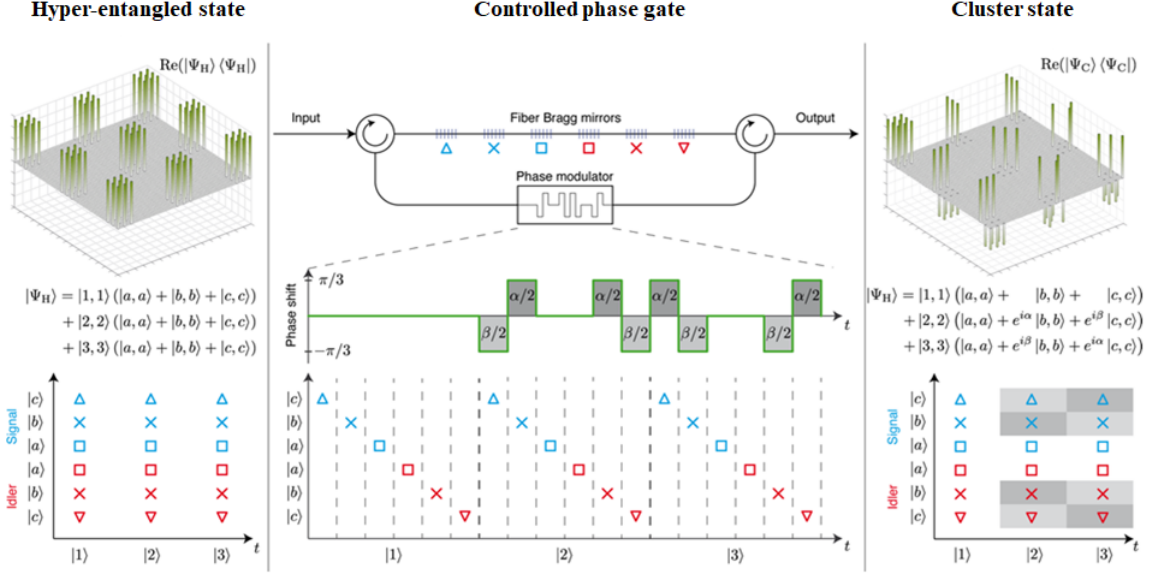


**Figure 6.3** – Generation of cluster states with a controlled phase gate. The two-photon hyper-entangled qudit state is simultaneously composed of three temporal modes  $|1\rangle$ ,  $|2\rangle$ ,  $|3\rangle$  and three frequency modes  $|a\rangle$ ,  $|b\rangle$ ,  $|c\rangle$  per each photon (the real part of the associated density matrix is depicted in the top left panel). A controlled phase gate gives access to the individual state terms by temporally dispersing the individual frequency modes into different time slots via a fiber Bragg grating array (see middle panel). An electro-optical modulator was used to change the phase of the individual state terms, here by  $\alpha/2$  and  $\beta/2$ . The photons then enter the fiber Bragg grating array from the opposite end, such that the frequency-to-time mapping is coherently reversed. By choosing the phases  $\alpha = 2\pi/3$  and  $\beta = -2\pi/3$ , the hyper-entangled state is transformed into a three-level cluster state (the real part of the associated density matrix is shown in the top right panel). [7]

Once the frequency-to-time-mapping was performed, the phase terms  $\alpha = 2\pi/3$  and  $\beta = -2\pi/3$  could be added coherently to specific terms of the input state  $|\Psi_{\text{Hyper}}\rangle$ . This action required an optical phase modulation that was implemented within the gate by means of an electro-optic phase modulator (EOM). This device was used to change the phase by  $\alpha/2$  and  $\beta/2$ , as shown in Figure 6.3. The EOM was driven by an arbitrary waveform generator synchronized to the 10 MHz reference clock of the mode-locked laser. Finally, the two-photon state entered again the FBG array from the opposite side through the second circulator, such that the frequency-to-time mapping could be coherently reversed. The described operation could be possible since time and frequency, although independent, are intrinsically the same degree of freedom (as one is the Fourier Transform of the other).

The output state of the controlled-phase gate thus resulted in the targeted cluster

state  $|\Psi_{\text{Cluster}}\rangle$  (the normalization factor is omitted here)

$$\begin{aligned}
|\Psi_{\text{Cluster}}\rangle = & |1_s, 1_i, a_s, a_i\rangle + |1_s, 1_i, b_s, b_i\rangle + |1_s, 1_i, c_s, c_i\rangle \\
& + |2_s, 2_i, a_s, a_i\rangle + e^{i2\pi/3} |2_s, 2_i, b_s, b_i\rangle + e^{-i2\pi/3} |2_s, 2_i, c_s, c_i\rangle \\
& + |3_s, 3_i, a_s, a_i\rangle + e^{-i2\pi/3} |3_s, 3_i, b_s, b_i\rangle + e^{i2\pi/3} |3_s, 3_i, c_s, c_i\rangle.
\end{aligned} \tag{6.2.2}$$

Figure 6.3 also reports a comparison between the density matrices of the separable and the cluster states  $\rho_{\text{H}} = |\Psi_{\text{Hyper}}\rangle\langle\Psi_{\text{Hyper}}|$  and  $\rho_{\text{C}} = |\Psi_{\text{Cluster}}\rangle\langle\Psi_{\text{Cluster}}|$  [7]. The phase terms distinguishing  $\rho_{\text{H}}$  and  $\rho_{\text{C}}$  are responsible for the fact that  $\rho_{\text{H}}$  is separable, while  $\rho_{\text{C}}$  exhibits genuine three-partite entanglement. This means that any temporal projection measurement of the quantum state  $|\Psi_{\text{Cluster}}\rangle$  affects the frequency-entangled sub-state, and vice versa (see section 6.4).

Immediately after the phase gate, the photons were sent to a programmable amplitude and phase filter with one input and two output ports such that signal and idler could be routed to different characterization setups. One output was connected to a stabilized two-arm interferometer<sup>1</sup> [155] with a 24 ns unbalance between the two arm lengths, which was used for time-bin projections (see Figure 6.2). The other output was connected to an electro-optic phase modulator which mixes different frequency components and was used for frequency-bin projections (see Figure 6.2). Finally, signal and idler were sent to two different superconducting single-photon detectors (see Figure 6.2). The setup depicted in the lower panel of Figure 6.2 was used to measure the witness expectation value (subsection 6.3.2), as well as for one-way quantum processing operations (section 6.4) via time- and frequency-projections.

### 6.3 Witness for four-partite three-level cluster states

In this section we present the witness operator that has been derived by following the theoretical approach of [5], to confirm the generation of genuine four-partite three-level entanglement. The measured expectation value of this witness was further used to test the impact of incoherent, phase and amplitude noise on the cluster state (see subsection 6.3.3) [7].

---

1. The two-arm interferometer was stabilized through a scheme that makes use of a reference laser and active feedback (such a scheme is patented [155] and is the topic of an upcoming publication).

### 6.3.1 Stabilizers

According to Eq. (5.2.7), the witness of high-dimensional cluster states requires the use of the main stabilizers, as well as of their transpose conjugates.

In order to derive the main stabilizers of the compact cluster state  $|C_{4,3}\rangle$  (i.e.  $|\Psi_{\text{Cluster}}\rangle$ ), it was necessary to first consider the main stabilizers of the linear form  $|\phi_{4,3}\rangle$ , and then to transform them accordingly. The main stabilizers of  $|\phi_{4,3}\rangle$  were derived from Eqs. (3.4.2) and (3.4.3), and are [5]:

$$\begin{aligned}\mathcal{S}_1^{\phi_{4,3}} &= X_1 Z_2 \mathbb{I}_3 \mathbb{I}_4 \\ \mathcal{S}_2^{\phi_{4,3}} &= Z_1 X_2 Z_3 \mathbb{I}_4 \\ \mathcal{S}_3^{\phi_{4,3}} &= \mathbb{I}_1 Z_2 X_3 Z_4 \\ \mathcal{S}_4^{\phi_{4,3}} &= \mathbb{I}_1 \mathbb{I}_2 Z_3 X_4,\end{aligned}\tag{6.3.1}$$

where

$$Z = \begin{pmatrix} 1 & 0 & 0 \\ 0 & \omega & 0 \\ 0 & 0 & \omega^2 \end{pmatrix}, \quad X = \begin{pmatrix} 0 & 0 & 1 \\ 1 & 0 & 0 \\ 0 & 1 & 0 \end{pmatrix}, \quad \mathbb{I} = \begin{pmatrix} 1 & 0 & 0 \\ 0 & 1 & 0 \\ 0 & 0 & 1 \end{pmatrix}.\tag{6.3.2}$$

are the generalized  $3 \times 3$  Pauli matrices  $Z$  and  $X$ , with  $\omega = e^{i2\pi/3}$  [5, 7].

Since the compact cluster state  $|C_{4,3}\rangle$  was obtained by applying the  $3 \times 3$   $W$  matrix (defined in Appendix G) to qutrits 1 and 4, and the identity to qutrits 2 and 3, the four main stabilizers of  $|C_{4,3}\rangle$  were similarly derived by converting  $\mathcal{S}_k^{\phi_{4,3}}$  ( $k = 1, 2, 3, 4$ ) into  $\mathcal{S}_k^{C_{4,3}}$ . From Eqs. (1.8.12) of section 1.8, which relate  $W$ ,  $X$  and  $Z$  (as well as the respective transpose conjugates), the main stabilizers of  $|C_{4,3}\rangle$  result in:

$$\begin{aligned}\mathcal{S}_1^{C_{4,3}} &= Z_1^\dagger Z_2 \mathbb{I}_3 \mathbb{I}_4 \\ \mathcal{S}_2^{C_{4,3}} &= X_1 X_2 Z_3 \mathbb{I}_4 \\ \mathcal{S}_3^{C_{4,3}} &= \mathbb{I}_1 Z_2 X_3 X_4 \\ \mathcal{S}_4^{C_{4,3}} &= \mathbb{I}_1 \mathbb{I}_2 Z_3 Z_4^\dagger.\end{aligned}\tag{6.3.3}$$

Once the operators  $\mathcal{S}_k^{C_{4,3}}$  were derived, it was necessary to validate that these were actually stabilizers for the compact cluster state. This means that the eigenvalue equations  $\mathcal{S}_k^{C_{4,3}} |C_{4,3}\rangle = |C_{4,3}\rangle$  must be satisfied analytically. To this end, we considered the action

of the  $3 \times 3$  Pauli matrix on the computational basis, which is

$$\begin{aligned} Z|0\rangle &= |0\rangle, & Z^\dagger|0\rangle &= |0\rangle \\ Z|1\rangle &= \omega|1\rangle, & Z^\dagger|1\rangle &= \omega^2|1\rangle \\ Z|2\rangle &= \omega^2|2\rangle, & Z^\dagger|2\rangle &= \omega|2\rangle \end{aligned} \tag{6.3.4}$$

$$\begin{aligned} X|0\rangle &= |1\rangle, & X^\dagger|0\rangle &= |2\rangle \\ X|1\rangle &= |2\rangle, & X^\dagger|1\rangle &= |0\rangle \\ X|2\rangle &= |0\rangle, & X^\dagger|2\rangle &= |1\rangle. \end{aligned} \tag{6.3.5}$$

From these transformations, it can be seen that the cluster state  $|C_{4,3}\rangle$  remains unchanged under the action of each operator  $\mathcal{S}_k^{C_{4,3}}$ , which confirms that this is actually a stabilizer for  $|C_{4,3}\rangle$ .

The linear combinations of the four main stabilizers, as well as of their transpose conjugates, give rise to a set of distinct  $3^4 = 81$  stabilizers reported in Appendix J. The Pauli group (see section 1.8) containing all the matrices which compose the 81 stabilizers gives  $\mathcal{P} = \{\mathbb{I}, X, X^\dagger, Z, Z^\dagger, Y, Y^\dagger, V, V^\dagger\}$ , where  $Y = XZ$  and  $V = XZ^\dagger$  (see Eq. (5.3.3)).

The relationship between a generalized Pauli matrix and its transpose conjugate expressed in Eq. (1.8.6) can be extended directly to stabilizers as

$$(\mathcal{S}^n)^\dagger = (\mathcal{S})^{d-n}, \tag{6.3.6}$$

where  $n = 1, \dots, d$ . Furthermore, by definition,  $\mathcal{S}^d = \mathbb{I}$ . In the specific case of  $d = 3$ , the relations become [5]:

$$\begin{aligned} Z^2 &= Z^\dagger, & Z^3 &= \mathbb{I} \\ X^2 &= X^\dagger, & X^3 &= \mathbb{I} \\ \mathcal{S}_k^2 &= \mathcal{S}_k^\dagger, & \mathcal{S}_k^3 &= \mathbb{I} \quad \forall k. \end{aligned} \tag{6.3.7}$$

Here, we made use of Eqs. (6.3.7) in order to derive the explicit expression of the witness operator for the four-partite three-level compact cluster state (see subsection 6.3.2).

### 6.3.2 Entanglement witness

As a starting point for the witness derivation, we write the density matrix of the cluster state by making use of the main stabilizers of  $|C_{4,3}\rangle$  as

$$|C_{4,3}\rangle\langle C_{4,3}| = \prod_{k=1}^4 \frac{\mathcal{S}_k^{(C_{4,3})} + \mathcal{S}_k^{\dagger(C_{4,3})} + \mathbb{I}}{3}. \tag{6.3.8}$$

The stabilizers resulting from Eq. (6.3.8) can further be split into two orthogonal sets that include only the matrices  $\mathbb{I}$ ,  $X$ ,  $X^\dagger$ ,  $Z$ , and  $Z^\dagger$ . This leads to a witness operator  $\mathcal{W}_{2S}^{(C_{4,3})}$  consisting of just two measurement settings (see chapter 3 and chapter 5), which is given by

$$\begin{aligned}
\mathcal{W}_{2S}^{(C_{4,3})} &= 2\mathbb{I} - \frac{3}{2} \prod_{\text{odd } k} \frac{\mathcal{S}_k^{(C_{4,3})} + \mathcal{S}_k^{\dagger(C_{4,3})} + \mathbb{I}}{3} - \frac{3}{2} \prod_{\text{even } k} \frac{\mathcal{S}_k^{(C_{4,3})} + \mathcal{S}_k^{\dagger(C_{4,3})} + \mathbb{I}}{3} \\
&= 2\mathbb{I} - \frac{1}{4} \left( \mathbb{I}_1 \mathbb{I}_2 Z_3 Z_4^\dagger + \mathbb{I}_1 \mathbb{I}_2 Z_3^\dagger Z_4 + Z_1^\dagger Z_2 \mathbb{I}_3 \mathbb{I}_4 + Z_1 Z_2^\dagger \mathbb{I}_3 \mathbb{I}_4 \right) \\
&\quad - \frac{1}{4} \left( \mathbb{I}_1 Z_2 X_3 X_4 + \mathbb{I}_1 Z_2^\dagger X_3^\dagger X_4^\dagger + \frac{Z_1 \mathbb{I}_2 X_3 X_4 + Z_1^\dagger Z_2^\dagger X_3 X_4}{2} + \frac{Z_1^\dagger \mathbb{I}_2 X_3^\dagger X_4^\dagger + Z_1 Z_2 X_3^\dagger X_4^\dagger}{2} \right) \\
&\quad - \frac{1}{4} \left( X_1 X_2 Z_3 \mathbb{I}_4 + X_1^\dagger X_2^\dagger Z_3^\dagger \mathbb{I}_4 + \frac{X_1 X_2 \mathbb{I}_3 Z_4 + X_1 X_2 Z_3^\dagger Z_4^\dagger}{2} + \frac{X_1^\dagger X_2^\dagger \mathbb{I}_3 Z_4^\dagger + X_1^\dagger X_2^\dagger Z_3 Z_4}{2} \right).
\end{aligned} \tag{6.3.9}$$

Excluding the first term, the witness contains 16 elements: eight of them are the transpose conjugate of the other eight. The goal is measuring the expectation value of the witness  $\mathcal{W}_{2S}^{(C_{4,3})}$ , which must be a scalar. To this purpose, we consider that the real part of an imaginary number  $c$  is given by  $\text{Re}(c) = (c + c^\dagger)/2$ . We can thus write the expectation value of the witness as

$$\begin{aligned}
\langle \mathcal{W}_{2S}^{(C_{4,3})} \rangle &= \frac{5}{3} \text{Re} \left( \langle \mathbb{I}_1 \mathbb{I}_2 Z_3 Z_4^\dagger \rangle + \langle Z_1^\dagger Z_2 \mathbb{I}_3 \mathbb{I}_4 \rangle + \langle \mathbb{I}_1 Z_2 X_3 X_4 \rangle + \langle X_1 X_2 Z_3 \mathbb{I}_4 \rangle \right. \\
&\quad \left. + \langle Z_1 \mathbb{I}_2 X_3 X_4 \rangle + \langle Z_1^\dagger Z_2^\dagger X_3 X_4 \rangle + \langle X_1 X_2 \mathbb{I}_3 Z_4 \rangle + \langle X_1 X_2 Z_3^\dagger Z_4^\dagger \rangle \right).
\end{aligned} \tag{6.3.10}$$

Since high dimensional stabilizers are not Hermitian operators, their expectation values can also have imaginary components. However, the linear combination of stabilizers, as it appears in Eq. (6.3.10), results in a real number, as it is required for any observable (i.e. the witness). In Appendix I, we provide the analytical proof that any combination of stabilizers of the form in Eq. (6.3.10) always result in a Hermitian operator [5].

Only two types of projections measurements are needed to determine the expectation value of  $\mathcal{W}_{2S}^{(C_{4,3})}$ : one in the basis of  $\mathbb{I}$  and  $Z$  (i.e. in the computational basis), and one in the basis of  $X$  (i.e. in the superposition  $\{|x_j\rangle\}$ , see Eq. (G.0.4)). According to the physical encoding that we used for the cluster state  $|\Psi_{\text{Cluster}}\rangle$  of Eq. (6.2.2), qutrits 1 and 2 of both signal and idler were measured in the time domain, while qutrits 3 and 4 in the frequency domain.

The expectation value of the witness was determined by measuring the individual expectation values of the eight stabilizers of Eq. (6.3.10). This necessitated 81 separate measurements per operator, since each stabilizer was measured in the eigenbasis of the

generalized Pauli matrices composing it. This led to a total of  $81 \times 8 = 648$  measurements that were necessary to determine  $\langle \mathcal{W}_{2S}^{(C_{4,3})} \rangle$ . A specific task accomplished here was deriving the explicit form in terms of projections and probability amplitudes of all the 648 measurements to be performed experimentally.

The here pursued theoretical investigation has led to the following observations about the stabilizer measurements. The operators  $\mathbb{I}_1 \mathbb{I}_2 Z_3 Z_4^\dagger$  and  $Z_1^\dagger Z_2 \mathbb{I}_3 \mathbb{I}_4$  must be measured with respect to the eigenvectors  $|1\rangle, |2\rangle, |3\rangle$  for qutrits 1 and 2, and  $|a\rangle, |b\rangle, |c\rangle$  for qutrits 3 and 4. The stabilizers  $\mathbb{I}_1 Z_2 X_3 X_4$ ,  $Z_1 \mathbb{I}_2 X_3 X_4$  and  $Z_1^\dagger Z_2^\dagger X_3 X_4$  must be detected in the basis  $|1\rangle, |2\rangle, |3\rangle$  for qutrits 1 and 2, and  $|f1\rangle, |f2\rangle, |f3\rangle$ , for qutrits 3 and 4, with  $|f1\rangle = |a\rangle + |b\rangle + |c\rangle$ ,  $|f2\rangle = |a\rangle + e^{i2\pi/3} |b\rangle + e^{-i2\pi/3} |c\rangle$ , and  $|f3\rangle = |a\rangle + e^{-i2\pi/3} |b\rangle + e^{i2\pi/3} |c\rangle$ . Finally,  $X_1 X_2 Z_3 \mathbb{I}_4$ ,  $X_1 X_2 Z_3 \mathbb{I}_4$ ,  $X_1 X_2 \mathbb{I}_4 Z_4$ , and  $X_1 X_2 Z_3^\dagger Z_4^\dagger$  must be measured in the eigenbasis  $|t1\rangle, |t2\rangle, |t3\rangle$ , for qutrits 1 and 2, with  $|t1\rangle = |1\rangle + |2\rangle + |3\rangle$ ,  $|t2\rangle = |1\rangle + e^{(i2\pi/3)} |2\rangle + e^{(-i2\pi/3)} |3\rangle$ , and  $|t3\rangle = |1\rangle + e^{-i2\pi/3} |2\rangle + e^{i2\pi/3} |3\rangle$ , and  $|a\rangle, |b\rangle, |c\rangle$  for qutrits 3 and 4 [7].

These projections were performed as follows. In the experimental setup we could directly implement projections on the time modes  $|1\rangle, |2\rangle, |3\rangle$  via temporal gating in the detection; on the frequency modes  $|a\rangle, |b\rangle, |c\rangle$  via optical filtering; and on the frequency-bin superpositions  $|f1\rangle, |f2\rangle, |f3\rangle$  through electro-optic modulation. In order to perform projections on the time-bin superpositions  $|t1\rangle, |t2\rangle, |t3\rangle$ , we proceed as follows: we assessed the phases of the cluster state through simultaneous projections in the superposition of two time bins each. These were implemented with an unbalanced two-arm interferometer [19]. Then, the projections  $|t1\rangle, |t2\rangle, |t3\rangle$  were reconstructed through the measured interference patterns. A more detailed description on how the projections were accomplished is provided in section 6.4.

The resulting values of all these projections were extracted by experimentally determining  $3 \times 81 = 243$  parameters, which can take real values between 0 and 1. These 243 outcomes were used then to calculate the expectation value of each stabilizer composing  $\mathcal{W}_{2S}^{(C_{4,3})}$ , which resulted in eight complex numbers having an absolute value smaller than one (see Figure 6.4). The expectation value of the whole witness was finally estimated by taking the real part of the expectation values of the eight stabilizers (individually, before summing them up), and was found to be (see Figure 6.4)

$$\langle \mathcal{W}_{2S}^{(C_{4,3})} \rangle = -0.28 \pm 0.04. \quad (6.3.11)$$

Such a negative value confirmed (within the range of 7 standard deviations) that the

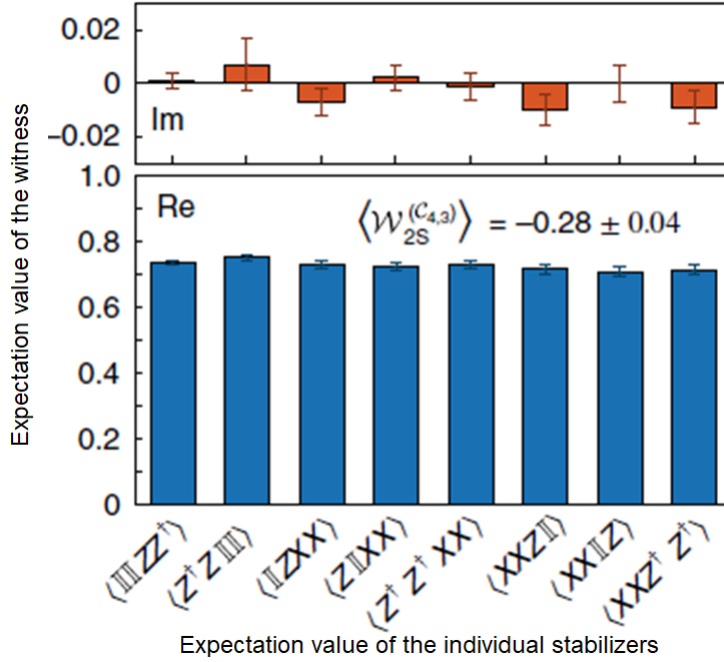


**Figure 6.4** – Measurement of the entanglement witness. Real (blue bars) and imaginary (red bars) parts of the measured expectation values for the individual terms of the cluster state witness. The expectation value for each term can be complex due to the non-Hermitian properties of the generalized Pauli matrices; however, only the eight real parts contribute to the witness expectation value, which results in the real negative number  $-0.28 \pm 0.04$ . [7]

realized cluster state presented genuine four-partite three-level entanglement [7].

### 6.3.3 Witness distribution and noise tolerance of cluster states

The measured witness operator can be used to investigate the impact of incoherent, phase and amplitude noise on the realized cluster state. This task was accomplished through both a theoretical and a numerical approach. The former relies on the noise threshold  $\varepsilon_{\text{th}}$  that was derived in [5] and that is reported in Eq. (5.2.14) of subsection 5.2.1. The latter is based on Monte Carlo simulations. These were chosen in order to reproduce numerically the randomness of the noise contributions, as well as in order to infer the distribution of the witness expectation value.

We specifically considered the impact of white (or incoherent) noise, which transforms a cluster state as Eq. (5.2.9). The white noise model is particularly useful in this analysis, since it allows us to distinguish different noise sources. For example, incoherent noise has impact and affects the purity of a quantum state. Losses and detection are typical sources

<b>Projections</b>	$\phi_{2,f}$ (rad)	$\phi_{3,f}$ (rad)	<b>Visibility</b> $V_{(11,22)}^t$	<b>Visibility</b> $V_{(22,33)}^t$
$ a_s, a_i\rangle$	$0.06 \pm 0.02$	$-0.06 \pm 0.02$	80.2% > 70.7%	83.7% > 70.7%
$ b_s, b_i\rangle$	$0.65 \pm 0.02$	$-0.72 \pm 0.02$	76.7% > 70.7%	74.9% > 70.7%
$ c_s, c_i\rangle$	$-0.67 \pm 0.02$	$0.69 \pm 0.02$	77.6% > 70.7%	72.2% > 70.7%
	$\phi_{t,2}$	$\phi_{t,3}$	<b>Visibility</b> $V_{(aa,bb,cc)}^f$	
$ 1_s, 1_i\rangle$	$0.087 \pm 0.03$	$0.01 \pm 0.03$	83.4% > 77.4%	
$ 2_s, 2_i\rangle$	$0.594 \pm 0.03$	$-0.667 \pm 0.03$	80.7% > 77.4%	
$ 3_s, 3_i\rangle$	$-0.638 \pm 0.02$	$0.628 \pm 0.02$	78.8% > 77.4%	

**Table 6.1** – Phases and visibilities extracted via quantum interference characterization. Such operation was performed on the measurement-based frequency- and time-bin qudits generated from the cluster state. The phase values are obtained from the relative offset of the quantum interference measurements with respect to the non-manipulated state. [7]

of incoherent noise. On the other hand, there are noise sources, such as amplitude and phase noise, that do not affect the purity of the quantum state. In that case, they can be incorporated into the wave function by properly adjusting its amplitude and phase, which were determined, together with their respective errors, via quantum interference (see Table 6.1). Starting from these values, we assumed a Gaussian error distribution for each individual input parameter and calculated the expectation value of the witness one million times.

These calculations are summarized in normalized histograms reported in Figure 6.5-a,b,c. The witness bound was then determined for different noise input sources (i.e. incoherent, amplitude and phase noise). To this end, we calculated the associated operator for input parameters with different noise sources and average strengths. In each calculation, only two noise sources were considered at a time, while the remaining one was kept at zero. For diagrams in Figure 6.5-a,b involving incoherent noise, we first set a fixed value for this term and then generated ten million random input values for either the phases or amplitudes (the incoherent noise value was finally changed for different rounds of simulations). Whereas, for the diagram in Figure 6.5-c, where both amplitude and phase noise were open parameters, we generated one billion random input settings. The random noise inputs were all provided through Monte Carlo simulations. The expectation value of the witness was finally calculated for each simulated noise input. The outcomes

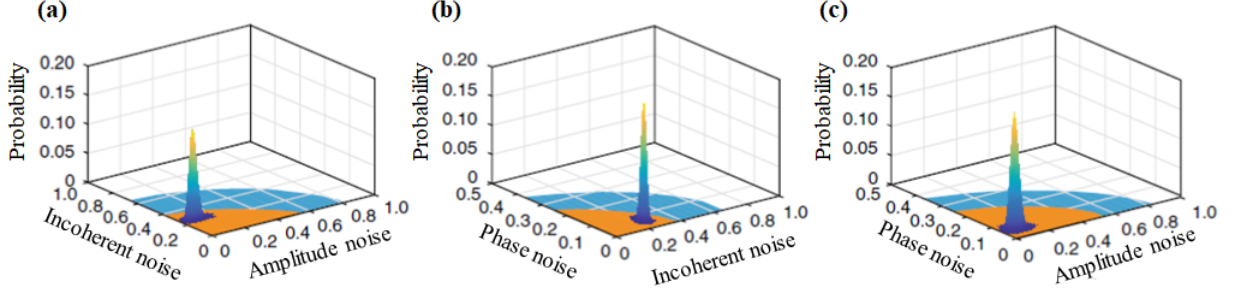


**Figure 6.5** – Witness noise distribution. Monte Carlo simulations for different noise contributions. The regions for which the optimal and measured witness operators confirm the existence of a cluster state for different sources of noise are indicated by blue- and orange-shaded areas, respectively. The witness bounds are shown for combinations of (a) incoherent and amplitude noise, (b) phase and incoherent noise, and (c) phase and amplitude noise. In all the diagrams, the vertical axis represents the probability that the witness is affected by that noise contribution (i.e., incoherent, amplitude, and phase noise). The measurements (peaks in the respective diagrams) indicate that the largest contributor to state imperfection in our system is incoherent noise. [7]

were then sorted according to the resulting positive and negative witness values, as well as their average noise. The vertical axis in Figure 6.5-a,b,c represents the probability that the measured witness is affected by that specific noise contribution (i.e., incoherent, amplitude, and phase noise).

From Monte Carlo simulations, we determined that the here realized high dimensional cluster state can endure high amounts of amplitude and phase noise. More precisely, this can tolerate as much as 83% of average amplitude fluctuations and up to 37% error in the phase terms (see Figure 6.5-a,b,c). The measured witness can tolerate instead 55% and 25% for amplitudes and phases, respectively.

The noise amplitude was evaluated as the average over the absolute deviations from the ideal value, normalized by the latter:  $\sigma_{\text{ampl}} = 3 \times \frac{1}{9} \sum_{i=1}^9 |a_i - \frac{1}{3}|$ , where  $a_i$  are the nine different amplitude terms in the wave function  $|\Psi_{\text{Cluster}}\rangle$  and  $1/3$  is the ideal value. Similarly, the noise phase has been evaluated as the average over the absolute phase deviation from the ideal value, normalized by the optimal phase terms:  $\sigma_{\text{phase}} = \frac{3}{2\pi} \times \frac{1}{9} \sum_{i=1}^9 |\theta_i - \varphi_{\text{ideal}}|$ , where  $\varphi_{\text{ideal}} = [0, 2\pi/3, -2\pi/3]$  is the ideal phase settings, while  $\theta_i$  are the nine different measured phase values that have been extracted from quantum interference (see Eqs. (6.4.2) of section 6.4). The state bound for the witness was finally determined as the points where over 95% of all calculated witnesses resulted in a negative

expectation value.

From the analytical expression of the noise threshold  $\varepsilon_{\text{th}}$  in Eq. (5.2.1), we extracted the noise that a four-partite three-level cluster state can tolerate up to losing its cluster state properties. With respect to the measured witness  $\mathcal{W}_{2S}^{(C_{4,3})}$ , the cluster state can tolerate up to 37.5% of incoherent noise. These results provide an experimental validation of the conclusion made in chapter 5:  $d$ -level cluster states are more noise tolerant than the two-level counterparts. To show this, the four-qutrit cluster state can be directly compared with a four-qubit cluster state, which can be mixed only with up to 33% of incoherent noise. A six-qubit cluster state (which has a slightly lower computational power compared to the four-qutrit state demonstrated here) can tolerate only 28.5% of incoherent noise.

## 6.4 One-way quantum computing operations

In order to confirm that the cluster state could be used for one-way quantum operations, we validated that performing specific two-partite projections either in time or in frequency, led to the generation of different and orthogonal bipartite states that are entangled in frequency and in time, respectively.

We validated the presence of these bipartite states via quantum interference measurements, from which the amplitudes and phases of the cluster state could be extracted. The orthogonality of the bipartite states was confirmed through estimating the relative phase shift in their respective quantum interference pattern, while the entanglement of the projected states was verified via Bell inequality violations.

We now report the details on how to extract amplitude and phase from the measured cluster state  $|\Psi_{\text{Cluster}}\rangle$  [7].

The most generic wave function of a four-partite qutrit hyper-entangled state is given by

$$\begin{aligned} |\Psi_{\text{Hyper}}\rangle = & m_{1,a} |1_s, 1_i, a_s, a_i\rangle + m_{1,b} |1_s, 1_i, b_s, b_i\rangle + m_{1,c} |1_s, 1_i, c_s, c_i\rangle \\ & + m_{2,a} |2_s, 2_i, a_s, a_i\rangle + m_{2,b} |2_s, 2_i, b_s, b_i\rangle + m_{2,c} |2_s, 2_i, c_s, c_i\rangle \\ & + m_{3,a} |3_s, 3_i, a_s, a_i\rangle + m_{3,b} |3_s, 3_i, b_s, b_i\rangle + m_{3,c} |3_s, 3_i, c_s, c_i\rangle, \end{aligned} \quad (6.4.1)$$

where  $m_{t,f} = |m_{t,f}|e^{i\phi_{t,f}}$  are complex numbers with amplitude  $|m_{t,f}|$  and phase  $\phi_{t,f}$ . The

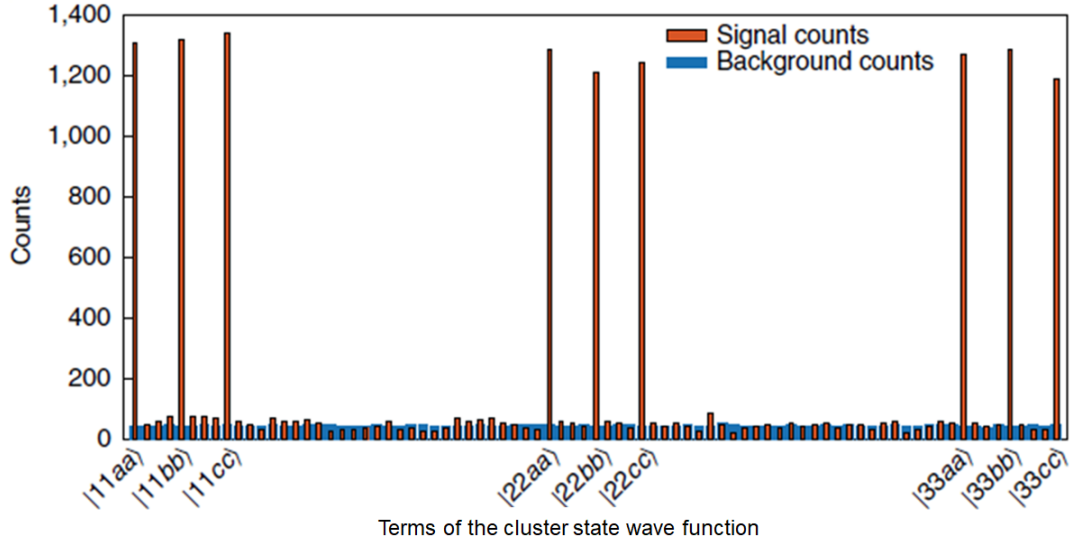


**Figure 6.6** – Experimental demonstration of cluster state generation. Measured photon projections on the 81 diagonal elements of the cluster state density matrix  $|\Psi_C\rangle\langle\Psi_C|$ , the representation of which is reported at the top right of Figure 6.3. [7]

subscripts  $t = 1, 2, 3$  and  $f = a, b, c$  denote the time and frequency modes, respectively. For the normalization criterion, the coefficients must obey the condition  $\sum_{t,f} |m_{t,f}|^2 = 1$ .

The amplitudes  $|m_{t,f}|$  were determined by performing  $3^4 = 81$  coincidence measurements between all possible combinations of temporal and frequency modes. The result is reported in Figure 6.6, which shows the measured photon projections on the 81 diagonal elements (i.e., signal counts, which are marked in red in Figure 6.6) of the density matrix  $\rho_C$  [7]. It can be seen that the diagonal elements are the only non-vanishing terms of the measured wave function, as it is expected from the theory (see Eq. (6.1.3)). The background counts (marked in blue in Figure 6.6) were determined by considering the ratio between the signal-idler coherence function  $g_{s,i}^{(2)}$  and the cross-correlation level at larger pulse separations (but not at zero time delay).

The phases  $\phi_{t,f}$  were determined via quantum interference measurements, which means by performing projections on time- and frequency-bin bases and then by measuring the remaining parties in different superpositions. This resulted in nine different patterns (see Figure 6.7).

For time-bin quantum interference (measured by selecting two temporal modes), projections on the frequency basis  $\{|a_s, a_i\rangle, |b_s, b_i\rangle, |c_s, c_i\rangle\}$  were performed through optical filtering. Then, a two-arm interferometer was used for simultaneous projections on time-

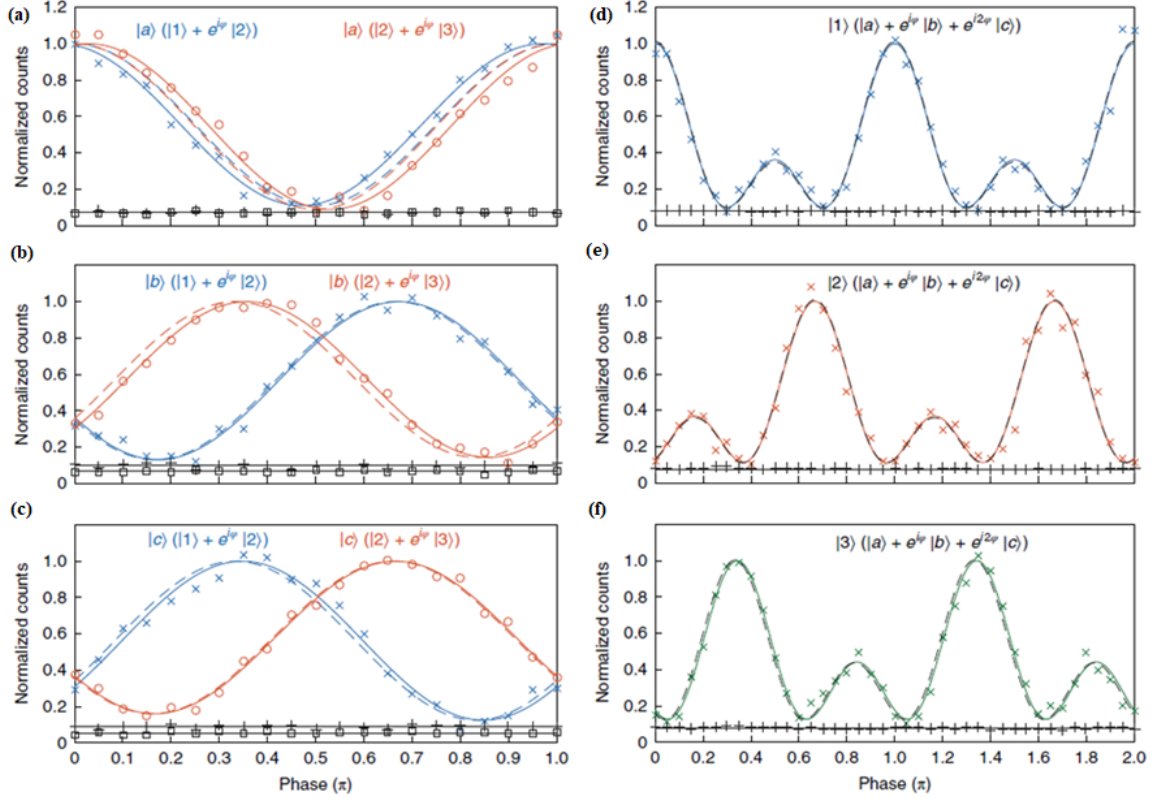


**Figure 6.7** – Quantum interference measurements for high-dimensional one-way computation operations. (a–c) The time-bin quantum interference, measured by selecting two temporal modes, results in different phase shifts after projecting the cluster states on the frequency modes  $\{|a_s, a_i\rangle, |b_s, b_i\rangle, |c_s, c_i\rangle\}$ . (d–f) Likewise, the frequency-bin quantum interference, measured by selecting three frequency modes, results in different phase shifts after projecting the cluster state on the temporal modes  $\{|1_s, 1_i\rangle, |2_s, 2_i\rangle, |3_s, 3_i\rangle\}$ . The quantum interferences follow the expected functions for the ideal, orthogonal two-partite states (dashed line: theory, solid line: fit). The measured phase values, together with the visibility (see Table 6.1), confirm the generation of orthogonal entangled qudit states through measurement-based operations. [7]

bin superpositions, that is  $|1\rangle + e^{i\varphi}|2\rangle$  and  $|2\rangle + e^{i\varphi}|3\rangle$  per photon, which resulted into different phase shifts (i.e. the relative position of the maximum with respect to the zero phase). The relative phase offset between the quantum interference measurements could be finally used to extract the relative phases between the coefficients of the wave function.

For frequency-bin quantum interference (measured by selecting three spectral modes), projections on the time-basis  $\{|1_s, 1_i\rangle, |2_s, 2_i\rangle, |3_s, 3_i\rangle\}$  were performed through temporal gating (in the detection). The frequency-bin projections were thus performed by first adding spectral phases and then by mixing the three frequency components via electro-optic modulation. The spectral phase was adjusted such that projections of the form

$|a\rangle + e^{i\varphi} |b\rangle + e^{i2\varphi} |c\rangle$  could be accomplished.

Finally, a fit between the predicted functions and the measured interference patterns was performed such that the individual phases of the wave function could be extracted. These, together with their estimated (Gaussian) error, are listed in Table 6.1 [7].

We thus confirmed the generation of the following bi-partite states:

$$\begin{aligned}
|\psi_{a,a}\rangle &= 0.58 |1_s, 1_i\rangle + 0.577e^{i0.06\pi} |2_s, 2_i\rangle + 0.574e^{-i0.06\pi} |3_s, 3_i\rangle \\
|\psi_{b,b}\rangle &= 0.588 |1_s, 1_i\rangle + 0.563e^{i0.65\pi} |2_s, 2_i\rangle + 0.581e^{-i0.72\pi} |3_s, 3_i\rangle \\
|\psi_{c,c}\rangle &= 0.596 |1_s, 1_i\rangle + 0.574e^{-i0.67\pi} |2_s, 2_i\rangle + 0.562e^{i0.69\pi} |3_s, 3_i\rangle \\
|\psi_{1,1}\rangle &= 0.574 |a_s, a_i\rangle + 0.577e^{i0.087\pi} |b_s, b_i\rangle + 0.581e^{i0.01\pi} |c_s, c_i\rangle \\
|\psi_{2,2}\rangle &= 0.586 |a_s, a_i\rangle + 0.569e^{i0.594\pi} |b_s, b_i\rangle + 0.576e^{-i0.667\pi} |c_s, c_i\rangle \\
|\psi_{3,3}\rangle &= 0.582 |a_s, a_i\rangle + 0.586e^{-i0.638\pi} |b_s, b_i\rangle + 0.564e^{i0.628\pi} |c_s, c_i\rangle .
\end{aligned} \tag{6.4.2}$$

In order to validate the orthogonality of these measured wave functions, we calculated the modulus squares of their scalar products, which resulted in:

$$\begin{aligned}
|\langle\psi_{a,a}|\psi_{b,b}\rangle|^2 &= 0.009 \pm 0.02 \approx 0 \\
|\langle\psi_{a,a}|\psi_{c,c}\rangle|^2 &= 0.011 \pm 0.02 \approx 0 \\
|\langle\psi_{b,b}|\psi_{c,c}\rangle|^2 &= 0.009 \pm 0.02 \approx 0 \\
|\langle\psi_{1,1}|\psi_{2,2}\rangle|^2 &= 0.027 \pm 0.02 \approx 0 \\
|\langle\psi_{1,1}|\psi_{3,3}\rangle|^2 &= 0.002 \pm 0.02 \approx 0 \\
|\langle\psi_{2,2}|\psi_{3,3}\rangle|^2 &= 0.012 \pm 0.02 \approx 0.
\end{aligned} \tag{6.4.3}$$

The fact that the obtained values approach zero (within the measurement uncertainties) confirms the orthogonality of the resulting two-partite states [7].

Finally, we extracted the visibility from each quantum interference pattern. From the values listed in Table 6.1, it can be seen that the raw (i.e. without background subtraction) visibilities violate their respective Bell inequalities (see subsection 2.3.1). This confirmed that the two-partite states obtained from projections were generated in Bell-type states.

The results reported in Eq. (6.4.2), imply an important conclusion; the bipartite states

obtained from projections in the frequency domain were generated in the form

$$\begin{aligned}
|\psi_{a,a}\rangle &\approx 1/\sqrt{3}(|1,1\rangle + |2,2\rangle + |3,3\rangle), \\
|\psi_{b,b}\rangle &\approx 1/\sqrt{3}(|1,1\rangle + e^{i2\pi/3}|2,2\rangle + e^{-i2\pi/3}|3,3\rangle), \\
|\psi_{c,c}\rangle &\approx 1/\sqrt{3}(|1,1\rangle + e^{-i2\pi/3}|2,2\rangle + e^{i2\pi/3}|3,3\rangle).
\end{aligned}
\tag{6.4.4}$$

Similarly, the bipartite states obtained from projections in the time domain resulted in the expressions

$$\begin{aligned}
|\psi_{1,1}\rangle &\approx 1/\sqrt{3}(|a,a\rangle + |b,b\rangle + |c,c\rangle), \\
|\psi_{2,2}\rangle &\approx 1/\sqrt{3}(|a,a\rangle + e^{i2\pi/3}|b,b\rangle + e^{-i2\pi/3}|c,c\rangle), \\
|\psi_{3,3}\rangle &\approx 1/\sqrt{3}(|a,a\rangle + e^{-i2\pi/3}|b,b\rangle + e^{i2\pi/3}|c,c\rangle).
\end{aligned}
\tag{6.4.5}$$

In particular, the two-partite quantum states of Eqs. (6.4.4) and (6.4.5) are maximally entangled in time and frequency, respectively. A comparison between the amplitude and phases experimentally extracted to obtain Eq. (6.4.2) and the ideal ones reported in Eqs. (6.4.4) and (6.4.5) shows that these are almost comparable. This further demonstrate that the two-partite qutrit states created via two-qutrit time and frequency projections are maximally entangled. This agrees with the working principle of one-way quantum computing described throughout this thesis.

This results further leads us to the conclusion that the hyper-entangled based cluster state realized here can be used for measurement-based quantum computing operations. More precisely, such a use is possible only because the hyper-entanglement of the cluster state (after the controlled-phase gate) is genuine and not bi-separable (as it was before its transformation). No one-way quantum computing is reachable indeed through a separable time- and frequency- hyper-entangled state, as two-party projections in the time domain do not generate two-partite frequency-entanglement and vice versa. This is due to the lack of quantum correlation between time and frequency entanglement. From an experimental perspective, this means that the visibilities extracted from the quantum interference patterns do not violate the Bell inequality. In general, a hyper-entangled wave function can be used to perform one-way quantum computing, provided that there is entanglement not only between the same degree of freedom, but also between different degrees of freedom. In other words, a condition of genuine multipartite entanglement between all the physical observables is needed to perform one-way quantum computing, as in a cluster state.

The proof-of-principle high-dimensional one-way quantum processing which we demonstrated in this research work can offer promising routes towards implementing computing algorithms by means of cluster states. In principle, performing meaningful algorithms may require to increase the number of parties, which is however a significant challenge for all known photonic platforms. This is because increasing the number of particles entails several disadvantages. For example, multi-photon states that are generated by multiple spontaneous parametric processes are hampered by the fact that the state purity decreases as the number of photons increases [96]. Moreover, quantum systems suffer significant reduction in their coherent time or detection rate when the number of particles becomes larger (see subsection 2.5.2). This limits the number of physical photons much below the number of parties that is required for meaningful quantum computation tasks. On the other hand, the use of a few photons increases both detection rate and coherence time, at the same time reducing significantly scale and complexity of the optical platforms, while increasing, in parallel, their robustness towards incoherent noise. In light of this, realizing large cluster states with a low number of photons can be crucial in order to reach powerful computation tasks. This can be specifically obtained by recurring to high-dimensional few-photon hyper-entangled cluster states.

The result presented here, which exploits hyper-entanglement in higher dimensions, can definitely provide a route towards this purpose. This further leverages on the recent demonstration that multiple photons can also carry hyper-entanglement [156]. The Effective Quantum Resource Rate (EQRR) can definitely benefit from the use of few-photon hyper-entangled cluster states, especially compared to multi-photon two-level cluster states. The largest qubit cluster states that have been realized thus far consist of six [144] and eight [146] photons, having Hilbert space sizes of  $\mathcal{H}_{6,2} = 2^6 = 64$  and  $\mathcal{H}_{8,2} = 2^8 = 256$ , respectively. Such states are characterized by a detection rate (DR) of  $DR_{6,2} = 12$  mHz and  $DR_{8,2} = 0.89$  mHz. This results in an effective quantum resource rate ( $EQRR_{\mathcal{H}} = \mathcal{H} \cdot DR$ ) of  $EQRR_{64} = 0.768$  Hz and  $EQRR_{256} = 0.228$  Hz, respectively. Although impressive for current technology, these values are still moderate, mainly limited by the use of multiple photons (six and eight, specifically).

Let us now consider the novel cluster state presented in this thesis, which consists of four qutrits, yet two physical photons, and reach a Hilbert space size of  $\mathcal{H}_{4,3} = 3^4 = 81$ . This is the same as the Hilbert space size of 6.34 qubits, according to the conversion from

the number of qudits to the number of qubits given by

$$\text{number of qubits} = \log_2 d^{(\text{number of qudits})}. \quad (6.4.6)$$

With such a Hilbert space size we could achieve a  $\text{DR}_{4,3} = 1$  Hz, which already resulted in an  $\text{EQRR}_{81} = 81$  Hz. This value is much higher compared to those related to six- and eight-photon qubits, since it relies on the use of just two physical particles.

Finally, in contrast with multi-photon qubits, hyper-entangled few-qudit states can allow for deterministic operations. In these systems, the computational flow could be achieved in such a way that the hyper-entangled parties are measured simultaneously, while the feed-forward (see introduction of chapter 3) is implemented between the different photons. As an example, let us consider a six-photon cluster state that is hyper-entangled in four degrees of freedom, each of them being in a superposition of 16 levels. This state has a Hilbert space size of  $\mathcal{H}_{24,16} = 16^{24}$ , which is the same as the Hilbert space size of a 96-qubit system (i.e.  $\mathcal{H}_{96,2} = 2^{96}$ ). In that case, the computational flow would involve the two-dimensional lattice which is depicted in Figure 6.8 [7]. Some of the parties are carried by the photons, while the others by the hyper-entangled degrees of freedom. As long as the degrees of freedom belong to the same photon, they can be measured simultaneously, while feed-forward can be implemented between adjacent photons.

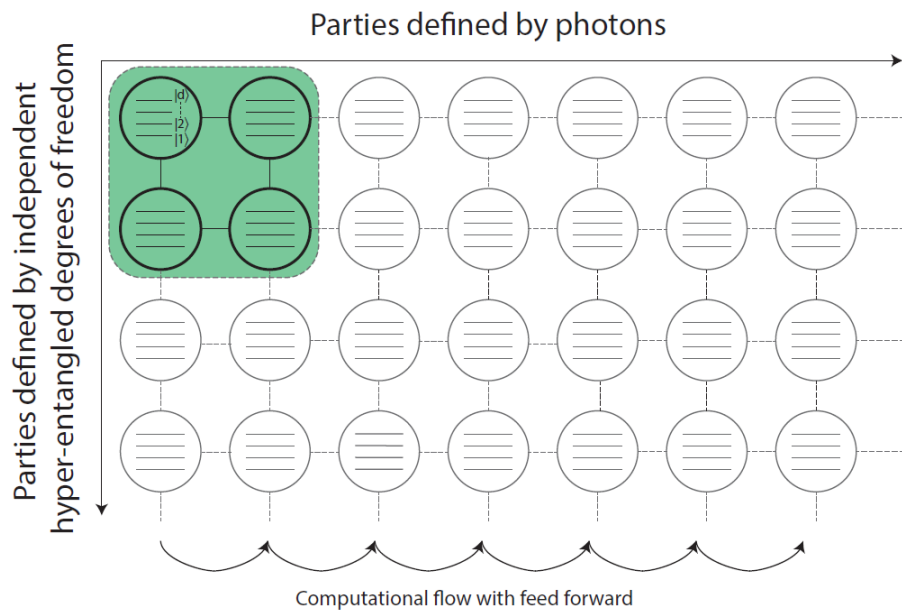


**Figure 6.8** – One-way quantum computing implementation on  $d$ -level hyper-entangled cluster states. For the cluster state represented in a two-dimensional lattice, some of the parties are carried by photons, while the others by the hyper-entanglement between the photon degrees of freedom. Each party of the array is in a  $d$ -level superposition. The computational flow goes from left to right, and feed-forward is implemented between adjacent photon detections. The green shaded area represents the experimentally achieved four-partite compact cluster state. In a next step, the number of hyper-entangled parties, the number of photons, as well as the dimensionality of the superposition, need to be increased in order to reach higher computational performances. [7]

# Conclusions

In this thesis, we have focused on the theoretical investigation of the entanglement phenomenon as well as on complex entangled quantum states, with specific attention to photons.

This investigation resulted in the first ever experimental realization of high-dimensional frequency-entangled photon pairs on a photonic chip. We could reach a dimensionality of up to  $d = 10$  per single photon, while we could coherently manipulate the generated photon states up to  $d = 4$ . The quantum state dimensionality was validated here through the Schmidt mode decomposition by evaluating the Schmidt number of the generated frequency modes. The two-photon state entanglement was characterized instead by measuring quantum interference and quantum state tomography in the case of  $d = 2, 3$ , and  $4$ . From each quantum interference pattern, we extracted the respective visibility that was then used for Bell's inequality violation. Since all the visibilities exceeded their respective threshold imposed by local realism, we could confirm that the demonstrated photon pairs were generated in a Bell state exhibiting nonlocal correlations. From quantum state tomography, we reconstructed the density matrix of each generated quantum state. We then extracted the respective fidelity, which provides information about the quality of a measured quantum system. All the fidelities largely exceeded the value of 50% (i.e. the threshold value), thus validating a good agreement between the realized two-photon states and the ideal maximally entangled Bell states.

The realized frequency-entangled states provided the basis for investigating more complex entangled systems. Our motivation relied on the fact that, despite the crucial importance of entanglement, a complete characterization of this phenomenon is still an open issue, especially when the number of parties as well as the single-party dimensionality increase. In this case, making use of full quantum state tomography for quantum state and entanglement characterization is neither reasonable or feasible from a theoretical nor

from an experimental point of view, due to the several and complex measurements that are required for determining it. In order to address the challenge of a complete entanglement characterization, we developed a multipartite  $d$ -level entanglement witness that is capable of detecting the presence of any arbitrarily complex pure quantum state, as well as its eventual entanglement. A main goal in the derivation of this operator was to make it as feasible as possible to measure in practice, which is significantly in contrast with established theoretically optimal witness operators. We developed a general approach allowing us to construct experimentally optimal entanglement witnesses that provide a good trade-off between (white) noise tolerance and experimental complexity. The detection of the here derived witnesses demands indeed measurements that are reduced in number and complexity, while still having a good noise robustness. We used this approach to derive a witness capable of detecting the genuine multipartite entanglement of  $d$ -level cluster states. To this end, we made use of high dimensional stabilizers that, since formed by the generalized Pauli matrices, can be measured by means of single-qudit projections, thus resulting relatively easy to measure in practice. We further showed how to customize a witness towards experimental restrictions by considering the explicit example of a four-partite three-level optical cluster state. It is always possible to measure a witness by making use of just a specific set of stabilizers, which are chosen according to the measurement capabilities. Finally, we showed that it is possible to construct a witness by making use of partial operators instead of stabilizers. It can happen indeed that stabilizers cannot be measured, since the available measurement settings allow us to perform projections on a number of levels that is lower with respect to the state dimensionality. We also exploited the novel witness to test the robustness of cluster states towards white noise. We demonstrated that the noise robustness increases as the single-state dimensionality  $d$  increases, while decreasing when the number of parties increases. We finally found that different experimental restrictions lead to different optimal witnesses as well as to different noise sensitivities for the same given quantum state.

We have demonstrated the first ever realization of a four-partite three-level optical cluster state. To this end, we made use of two photons and exploited the concept of hyper-entanglement, for the first time ever in both the time and frequency domains. The starting point of this realization was a two-photon product state that was simultaneous entangled in time and frequency. We then converted such a state into the targeted

cluster state through a novel controlled phase gate providing the access to each state term. This gate relied on a frequency-to-time mapping, where each frequency mode was temporally dispersed in different time slots, as well as on a phase modulator that was used to change the phase to specific frequency modes. We validated the genuine four-partite entanglement of the demonstrated cluster state by measuring a negative expectation value of the witness operator developed here, given by  $-0.28 \pm 0.04$ . This witness was used to test the robustness of the measured cluster state to incoherent amplitude and phase noise. We found that up to 37.5 % of white noise can be tolerated, in contrast with 33% of noise tolerated by an ideal four-qubit cluster state. Finally, we demonstrated proof-of-concept high-dimensional one-way quantum processing. We validated that projecting any qutrit pair in the time-bin basis resulted in orthogonal two-partite states that were entangled in frequency. Similarly, projecting in the frequency-bin basis led to orthogonal two-partite states entangled in time. We demonstrated the orthogonality as well as the entanglement of the two-partite states via quantum interference measurements, from which we extracted phases and amplitudes of the resulting wave functions, as well as the associated visibility. We found that all the measured visibilities violated the respective Bell inequality.

The entanglement witness demonstrated in this thesis was specifically designed for pure quantum states, i.e. those which do not interact with the environment. We could apply then such a witness to demonstrate the genuine multipartite entanglement of optical cluster states since photons can be described as pure states. Most of the results and conclusions that have been achieved in this theoretical work are based on the assumption that the density matrix is in a pure quantum state. Our method can however be judiciously modified such that it relies on the assumption that the underlying physical quantum system is in a mixed state.

Examples of mixed states are, in general, solid-state platforms, such as trapped ions, cold atoms, and superconducting electrons. In contrast to photons, solid-state systems do interact with the environment. For this reason, they are labeled as ‘open systems’. This interaction can also induce dissipation, decoherence (i.e. a loss of a definite phase relation between the quantum states of a system), and can even entangle the quantum system with the environment. The interaction thus introduces a dynamic entanglement, which means that the entanglement may undergo evolution. An evolving entanglement can have several applications in many fields, such as quantum-state engineering, as well

as quantum computing and simulation. A complete knowledge about the evolution of entanglement as well as of the quantum system is thus necessary in order to exploit this phenomenon. Common approaches towards this aim are mainly based on entanglement monotones, which however require quantum state tomography techniques that are not feasible either in the theory or in the practice. As a consequence, a complete entanglement characterization in open systems is still an open issue, especially in the case of multipartite and/or multilevel systems. Moreover, determining the amount of entanglement of an open quantum system does not provide enough knowledge about its evolution. For example, information is still missing about state structure and phase, as well as about the type of entanglement, which are of extreme importance in evolving systems.

On the contrary, a witness operator provides information about the evolution of both the quantum state and of its eventual entanglement. An entanglement witness that is capable of detecting the presence as well as the entanglement of any arbitrarily complex mixed state can thus address the issue of entanglement characterization in interacting open systems. From an experimental perspective, it is necessary that such a witness can accomplish this task in an affordable manner and that this can be further adapted to measurement conditions and settings. The theoretical approach that we presented in this thesis, under judicious modifications, can pave the way toward this direction. In this sense, our method is of significant importance for both fundamental physics and for applications of entangled open systems. Deriving an entanglement witness for open (mixed) quantum systems is one of the main research lines to be pursued after the PhD studies. In line with the theoretical, yet experimentally-oriented, work described in this thesis, the specific research plan here is to develop and lead the theory to formulate a ‘mixed-state’ entanglement witness in such a way that this can be measured in an experimentally feasible manner. Deriving such a witness is indeed a crucial step towards realizing experiments involving open quantum systems in which the entanglement evolves and to investigate as well as understand how the entanglement changes.

We have also presented here experimental results that can contribute to pave the way to exploit quantum optics for the development of photon-based technologies, as well as for their real-world applications. In order to make this possible, the first step is to reduce the scale and costs of the used devices as much as possible. Our work can contribute to this direction, as the demonstrated photons have been generated by

using an integrated platform and have been manipulated through fiber-based components that are compatible with off-the-shelf telecommunications infrastructures. Finally, the experimental results demonstrated here still represent proof-of-concept demonstrations. As a future research direction, our goal is to consider practical and near-term applications of the results presented here, specifically in the field of quantum communications. In this sense, we aim to explore quantum key distribution, quantum repeaters, and quantum teleportation.

# Conclusions

Dans cette thèse, nous nous sommes concentrés sur l'investigation théorique du phénomène d'enchevêtrement ainsi que de certains états complexes enchevêtrés, en focalisant notre attention sur le comportement des photons.

Cette étude a conduit à la première réalisation expérimentale d'une plate-forme optique intégrée (on-chip) de paires de photons multidimensionnels enchevêtrés en fréquence. Nous avons pu expérimentalement atteindre une dimension  $d = 10$  par photon, tandis que nous avons pu manipuler de manière cohérente les photons générés jusqu'à la dimension  $d = 4$ . Pour démontrer la dimension atteinte par chaque photon, nous avons utilisé la décomposition en modes de Schmidt, afin de déterminer le nombre de Schmidt de modes de fréquence. L'enchevêtrement de deux photons a plutôt été caractérisé par la mesure de l'interférence et la tomographie quantiques dans le cas de  $d = 2, 3$  et  $4$ . Ensuite, nous avons extrait de chacune des trois figures d'interférence la visibilité respective, qui a été utilisée par la suite pour vérifier que les états enchevêtrés générés violaient les inégalités de Bell dans les cas  $d = 2, 3$  et  $4$ , respectivement. Comme toutes les visibilités dépassaient leur seuil respectif imposé par le réalisme local, nous avons pu confirmer que les paires de photons ont été générées dans un état de Bell qui présente des corrélations non locales. Enfin, par tomographie quantique, nous avons reconstruit la matrice de densité des états générés aussi dans les cas  $d = 2, 3$  et  $4$ . Pour chaque matrice de densité, nous avons extrait la fidélité respective, qui sert à déterminer la qualité d'un état quantique mesuré expérimentalement et combien il se rapproche de l'état idéal. Toutes les fidélités dépassaient largement la valeur de 50% (c'est-à-dire la valeur de seuil), valident ainsi un bon accord entre les états à deux photons réalisés et les états idéaux de Bell (qui ont un enchevêtrement maximal).

La réalisation des états enchevêtrés en fréquence susmentionnés a fourni la base pour étudier des systèmes enchevêtrés plus complexes. La raison principale pour laquelle nous

avons entrepris cette recherche est , bien que l’enchèvement soit d’une importance fondamentale, une description complète de ce phénomène reste encore une problématique ouverte, surtout dans le cas où le nombre de parties du système et / ou la dimension (c’est-à-dire le nombre de niveaux quantiques) par partie augmente. Dans ce cas, l’utilisation de la tomographie pour caractériser un état quantique et son enchevêtrement n’est pas raisonnable ou faisable, ni théoriquement ni expérimentalement, en raison des nombreuses et complexes mesures nécessaires pour la tomographie quantique. Afin de résoudre le problème de la caractérisation complète de l’enchèvement, nous avons développé un témoin d’enchèvement (entanglement witness) multipartite ayant  $d$  niveaux capable d’identifier la présence de tout état quantique pur et arbitrairement complexe, ainsi que son éventuel enchevêtrement. Un objectif principal que nous nous sommes fixé pour obtenir cet opérateur était de rendre sa mesure aussi simple que possible d’un point de vue expérimental, en contraste avec d’autres witnesses de l’enchèvement théoriquement optimaux et déjà connus dans la littérature. Plus précisément, nous avons développé une approche théorique qui permet de construire des témoins d’enchèvement optimaux du point de vue expérimental et qui offrent en même temps un bon compromis entre la robustesse au bruit expérimental (blanc) et la complexité instrumentale requise pour les mesurer. La détermination expérimentale du witness dérivé nécessite des mesures réduites en nombre et en complexité, tout en étant assez résistante au bruit. En utilisant cette approche, nous avons dérivé un témoin capable de détecter le véritable enchevêtrement multipartite des états cluster à  $d$  niveaux quantiques (qudits). À cette fin, nous avons utilisé des stabilisateurs multidimensionnels qui, formés par les matrices de Pauli généralisées, peuvent être mesurés par des projections sur les qudits individuels, relativement simples à mesurer expérimentalement. En outre, nous avons montré comment adapter le witness aux restrictions expérimentales en tenant compte de l’exemple spécifique d’un cluster à trois niveaux quantiques (qutrit) et à quatre parties (quadripartite). Nous avons également montré qu’il est toujours possible de mesurer un witness en utilisant uniquement un ensemble spécifique de stabilisateurs, choisis en fonction des capacités avec lesquelles ils peuvent être mesurés en laboratoire. Ainsi, nous avons montré qu’il est possible de construire un témoin en utilisant des opérateurs partiels (ou de trace) au lieu des stabilisateurs. En effet, il se peut que les stabilisateurs ne puissent pas être mesurés, car les instruments disponibles en laboratoire permettent d’effectuer des projections seulement

sur un nombre de niveaux inférieur à celui du système quantique analysé. Enfin, nous avons utilisé le nouveau témoin d’entrelacement dérivé ici pour tester la résistance des états cluster au bruit blanc, en démontrant que ce dernier augmente avec la dimension de chaque partie et qu’il diminue avec l’augmentation du nombre de parties. Nous avons finalement constaté que, pour le même état quantique, différentes restrictions expérimentales conduisent à différents témoins optimaux ainsi qu’à différentes sensibilités pour un même type de bruit.

Nous avons démontré la première réalisation d’un état cluster de photons quadripartite et à trois niveaux. Pour cela, nous avons utilisé deux photons et exploité le concept d’hyper-entrelacement pour la première fois en temps et en fréquence. Le point de départ de cette réalisation était un état de produit à deux photons simultanément entrelacés en temps et en fréquence. Nous avons ensuite converti cet état en l’état de cluster préfixé à travers une nouvelle porte à phase contrôlée capable d’accéder à chaque terme de l’état en changeant sa phase. Le principe de fonctionnement de cette porte compte sur un mapping fréquence-temps (effectuée par un Bragg Rating array réalisé en fibre), où chaque mode spectral est temporellement réparti dans différentes tranches de temps, ainsi que sur un modulateur électro-optique utilisé pour changer la phase de modes spectraux spécifiques. Nous avons validé le véritable entrelacement quadripartite de l’état cluster démontré ici en mesurant une valeur d’attente négative de l’opérateur witness que nous avons développé et qui a abouti à une valeur de  $-0.28 \pm 0.04$ . Cet opérateur a été utilisé pour tester la robustesse de l’état cluster au bruit incohérent (ou blanc), d’amplitude et de phase. Nous avons constaté que jusqu’à 37.5% de bruit blanc peut être toléré, étant plus résistant qu’un état cluster quadripartite à deux niveaux (qubits), qui peut tolérer jusqu’à 33% de bruit blanc. Nous avons enfin démontré la preuve de concept d’un traitement quantique multidimensionnel unidirectionnel (« one-way »). Nous avons confirmé que projeter n’importe quelle paire de qubits de l’état cluster dans la base de temps conduit à la génération d’états orthogonaux bipartites qui ont un entrelacement maximal en fréquence. De même, projeter dans la base de fréquence conduit à la génération des états orthogonaux bipartites qui ont un entrelacement maximal en fonction du temps. Nous avons démontré l’orthogonalité et aussi l’entrelacement de ces états à travers des mesures d’interférence quantique, à partir desquelles nous avons extrait les phases et les amplitudes des fonctions d’onde résultantes ainsi que les visibilités respectives. Toutes les

visibilités mesurées violaient l'inégalité de Bell correspondante.

Le témoin d'enchèvement présenté dans cette thèse a été construit spécifiquement pour les états quantiques purs, c'est-à-dire des états qui n'interagissent pas avec l'environnement. La plupart des résultats et des conclusions obtenus dans cette recherche théorique sont basés sur l'hypothèse que la matrice de densité du système examinée est à un état pur. Cependant, la méthode que nous avons développée peut être modifiée de manière appropriée, de sorte qu'elle est basée sur l'hypothèse que la matrice de densité est à un état mixte.

Des exemples d'états mixtes sont, en général, les plates-formes à l'état solide, comme les ions piégés, les atomes froids et les électrons supraconducteurs, qui, contrairement aux photons, interagissent avec l'environnement ( pour cette raison ils sont définis comme « systèmes ouverts »). L'interaction avec l'environnement peut souvent introduire une dissipation, une décohérence (c.-à-d. la perte d'une relation de phase définie entre les états d'un système quantique) et aussi elle peut créer un enchèvement entre le système quantique et l'environnement. Dans ce cas, on parle de la « dynamique » d'enchèvement, ce qui signifie que l'enchèvement peut évoluer. Un enchèvement en évolution peut avoir de nombreuses applications dans différents domaines, par exemple l'ingénierie, les simulations et les calculs quantiques. Par conséquent, une connaissance complète de l'évolution de l'enchèvement dans les systèmes ouverts est nécessaire pour une application de ce phénomène. Les approches communément utilisés pour cet objectif sont principalement basées sur des « monotones d'enchèvement », qui nécessitent souvent des techniques de tomographie quantique qui ne sont pas fiables ou réalisables, ni en théorie ni en pratique. En conséquence, une caractérisation complète de l'enchèvement dans les systèmes ouverts reste une problématique ouverte, en particulier dans le cas de systèmes multipartites et/ou multidimensionnels. En outre, la seule quantification de l'enchèvement d'un système ouvert n'est pas suffisant pour connaître son évolution. Il ne fournit pas, par exemple, aucune information sur la structure et la phase de l'état, ou sur le type d'enchèvement, qui sont extrêmement importantes dans un système en évolution.

Au contraire, un opérateur witness fournit des informations sur l'évolution de l'état quantique et aussi sur son enchèvement. Un témoin d'enchèvement capable de détecter la présence et l'enchèvement de tout état mixte arbitrairement complexe peut

ainsi résoudre le problème de la caractérisation de l'enchevêtrement dans des systèmes ouverts et en interaction. D'un point de vue expérimental, il est essentiel que ce witness puisse accomplir cette tâche de manière abordable et que celle-ci puisse être aussi adaptée aux conditions et aux restrictions expérimentales. L'approche théorique présentée dans cette thèse, avec les modifications appropriées, peut ouvrir la voie vers cette direction. Notre méthode peut revêtir donc un rôle crucial tant pour la physique fondamentale que pour l'application des systèmes ouverts enchevêtrés. Dériver un témoin d'enchevêtrement pour des états quantiques mixtes est l'un des objectifs fondamentaux qui sera poursuivi après ce doctorat de recherche.

Dans cette thèse, nous avons présenté des résultats expérimentaux qui peuvent ouvrir la voie à l'optique quantique pour trouver une place dans le développement des technologies photoniques et aussi pour leurs applications concrètes. Afin de réussir à réaliser ces applications, la première étape est de réduire autant que possible la taille et les coûts des dispositifs utilisés. Notre travail peut contribuer à l'acquisition de cet objectif, car les photons démontrés ici ont été générés en utilisant une plate-forme intégrée et ils ont été manipulés avec des composants en fibre compatibles avec les infrastructures de télécommunication standard.

Enfin, les résultats expérimentaux démontrés dans ce manuscrit représentent encore une démonstration des principes. Comme future direction de nos recherches en ce sujet, notre objectif est de considérer les applications pratiques et à long terme des résultats présentés dans cette thèse, spécialement dans le domaine des communications quantiques. En particulier, nous visons la cryptographie quantique (distribution de clé quantique), aux répéteurs quantiques, et aussi à la téléportation quantique.

# Conclusioni

In questa tesi abbiamo rivolto la nostra attenzione ed esaminato da un punto di vista teorico il fenomeno dell'entanglement e specifici stati entangled complessi, concentrandoci in particolare sui fotoni.

Una tale indagine ha condotto alla prima realizzazione sperimentale su una piattaforma ottica integrata (“on-chip”) di coppie di fotoni multidimensionali che presentano entanglement in frequenza. Siamo stati in grado di generare fotoni con dimensione pari a  $d = 10$  per singolo fotone, mentre siamo riusciti a manipolare in maniera coerente i fotoni fino a una dimensione pari a  $d = 4$ . Al fine di dimostrare la dimensione raggiunta per singolo fotone, abbiamo fatto uso della decomposizione in modi di Schmidt, determinando il numero di Schmidt dei modi in frequenza. L'entanglement dei due fotoni è stato invece caratterizzato tramite misure di interferenza e tomografia quantistica per i casi  $d = 2, 3$  e  $4$ . Da ciascuna delle tre figure di interferenza abbiamo dunque estratto la rispettiva visibilità che è stata a sua volta utilizzata per verificare che gli stati entangled generati violassero le disuguaglianze di Bell nei casi  $d = 2, 3$ , e  $4$ , rispettivamente. Dal momento che tutte e tre le visibilità qui misurate superavano la rispettiva soglia imposta dal realismo locale, abbiamo potuto confermare che le coppie di fotoni sono state generate effettivamente in uno stato di Bell (esse presentano quindi correlazioni non locali). Infine, tramite tomografia quantistica, abbiamo ricostruito la matrice di densità degli stati generati, sempre nei casi  $d = 2, 3$  e  $4$ . Da ciascuna matrice densità abbiamo quindi estratto il rispettivo parametro di fedeltà, che serve a determinare la qualità di uno stato quantistico misurato sperimentalmente e quanto esso si approssima al corrispondente stato ideale. Tutti i parametri di fedeltà misurati hanno ampiamente superato il 50% (considerato il valore di soglia), convalidando così un buon accordo tra gli stati a due fotoni realizzati sperimentalmente e gli stati ideali di Bell (i quali hanno entanglement massimo).

La realizzazione degli stati entangled in frequenza di cui sopra ha fornito le basi per

indagare sistemi entangled più complessi. Il motivo principale per cui abbiamo intrapreso questa linea di ricerca è che, nonostante l'entanglement sia di fondamentale importanza, una completa caratterizzazione di tale fenomeno è tuttora una questione aperta, soprattutto nel caso in cui il numero delle parti e/o la dimensione per singola parte aumentino. In questo caso, usare la tomografia per caratterizzare uno stato quantistico o il suo entanglement non è ragionevole o fattibile né da un punto di vista teorico né da un punto di vista sperimentale, a causa delle parecchie e complesse misure di cui necessita la tomografia quantistica. Al fine di superare il problema di una completa caratterizzazione dell'entanglement, abbiamo qui sviluppato un entanglement witness multipartito e a  $d$  livelli in grado di individuare la presenza di qualsiasi stato quantistico puro e arbitrariamente complesso, così come di determinarne l'eventuale entanglement. Un obiettivo principale che ci siamo prefissati per derivare questo operatore era di rendere la sua misura il più semplice possibile da un punto di vista sperimentale, in forte contrasto con i witnesses noti in letteratura ed ottimali da un punto di vista teorico. Nello specifico, abbiamo sviluppato un approccio generale che permette di costruire entanglement witnesses che sono ottimali da un punto di vista sperimentale e che forniscono al tempo stesso un buon compromesso tra resistenza al rumore sperimentale (bianco) e complessità strumentale richiesta per la loro misura. Determinare sperimentalmente il witness qui derivato richiede infatti misure che sono ridotte sia in numero sia complessità, essendo al tempo stesso abbastanza resistente al rumore. Tramite questo approccio abbiamo derivato un witness capace di rilevare l'entanglement genuino multipartito di cluster states a  $d$  livelli. A tale scopo, ci siamo serviti di stabilizzatori multidimensionali che, essendo formati da matrici di Pauli generalizzate, possono essere misurati tramite proiezioni sui singoli qudits, risultando così relativamente semplici da misurare nella pratica. In più, abbiamo mostrato come adattare il witness rispetto alle restrizioni sperimentali, prendendo in considerazione l'esempio specifico di un cluster state quadripartito e a tre livelli. Abbiamo anche dimostrato che è sempre possibile misurare un witness utilizzando soltanto un set specifico di stabilizzatori, scelti appositamente in base alle capacità con cui si può misurarli in laboratorio. Infine, abbiamo mostrato che, nel caso di condizioni sperimentali che impediscano di misurare gli stabilizzatori, è possibile sostituire questi ultimi con gli operatori parziali (o di traccia). Per esempio, quando gli strumenti disponibili in laboratorio permettono di effettuare proiezioni solamente rispetto ad un numero di livelli

inferiore rispetto ai livelli del sistema quantistico in analisi, non è possibile misurare uno stabilizzatore, mentre un operatore parziale sì. Infine, abbiamo utilizzato il witness qui derivato per testare la resistenza dei cluster states al rumore bianco, dimostrando che essa aumenta al crescere della dimensione  $d$  di ciascuna parte, mentre si riduce all'aumentare del numero di parti. Abbiamo finalmente trovato che, dato uno stesso stato quantistico, restrizioni sperimentali differenti conducono a diversi witness ottimali e a diverse sensibilità allo stesso tipo di rumore.

Abbiamo dimostrato la prima realizzazione in assoluto di cluster state di fotoni quadripartito e a tre livelli (qutrit). A tal fine abbiamo fatto uso di due fotoni e del concetto di hyper-entanglement per la prima volta in tempo e frequenza. Il punto di partenza della suddetta realizzazione è stato uno stato-prodotto di due fotoni simultaneamente entangled in tempo e frequenza. Esso è stato quindi trasformato nello stato cluster prefissato attraverso un “controlled-phase gate” ivi sviluppato, in grado di accedere a ciascuna componente dello stato in input cambiandone la fase. Il gate è basato sulla mappatura frequenza-tempo (effettuata tramite un Bragg grating array in fibra), dove ciascun modo spettrale viene distribuito temporalmente in diverse slots temporali, e su un modulatore elettro-ottico usato per cambiare la fase di specifici modi spettrali. L'entanglement genuino quadripartito del cluster state è stato quindi confermato dal valore di aspettazione negativo dell'operatore witness sopra descritto, il quale è risultato pari a  $-0.28 \pm 0.04$ . Questo stesso operatore è stato poi usato per testare la resistenza del nostro stato cluster al rumore incoerente (bianco), al rumore di ampiezza e a quello di fase. Esso in particolare può sopportare fino al 37.5% di rumore bianco, dimostrandosi così più robusto rispetto a un cluster state ideale quadripartito e a due livelli (qubit), il quale può invece tollerare un rumore pari al 33%. Abbiamo infine dimostrato la prova di concetto di “one-way” quantum processing multidimensionale. Proiettando sulla base di misura dei tempi qualsiasi coppia di qutrit del cluster, si generano stati ortogonali bipartiti che presentano entanglement massimo in frequenza. Analogamente, proiettando sulla base delle frequenze, si generano stati ortogonali bipartiti che sono massimamente entangled in tempo. Sia l'ortogonalità sia l'entanglement sono stati quindi verificati tramite misure di interferenza quantistica, da cui abbiamo estratto nei rispettivi casi ampiezza e fase delle funzioni d'onda risultanti e le rispettive visibilità, che hanno tutte violato le corrispondenti disuguaglianze di Bell.

L'entanglement witness dimostrato in questa tesi è stato costruito specificamente per stati quantistici puri, cioè non interagenti con l'ambiente. La maggior parte dei risultati e delle conclusioni ottenuti in questo lavoro teorico si basa sul presupposto che la matrice densità del sistema in esame sia descritta da uno stato puro. Il metodo da noi sviluppato può tuttavia essere opportunamente modificato in modo tale che si basi sul presupposto che la matrice densità si trovi in uno stato misto.

Esempi di stati misti sono, in generale, piattaforme a stato solido, come ioni intrappolati, atomi freddi ed elettroni superconduttivi, che, contrariamente ai fotoni, interagiscono con l'ambiente (per questo vengono spesso definiti "sistemi aperti"). L'interazione con l'ambiente spesso introduce dissipazione, decoerenza (cioè perdita di un definito rapporto di fase tra i diversi stati di un sistema quantistico) e può creare un entanglement tra il sistema quantistico stesso e l'ambiente. Si parla in questo caso di "dinamica" dell'entanglement, nel senso che questo può essere soggetto ad evoluzione. Un entanglement "dinamico" trova applicazioni in diversi campi, quali simulazioni, computazioni e ingegneria quantistiche. Pertanto, una completa conoscenza di come si evolve l'entanglement in sistemi aperti si rivela necessaria per una sua piena applicazione. Gli approcci comunemente utilizzati a tale scopo si basano prevalentemente sulle cosiddette "entanglement monotones", mirate appunto a quantificare l'entanglement di un sistema. Questi approcci, però, richiedono di solito tecniche di tomografia quantistica che non sono fattibili sia teoricamente sia sperimentalmente. Di conseguenza, una completa caratterizzazione dell'entanglement in sistemi aperti è ancora una questione aperta, soprattutto nel caso di sistemi multipartiti e/o multidimensionali. Inoltre, la sola quantificazione dell'entanglement di un sistema aperto non è sufficiente per conoscerne l'evoluzione; per esempio, non fornisce alcuna informazione sulla struttura e sulla fase dello stato, o sul tipo di entanglement, che sono di estrema importanza nei sistemi in evoluzione.

Al contrario, un operatore witness fornisce informazioni sia sull'evoluzione dello stato quantistico sia sull'entanglement in esso presente. Un entanglement witness in grado di rilevare la presenza e l'entanglement di uno stato misto qualsivoglia complesso può dunque affrontare e risolvere il problema della caratterizzazione di entanglement in sistemi aperti e interagenti. Da un punto di vista sperimentale, è fondamentale che il witness permetta di svolgere questo compito in maniera fattibile e che possa essere a sua volta adattato alle condizioni e alle restrizioni sperimentali. Il metodo teorico presentato in questa tesi, sotto

opportune modifiche, può avviare la strada verso questo obiettivo. Il nostro metodo può quindi rivelarsi di grande importanza sia per la fisica fondamentale sia per l'applicazione dei sistemi entangled aperti. Derivare un entanglement witness per stati quantistici misti è una delle principali linee di ricerca da seguire dopo il dottorato di ricerca.

I risultati sperimentali che sono stati presentati in questa tesi possono contribuire ad inserire l'ottica quantistica nello sviluppo delle tecnologie fotoniche, così come alla loro applicazione nel "mondo reale". Per rendere tale applicazione possibile, il primo passo fondamentale è quello di ridurre il più possibile le dimensioni e i costi dei dispositivi usati dalle tecnologie fotoniche. Il nostro lavoro può contribuire verso questa direzione, dal momento che i fotoni qui dimostrati sono stati generati usando una piattaforma integrata e manipolati con componenti in fibra compatibili con le infrastrutture standard usate per nel campo delle telecomunicazioni.

Infine, i risultati sperimentali qui dimostrati rappresentano ancora delle prove di concetto. Come linea futura di ricerca, il nostro obiettivo è considerare applicazioni pratiche e a lungo termine dei risultati qui presentati, soprattutto nel campo delle telecomunicazioni quantistiche. In particolare, miriamo alla quantum key distribution, ai quantum repeaters e al teletrasporto quantistico.

# Appendix A

## Origin of the Bell inequality for qubits

The origin of the CHSH inequality, as well as of the threshold necessary for its violation, can be understood considering the square of the Bell operator [157]

$$B_{\text{CHSH}}^2 = 4\mathbb{I}_A \otimes \mathbb{I}_B - [A_1, A_2] \otimes [B_1, B_2], \quad (\text{A.0.1})$$

where  $\mathbb{I}_{A,B}$  is the identity operator relative to the measurement settings  $A_{1,2}$  and  $B_{1,2}$ , respectively.

The symbol  $[O_1, O_2]$  is the so-called commutator that, given two generic observables  $O_1$  and  $O_2$ , is defined as  $[O_1, O_2] = O_1 \cdot O_2 - O_2 \cdot O_1$ . Two scenarios may occur, either the commutator is zero, i.e.  $[O_1, O_2] = 0$ , or it is different from zero, i.e.  $[O_1, O_2] \neq 0$ . In the former case, the observables commute and are defined as ‘compatible’, while in the latter case these do not commute and are defined as ‘incompatible’. As a postulate of quantum mechanics, two observables  $O_1$  and  $O_2$  having the same set of eigenvalues and eigenstates, as well as acting on two independent Hilbert spaces, are compatible. Otherwise, the observables are incompatible.

According to local realism (*LR*), all observables commute (i.e.,  $[A_1, A_2] = [B_1, B_2] = 0$ ). From Eq. (A.0.1), the classical value of  $\langle B_{\text{CHSH}} \rangle$  thus results in

$$\langle B_{\text{CHSH}} \rangle_{LR} = \sqrt{\langle B_{\text{CHSH}}^2 \rangle} = \sqrt{4} = 2. \quad (\text{A.0.2})$$

On the other hand, quantum mechanics does predict the existence of non-commuting observables. Therefore, from Eq. (A.0.1), the maximum quantum value (*QM*) that  $\langle B_{\text{CHSH}} \rangle$

can reach is given by

$$\langle B_{\text{CHSH}} \rangle_{QM} = \sqrt{8} = 2\sqrt{2}. \quad (\text{A.0.3})$$

The result of Eq. (A.0.3) originates from the fact that 2 is the largest possible eigenvalue (in modulus) that any commutator of two Hermitian operators can reach. This value is specifically obtained from the commutation rules between the Pauli matrices and that are reported in section 1.7.

Finally, the square root of any operator  $O$  is related to its expectation value as

$$\langle O \rangle \leq \sqrt{\langle O^2 \rangle}. \quad (\text{A.0.4})$$

Combining Eq. (A.0.4) with Eq. (A.0.3), the CHSH inequality reported in Eq. (2.3.2) of section 2.3 can be obtained. The necessary and sufficient condition to violate the CHSH inequality is that the commutator between the observables  $A_{1,2}$  and  $B_{1,2}$  must be nonvanishing in all possible measurement bases (i.e.  $[A_1, A_2] \neq [B_1, B_2] \neq 0$ ) [52].

# Appendix B

## Origin of the Bell inequality for qudits

The configuration of the experimental setting needed to derive the Bell inequalities for high dimensional systems is similar as that described in section 2.3 and in Figure 2.1. The main difference is that now the measurement settings  $A_{1,2}$  and  $B_{1,2}$  can have  $d$  possible outcomes (i.e.  $0, 1, \dots, d-1$ ). We here follow the approach derived in [13] to derive the Bell inequalities for two-partite qudit systems.

A local hidden variable theory can be described by  $d^4$  probabilities  $c_{jklm}$  ( $j, k, l, m = 0, \dots, d-1$ ). These are the probabilities that Alice's local variable ( $jk$ ) specifies that the settings  $A_1$  and  $A_2$  give the outcomes  $j$  and  $k$ , respectively. Similarly,  $c_{jklm}$  include the probabilities that Bob's local variable ( $lm$ ) specifies that  $B_1$  and  $B_2$  results in the measurement outcome  $l$  and  $m$ , respectively.

The joint probabilities between the two settings are thus [13]

$$\begin{aligned} P(A_1 = j, B_1 = l) &= \sum_{km} c_{jklm} \\ P(A_1 = j, B_2 = m) &= \sum_{kl} c_{jklm} \\ P(A_2 = k, B_1 = l) &= \sum_{jm} c_{jklm} \\ P(A_2 = k, B_2 = m) &= \sum_{jl} c_{jklm}. \end{aligned} \tag{B.0.1}$$

Without loss of generality, let us consider the local variables such that  $A_1 = j$ ,  $A_2 = k$ ,

$B_1 = l, B_2 = m$ . This results in

$$\begin{aligned} r' &\equiv B_1 - A_1 = l - j, \\ s' &\equiv A_2 - B_1 = k - l, \\ t' &\equiv B_2 - A_2 = m - k, \\ u' &\equiv A_1 - B_2 = j - m. \end{aligned}$$

In a local hidden variable theory, while  $r', s',$  and  $t'$  can be freely chosen, the difference  $u'$  is strictly bound by the constraint

$$r' + s' + t' + u' = 0. \quad (\text{B.0.2})$$

In the approach derived in [13], this constraint plays a crucial role, since the Bell inequalities are written in such a way that their maximum value can be attained only if this constrain is defeated. The simplest Bell expression  $I$  thus reads

$$I \equiv P(A_1 = B_1) + P(B_1 = A_2 + 1) + P(A_2 = B_2) + P(B_2 = A_1), \quad (\text{B.0.3})$$

where  $P(A_a = B_b + k) \equiv \sum_{j=0}^{d-1} P(A_a = j, B_b = j + k \pmod{d})$  is the probability that the measurements  $A_a$  and  $B_b$  have the outcomes differing, modulo  $d$ , by  $k$ . While in local realism, due to the constraint of Eq. (B.0.2),  $I_{LR} \leq 3$ , nonlocal quantum correlations can attain  $I_{QM} = 4$ , since they can satisfy all four relations.

For a  $d$ -level system with  $d \geq 2$  the expression of Eq. (B.0.3) becomes [[13]

$$\begin{aligned} I_d \equiv \sum_{k=0}^{\lfloor d/2 \rfloor - 1} \left( 1 - \frac{2k}{d-1} \right) &\left\{ P(A_1 = B_1 + k) + P(B_1 = A_2 + k + 1) + P(A_2 = B_2 + k) \right. \\ &+ P(B_2 = A_1 + k) - [P(A_1 = B_1 - k - 1) + P(B_1 = A_2 - k) \\ &\left. + P(A_2 = B_2 - k - 1) + P(B_2 = A_1 - k - 1)] \right\}, \end{aligned} \quad (\text{B.0.4})$$

where  $\lfloor x \rfloor$  denotes the integer part. Independently of the dimensionality  $d$ , the maximum value that this expression can reach in the local realism is  $I_d^{max}(LR) = 2$ , while, for nonlocal quantum correlations, the maximal value is given by  $I_d^{max} = 4$ .

Let us consider now the specific case of a two-partite  $d$ -level maximally entangled state:

$$|\psi\rangle = \frac{1}{\sqrt{d}} \sum_{j=0}^{d-1} |j\rangle_A \otimes |j\rangle_B. \quad (\text{B.0.5})$$

The Bell expression for this state reads (for simplicity, the details about its derivation are omitted here, while they can be found in [13])

$$I_d(QM) \equiv \sum_{k=0}^{\lfloor d/2 \rfloor - 1} \left( 1 - \frac{2k}{d-1} \right) q_k - q_{-(k+1)}, \quad (\text{B.0.6})$$

where  $q_c = 1 / \{2d^3 \sin^2[\pi(c + 1/4)/d]\}$ . The coefficient  $c$  is an integer number satisfying the condition  $q_0 > q_{-1} > q_1 > q_{-2} > q_2 > \dots > q_{-\lfloor d/2 \rfloor} > q_{\lfloor d/2 \rfloor}$  [13]. It can be seen that, denoting by  $p$  the probability that the entangled state  $|\psi\rangle$  is affected by white noise (introduced in subsection 3.3.2 and subsection 5.2.1), the Bell expression  $I_d$  is certainly violated if

$$p > \frac{2}{I_d(QM)} = p_d^{\min}. \quad (\text{B.0.7})$$

Considering the specific examples of  $d = 2, 3, 4$  and  $d \rightarrow \infty$ , the noise sensitivity threshold  $p_d^{\min}$  results:

$$p_{d=2}^{\min} = \frac{1}{\sqrt{2}} \simeq 0.7071 \quad (\text{B.0.8a})$$

$$p_{d=3}^{\min} = \frac{6\sqrt{3} - 9}{2} \simeq 0.69615 \quad (\text{B.0.8b})$$

$$p_{d=4}^{\min} = \frac{3}{\sqrt{2} + \sqrt{10 - \sqrt{2}}} \simeq 0.69055 \quad (\text{B.0.8c})$$

$$p_{d \rightarrow \infty}^{\min} = \frac{\pi^2}{16 \times \textit{Catalan}} \simeq 0.67344, \quad (\text{B.0.8d})$$

where  $\textit{Catalan} \cong 0.9159$  is the Catalan constant [13].

# Appendix C

## Examples of GHZ states

$N = 3, d = 2$ . A three-partite qubit GHZ state, expressed in the computational basis  $\{|0\rangle, |1\rangle\}$ , is given by

$$|\text{GHZ}\rangle_{3,2} = \frac{1}{\sqrt{2}} (|0\rangle_1 |0\rangle_2 |0\rangle_3 + |1\rangle_1 |1\rangle_2 |1\rangle_3). \quad (\text{C.0.1})$$

It can be seen that tracing  $|\text{GHZ}\rangle_{3,2}$  over, e.g. qubit 1, results in the unentangled mixture  $\frac{1}{2}(|0_2 0_3\rangle\langle 0_2 0_3| + |1_2 1_3\rangle\langle 1_2 1_3|)$ .

$N = 4, d = 2$ . The wave function of a four-partite qubit GHZ state is

$$|\text{GHZ}\rangle_{4,2} = \frac{1}{\sqrt{2}} (|0\rangle_1 |0\rangle_2 |0\rangle_3 |0\rangle_4 + |1\rangle_1 |1\rangle_2 |1\rangle_3 |1\rangle_4). \quad (\text{C.0.2})$$

Tracing the state  $|\text{GHZ}\rangle_{4,2}$  over qubit 2, results in the mixed state  $\frac{1}{2}(|0_1 0_3 0_4\rangle\langle 0_1 0_3 0_4| + |1_1 1_3 1_4\rangle\langle 1_1 1_3 1_4|)$ , which is not entangled.

$N = 3, d = 3$ . A three-partite three-level GHZ state, expressed in the computational basis  $\{|0\rangle, |1\rangle, |2\rangle\}$  reads

$$|\text{GHZ}\rangle_{3,3} = \frac{1}{\sqrt{3}} (|0\rangle_1 |0\rangle_2 |0\rangle_3 + |1\rangle_1 |1\rangle_2 |1\rangle_3 + |2\rangle_1 |2\rangle_2 |2\rangle_3). \quad (\text{C.0.3})$$

In analogy with the qubit case, tracing the state  $|\text{GHZ}\rangle_{3,3}$  over, for example, qutrit 3, results in the unentangled mixture  $\frac{1}{2}(|0_1 0_2\rangle\langle 0_1 0_2| + |1_1 1_2\rangle\langle 1_1 1_2| + |2_1 2_2\rangle\langle 2_1 2_2|)$ .

$N = 4, d = 3$ . A four-partite qutrit GHZ state is given by

$$|\text{GHZ}\rangle_{4,3} = \frac{1}{\sqrt{2}} (|0\rangle_1 |0\rangle_2 |0\rangle_3 |0\rangle_4 + |1\rangle_1 |1\rangle_2 |1\rangle_3 |1\rangle_4 + |2\rangle_1 |2\rangle_2 |2\rangle_3 |2\rangle_4). \quad (\text{C.0.4})$$

Tracing the state  $|\text{GHZ}\rangle_{4,3}$  over qutrit 4, results in the unentangled mixed state  $\frac{1}{2} (|0_1 0_2 0_3\rangle \langle 0_1 0_2 0_3| + |1_1 1_2 1_3\rangle \langle 1_1 1_2 1_3| + |2_1 2_2 2_3\rangle \langle 2_1 2_2 2_3|)$ .

# Appendix D

## Quantum state tomography formalism

The wave function of a two-photon frequency-qubit entangled state results in  $|\psi\rangle = \frac{1}{\sqrt{2}}(|a_s, a_i\rangle + |b_s, b_i\rangle)$ , where  $a$  and  $b$  denotes the frequency modes of the signal ( $s$ ) and the idler ( $i$ ), see subsection 2.2.3. For such a state, QST requires at least  $2^4 = 16$  measurements. In order to use them to reconstruct the density matrix, it is opportune to convert the  $2 \times 2$  matrix  $\rho = |\psi\rangle\langle\psi|$  into a 16-dimensional column vector [8]. This can be obtained by using a set of 16 linearly independent  $4 \times 4$  matrices  $\{\Gamma_\nu\}$  having the properties

$$\text{Tr}(\Gamma_\nu \cdot \Gamma_\mu) = \delta_{\nu,\mu} \quad (\text{D.0.1})$$

and

$$A = \sum_{\nu=1}^{16} \Gamma_\nu \text{Tr}(\Gamma_\nu \cdot A) \quad \forall A. \quad (\text{D.0.2})$$

Here,  $A$  is an arbitrary  $4 \times 4$  matrix and  $\delta_{\nu,\mu}$  is the  $\delta$ -Kronecker defined such that  $\delta_{\nu,\mu} = 1$  for  $\nu = \mu$ , and 0 otherwise. It can be found that the set  $\{\Gamma_\nu\}$  is given by the Pauli matrices  $\sigma_i \otimes \sigma_j$  ( $i, j = 0, x, y, z$ ) [8]. Using these matrices,  $\rho$  can be written as

$$\rho = \sum_{\nu=1}^{16} \Gamma_\nu r_\nu, \quad (\text{D.0.3})$$

where  $r_\nu$  is the  $\nu$ -th element of a 16-element column vector, and is given by

$$r_\nu = \text{Tr}(\Gamma_\nu \cdot \rho). \quad (\text{D.0.4})$$

Let us represent the projection measurements in a matrix form as  $\mu_\nu = |\psi_\nu\rangle\langle\psi_\nu|$ . The average number of coincidence counts that is observed in a given experimental run is thus

defined as

$$n_\nu = \mathcal{N} \langle \psi_\nu | \rho | \psi_\nu \rangle, \quad (\text{D.0.5})$$

where  $\mathcal{N}$  is a constant depending on the experimental setup (for example, the efficiency of the detector). Replacing Eq. (D.0.3) into Eq. (D.0.5) leads to

$$n_\nu = \mathcal{N} \sum_{\mu=1}^{16} B_{\nu,\mu} r_\mu, \quad (\text{D.0.6})$$

where

$$B_{\nu,\mu} = \langle \psi_\nu | \Gamma_\mu | \psi_\nu \rangle. \quad (\text{D.0.7})$$

Providing that the matrix  $B_{\nu,\mu}$  is nonsingular (i.e. it is invertible), then Eq. (D.0.6) can be inverted to give

$$r_\nu = (\mathcal{N})^{-1} \sum_{\mu=1}^{16} (B^{-1})_{\nu,\mu} n_\mu. \quad (\text{D.0.8})$$

The density matrix finally results

$$\rho = (\mathcal{N})^{-1} \sum_{\mu=1}^{16} M_\nu n_\nu, \quad (\text{D.0.9})$$

with

$$M_\nu = \sum_{\mu=1}^{16} (B^{-1})_{\nu,\mu} \Gamma_\mu. \quad (\text{D.0.10})$$

Let us assume that the 16 frequency projections to implement for QST are those reported in Table D.1 [8, 108]. In this case, it can be seen that  $Tr(M_\nu) = 1$  for  $\nu = 1, 2, 3, 4$  and  $Tr(M_\nu) = 0$  for any other value of  $\nu$  [8]. Upon these conditions, the parameter  $\mathcal{N}$  results

$$\begin{aligned} \mathcal{N} &= \sum_{\nu=1}^4 n_\nu \\ &= \mathcal{N} \left( \langle a, a | \rho | a, a \rangle + \langle a, b | \rho | a, b \rangle \right. \\ &\quad \left. \langle b, a | \rho | b, a \rangle + \langle b, b | \rho | b, b \rangle \right). \end{aligned} \quad (\text{D.0.11})$$

The final formula for the tomographic reconstruction of the density matrix is thus

$$\rho = \left( \sum_{\nu=1}^{16} M_\nu n_\nu \right) / \left( \sum_{\nu=1}^4 n_\nu \right). \quad (\text{D.0.12})$$

$\nu$	Projection mode 1	Projection mode 2
1	$ a\rangle$	$ a\rangle$
2	$ a\rangle$	$ b\rangle$
3	$ b\rangle$	$ a\rangle$
4	$ b\rangle$	$ b\rangle$
5	$ b\rangle$	$ +\rangle$
6	$ a\rangle$	$ +\rangle$
7	$ +\rangle$	$ +\rangle$
8	$ L\rangle$	$ +\rangle$
9	$ L\rangle$	$ a\rangle$
10	$ L\rangle$	$ b\rangle$
11	$ L\rangle$	$ L\rangle$
12	$ a\rangle$	$ L\rangle$
13	$ b\rangle$	$ L\rangle$
14	$ +\rangle$	$ L\rangle$
15	$ +\rangle$	$ a\rangle$
16	$ +\rangle$	$ b\rangle$

**Table D.1** – Example of tomographic analysis for a quantum experiment. Each photon of the two-qubit state  $|\psi\rangle = \frac{1}{\sqrt{2}}(|a_s, a_i\rangle + |b_s, b_i\rangle)$  is projected into single as well as superposition of ( $2^4 = 16$ ) frequency modes. The number of coincidence counts (not reported in this table) measured through these projections provides a set of 16 data allowing for density matrix reconstruction. Here, the notation  $|+\rangle = (|a\rangle + |b\rangle)/\sqrt{2}$  and  $|L\rangle = (|a\rangle + i|b\rangle)/\sqrt{2}$  is used, with  $|a\rangle$  and  $|b\rangle$  denoting the single frequency modes. Adapted from [8, 108]

In chapter 4, we describe the experimental setting for frequency projections that have been used in [6] for high-dimensional quantum state tomography.

As discussed in section 2.6, the density matrix reconstructed through quantum state tomography typically does not comply with the requirements of being Hermitian and positive-definite, as necessary for a physically realistic density matrix [8]. This problem can be avoided experimentally by recurring to the maximum-likelihood estimation approach, a simple version of which has been proposed in [8]. In this appendix we report on the steps proposed by the cited reference. These steps are:

- (i) Generating a formula describing the physical density matrix that exhibits the properties of normalization, Hermiticity, and positivity. This matrix is a function of  $2^{2N}$  variables  $\{t_1, t_2, \dots, t_{2^{2N}}\}$  and is denoted as  $\rho_{\text{phys}}(t_1, t_2, \dots, t_{2^{2N}})$ . In the specific case of the two-qubit system considered in this appendix, the density matrix is a function of 16 variables, namely  $\{t_1, t_2, \dots, t_{16}\}$ , and it is denoted as  $\rho_{\text{phys}}(t_1, t_2, \dots, t_{16})$ .
- (ii) Introducing a ‘likelihood function’ that quantifies how good the density matrix  $\rho_{\text{phys}}(t_1, t_2, \dots, t_{16})$  is with respect to the measured data. Such a function depends on both the 16 real parameters  $t_\nu$  (for simplicity, we consider only the specific case of a two-qubit entangled state) and on the 16 experimental data  $n_\nu$ , which are exactly the 16 measured coincidence counts. The likelihood function is denoted as  $\mathcal{L}(t_1, t_2, \dots, t_{16}; n_1, n_2, \dots, n_{16})$ . Assuming that the noise associated to the coincidence counts has a Gaussian distribution, the probability of obtaining the 16 counts set  $\{n_1, n_2, \dots, n_{16}\}$  is

$$P(n_1, n_2, \dots, n_{16}) = \frac{1}{N_{\text{norm}}} \prod_{\nu=1}^{16} \exp\left[-\frac{(n_\nu - \bar{n}_\nu)^2}{2\sigma_\nu^2}\right], \quad (\text{D.0.13})$$

where  $\bar{n}_\nu = \mathcal{N}\langle\psi_\nu|\rho|\psi_\nu\rangle$  is the mean value for the coincidence count  $n_\nu$ ,  $\sigma_\nu$  is the associated standard deviation, and  $N_{\text{norm}}$  is the normalization constant. In the example considered here, the number of expected counts for the  $\nu$ -th measurement is

$$\bar{n}_\nu(t_1, t_2, \dots, t_{16}) = \mathcal{N}\langle\psi_\nu|\rho(t_1, t_2, \dots, t_{16})|\psi_\nu\rangle. \quad (\text{D.0.14})$$

Therefore, the probability (i.e., the likelihood) that the matrix  $\rho_{\text{phys}}(t_1, t_2, \dots, t_{16})$

can produce the measured coincidence counts  $\{n_1, n_2, \dots, n_{16}\}$  is given by

$$P(n_1, \dots, n_{16}) = \frac{1}{N_{\text{norm}}} \prod_{\nu=1}^{16} \exp \left[ -\frac{(\mathcal{N} \langle \psi_\nu | \rho_{\text{phys}}(t_1, \dots, t_{16}) | \psi_\nu \rangle - n_\nu)^2}{2\mathcal{N} \langle \psi_\nu | \rho_{\text{phys}}(t_1, \dots, t_{16}) | \psi_\nu \rangle} \right], \quad (\text{D.0.15})$$

where  $\mathcal{N} = \sum_{\nu=1}^4 n_\nu$ . By neglecting the dependence of the normalization constant on  $t_1, \dots, t_{16}$  (as allowed by the fact that  $N_{\text{norm}}$  only weakly affects the solution for the most likely state), it is better to find the maximum value of the logarithm of  $P(n_1, \dots, n_{16})$  in such a way to simplify the estimation of the best likelihood function. Therefore, the optimization process can be solved by finding the maximum of the function

$$\mathcal{L}(n_1, \dots, n_{16}) = \sum_{\nu=1}^{16} \frac{(\mathcal{N} \langle \psi_\nu | \rho_{\text{phys}}(t_1, \dots, t_{16}) | \psi_\nu \rangle - n_\nu)^2}{2\mathcal{N} \langle \psi_\nu | \rho_{\text{phys}}(t_1, \dots, t_{16}) | \psi_\nu \rangle}, \quad (\text{D.0.16})$$

which is the ‘likelihood’ function that is used for numerical optimization [8].

- (iii) By making use of numerical optimization techniques, finding the optimum set of variables  $\{t_1^{\text{opt}}, t_2^{\text{opt}}, \dots, t_{16}^{\text{opt}}\}$  for which the function  $\mathcal{L}(t_1, t_2, \dots, t_{16}; n_1, n_2, \dots, n_{16})$  has its maximal value. The best estimation of the density matrix is thus  $\rho(t_1^{\text{opt}}, t_2^{\text{opt}}, \dots, t_{16}^{\text{opt}})$ . In the cited reference [8], the starting point of the numerical optimization is an initial estimation for the values of  $t_1, \dots, t_{16}$ , which are assessed by making use of the density matrix reconstructed through quantum state tomography. Since this density matrix may be not positive definite, the so-retrieved  $t_\nu$  values are not necessarily real and, for this reason, the initial estimation only considers their real part. In the specific example of this appendix, the maximum likelihood estimation results in a density matrix having eigenvalues 0.986022, 0.0139777, 0, and 0 (thus featuring eigenvalues comprised in the interval  $[0, 1]$  as required for a physical density matrix [8, 108]), while  $\text{Tr}\{\rho^2\} = 0.972435$ . This means that the maximum likelihood estimation has real and non-negative eigenvalues (i.e., it is Hermitian and positive definite, respectively), and that it can be considered unitary (since the trace of its square approaches one). In other words, while the tomographic reconstruction provides a nonphysical density matrix, the maximum likelihood estimation gives a physical density matrix of the measured two-qubit entangled photon state [8].

In the results shown in subsection 4.2.3 of this thesis, the maximum likelihood estimation has been used in order to ensure the positivity of the measured density matrices of the

generated frequency-entangled two-photon states. More precisely, the procedure was similar to that explained in this appendix but extended to the cases  $d = 2, 3$ , and  $4$ , according to [109]. The maximum likelihood function was estimated by making use of a MATLAB code that had been programmed within the research group already in 2015. Using the measured coincidence counts  $n_{\nu}$  to launch the code and estimate the maximum likelihood function was not part of the specific tasks that were accomplished for the purpose of this thesis.

# Appendix E

## Examples of qubit cluster states

$N = 2$ ,  $d = 2$ . The wave function of a two-partite qubit linear cluster state is [98]

$$|\phi_{2,2}\rangle = \frac{1}{2} (|0_1, 0_2\rangle + |0_1, 1_2\rangle + |1_1, 0_2\rangle - |1_1, 1_2\rangle). \quad (\text{E.0.1})$$

In order to better visualize the state transformation, it is convenient to rewrite it in the form

$$\begin{aligned} |\phi_{2,2}\rangle &= \frac{1}{\sqrt{2}} \left[ \frac{1}{\sqrt{2}} |0_1\rangle (|0_2\rangle + |1_2\rangle) + \frac{1}{\sqrt{2}} |1_1\rangle (|0_2\rangle - |1_2\rangle) \right] \\ &= \frac{1}{\sqrt{2}} \left[ \frac{1}{\sqrt{2}} |0_1\rangle |+_2\rangle + \frac{1}{\sqrt{2}} |1_1\rangle |-_2\rangle \right] \end{aligned} \quad (\text{E.0.2})$$

The compact cluster state  $|C_{2,2}\rangle$  having  $2^{2/2}$  terms can be obtained by applying the identity ( $\mathbb{I}$ ) and the Hadamard ( $H$ ) matrices to the first and the second qubits, respectively. Since the identity operator keeps any quantum state unchanged and considering the action of the Hadamard matrix on  $|\pm\rangle$  (see Eqs. (1.7.8) of section 1.7), the compact cluster state is given by

$$|C_{2,2}\rangle = \frac{1}{\sqrt{2}} (|0_1, 0_2\rangle + |1_1, 1_2\rangle). \quad (\text{E.0.3})$$

This transformation can be expressed by the equation  $\mathbb{I}_1 \otimes H_2 |\phi_{2,2}\rangle = |C_{2,2}\rangle$ . It can be seen that  $|C_{2,2}\rangle$  coincides with the Bell state  $|\Phi^+\rangle$  of Eq. (2.2.1). In this sense, the linear cluster state  $|\phi_{2,2}\rangle$  is equivalent (up to local unitary operations) to a Bell state [98].

$N = 3$ ,  $d = 2$ . The wave function of a three-partite linear cluster state is

$$\begin{aligned} |\phi_{3,2}\rangle &= \frac{1}{2^{3/2}} \left( |0_1, 0_2, 0_3\rangle + |0_1, 0_2, 1_3\rangle + |0_1, 1_2, 0_3\rangle - |0_1, 1_2, 1_3\rangle \right. \\ &\quad \left. + |1_1, 0_2, 0_3\rangle + |1_1, 0_2, 1_3\rangle - |1_1, 1_2, 0_3\rangle + |1_1, 1_2, 1_3\rangle \right), \end{aligned} \quad (\text{E.0.4})$$

which can be rewritten in the form

$$\begin{aligned}
|\phi_{3,2}\rangle &= \frac{1}{\sqrt{2}} \left[ \frac{1}{2} (|0_1\rangle + |1_1\rangle) |0_2\rangle (|0_3\rangle + |1_3\rangle) \right. \\
&\quad \left. + \frac{1}{2} (|0_1\rangle - |1_1\rangle) |1_2\rangle (|0_3\rangle - |1_3\rangle) \right] \\
&= \frac{1}{\sqrt{2}} \left[ \frac{1}{2} |+_1\rangle |0_2\rangle |+_3\rangle + \frac{1}{2} |-_1\rangle |1_2\rangle |-_3\rangle \right]
\end{aligned} \tag{E.0.5}$$

Applying the Hadamard matrix to qubits 1 and 3, and the identity to qubit 2, gives the  $2^{(3-1)/2}$ -term compact cluster state [98]

$$|C_{3,2}\rangle = \frac{1}{\sqrt{2}} (|0_1, 0_2, 0_3\rangle + |1_1, 1_2, 1_3\rangle). \tag{E.0.6}$$

A comparison with the GHZ state  $|\text{GHZ}_{3,2}\rangle$  of Eq. (C.0.1) shows that the two states are locally equivalent [98].

**$N = 4, d = 2$ .** Let us consider now the more interesting scenario of a four-partite linear cluster state. Its wave function is given by

$$\begin{aligned}
|\phi_{4,2}\rangle &= \frac{1}{4} \left( |0_1, 0_2, 0_3, 0_4\rangle + |0_1, 0_2, 0_3, 1_4\rangle + |0_1, 0_2, 1_3, 0_4\rangle - |0_1, 0_2, 1_3, 1_4\rangle \right. \\
&\quad + |0_1, 1_2, 0_3, 0_4\rangle + |0_1, 1_2, 0_3, 1_4\rangle + |0_1, 1_2, 1_3, 0_4\rangle - |0_1, 1_2, 1_3, 1_4\rangle \\
&\quad + |1_1, 0_2, 0_3, 0_4\rangle + |1_1, 0_2, 0_3, 1_4\rangle + |1_1, 0_2, 1_3, 0_4\rangle - |1_1, 0_2, 1_3, 1_4\rangle \\
&\quad \left. - |1_1, 1_2, 0_3, 0_4\rangle - |1_1, 1_2, 0_3, 1_4\rangle + |1_1, 1_2, 1_3, 0_4\rangle - |1_1, 1_2, 1_3, 1_4\rangle \right).
\end{aligned} \tag{E.0.7}$$

A judicious grouping of these 16 terms enables us to rewrite the cluster state as

$$\begin{aligned}
|\phi_{4,2}\rangle &= \frac{1}{2} \left( \frac{1}{2} (|+_1\rangle |0\rangle_2 |0\rangle_3 |+_4\rangle + |+_1\rangle |0\rangle_2 |1\rangle_3 |+_4\rangle \right. \\
&\quad \left. + |-\rangle_1 |1\rangle_2 |0\rangle_3 |+_4\rangle - |-\rangle_1 |1\rangle_2 |1\rangle_3 |-\rangle_4 \right).
\end{aligned} \tag{E.0.8}$$

Applying the Hadamard matrix to qubits 1 and 4, and the identity to qubits 2 and 3, leads to a 4-term compact cluster state given by [98]

$$|C_{4,2}\rangle = \frac{1}{2} (|0_1, 0_2, 0_3, 0_4\rangle + |0_1, 0_2, 1_3, 1_4\rangle + |1_1, 1_2, 0_3, 0_4\rangle - |1_1, 1_2, 1_3, 1_4\rangle). \tag{E.0.9}$$

A comparison between  $|C_{4,2}\rangle$  and  $|\text{GHZ}_{4,2}\rangle$  of Eq. (C.0.2) immediately shows that the two states are significantly different. An analogue feature holds for a number of parties  $N \geq 4$  [7, 98].

Let now analyze the properties of  $|C_{4,2}\rangle$ , i.e. maximal connectedness and persistency of entanglement. For that purpose, the state  $|C_{4,2}\rangle$  is rewritten in the form

$$\begin{aligned}
|C_{4,2}\rangle &= \frac{1}{2} [ |0_1, 0_2\rangle (|0_3, 0_4\rangle + |1_3, 1_4\rangle) + |1_1, 1_2\rangle (|0_3, 0_4\rangle - |1_3, 1_4\rangle) ] \\
&= \frac{1}{\sqrt{2}} ( |0_1, 0_2\rangle |\Phi^+\rangle_{3,4} + |1_1, 1_2\rangle |\Phi^-\rangle_{3,4} ),
\end{aligned} \tag{E.0.10}$$

where  $|\Phi^\pm\rangle_{3,4}$  are the Bell states defined in Eq. (2.2.1). Measuring qubits 1 and 2 via projections of the form  $|0_1, 0_2\rangle$  and  $|1_1, 1_2\rangle$ , leads to the remaining qubits 3 and 4 to be projected into the Bell states  $|\Phi^\pm\rangle_{3,4}$ . For a detailed experimental description of these projections, the reader is referred to extension in higher dimension reported in chapter 6 [7]. Furthermore, only a second projection measurement can disentangle the state completely, according to the fact that the persistency of entanglement of  $|C_{4,2}\rangle$ , i.e.  $[4/2]$ . On the other hand, as it was reported in Appendix C, tracing out any party of  $|\text{GHZ}_{4,2}\rangle$  forces the remaining parts to collapse in an unentangled mixture. This testifies that the four-partite GHZ states does not exhibit maximal connectedness, as well as its persistency of entanglement is lower than that of the cluster state (specifically, it is equal to one).

The four main stabilizers of the linear cluster state  $|\phi_{4,2}\rangle$  are [33]

$$\begin{aligned}
\mathcal{S}_1^{(\phi_{4,2})} &= \sigma_x^{(1)} \sigma_z^{(2)} \sigma_0^{(3)} \sigma_0^{(4)}, \\
\mathcal{S}_2^{(\phi_{4,2})} &= \sigma_z^{(1)} \sigma_x^{(2)} \sigma_z^{(3)} \sigma_0^{(4)}, \\
\mathcal{S}_3^{(\phi_{4,2})} &= \sigma_0^{(1)} \sigma_z^{(2)} \sigma_x^{(3)} \sigma_z^{(4)}, \\
\mathcal{S}_4^{(\phi_{4,2})} &= \sigma_0^{(1)} \sigma_0^{(2)} \sigma_z^{(3)} \sigma_x^{(4)}.
\end{aligned} \tag{E.0.11}$$

The four main stabilizers of  $|C_{4,2}\rangle$  are different, in particular:

$$\begin{aligned}
\mathcal{S}_1^{(C_{4,2})} &= \sigma_z^{(1)} \sigma_z^{(2)} \sigma_0^{(3)} \sigma_0^{(4)}, \\
\mathcal{S}_2^{(C_{4,2})} &= \sigma_x^{(1)} \sigma_x^{(2)} \sigma_z^{(3)} \sigma_0^{(4)}, \\
\mathcal{S}_3^{(C_{4,2})} &= \sigma_0^{(1)} \sigma_z^{(2)} \sigma_x^{(3)} \sigma_x^{(4)}, \\
\mathcal{S}_4^{(C_{4,2})} &= \sigma_0^{(1)} \sigma_0^{(2)} \sigma_z^{(3)} \sigma_z^{(4)}.
\end{aligned} \tag{E.0.12}$$

The stabilizers  $\mathcal{S}_k^{(C_{4,2})}$  are specifically obtained by applying the Hadamard matrix to the Pauli matrices acting on qubits 1 and 4 (see Eqs. (1.7.9) of section 1.7), and applying the identity to the Pauli matrices acting on qubits 2 and 3.

More in general, the stabilizers of a compact cluster state can be obtained by applying the unitary operations that are used to convert  $|\phi_{N,2}\rangle$  into  $|C_{N,2}\rangle$ , to the Pauli matrices acting on the qubits that have been transformed.

The stabilizer groups of the linear as well as of the compact cluster states consist of  $2^4 = 16$  stabilizing operators. These are (the indices labelling the qubits have been

omitted for brevity)

$$\begin{aligned}
\mathcal{S}^{(\phi_{4,2})} = & \left\{ \sigma_x \sigma_z \sigma_0 \sigma_0, \sigma_z \sigma_x \sigma_z \sigma_0, \sigma_0 \sigma_z \sigma_x \sigma_z, \sigma_0 \sigma_0 \sigma_z \sigma_x, \right. \\
& \sigma_x \sigma_0 \sigma_x \sigma_z, \sigma_z \sigma_y \sigma_y \sigma_z, \sigma_x \sigma_0 \sigma_y \sigma_y, \sigma_z \sigma_y \sigma_x \sigma_y, \\
& \sigma_y \sigma_y \sigma_z \sigma_0, \sigma_x \sigma_z \sigma_z \sigma_x, \sigma_z \sigma_x \sigma_0 \sigma_x, \sigma_0 \sigma_z \sigma_y \sigma_y, \\
& \left. \sigma_y \sigma_y \sigma_0 \sigma_x, \sigma_y \sigma_x \sigma_x \sigma_y, \sigma_y \sigma_x \sigma_y \sigma_z, \sigma_0 \sigma_0 \sigma_0 \sigma_0 \right\},
\end{aligned} \tag{E.0.13}$$

and

$$\begin{aligned}
\mathcal{S}^{(C_{4,2})} = & \left\{ \sigma_z \sigma_z \sigma_0 \sigma_0, \sigma_x \sigma_x \sigma_z \sigma_0, \sigma_0 \sigma_z \sigma_x \sigma_x, \sigma_0 \sigma_0 \sigma_z \sigma_z, \right. \\
& \sigma_z \sigma_0 \sigma_x \sigma_x, \sigma_x \sigma_y \sigma_y \sigma_x, -\sigma_z \sigma_0 \sigma_y \sigma_y, -\sigma_x \sigma_y \sigma_x \sigma_y, \\
& -\sigma_y \sigma_y \sigma_z \sigma_0, \sigma_z \sigma_z \sigma_z \sigma_z, \sigma_x \sigma_x \sigma_0 \sigma_z, -\sigma_0 \sigma_z \sigma_y \sigma_y, \\
& \left. -\sigma_y \sigma_y \sigma_0 \sigma_z, \sigma_y \sigma_x \sigma_x \sigma_y, -\sigma_y \sigma_x \sigma_y \sigma_x, \sigma_0 \sigma_0 \sigma_0 \sigma_0 \right\},
\end{aligned} \tag{E.0.14}$$

respectively.

# Appendix F

## Witness for four-partite qubit cluster states

We consider here the example of the stabilizer witness for the linear cluster state  $|\phi_{4,2}\rangle$ . This can be obtained by expanding Eq. (3.3.5):

$$\begin{aligned} \mathcal{W}_{\text{opt}}^{(\phi_{4,2})} = 2\sigma_0 - \frac{1}{2} & \left( \sigma_x \sigma_z \sigma_0 \sigma_0 + \sigma_z \sigma_x \sigma_z \sigma_0 + \sigma_0 \sigma_z \sigma_x \sigma_z \right. \\ & \left. + \sigma_0 \sigma_0 \sigma_z \sigma_x + \sigma_x \sigma_0 \sigma_x \sigma_z + \sigma_z \sigma_x \sigma_0 \sigma_x \right), \end{aligned} \quad (\text{F.0.1})$$

where the order of the matrices represents the order of their action on the qubits. Measuring the expectation value of  $\mathcal{W}_{\text{opt}}^{(\phi_{4,2})}$  implies a measurement of the expectation values of all the stabilizers composing it. We here refer to this witness in order to show how the expectation value can be measured through few projections requiring only two measurement settings. To that purpose, without loss of generality, we consider here just the stabilizer  $\mathcal{S}_1^{(\phi_{4,2})} = \sigma_x^{(1)} \sigma_z^{(2)}$ . For simplicity, the two identities acting on qubits 3 and 4 are omitted. By expressing the Pauli matrices in their respective eigenbasis, this stabilizer becomes [5]

$$\begin{aligned} \mathcal{S}_1^{(\phi_{4,2})} = \sigma_x^{(1)} \sigma_z^{(2)} & = (|+\rangle\langle+| - |-\rangle\langle-|)^{(1)} \otimes (|0\rangle\langle 0| - |1\rangle\langle 1|)^{(2)} \\ & = |+, 0\rangle\langle+, 0| - |+, 1\rangle\langle+, 1| - |-, 0\rangle\langle-, 0| + |-, 1\rangle\langle-, 1|. \end{aligned} \quad (\text{F.0.2})$$

The notation  $|+, 0\rangle$  means that projection  $|+\rangle$  and  $|0\rangle$  are applied to qubits 1 and 2, respectively. Measuring the expectation value of  $\mathcal{S}_1^{(\phi_{4,2})}$  with respect to  $|\psi\rangle$  thus requires only four projections, i.e. [5]

$$\langle \mathcal{S}_1^{(\phi_{4,2})} \rangle = \langle \psi | \mathcal{S}_1^{(\phi_{4,2})} | \psi \rangle = |\langle 0, + | \psi \rangle|^2 - |\langle 0, - | \psi \rangle|^2 - |\langle 1, + | \psi \rangle|^2 + |\langle 1, - | \psi \rangle|^2. \quad (\text{F.0.3})$$

From the expression above, it results that measuring the expectation value  $\langle \mathcal{S}_1^{(\phi_{4,2})} \rangle$  just requires to project the first qubit of  $|\psi\rangle$  into the basis  $\{|0\rangle, |1\rangle\}$ , and the second qubit into the basis  $\{|+\rangle, |-\rangle\}$ . Although omitted, measuring qubits 3 and 4 in the basis of  $\sigma_0$  needs projections on  $\{|0\rangle, |1\rangle\}$ . Only the two measurement settings  $\{|0\rangle, |1\rangle\}$  and  $\{|+\rangle, |-\rangle\}$  are thus needed to measure  $\langle \mathcal{S}_1^{(\phi_{4,2})} \rangle$  (and thus  $\langle \mathcal{W}_{\text{opt}}^{(\phi_{4,2})} \rangle$ ).

The witness  $\mathcal{W}_{\text{opt}}^{(C_{4,2})}$  designed to detect  $|C_{4,2}\rangle$  can be derived from  $\mathcal{W}_{\text{opt}}^{(\phi_{4,2})}$  by applying the same unitary operations that are used to convert  $|\phi_{4,2}\rangle$  into  $|C_{4,2}\rangle$  (and then  $\mathcal{S}^{(\phi_{4,2})}$  into  $\mathcal{S}^{(C_{4,2})}$ ). The resulting witness  $\mathcal{W}_{\text{opt}}^{(C_{4,2})}$  is thus given by

$$\begin{aligned} \mathcal{W}_{\text{opt}}^{(C_{4,2})} = 2\sigma_0 - \frac{1}{2} & \left( \sigma_z \sigma_z \sigma_0 \sigma_0 + \sigma_x \sigma_x \sigma_z \sigma_0 + \sigma_0 \sigma_z \sigma_x \sigma_x \right. \\ & \left. + \sigma_0 \sigma_0 \sigma_z \sigma_z + \sigma_z \sigma_0 \sigma_x \sigma_x + \sigma_x \sigma_x \sigma_0 \sigma_z \right). \end{aligned} \quad (\text{F.0.4})$$

# Appendix G

## Examples of qudit cluster states

$N = 2$ ,  $d = 3$ . Following Eq. (3.4.1) and using the computational basis  $\{|0\rangle, |1\rangle, |2\rangle\}$ , the wave function  $|\phi_{2,3}\rangle$  of a two-partite qutrit linear cluster state is given by

$$\begin{aligned} |\phi_{2,3}\rangle = & \frac{1}{3} \left( |0_1, 0_2\rangle + |0_1, 1_2\rangle + |0_1, 2_2\rangle \right. \\ & + |1_1, 0_2\rangle + \omega |1_1, 1_2\rangle + \omega^2 |1_1, 2_2\rangle \\ & \left. + |2_1, 0_2\rangle + \omega^2 |2_1, 1_2\rangle + \omega |2_1, 2_2\rangle \right), \end{aligned} \quad (\text{G.0.1})$$

where  $\omega = e^{i2\pi/3}$  and  $\omega^2 = e^{i4\pi/3} = e^{-i2\pi/3}$ . In a vector form, the computational basis is expressed as

$$|0\rangle = \begin{pmatrix} 1 \\ 0 \\ 0 \end{pmatrix} \quad |1\rangle = \begin{pmatrix} 0 \\ 1 \\ 0 \end{pmatrix} \quad |2\rangle = \begin{pmatrix} 0 \\ 0 \\ 1 \end{pmatrix}. \quad (\text{G.0.2})$$

In order to better visualize how the linear cluster state  $|\phi_{2,3}\rangle$  can be reduced in the compact form, it is more convenient to rewrite it as

$$|\phi_{2,3}\rangle = \frac{1}{\sqrt{3}} (|0\rangle_1 |x_0\rangle_2 + |1\rangle_1 |x_1\rangle_2 + |2\rangle_1 |x_2\rangle_2) \quad (\text{G.0.3})$$

where

$$\begin{aligned} |x_0\rangle &= \frac{1}{\sqrt{3}} (|0\rangle + |1\rangle + |2\rangle) \\ |x_1\rangle &= \frac{1}{\sqrt{3}} (|0\rangle + \omega |1\rangle + \omega^2 |2\rangle) \\ |x_2\rangle &= \frac{1}{\sqrt{3}} (|0\rangle + \omega^2 |1\rangle + \omega |2\rangle), \end{aligned} \quad (\text{G.0.4})$$

(see section 1.8). Similarly to the qubit case, the state  $|\phi_{2,3}\rangle$  can be reduced to the compact form  $|C_{2,3}\rangle$  having  $3^{2/2} = 3$  terms by applying the  $3 \times 3$  identity  $\mathbb{I}_3$  and the

Walsh-Hadamard  $W_{d=3} \equiv W$  matrices (see section 1.8) to the first and the second qutrits, respectively. These matrices are defined as

$$\mathbb{I}_{d=3} = \begin{pmatrix} 1 & 0 & 0 \\ 0 & 1 & 0 \\ 0 & 0 & 1 \end{pmatrix} \quad (\text{G.0.5})$$

$$W = \frac{1}{\sqrt{3}} \begin{pmatrix} 1 & 1 & 1 \\ 1 & \omega^2 & \omega \\ 1 & \omega & \omega^2 \end{pmatrix}, \quad W^\dagger = W^{-1} = \begin{pmatrix} 1 & 1 & 1 \\ 1 & \omega & \omega^2 \\ 1 & \omega^2 & \omega \end{pmatrix}.$$

The action of  $W$  and  $W^\dagger$  on the quantum states  $|j\rangle$  and  $|x_j\rangle$  (with  $j = 0, 1, 2$ ) gives

$$\begin{aligned} W|x_0\rangle &= |0\rangle, & W|0\rangle &= |x_0\rangle \\ W|x_1\rangle &= |1\rangle, & W|1\rangle &= |x_1\rangle \\ W|x_2\rangle &= |2\rangle, & W|2\rangle &= |x_2\rangle, \end{aligned} \quad (\text{G.0.6})$$

while the identity matrix keeps any state unchanged. In light of this, the obtained compact cluster state are associated to the wave function

$$|C_{2,3}\rangle = \frac{1}{\sqrt{3}} (|0_1, 0_2\rangle + |1_1, 1_2\rangle + |2_1, 2_2\rangle). \quad (\text{G.0.7})$$

This state coincides with a three-level Bell state (see Eq. (B.0.5)). In this sense, the two states are locally equivalent.

**$N = 3, d = 3$ .** The wave function of a three-partite three-level linear cluster state, consisting of  $3^{(3+1)/2} = 9$  terms, is given by

$$|\phi_{3,3}\rangle = \frac{1}{\sqrt{3}} (|x_0\rangle_1 |0\rangle_2 |x_0\rangle_3 + |x_1\rangle_1 |1\rangle_2 |x_1\rangle_3 + |x_2\rangle_1 |2\rangle_2 |x_2\rangle_3) \quad (\text{G.0.8})$$

with  $|x_0\rangle, |x_1\rangle, |x_2\rangle$  defined above. By applying the matrix  $W$  to qutrits 1 and 3, and the identity  $\mathbb{I}$  to qutrit 2, the linear cluster state is transformed into the compact form  $|C_{3,3}\rangle$  having  $3^{(3-1)/2} = 3$  terms, which gives

$$|C_{3,3}\rangle = \frac{1}{\sqrt{3}} (|0_1, 0_2, 0_3\rangle + |1_1, 1_2, 1_3\rangle + |2_1, 2_2, 2_3\rangle). \quad (\text{G.0.9})$$

From a comparison between  $|C_{3,3}\rangle$  and the GHZ state  $|\text{GHZ}_{3,3}\rangle$  of Eq. (C.0.3), it can be seen that they are locally equivalent.

# Appendix H

## Projection measurements for quantum interference and quantum state tomography

We report here the projections that were derived theoretically in order to measure quantum interference and quantum state tomography for  $d = 2, 3,$  and  $4$  [6].

**$d = 2$ .** In order to reconstruct the density matrix of the qubit state  $|\psi_{d=2}\rangle = 1/\sqrt{2}(|a\rangle_s |a\rangle_i + |b\rangle_s |b\rangle_i)$ , with  $a$  and  $b$  representing the frequency modes, we choose to project each photon in the states

$$\begin{aligned} & |\bar{k}\rangle \\ & |\bar{k} + 1\rangle \\ & \frac{1}{\sqrt{2}} (|\bar{k}\rangle + |\bar{k} + 1\rangle) \\ & \frac{1}{\sqrt{2}} (|\bar{k}\rangle + i|\bar{k} + 1\rangle). \end{aligned} \tag{H.0.1}$$

This led to 16 different two-level projections.

**$d = 3$ .** The density matrix of the qutrit state  $|\psi_{d=3}\rangle = 1/\sqrt{3}(|a\rangle_s |a\rangle_i + |b\rangle_s |b\rangle_i + |c\rangle_s |c\rangle_i)$  was reconstructed by projecting each photon

into the following nine different eigenvectors:

$$\begin{aligned}
& \frac{1}{\sqrt{2}} (|\bar{k}\rangle + |\bar{k} + 1\rangle) \\
& \frac{1}{\sqrt{2}} (|\bar{k}\rangle + |\bar{k} + 2\rangle) \\
& \frac{1}{\sqrt{2}} (|\bar{k} + 1\rangle + |\bar{k} + 2\rangle) \\
& \frac{1}{\sqrt{2}} (e^{i\frac{2\pi}{3}} |\bar{k}\rangle + e^{-i\frac{2\pi}{3}} |\bar{k} + 1\rangle) \\
& \frac{1}{\sqrt{2}} (e^{-i\frac{2\pi}{3}} |\bar{k}\rangle + e^{i\frac{2\pi}{3}} |\bar{k} + 1\rangle) \\
& \frac{1}{\sqrt{2}} (e^{i\frac{2\pi}{3}} |\bar{k}\rangle + e^{-i\frac{2\pi}{3}} |\bar{k} + 2\rangle) \\
& \frac{1}{\sqrt{2}} (e^{-i\frac{2\pi}{3}} |\bar{k}\rangle + e^{i\frac{2\pi}{3}} |\bar{k} + 2\rangle) \\
& \frac{1}{\sqrt{2}} (e^{i\frac{2\pi}{3}} |\bar{k} + 1\rangle + e^{-i\frac{2\pi}{3}} |\bar{k} + 2\rangle) \\
& \frac{1}{\sqrt{2}} (e^{-i\frac{2\pi}{3}} |\bar{k} + 1\rangle + e^{i\frac{2\pi}{3}} |\bar{k} + 2\rangle).
\end{aligned} \tag{H.0.2}$$

They resulted into 81 total three-level projections.

**$d = 4$ .** Finally, the density matrix of the four-level state  $|\psi_{d=4}\rangle = 1/\sqrt{2}(|a\rangle_s |a\rangle_i + |b\rangle_s |b\rangle_i + |c\rangle_s |c\rangle_i + |d\rangle_s |d\rangle_i)$  was obtained by projecting each photon

into the sixteen different eigenvectors that are listed below:

$$\begin{aligned}
& \frac{1}{\sqrt{3}} (|\bar{k} + 1\rangle + |\bar{k} + 2\rangle + |\bar{k} + 3\rangle) \\
& \frac{1}{\sqrt{3}} (|\bar{k} + 1\rangle + e^{i\frac{2\pi}{3}} |\bar{k} + 2\rangle + e^{-i\frac{2\pi}{3}} |\bar{k} + 3\rangle) \\
& \frac{1}{\sqrt{3}} (|\bar{k} + 1\rangle + e^{-i\frac{2\pi}{3}} |\bar{k} + 2\rangle + e^{i\frac{2\pi}{3}} |\bar{k} + 3\rangle) \\
& \frac{1}{\sqrt{3}} (e^{i\frac{2\pi}{3}} |\bar{k} + 1\rangle + |\bar{k} + 2\rangle + |\bar{k} + 3\rangle) \\
& \frac{1}{\sqrt{3}} (|\bar{k}\rangle + |\bar{k} + 2\rangle + |\bar{k} + 3\rangle) \\
& \frac{1}{\sqrt{3}} (|\bar{k}\rangle + e^{i\frac{2\pi}{3}} |\bar{k} + 2\rangle + e^{-i\frac{2\pi}{3}} |\bar{k} + 3\rangle) \\
& \frac{1}{\sqrt{3}} (|\bar{k}\rangle + e^{-i\frac{2\pi}{3}} |\bar{k} + 2\rangle + e^{i\frac{2\pi}{3}} |\bar{k} + 3\rangle) \\
& \frac{1}{\sqrt{3}} (|\bar{k}\rangle + e^{i\frac{2\pi}{3}} |\bar{k} + 2\rangle + |\bar{k} + 3\rangle) \\
& \frac{1}{\sqrt{3}} (|\bar{k}\rangle + |\bar{k} + 1\rangle + |\bar{k} + 3\rangle) \\
& \frac{1}{\sqrt{3}} (|\bar{k}\rangle + e^{i\frac{2\pi}{3}} |\bar{k} + 1\rangle + e^{-i\frac{2\pi}{3}} |\bar{k} + 3\rangle) \\
& \frac{1}{\sqrt{3}} (|\bar{k}\rangle + e^{-i\frac{2\pi}{3}} |\bar{k} + 1\rangle + e^{i\frac{2\pi}{3}} |\bar{k} + 3\rangle) \\
& \frac{1}{\sqrt{3}} (|\bar{k}\rangle + |\bar{k} + 1\rangle + e^{i\frac{2\pi}{3}} |\bar{k} + 3\rangle) \\
& \frac{1}{\sqrt{3}} (|\bar{k}\rangle + |\bar{k} + 1\rangle + |\bar{k} + 2\rangle) \\
& \frac{1}{\sqrt{3}} (|\bar{k}\rangle + e^{i\frac{2\pi}{3}} |\bar{k} + 1\rangle + e^{-i\frac{2\pi}{3}} |\bar{k} + 2\rangle) \\
& \frac{1}{\sqrt{3}} (|\bar{k}\rangle + e^{-i\frac{2\pi}{3}} |\bar{k} + 1\rangle + e^{i\frac{2\pi}{3}} |\bar{k} + 2\rangle) \\
& \frac{1}{\sqrt{3}} (e^{i\frac{2\pi}{3}} |\bar{k}\rangle + |\bar{k} + 1\rangle + |\bar{k} + 2\rangle).
\end{aligned} \tag{H.0.3}$$

This resulted into 256 projection measurements.

# Appendix I

## Maximal eigenvalue of $\Theta$

We here prove that the largest measurement outcome of the operator  $\Theta$  introduced in Eq. (5.2.6) of section 5.2 is equal to 1. This value represents specifically the worse possible experimental scenario, and can be obtained only when  $\Theta$  is applied to a quantum state that is the eigenvector of  $\Theta$  with the largest possible eigenvalue. As a consequence, any other quantum state provides eigenvalues ranging from 0 to 1 (the upper bound excluded). In the specific case analyzed here, the maximal eigenvalue of  $\Theta$  is provided by the cluster state  $|C_{N,d}\rangle$ . In order to demonstrate this, we write

$$\Theta = A + B - A \cdot B, \quad (\text{I.0.1})$$

where we introduce the observables

$$\begin{aligned} A &= \prod_{\text{odd } k} \frac{1}{d} \sum_{l=1}^d \mathcal{S}_k^{(l)} \\ B &= \prod_{\text{even } k} \frac{1}{d} \sum_{l=1}^d \mathcal{S}_k^{(l)} \\ A \cdot B &= \prod_{k=1}^N \frac{1}{d} \sum_{l=1}^d \mathcal{S}_k^{(l)}, \end{aligned}$$

which are linear combinations of the stabilizers  $\mathcal{S}_k^{(l)}$ , with  $l$  denoting the power degree. In particular,  $A$  includes those measurements in which  $X$  is applied only to the odd qudits, and  $Z$  only to the even qudits. On the contrary,  $B$  contains those measurements where  $X$  is applied only to the even qudits, while  $Z$  to the odd qudits. It is now necessary to find the maximal eigenvalue  $\lambda_{\max}$  of  $\Theta$ , i.e.

$$\langle A \rangle + \langle B \rangle - \langle A \cdot B \rangle \leq \lambda_{\max}. \quad (\text{I.0.2})$$

For this purpose, we first find that the highest eigenvalue of both  $A$  and  $B$  is 1, i.e.  $\langle C_{N,d} | A | C_{N,d} \rangle = 1$  and  $\langle C_{N,d} | B | C_{N,d} \rangle = 1$ , respectively. This value can be obtained only when  $A$  and  $B$  are applied to the cluster state. To prove this, although stabilizers are not individually Hermitian operators,  $A$  and  $B$  are Hermitian. This means that  $A$  and  $B$  are observables possessing real eigenvalues. We demonstrate here this property by making use of the relation between a stabilizer and its transpose conjugate, which reads

$$(\mathcal{S}^n)^\dagger = \mathcal{S}^{d-l}, \quad (\text{I.0.3})$$

where  $l = 1, \dots, d$ . This equality of Eq. (I.0.3) originates in turn by a similar link existing between each generalized Pauli matrix and its transpose conjugates. From Eq. (I.0.3), the operators  $A$  and  $A^\dagger$  can be thus written as

$$A = \prod_{\text{odd } k} \frac{\mathcal{S}_k^{(1)} + \mathcal{S}_k^{(2)} + \mathcal{S}_k^{(3)} + \dots + \mathcal{S}_k^{(d-2)} + \mathcal{S}_k^{(d-1)} + \mathcal{S}_k^{(d)}}{d} \quad (\text{I.0.4})$$

$$A^\dagger = \prod_{\text{odd } k} \frac{\mathcal{S}_k^{(1)\dagger} + \mathcal{S}_k^{(2)\dagger} + \mathcal{S}_k^{(3)\dagger} + \dots + \mathcal{S}_k^{(d-2)\dagger} + \mathcal{S}_k^{(d-1)\dagger} + \mathcal{S}_k^{(d)\dagger}}{d} \quad (\text{I.0.5})$$

respectively, where, by definition,  $\mathcal{S}_k^{(0)} = \mathcal{S}_k^{(d)} = \mathbb{I}$ . A comparison between  $A$  and  $A^\dagger$  immediately shows that  $A = A^\dagger$ , which means that  $A$  is Hermitian. An analogous argument holds for  $B$  and  $A \cdot B$ , although this is not explicitly demonstrated here.

According to the definition of stabilizer provided in section 3.2, given a quantum state  $|\psi\rangle$ , its stabilizer  $\mathcal{S}_\psi$  is defined as satisfying the eigenvalue equation  $\mathcal{S}_\psi |\psi\rangle = |\psi\rangle$ . For any other quantum state, the condition  $\mathcal{S}_\psi |\phi\rangle = \beta |\psi\rangle$  exists, where  $0 \leq \beta < 1$ , while  $\beta$  is equal to 1 only if  $|\phi\rangle = |\psi\rangle$ . The largest expectation value of  $\mathcal{S}_\psi$  is thus 1 and can be only reached when the operator is applied to  $|\psi\rangle$  [158]. Since  $A$ ,  $B$ , and  $A \cdot B$  are linear combination of stabilizers, such a property can be directly applied to them. From this, it can be concluded that  $0 \leq \langle A \rangle \leq 1$ ,  $0 \leq \langle B \rangle \leq 1$  and  $0 \leq \langle A \cdot B \rangle \leq 1$ .

With this in mind and considering Eq. (I.0.2), we need to prove now that  $\langle \Theta \rangle \leq 1$ . To this end, we make use of the definition of variance and covariance of quantum operators [159]. In this specific case, the variance of  $A$  is given by

$$\text{Var}(A) = \langle A \cdot A \rangle - \langle A \rangle \cdot \langle A \rangle, \quad (\text{I.0.6})$$

while the covariance between  $A$  and  $B$  results in

$$\text{Cov}(A, B) = \langle A \cdot B \rangle - \langle A \rangle \cdot \langle B \rangle. \quad (\text{I.0.7})$$

Variance and covariance are related each other by the Cauchy-Schwarz inequality:

$$0 \leq |\text{Cov}(A, B)|^2 \leq \text{Var}(A) \cdot \text{Var}(B). \quad (\text{I.0.8})$$

Bearing in mind the definition provided in Eqs. (I.0.7) and (I.0.2), we can then write

$$\langle A \rangle + \langle B \rangle - \langle A \cdot B \rangle = \langle A \rangle + \langle B \rangle - \langle A \rangle \cdot \langle B \rangle - \text{Cov}(A, B) \leq \lambda_{\max}. \quad (\text{I.0.9})$$

Since  $A$  and  $B$  have a set of common eigenfunctions (here, the cluster states), their commutator is zero, i.e.  $[A, B] = [B, A] = 0$  [3, 4, 160, 161]. This means that  $A$  and  $B$  are independent operators. This implies that the covariance between  $A$  and  $B$  is zero, which leads to

$$\langle A \rangle + \langle B \rangle - \langle A \rangle \cdot \langle B \rangle \leq \lambda_{\max}. \quad (\text{I.0.10})$$

The conditions  $0 \leq \langle A \rangle \leq 1$  and  $0 \leq \langle B \rangle \leq 1$  that we showed above immediately lead to the inequality  $\lambda_{\max} \leq 1$ . This confirms that the maximal expectation value of  $\Theta$  is 1, i.e.  $\langle \Theta \rangle \leq \lambda_{\max} = 1$ .

# Appendix J

## List of the 81 cluster state stabilizers

List of the 81 stabilizers of $ C_{4,3}\rangle$		
$\mathcal{S}_1 = Z^\dagger Z \text{III}$	$\mathcal{S}_{28} = VY \text{I}Z$	$\mathcal{S}_{55} = ZZY^\dagger V^\dagger$
$\mathcal{S}_2 = XXZ \text{II}$	$\mathcal{S}_{29} = Z^\dagger Z^\dagger YV$	$\mathcal{S}_{56} = \omega^2 X^\dagger Y^\dagger V^\dagger V^\dagger$
$\mathcal{S}_3 = \text{I}ZXX$	$\mathcal{S}_{30} = Y^\dagger Y^\dagger VX$	$\mathcal{S}_{57} = VYZ \text{II}$
$\mathcal{S}_4 = \text{III}ZZ^\dagger$	$\mathcal{S}_{31} = Z^\dagger Z^\dagger VY$	$\mathcal{S}_{58} = Z^\dagger Z^\dagger XX$
$\mathcal{S}_5 = ZZ^\dagger \text{III}$	$\mathcal{S}_{32} = Y^\dagger V^\dagger \text{II}Z^\dagger$	$\mathcal{S}_{59} = Z^\dagger ZZZ^\dagger$
$\mathcal{S}_6 = X^\dagger X^\dagger Z^\dagger \text{II}$	$\mathcal{S}_{33} = Z^\dagger \text{IV}^\dagger Y^\dagger$	$\mathcal{S}_{60} = Y^\dagger V^\dagger Z^\dagger \text{II}$
$\mathcal{S}_7 = \text{II}Z^\dagger X^\dagger X^\dagger$	$\mathcal{S}_{34} = \omega^2 Y^\dagger X^\dagger Y^\dagger X^\dagger$	$\mathcal{S}_{61} = Z^\dagger \text{II}X^\dagger X^\dagger$
$\mathcal{S}_8 = \text{III}Z^\dagger Z$	$\mathcal{S}_{35} = Y^\dagger V^\dagger ZZ$	$\mathcal{S}_{62} = Z^\dagger ZZ^\dagger Z$
$\mathcal{S}_9 = \omega VVVV$	$\mathcal{S}_{36} = Z^\dagger \text{I}Y^\dagger V^\dagger$	$\mathcal{S}_{63} = \omega XY YX$
$\mathcal{S}_{10} = \omega VVXY$	$\mathcal{S}_{37} = \omega XYVV$	$\mathcal{S}_{64} = XXZ^\dagger Z^\dagger$
$\mathcal{S}_{11} = VXY^\dagger Y^\dagger$	$\mathcal{S}_{38} = \omega YXYX$	$\mathcal{S}_{65} = YVZ \text{II}$
$\mathcal{S}_{12} = VXX^\dagger V^\dagger$	$\mathcal{S}_{39} = \omega XYXY$	$\mathcal{S}_{66} = XVV^\dagger X^\dagger$
$\mathcal{S}_{13} = Y^\dagger Y^\dagger XV$	$\mathcal{S}_{40} = YVZ^\dagger Z^\dagger$	$\mathcal{S}_{67} = XX \text{I}Z$
$\mathcal{S}_{14} = Y^\dagger Y^\dagger YY$	$\mathcal{S}_{41} = XVY^\dagger Y^\dagger$	$\mathcal{S}_{68} = \text{I}ZYV$
$\mathcal{S}_{15} = \omega^2 Y^\dagger X^\dagger X^\dagger Y^\dagger$	$\mathcal{S}_{42} = YYV^\dagger X^\dagger$	$\mathcal{S}_{69} = Z \text{I}XX$
$\mathcal{S}_{16} = \omega^2 Y^\dagger X^\dagger V^\dagger V^\dagger$	$\mathcal{S}_{43} = YV \text{I}Z$	$\mathcal{S}_{70} = X^\dagger V^\dagger VX$
$\mathcal{S}_{17} = \omega YXVV$	$\mathcal{S}_{44} = XVX^\dagger V^\dagger$	$\mathcal{S}_{71} = \text{II}ZVY$
$\mathcal{S}_{18} = \omega YXXY$	$\mathcal{S}_{45} = Z \text{II}YV$	$\mathcal{S}_{72} = ZZ^\dagger ZZ^\dagger$
$\mathcal{S}_{19} = YYY^\dagger Y^\dagger$	$\mathcal{S}_{46} = X^\dagger V^\dagger XV$	$\mathcal{S}_{73} = X^\dagger X^\dagger \text{II}Z^\dagger$
$\mathcal{S}_{20} = YYX^\dagger V^\dagger$	$\mathcal{S}_{47} = V^\dagger X^\dagger VX$	$\mathcal{S}_{74} = \text{II}Z^\dagger V^\dagger Y^\dagger$
$\mathcal{S}_{21} = V^\dagger X^\dagger XV$	$\mathcal{S}_{48} = Z \text{II}VY$	$\mathcal{S}_{75} = V^\dagger Y^\dagger Z^\dagger \text{II}$

$\mathcal{S}_{22} = V^\dagger X^\dagger Y Y$	$\mathcal{S}_{49} = X^\dagger V^\dagger Y Y$	$\mathcal{S}_{76} = Z Z X^\dagger X^\dagger$
$\mathcal{S}_{23} = \omega^2 V^\dagger V^\dagger X^\dagger Y^\dagger$	$\mathcal{S}_{50} = V^\dagger Y^\dagger \mathbb{I} Z^\dagger$	$\mathcal{S}_{77} = Z X^\dagger Z^\dagger Z$
$\mathcal{S}_{24} = \omega^2 V^\dagger V^\dagger V^\dagger V^\dagger$	$\mathcal{S}_{51} = Z Z V^\dagger Y^\dagger$	$\mathcal{S}_{78} = \omega^2 X^\dagger Y^\dagger Y^\dagger X^\dagger$
$\mathcal{S}_{25} = \omega V V Y X$	$\mathcal{S}_{52} = q^2 X^\dagger Y^\dagger X^\dagger Y^\dagger$	$\mathcal{S}_{79} = X^\dagger X^\dagger Z Z$
$\mathcal{S}_{26} = V Y Z^\dagger Z^\dagger$	$\mathcal{S}_{53} = \omega^2 V^\dagger V^\dagger Y^\dagger X^\dagger$	$\mathcal{S}_{80} = \mathbb{I} Z^\dagger Y^\dagger V^\dagger$
$\mathcal{S}_{27} = V X V^\dagger X^\dagger$	$\mathcal{S}_{54} = V^\dagger Y^\dagger Z Z$	$\mathcal{S}_{81} = \mathbb{I} \mathbb{I} \mathbb{I} \mathbb{I}$

# List of publications in scientific journals<sup>1</sup>

1. M. Kues, C. Reimer, **S. Sciara**, P. Roztockki, M. Islam, L. Romero Cortés, Y. Zhang, B. Fischer, S. Loranger, R. Kashyap, A. Cino, S.T. Chu, B.E. Little, D.J. Moss, J. Azaña, L. Caspani, W.J. Munro, and R. Morandotti, “Cluster states go high-dimensional with time and frequency”, *Optics & Photonics News- Special Issue in Optics 2019*, accepted on October 4, 2019.
2. **S. Sciara**, P. Roztockki, C. Rimoldi, M. Chemnitz, B Fischer, L. Romero Cortés, W.J. Munro, D.J. Moss, L. Caspani, C. Reimer, M. Kues, J. Azaña, and R. Morandotti, “Generation and processing of complex photon states with quantum frequency combs”, *IEEE Photonics Technology Letters* (Invited), published online on September 30, 2019 (DOI: 10.1109/LPT.2019.2944564).
3. **S. Sciara**, C. Reimer, M. Kues, P. Roztockki, A. Cino, D.J. Moss, L. Caspani, W.J. Munro, and R. Morandotti, “Universal n-partite d-level pure-state entanglement witness based on realistic measurement settings”, *Physical Review Letters* vol. 122, p.120501, 2019.
4. C. Reimer, S. Sciara, P. Roztockki, M. Islam, L. Romero Cortés, Y. Zhang, B. Fischer, S. Loranger, R. Kashyap, A. Cino, S.T. Chu, B.E. Little, D.J. Moss, L. Caspani, W.J. Munro, J. Azaña, M. Kues, and R. Morandotti, “High-dimensional one-way quantum processing implemented on d-level cluster states”, *Nature Physics*, vol. 15, pp. 148-153, 2019.
5. P. Roztockki, **S. Sciara**, C. Reimer, L. Romero Cortés, Y. Zhang, B. Wetzel, M.

---

1. Papers related to the results presented in this thesis as well as containing that topic for the first time are listed in bold. In that case, “S. Sciara” is underlined.

- Islam, B. Fischer, A. Cino, S.T. Chu, B.E. Little, D.J. Moss, L. Caspani, J. Azaña, M. Kues, and R. Morandotti, “Complex quantum state generation and coherent control based on integrated frequency combs”, *Journal Lightwave Technology*, vol. 37, pp. 338-344, 2019.
6. B. MacLellan, P. Roztock, M. Kues, C. Reimer, L. Romero Cortés, Y. Zhang, **S. Sciara**, B. Wetz, A. Cino, S.T. Chu, B.E. Little, D.J. Moss, L. Caspani, J. Azaña, and R. Morandotti, “Generation and coherent control of pulsed quantum frequency combs”, *Journal of Visualized Experiments* (136), e57517,doi:10.3791/57517, 2018.
  7. C. Reimer, Y. Zhang, P. Roztock, **S. Sciara**, L. Romero Cortés, M. Islam, B. Fischer, B. Wetz, A. Cino, S.T. Chu, B.E. Little, D.J. Moss, L. Caspani, J. Azaña, M. Kues, and R. Morandotti, “On-chip frequency combs and telecommunications signal processing meet quantum optics”, *Frontiers of Optoelectronics*, vol. 11 (2), pp. 134-147, 2018.
  8. M. Kues, C. Reimer, P. Roztock, L. Romero Cortés, **S. Sciara**, B. Wetz, A. Cino, S.T. Chu, B.E. Little, D.J. Moss, L. Caspani, J. Azaña, and R. Morandotti, “ENTANGLED LIGHT: Scaling on-chip entangled photon states to higher dimensions”, *Optics & Photonics News- Special Issue in Optics 2017*, p. 37, 2017.
  9. P. Roztock, M. Kues, C. Reimer, B. Wetz, **S. Sciara**, Y. Zhang, A. Cino, B.E. Little, S.T. Chu, D.J. Moss, and R. Morandotti, “Practical system for the generation of pulsed quantum frequency combs”, *Optics Express*, vol. 26, pp. 18940-18949, 2017
  10. M. Kues, C. Reimer, P. Roztock, L. R. Cortés, **S. Sciara**, B. Wetz, Y. Zhang, A. Cino, S.T. Chu, B.E. Little, D.J. Moss, L. Caspani, J. Azaña, and R. Morandotti, “On-chip generation of high-dimensional entangled quantum states and their coherent control”, *Nature*, vol. 546, pp. 622-626, 2017.
  11. **S. Sciara**, R. Lo Franco, and G. Compagno, “Schmidt decomposition made universal to unveil the entanglement of identical particles”, <http://www.2physics.com/2017/05/schmidt-decomposition-made-universal-to.html>, 2017.
  12. **S. Sciara**, R. Lo Franco, and G. Compagno, “Universality of Schmidt decompo-

sition and particle identity”, *Scientific Reports*, vol. 4, p. 44675, 2017.<sup>2</sup>

## Patents

1. M. Kues\*, C. Reimer\*, **S. Sciara\***, P. Roztocki\*, L. Romero Cortés, Y. Jestin, J. Azaña, and R. Morandotti, “Method and system for the generation and control of high-dimensional multi-partite quantum states”, International Application Number: PCT/CA2018/051512, International Filing Date: 28/11/2018, Publication Number: WO/2019/104426, Publication Date: 06/06/2019 (\* These authors contributed equally).

---

2. Publications 11 and 12 are associated to research work that has been pursued during the Master degree.

# List of presentations

1. **S. Sciara**, M. Kues, C. Reimer, P. Roztock, M. Islam, L. Romero Cortés, Y. Zhang, B. Fischer, S. Loranger, R. Kashyap, A. Cino, S.T. Chu, B.E. Little, D.J. Moss, L. Caspani, W.J. Munro, J. Azaña, and R. Morandotti, “Quantum frequency combs for the on-chip generation, coherent control and processing of complex entangled photon states”, Canadian Semiconductor Science and Technology Conference, Saskatoon (SK), Canada, July 28- August 1, 2019 (oral).
2. **S. Sciara**, C. Reimer, M. Kues, P. Roztock, A. Cino, D.J. Moss, L. Caspani, W.J. Munro, and R. Morandotti, “Universal multipartite d-level entanglement witnesses for realistic measurement settings”, CLEO Europe, Munich, Germany, June 23-27, 2019 (oral).
3. **S. Sciara**, C. Reimer, M. Kues, P. Roztock, A. Cino, D.J. Moss, L. Caspani, W.J. Munro, and R. Morandotti, “Universal multipartite d-level entanglement witnesses for realistic measurement settings”, Photonics North Conference, Québec City (QC), Canada, May 21-23, 2019 (oral).
4. **S. Sciara**, M. Kues, C. Reimer, P. Roztock, L. Romero Cortés, B. Wetz, Y. Zhang, L. Caspani, A. Cino, S.T. Chu, D.J. Moss, J. Azaña, and R. Morandotti, “On-chip generation and coherent control of entangled d-level biphoton states”, Photonics North Conference, Montréal (QC), Canada, June 5-7, 2018 (oral).
5. M. Kues, C. Reimer, **S. Sciara**, P. Roztock, B. Wetz, L. Caspani, S.T. Chu, D.J. Moss, and R. Morandotti, “Generation of correlated photons”, Photonics North Conference, Montréal (QC), Canada, June 5-7, 2018 (oral).
6. **S. Sciara**, M. Kues, C. Reimer, P. Roztock, B. Wetz, Y. Bromberg, B.E. Little, S.T. Chu, D.J. Moss, L. Caspani, and R. Morandotti, “On-chip quantum state generation by means of integrated frequency combs”, IEEE Photonics Society

Summer Topicals Meeting Series, San Juan, Puerto Rico (USA), July 10-12, 2017 (oral).

7. **S. Sciara**, M. Kues, C. Reimer, P. Roztockki, B. Wetzal, F. Grazioso, B.E. Little, S.T. Chu, T. Johnston, Y. Bromberg, L. Caspani, D.J. Moss, and R. Morandotti, “On-chip frequency combs for scalable quantum state generation”, Photonics North Conference, Ottawa (ON), Canada, June 6-8, 2017 (oral).
8. **S. Sciara**, R. Lo Franco, and G. Compagno, “Schmidt decomposition for systems of identical particles”, *International School of Physics “Enrico Fermi”-Italian Physical Society*, Course 197- Foundations of quantum theory, Lake Como, Varenna, Italy, July 8-13, 2016 (poster).
9. **S. Sciara**, R. Lo Franco, and G. Compagno, “Schmidt decomposition for systems of identical particles”, Photonics North Conference, Québec City (QC), Canada, May 24-26, 2016 (poster).
10. **S. Sciara**, R. Lo Franco, and G. Compagno, “Schmidt decomposition for systems of identical particles”, International OSA Network of Students (IONS), Québec City (QC), Canada, May 20-22, 2016 (oral).

# List of conference proceedings

1. **S. Sciara**, C. Reimer, P. Roztockki, M. Islam, L. Romero Cortés, B. Fischer, S. Loranger, R. Kashyap, A. Cino, S.T. Chu, B.E. Little, D.J. Moss, L. Caspani, W.J. Munro, J. Azaña, M. Kues, and R. Morandotti, “Generation and coherent processing of complex entangled photon states through integrated quantum frequency combs”, International Conference of Quantum, Nonlinear and Nanophotonics (IC-QNN), Sofia, Bulgaria, September 2-4, 2019 (plenary).
2. M. Kues, C. Reimer, **S. Sciara**, P. Roztockki, M. Islam, L. Romero Cortés, Y. Zhang, B. Fischer, S. Loranger, R. Kashyap, A. Cino, S.T. Chu, B.E. Little, D.J. Moss, L. Caspani, W.J. Munro, J. Azaña, and R. Morandotti, “D-dimensional frequency-time entangled cluster states with on-chip frequency combs”, Integrated Photonics Research, Silicon and Nanophotonics, Burlingame, California (USA), July 29- August 1, 2019 (oral).
3. **S. Sciara**, M. Kues, C. Reimer, P. Roztockki, B. Wetzal, B.E. Little, S.T. Chu, D.J. Moss, L. Caspani, and R. Morandotti, “Integrated frequency combs for the on-chip generation of optical quantum states”, META 2019 International Conference on Metamaterials, Photonics Crystals and Plasmonics, Lisbon, Portugal, July 23-26, 2019 (oral).
4. L. Caspani, **S. Sciara**, C. Reimer, P. Roztockki, M. Islam, L. Romero Cortés, Y. Zhang, B. Fischer, S. Loranger, R. Kashyap, A. Cino, S.T. Chu, B.E. Little, D.J. Moss, W.J. Munro, J. Azaña, M. Kues, and R. Morandotti, “ Generation of on-chip d-dimensional entangled cluster states and their characterization via optimal entanglement witnesses”, META 2019 International Conference on Metamaterials, Photonics Crystals and Plasmonics, Lisbon, Portugal, July 23-26, 2019 (oral).
5. P. Roztockki, C. Reimer, **S. Sciara**, M. Islam, L. Romero Cortés, Y. Zhang, B. Fischer, S. Loranger, R. Kashyap, A. Cino, S.T. Chu, B.E. Little, D.J. Moss, L.

- Caspani, W.J. Munro, J. Azaña, M. Kues, and R. Morandotti, “Kerr combs and telecommunications components for the generation and high-dimensional quantum processing of d-level cluster states”, ICTON 2019 International Conference on Transparent Optical Networks, Angers, France, July 9-13, 2019 (oral).
6. **S. Sciara**, C. Reimer, M. Kues, P. Roztocky, M. Islam, L. Romero Cortés, Y. Zhang, B. Fischer, S. Loranger, R. Kashyap, A. Cino, S.T. Chu, B.E. Little, D.J. Moss, L. Caspani, W.J. Munro, J. Azaña, and R. Morandotti, “On-chip generation, coherent control and processing of complex entangled photon states”, IEEE Photonics Society Summer Topicals Meeting Series, Ft. Lauderdale, Florida (USA), July 8-10, 2019 (oral).
  7. M. Kues, C. Reimer, **S. Sciara**, P. Roztocky, M. Islam, L. Romero Cortés, Y. Zhang, B. Fischer, S. Loranger, R. Kashyap, A.Cino, S.T. Chu, B.E. Little, D.J. Moss, L. Caspani, W.J. Munro, J. Azaña, and R. Morandotti, “Optical d-level frequency-time-based cluster states”, CLEO Europe, Munich, Germany, June 23-27, 2019 (oral).
  8. P. Roztocky, C. Reimer, **S. Sciara**, M. Islam, L. Romero Cortés, Y. Zhang, B. Fischer, S. Loranger, R. Kashyap, A.Cino, S.T. Chu, B.E. Little, D.J. Moss, L. Caspani, W.J. Munro, J. Azaña, M. Kues, and R. Morandotti, “Hyper-entanglement in time and frequency”, CLEO Europe, Munich, Germany, June 23-27, 2019 (poster).
  9. P. Roztocky, M. Islam, C. Reimer, B. Fischer, **S. Sciara**, Y. Zhang, D.J. Moss, M. Kues, and R. Morandotti, “Removing phase ambiguity in fiber-based interferometers for coherent time-bin operations”, CLEO Europe, Munich, Germany, June 23-27, 2019 (poster).
  10. P.Roztocky, C. Reimer, **S. Sciara**, M. Islam, L. Romero Corteés, Y. Zhang, B. Fischer, S. Loranger, R. Kashyap, A. Cino, S.T. Chu, B.E. Little, D.J. Moss, L. Caspani, W.J. Munro, J. Azaña, M. Kues, and R. Morandotti, “Optical d-level frequency-time-based cluster states”, Photonics North Conference, Québec City (QC), Canada, May 21-23, 2019 (oral).
  11. B. Fischer, P. Roztocky, M. Islam, C. Reimer, **S. Sciara**, Y. Zhang, D.J. Moss, M. Kues, and R. Morandotti, “Phase retrieval in fiber-based interferometers”, Photonics North Conference, Québec City (QC), Canada, May 21-23, 2019 (oral).

12. C. Reimer, M. Kues, **S. Sciara**, P. Roztock, M. Islam, L. Romero Cortés, Y. Zhang, B. Fischer, S. Loranger, R. Kashyap, A. Cino, S.T. Chu, B.E. Little, D.J. Moss, L. Caspani, W.J. Munro, J. Azaña, and R. Morandotti, “High-dimensional one-way quantum computation operations with on-chip optical d-level cluster states”, CLEO, San Jose, California (USA), May 5-10, 2019 (oral).
13. M. Kues, C. Reimer, **S. Sciara**, P. Roztock, M. Islam, L. Romero Cortés, Y. Zhang, B. Fischer, S. Loranger, R. Kashyap, A. Cino, S.T. Chu, B.E. Little, D.J. Moss, L. Caspani, W.J. Munro, J. Azaña, and R. Morandotti, “High-dimensional one-way quantum processing enabled by optical d-level cluster states”, Quantum Information and Measurement, Rome, Italy, April 4-6, 2019 (oral).
14. M. Kues, C. Reimer, **S. Sciara**, P. Roztock, M. Islam, L. Romero Cortés, Y. Zhang, B. Fischer, S. Loranger, R. Kashyap, A. Cino, S.T. Chu, B.E. Little, D.J. Moss, L. Caspani, W.J. Munro, J. Azaña, and R. Morandotti, “D-dimensional frequency-time entangled cluster states with on-chip/fiber-based photonic systems”, European Quantum Technology Conference 2019 (EQTC19), Grenoble, France, February 18-22, 2019 (oral).
15. **S. Sciara**, M. Kues, C. Reimer, P. Roztock, L. Romero Cortés, B. Wetz, Y. Zhang, A. Cino, S.T. Chu, B.E. Little, D.J. Moss, L. Caspani, J. Azaña, and R. Morandotti, “Generation and coherent manipulation of complex quantum states based on integrated frequency combs”, Photonics in Switching and Computing, Limassol, Cyprus, September 19-21, 2018 (oral).
16. M. Kues, C. Reimer, P. Roztock, L. Romero Cortés, **S. Sciara**, B. Wetz, Y. Zhang, A. Cino, S.T. Chu, B.E. Little, D.J. Moss, L. Caspani, J. Azaña, and R. Morandotti, “Complex entangled photon states on a chip”, Foundations & Advances in Nonlinear Science and 4th International Symposium Advances in Nonlinear Photonics, Minsk, Belarus, September 24-28, 2018 (oral).
17. Y. Zhang, M. Islam, P. Roztock, C. Reimer, **S. Sciara**, B. Fischer, Y. Bromberg, L. Caspani, S.T. Chu, B.E. Little, D.J. Moss, M. Kues, and R. Morandotti, “Noise contributions in on-chip four-photon states”, Photonics North Conference, Montréal (QC), Canada, June 5-7, 2018 (oral).
18. P. Roztock, M. Kues, C. Reimer, L. Romero Cortés, **S. Sciara**, B. Wetz, Y. Zhang, A. Cino, S.T. Chu, B.E. Little, D.J. Moss, L. Caspani, J. Azaña, and R.

- Morandotti, “Scalable on-chip generation and coherent control of complex optical quantum states ”, CLEO, San Jose, California (USA), May 13-18, 2018 (oral).
19. **S. Sciara**, M. Kues, P. Roztockki, C. Reimer, L. Romero Cortés, B. Wetzels, Y. Zhang, A. Cino, B.E. Little, S.T. Chu, D.J. Moss, L. Caspani, J. Azaña, and R. Morandotti, “Integrated frequency combs for on-chip generation of high-dimensional entangled photon states and their coherent control ”, SPIE Photonics Europe, Strasbourg, France, April 22-26, 2018 (oral).
  20. M. Kues, C. Reimer, P. Roztockki, L. Romero Cortés, **S. Sciara**, B. Wetzels, Y. Zhang, A. Cino, B.E. Little, S.T. Chu, D.J. Moss, L. Caspani, J. Azaña, and R. Morandotti, “High-dimensional optical quantum states from integrated frequency combs and their coherent control”, Photonics West, San Francisco, California (USA), January 27-February 1, 2018 (oral).
  21. P. Roztockki, M. Kues, C. Reimer, B. Wetzels, **S. Sciara**, Y. Zhang, A. Cino, S.T. Chu, B.E. Little, D.J. Moss, and R. Morandotti, “Practical excitation schemes for integrated micro-cavity based on quantum frequency combs”, Photonics West, San Francisco, California (USA), January 27-February 1, 2018 (oral).
  22. P. Roztockki, **S. Sciara**, M. Kues, C. Reimer, L.R. Cortes, B. Wetzels, Y. Zhang, A. Cino, S.T. Chu, B.E. Little, D.J. Moss, L. Caspani, J. Azaña, and R. Morandotti, “On-chip generation and coherent control of d-level entangled photon states through integrated frequency combs”, Quantum Technology International Conference, Paris, France, September 5-7, 2018 (oral).
  23. P. Roztockki, C. Reimer, M. Kues, **S. Sciara**, L. Romero Cortés, Y. Zhang, B. Wetzels, M. Islam, A. Cino, S.T. Chu, B.E. Little, D.J. Moss, L. Caspani, J. Azaña, M. Kues, and R. Morandotti, “Framework for complex quantum state generation and coherent control based on on-chip frequency combs”, Frontiers in Optics, Washington, District of Columbia (USA), September 16-20, 2018 (oral).
  24. C. Reimer, M. Kues, P. Roztockki, L. Romero Cortés, **S. Sciara**, B. Wetzels, Y. Zhang, A. Cino, S.T. Chu, B.E. Little, D.J. Moss, L. Caspani, J. Azaña, and R. Morandotti, “Integrated generation of high-dimensional entangled photon states and their coherent control”, Frontiers in Optics, Washington, District of Columbia (USA), September 16-20, 2018 (oral).

25. P. Roztocki, M. Kues, C. Reimer, L. Romero Cortés, **S. Sciara**, B. Wetzels, Y. Zhang, A. Cino, S.T. Chu, B.E. Little, D.J. Moss, L. Caspani, J. Azaña, and R. Morandotti, “On-chip Generation and Coherent Control of Complex Optical Quantum States”, URSI AT-RASC, Gran Canaria, Spain, May 28- June 1, 2018 (oral).
26. M. Kues, C. Reimer, P. Roztocki, L. R. Cortés, **S. Sciara**, B. Wetzels, Y. Zhang, A. Cino, S.T. Chu, B.E. Little, D.J. Moss, L. Caspani, J. Azaña, and R. Morandotti, “On-chip entangled d-level photon states – scalable generation and coherent processing”, CLEO, San Jose, California (USA), May 13-18, 2018 (oral).
27. C. Reimer, M. Kues, P. Roztocki, **S. Sciara**, L. Romero Cortés, B. Wetzels, Y. Zhang, A. Cino, S.T. Chu, B.E. Little, D.J. Moss, L. Caspani, J. Azaña, and R. Morandotti, “On-chip quantum optical frequency comb sources”, The Optical Networking and Communication Conference & Exhibition, San Diego, California (USA), March 8-12, 2018 (oral).
28. P. Roztocki, M. Kues, C. Reimer, L. Romero Cortés, **S. Sciara**, B. Wetzels, Y. Zhang, A. Cino, S.T. Chu, B.E. Little, D.J. Moss, L. Caspani, J. Azaña, and R. Morandotti, “Integrated generation of complex optical quantum states and their coherent control”, Nanophotonics Australasia, Melbourne, Australia, December 10-13, 2017 (oral).

# Bibliography

- [1] J. Sakurai, *Modern quantum mechanics*. Addison-Wesley, 1994.
- [2] D. J. Griffiths and D. F. Schroeter, *Introduction to quantum mechanics*. Cambridge University Press, 2017.
- [3] P. Dirac, *The principles of quantum mechanics*. Oxford University Press, 1958.
- [4] M. Nielsen and I. Chuang, *Quantum computation and quantum information*. Cambridge University Press, 2010.
- [5] S. Sciara, C. Reimer, M. Kues, P. Roztock, A. Cino, D. J. Moss, L. Caspani, W. J. Munro, and R. Morandotti, “Universal  $n$ -partite  $d$ -level pure-state entanglement witness based on realistic measurement settings,” *Phys. Rev. Lett.*, vol. 122, p. 120501, Mar 2019.
- [6] M. Kues, C. Reimer, P. Roztock, L. R. Cortés, S. Sciara, B. Wetz, Y. Zhang, A. Cino, S. T. Chu, B. E. Little, D. J. Moss, L. Caspani, J. Azaña, and R. Morandotti, “On-chip generation of high-dimensional entangled quantum states and their coherent control,” *Nature*, vol. 546, pp. 622–626, Jan 2017.
- [7] C. Reimer, S. Sciara, P. Roztock, M. Islam, L. Romero Cortés, Y. Zhang, B. Fischer, S. Loranger, R. Kashyap, A. Cino, S. T. Chu, B. E. Little, D. J. Moss, L. Caspani, W. J. Munro, J. Azaña, M. Kues, and R. Morandotti, “High-dimensional one-way quantum processing implemented on  $d$ -level cluster states,” *Nat. Phys.*, vol. 15, pp. 148–153, Feb 2019.
- [8] D. F. V. James, P. G. Kwiat, W. J. Munro, and A. G. White, “Measurement of qubits,” *Phys. Rev. A*, vol. 64, p. 052312, Oct 2001.

- [9] G. S. Thekkadath, L. Giner, Y. Chalich, M. J. Horton, J. Banker, and J. S. Lundeen, “Direct measurement of the density matrix of a quantum system,” *Phys. Rev. Lett.*, vol. 117, p. 120401, Sep 2016.
- [10] B. P. Lanyon, M. Barbieri, M. P. Almeida, T. Jennewein, T. C. Ralph, K. J. Resch, G. J. Pryde, J. L. O’Brien, A. Gilchrist, and A. G. White, “Simplifying quantum logic using higher-dimensional Hilbert spaces,” *Nat. Phys.*, vol. 5, p. 134, Dec 2009.
- [11] S. Lloyd, “Enhanced sensitivity of photodetection via quantum illumination,” *Science*, vol. 321, pp. 1463–1465, Sep 2008.
- [12] I. Ali-Khan, C. J. Broadbent, and J. C. Howell, “Large-alphabet quantum key distribution using energy-time entangled bipartite states,” *Phys. Rev. Lett.*, vol. 98, p. 060503, Feb 2007.
- [13] D. Collins, N. Gisin, N. Linden, S. Massar, and S. Popescu, “Bell inequalities for arbitrarily high-dimensional systems,” *Phys. Rev. Lett.*, vol. 88, p. 040404, Jan 2002.
- [14] D. Walls and G. J. Milburn, *Quantum optics*. Springer, 2010.
- [15] C. C. Gerry and P. L. Knight, *Introductory quantum optics*. Cambridge, 2005.
- [16] L. Rodney, *The quantum theory of light*. Oxford Science Publications, 2000.
- [17] A. Mair, A. Vaziri, G. Weihs, and A. Zeilinger, “Entanglement of the orbital angular momentum states of photons,” *Nature*, vol. 412, p. 313, Jul 2001.
- [18] J. Brendel, N. Gisin, W. Tittel, and H. Zbinden, “Pulsed energy-time entangled twin-photon source for quantum communication,” *Phys. Rev. Lett.*, vol. 82, pp. 2594–2597, Mar 1999.
- [19] C. Reimer, M. Kues, P. Roztocki, B. Wetzol, F. Grazioso, B. E. Little, S. T. Chu, T. Johnston, Y. Bromberg, L. Caspani, D. J. Moss, and R. Morandotti, “Generation of multiphoton entangled quantum states by means of integrated frequency combs,” *Science*, vol. 351, pp. 1176–1180, Mar 2016.

- [20] L. Olislager, J. Cussey, A. T. Nguyen, P. Emplit, S. Massar, J.-M. Merolla, and K. P. Huy, “Frequency-bin entangled photons,” *Phys. Rev. A*, vol. 82, p. 013804, Jul 2010.
- [21] J. Yin, J.-G. Ren, H. Lu, Y. Cao, H.-L. Yong, Y.-P. Wu, C. Liu, S.-K. Liao, F. Zhou, Y. Jiang, X.-D. Cai, P. Xu, G.-S. Pan, J.-J. Jia, Y.-M. Huang, H. Yin, J.-Y. Wang, Y.-A. Chen, C.-Z. Peng, and J.-W. Pan, “Quantum teleportation and entanglement distribution over 100-kilometre free-space channels,” *Nature*, vol. 488, pp. 185–188, Aug 2012.
- [22] M. Krenn, J. Handsteiner, M. Fink, R. Fickler, R. Ursin, M. Malik, and A. Zeilinger, “Twisted light transmission over 143 km,” *Proceedings of the National Academy of Sciences*, vol. 113, pp. 13648–13653, Nov 2016.
- [23] A. Boaron, G. Boso, D. Rusca, C. Vulliez, C. Autebert, M. Caloz, M. Perrenoud, G. Gras, F. Bussi eres, M.-J. Li, D. Nolan, A. Martin, and H. Zbinden, “Secure quantum key distribution over 421 km of optical fiber,” *Phys. Rev. Lett.*, vol. 121, p. 190502, Nov 2018.
- [24] J. Yin, Y. Cao, Y.-H. Li, S.-K. Liao, L. Zhang, J.-G. Ren, W.-Q. Cai, W.-Y. Liu, B. Li, H. Dai, G.-B. Li, Q.-M. Lu, Y.-H. Gong, Y. Xu, S.-L. Li, F.-Z. Li, Y.-Y. Yin, Z.-Q. Jiang, M. Li, J.-J. Jia, G. Ren, D. He, Y.-L. Zhou, X.-X. Zhang, N. Wang, X. Chang, Z.-C. Zhu, N.-L. Liu, Y.-A. Chen, C.-Y. Lu, R. Shu, C.-Z. Peng, J.-Y. Wang, and J.-W. Pan, “Satellite-based entanglement distribution over 1200 kilometers,” *Science*, vol. 356, pp. 1140–1144, Jun 2017.
- [25] T. Jennewein, C. Simon, G. Weihs, H. Weinfurter, and A. Zeilinger, “Quantum cryptography with entangled photons,” *Phys. Rev. Lett.*, vol. 84, pp. 4729–4732, May 2000.
- [26] D. S. Naik, C. G. Peterson, A. G. White, A. J. Berglund, and P. G. Kwiat, “Entangled state quantum cryptography: eavesdropping on the Ekert protocol,” *Phys. Rev. Lett.*, vol. 84, pp. 4733–4736, May 2000.
- [27] A. Rossi, G. Vallone, A. Chiuri, F. De Martini, and P. Mataloni, “Multipath entanglement of two photons,” *Phys. Rev. Lett.*, vol. 102, p. 153902, Apr 2009.

- [28] T. Pittman, “It’s a good time for time-bin qubits,” *Physics*, vol. 6, p. 110, Oct 2013.
- [29] N. Kiesel, C. Schmid, U. Weber, G. Tóth, O. Gühne, R. Ursin, and H. Weinfurter, “Experimental analysis of a four-qubit photon cluster state,” *Phys. Rev. Lett.*, vol. 95, p. 210502, Nov 2005.
- [30] K. Chen, C.-M. Li, Q. Zhang, Y.-A. Chen, A. Goebel, S. Chen, A. Mair, and J.-W. Pan, “Experimental realization of one-way quantum computing with two-photon four-qubit cluster states,” *Phys. Rev. Lett.*, vol. 99, p. 120503, Sep 2007.
- [31] G. Vallone, E. Pomarico, F. De Martini, and P. Mataloni, “Active one-way quantum computation with two-photon four-qubit cluster states,” *Phys. Rev. Lett.*, vol. 100, p. 160502, Apr 2008.
- [32] S. Haroche and J. M. Raimond, *Exploring the quantum- atoms, cavities, and photons*. Oxford University Press, 2006.
- [33] G. Tóth and O. Gühne, “Entanglement detection in the stabilizer formalism,” *Phys. Rev. A*, vol. 72, p. 022340, Aug 2005.
- [34] A. Zee, *Quantum field theory in a nutshell*. Princeton University Press, 2010.
- [35] J. Lawrence, “Mutually unbiased bases and ternary operator sets for  $n$  qutrits,” *Phys. Rev. A*, vol. 70, p. 012302, Jul 2004.
- [36] E. Schrödinger, “Die gegenwertige situation in der quantenmechanik,” *Naturwissenschaften*, vol. 23, p. 807, 1935.
- [37] D. Bruß, “Characterizing entanglement,” *J. Math. Phys.*, vol. 43, pp. 4237–4251, Aug 2002.
- [38] R. Horodecki, P. Horodecki, M. Horodecki, and K. Horodecki, “Quantum entanglement,” *Rev. Mod. Phys.*, vol. 81, pp. 865–942, Jun 2009.
- [39] M. Horodecki, P. Horodecki, and R. Horodecki, “Separability of mixed states: necessary and sufficient conditions,” *Phys. Lett. A*, vol. 223, pp. 1 – 7, May 1996.

- [40] A. Einstein, B. Podolsky, and N. Rosen, “Can quantum-mechanical description of physical reality be considered complete?,” *Phys. Rev.*, vol. 47, pp. 777–780, May 1935.
- [41] R. Raussendorf and H. J. Briegel, “A one-way quantum computer,” *Phys. Rev. Lett.*, vol. 86, pp. 5188–5191, May 2001.
- [42] H. Weinfurter, *Quantum communication with entangled photons*, vol. 42 of *Advances In Atomic, Molecular, and Optical Physics*. Academic Press, 2000.
- [43] M. Krenn, M. Malik, T. Scheidl, R. Ursin, and A. Zeilinger, *Quantum communication with photons*. Springer International Publishing, Dec 2016.
- [44] A. K. Ekert, “Quantum cryptography based on Bell’s theorem,” *Phys. Rev. Lett.*, vol. 67, pp. 661–663, Aug 1991.
- [45] D. Gottesman, “Class of quantum error-correcting codes saturating the quantum hamming bound,” *Phys. Rev. A*, vol. 54, pp. 1862–1868, Sep 1996.
- [46] C. H. Bennett and S. J. Wiesner, “Communication via one- and two-particle operators on Einstein-Podolsky-Rosen states,” *Phys. Rev. Lett.*, vol. 69, pp. 2881–2884, Nov 1992.
- [47] B. M. Terhal, “Detecting quantum entanglement,” *Theor. Comput. Sci.*, vol. 287, pp. 313 – 335, Sep 2002.
- [48] J. S. Bell, “On the Einstein Podolsky Rosen paradox,” *Physics*, vol. 1, pp. 195–200, Nov 1964.
- [49] H. Zhang, C. Zhang, X.-M. Hu, B.-H. Liu, Y.-F. Huang, C.-F. Li, and G.-C. Guo, “Arbitrary two-particle high-dimensional Bell-state measurement by auxiliary entanglement,” *Phys. Rev. A*, vol. 99, p. 052301, May 2019.
- [50] A. C. Dada, J. Leach, G. S. Buller, M. J. Padgett, and E. Andersson, “Experimental high-dimensional two-photon entanglement and violations of generalized Bell inequalities,” *Nat. Phys.*, vol. 7, pp. 667–680, May 2011.

- [51] F. Wang, M. Erhard, A. Babazadeh, M. Malik, M. Krenn, and A. Zeilinger, “Generation of the complete four-dimensional Bell basis,” *Optica*, vol. 4, pp. 1462–1467, Dec 2017.
- [52] M. C. Tichy, F. Mintert, and A. Buchleitner, “Essential entanglement for atomic and molecular physics,” *J. Phys. B: At., Mol. and Opt. Phys.*, vol. 44, no. 19, p. 192001, 2011.
- [53] C. H. Bennett, G. Brassard, C. Crépeau, R. Jozsa, A. Peres, and W. K. Wootters, “Teleporting an unknown quantum state via dual classical and Einstein-Podolsky-Rosen channels,” *Phys. Rev. Lett.*, vol. 70, pp. 1895–1899, Mar 1993.
- [54] L. Caspani, C. Xiong, B. J. Eggleton, D. Bajoni, M. Liscidini, M. Galli, R. Morandotti, and D. J. Moss, “Integrated sources of photon quantum states based on nonlinear optics,” *Light: Science & Applications*, vol. 6, p. e17100, Jan 2017.
- [55] M. Barbieri, C. Cinelli, P. Mataloni, and F. De Martini, “Polarization-momentum hyperentangled states: realization and characterization,” *Phys. Rev. A*, vol. 72, p. 052110, Nov 2005.
- [56] C. Cinelli, G. Di Nepi, F. De Martini, M. Barbieri, and P. Mataloni, “Parametric source of two-photon states with a tunable degree of entanglement and mixing: experimental preparation of Werner states and maximally entangled mixed states,” *Phys. Rev. A*, vol. 70, p. 022321, Aug 2004.
- [57] G. Vallone, E. Pomarico, P. Mataloni, F. De Martini, and V. Berardi, “Realization and characterization of a two-photon four-qubit linear cluster state,” *Phys. Rev. Lett.*, vol. 98, p. 180502, May 2007.
- [58] L. Caspani, C. Reimer, M. Kues, P. Roztocky, M. Clerici, B. Wetzal, Y. Jestin, M. Ferrera, M. Peccianti, A. Pasquazi, L. Razzari, B. E. Little, T. C. Sai, D. J. Moss, and R. Morandotti, “Multifrequency sources of quantum correlated photon pairs on-chip: a path toward integrated quantum frequency combs,” *Nanoph.*, vol. 5, pp. 351–362, Jun 2016.
- [59] A. Pasquazi, M. Peccianti, L. Razzari, D. J. Moss, S. Coen, M. Erkintalo, Y. K. Chembo, T. Hansson, S. Wabnitz, P. Del’Haye, X. Xue, A. M. Weiner, and

- R. Morandotti, “Micro-combs: a novel generation of optical sources,” *Phys. Rep.*, vol. 729, pp. 1 – 81, Jan 2018.
- [60] M. Kues, C. Reimer, J. M. Lukens, W. J. Munro, A. M. Weiner, D. J. Moss, and R. Morandotti, “Quantum optical microcombs,” *Nat. Photonics*, vol. 13, pp. 170–179, Feb 2019.
- [61] P. Roztocky, S. Sciara, C. Reimer, L. R. Cortés, Y. Zhang, B. Wetzels, M. Islam, B. Fischer, A. Cino, S. T. Chu, B. E. Little, D. J. Moss, L. Caspani, J. A. na, M. Kues, and R. Morandotti, “Complex quantum state generation and coherent control based on integrated frequency combs,” *J. Lightwave Technol.*, vol. 37, pp. 338–344, Jan 2019.
- [62] P. G. Kwiat, S. Barraza-Lopez, A. Stefanov, and N. Gisin, “Experimental entanglement distillation and ‘hidden’ non-locality,” *Nature*, vol. 409, pp. 1014–1017, Feb 2001.
- [63] P. G. Kwiat, A. J. Berglund, J. B. Altepeter, and A. G. White, “Experimental verification of decoherence-free subspaces,” *Science*, vol. 290, pp. 498–501, Oct 2000.
- [64] P. G. Kwiat, K. Mattle, H. Weinfurter, A. Zeilinger, A. V. Sergienko, and Y. Shih, “New high-intensity source of polarization-entangled photon pairs,” *Phys. Rev. Lett.*, vol. 75, pp. 4337–4341, Dec 1995.
- [65] M. Pelton, P. Marsden, D. Ljunggren, M. Tengner, A. Karlsson, A. Fragemann, C. Canalias, and F. Laurell, “Bright, single-spatial-mode source of frequency non-degenerate, polarization-entangled photon pairs using periodically poled KTP,” *Opt. Express*, vol. 12, pp. 3573–3580, Jul 2004.
- [66] G. Fujii, N. Namekata, M. Motoya, S. Kurimura, and S. Inoue, “Bright narrowband source of photon pairs at optical telecommunication wavelengths using a type-II periodically poled lithium niobate waveguide,” *Opt. Express*, vol. 15, pp. 12769–12776, Oct 2007.
- [67] K. Thyagarajan, J. Lugani, S. Ghosh, K. Sinha, A. Martin, D. B. Ostrowsky, O. Alibert, and S. Tanzilli, “Generation of polarization-entangled photons using type-

- II doubly periodically poled lithium niobate waveguides,” *Phys. Rev. A*, vol. 80, p. 052321, Nov 2009.
- [68] H. Jin, F. M. Liu, P. Xu, J. L. Xia, M. L. Zhong, Y. Yuan, J. W. Zhou, Y. X. Gong, W. Wang, and S. N. Zhu, “On-chip generation and manipulation of entangled photons based on reconfigurable lithium-niobate waveguide circuits,” *Phys. Rev. Lett.*, vol. 113, p. 103601, Sep 2014.
- [69] N. Matsuda, H. Le Jeannic, H. Fukuda, T. Tsuchizawa, W. J. Munro, K. Shimizu, K. Yamada, Y. Tokura, and H. Takesue, “A monolithically integrated polarization entangled photon pair source on a silicon chip,” *Sci. Rep.*, vol. 2, p. 817, Nov 2012.
- [70] N. Matsuda, P. Karkus, H. Nishi, T. Tsuchizawa, W. J. Munro, H. Takesue, and K. Yamada, “On-chip generation and demultiplexing of quantum correlated photons using a silicon-silica monolithic photonic integration platform,” *Opt. Express*, vol. 22, pp. 22831–22840, Sep 2014.
- [71] D. Bonneau, J. W. Silverstone, and M. G. Thompson, *Silicon quantum photonics*, pp. 41–82. Springer Berlin Heidelberg, 2016.
- [72] S. Azzini, D. Grassani, M. J. Strain, M. Sorel, L. G. Helt, J. E. Sipe, M. Liscidini, M. Galli, and D. Bajoni, “Ultra-low power generation of twin photons in a compact silicon ring resonator,” *Opt. Express*, vol. 20, pp. 23100–23107, Oct 2012.
- [73] D. Grassani, S. Azzini, M. Liscidini, M. Galli, M. J. Strain, M. Sorel, J. E. Sipe, and D. Bajoni, “Micrometer-scale integrated silicon source of time-energy entangled photons,” *Optica*, vol. 2, pp. 88–94, Feb 2015.
- [74] R. Wakabayashi, M. Fujiwara, K. ichiro Yoshino, Y. Nambu, M. Sasaki, and T. Aoki, “Time-bin entangled photon pair generation from Si micro-ring resonator,” *Opt. Express*, vol. 23, pp. 1103–1113, Jan 2015.
- [75] D. J. Moss, R. Morandotti, A. L. Gaeta, and M. Lipson, “New CMOS-compatible platforms based on silicon nitride and hydex for nonlinear optics,” *Nat. Photonics*, vol. 7, pp. 597–607, Jul 2013.
- [76] C. Reimer, L. Caspani, M. Clerici, M. Ferrera, M. Kues, M. Peccianti, A. Pasquazi, L. Razzari, B. E. Little, S. T. Chu, D. J. Moss, and R. Morandotti, “Integrated

- frequency comb source of heralded single photons,” *Opt. Express*, vol. 22, pp. 6535–6546, Mar 2014.
- [77] J. Mower, Z. Zhang, P. Desjardins, C. Lee, J. H. Shapiro, and D. Englund, “High-dimensional quantum key distribution using dispersive optics,” *Phys. Rev. A*, vol. 87, p. 062322, Jun 2013.
- [78] J. S. Bell, “On the problem of hidden variables in quantum mechanics,” *Rev. Mod. Phys.*, vol. 38, pp. 447–452, Jul 1966.
- [79] M. Giustina, M. A. M. Versteegh, S. Wengerowsky, J. Handsteiner, A. Hochrainer, K. Phelan, F. Steinlechner, J. Kofler, J.-A. Larsson, C. Abellán, W. Amaya, V. Pruneri, M. W. Mitchell, J. Beyer, T. Gerrits, A. E. Lita, L. K. Shalm, S. W. Nam, T. Scheidl, R. Ursin, B. Wittmann, and A. Zeilinger, “Significant-loophole-free test of Bell’s theorem with entangled photons,” *Phys. Rev. Lett.*, vol. 115, p. 250401, Dec 2015.
- [80] A. Cabello, A. Feito, and A. Lamas-Linares, “Bell’s inequalities with realistic noise for polarization-entangled photons,” *Phys. Rev. A*, vol. 72, p. 052112, Nov 2005.
- [81] J. F. Clauser, M. A. Horne, A. Shimony, and R. A. Holt, “Proposed experiment to test local hidden-variable theories,” *Phys. Rev. Lett.*, vol. 23, pp. 880–884, Oct 1969.
- [82] J. D. Franson, “Bell inequality for position and time,” *Phys. Rev. Lett.*, vol. 62, pp. 2205–2208, May 1989.
- [83] G. Lima, G. Vallone, A. Chiuri, A. Cabello, and P. Mataloni, “Experimental Bell-inequality violation without the postselection loophole,” *Phys. Rev. A*, vol. 81, p. 040101, Apr 2010.
- [84] J. Preskill, “Lecture notes for physics 229: quantum information and computation,” 1998.
- [85] S. Sciara, R. Lo Franco, and G. Compagno, “Universality of Schmidt decomposition and particle identity,” *Sci. Rep.*, vol. 7, p. 44675, Mar 2017.

- [86] M. Fedorov and N. Miklin, “Schmidt modes and entanglement,” *Contemporary Physics*, vol. 55, no. 2, pp. 94–109, 2014.
- [87] C. K. Law, I. A. Walmsley, and J. H. Eberly, “Continuous frequency entanglement: effective finite Hilbert space and entropy control,” *Phys. Rev. Lett.*, vol. 84, pp. 5304–5307, Jun 2000.
- [88] I. Jizan, L. G. Helt, C. Xiong, M. J. Collins, D.-Y. Choi, C. Joon Chae, M. Liscidini, M. J. Steel, B. J. Eggleton, and A. S. Clark, “Bi-photon spectral correlation measurements from a silicon nanowire in the quantum and classical regimes,” *Sci. Rep.*, vol. 5, p. 12557, Jul 2015.
- [89] A. Acín, A. Andrianov, L. Costa, E. Jané, J. I. Latorre, and R. Tarrach, “Generalized Schmidt decomposition and classification of three-quantum-bit states,” *Phys. Rev. Lett.*, vol. 85, pp. 1560–1563, Aug 2000.
- [90] W. Dür, “Multipartite bound entangled states that violate Bell’s inequality,” *Phys. Rev. Lett.*, vol. 87, p. 230402, Nov 2001.
- [91] O. Gühne, G. Tóth, P. Hyllus, and H. J. Briegel, “Bell inequalities for graph states,” *Phys. Rev. Lett.*, vol. 95, p. 120405, Sep 2005.
- [92] M. S. Williamson, L. Heaney, and W. Son, “Violation of multipartite Bell inequalities with classical subsystems via operationally local transformations,” *Phys. Rev. A*, vol. 82, p. 032105, Sep 2010.
- [93] V. Scarani, A. Acín, E. Schenck, and M. Aspelmeyer, “Nonlocality of cluster states of qubits,” *Phys. Rev. A*, vol. 71, p. 042325, Apr 2005.
- [94] M. Krenn, M. Huber, R. Fickler, R. Lapkiewicz, S. Ramelow, and A. Zeilinger, “Generation and confirmation of a (100x100)-dimensional entangled quantum system,” *Proc. Natl. Acad. Sci.*, vol. 111, pp. 6243–6247, Mar 2014.
- [95] Y. Guo, X.-M. Hu, B.-H. Liu, Y.-F. Huang, C.-F. Li, and G.-C. Guo, “Experimental witness of genuine high-dimensional entanglement,” *Phys. Rev. A*, vol. 97, p. 062309, Jun 2018.

- [96] L. Knips, C. Schwemmer, N. Klein, M. Wieśniak, and H. Weinfurter, “Multipartite entanglement detection with minimal effort,” *Phys. Rev. Lett.*, vol. 117, p. 210504, Nov 2016.
- [97] S. Schauer, M. Huber, and B. C. Hiesmayr, “Experimentally feasible security check for  $n$ -qubit quantum secret sharing,” *Phys. Rev. A*, vol. 82, p. 062311, Dec 2010.
- [98] H. J. Briegel and R. Raussendorf, “Persistent entanglement in arrays of interacting particles,” *Phys. Rev. Lett.*, vol. 86, pp. 910–913, Jan 2001.
- [99] W. Dür, G. Vidal, and J. I. Cirac, “Three qubits can be entangled in two inequivalent ways,” *Phys. Rev. A*, vol. 62, p. 062314, Nov 2000.
- [100] S. Wu and Y. Zhang, “Multipartite pure-state entanglement and the generalized Greenberger-Horne-Zeilinger states,” *Phys. Rev. A*, vol. 63, p. 012308, Dec 2000.
- [101] D. M. Greenberger, M. A. Horne, A. Shimony, and A. Zeilinger, “Bell’s theorem without inequalities,” *Am. J. Phys.*, vol. 58, no. 12, pp. 1131–1143, 1990.
- [102] P. G. Kwiat, “Hyper-entangled states,” *J. Mod. Opt.*, vol. 44, pp. 2173–2184, Jul 1997.
- [103] J. T. Barreiro, N. K. Langford, N. A. Peters, and P. G. Kwiat, “Generation of hyperentangled photon pairs,” *Phys. Rev. Lett.*, vol. 95, p. 260501, Dec 2005.
- [104] X.-H. Li and S. Ghose, “Complete hyperentangled Bell state analysis for polarization and time-bin hyperentanglement,” *Opt. Express*, vol. 24, pp. 18388–18398, Aug 2016.
- [105] M. Fiorentino and F. N. C. Wong, “Deterministic controlled-not gate for single-photon two-qubit quantum logic,” *Phys. Rev. Lett.*, vol. 93, p. 070502, Aug 2004.
- [106] C. H. Bennett, D. P. DiVincenzo, P. W. Shor, J. A. Smolin, B. M. Terhal, and W. K. Wootters, “Remote state preparation,” *Phys. Rev. Lett.*, vol. 87, p. 077902, Jul 2001.
- [107] J. T. Barreiro, T.-C. Wei, and P. G. Kwiat, “Beating the channel capacity limit for linear photonic superdense coding,” *Nat. Phys.*, vol. 4, pp. 282–286, Mar 2008.

- [108] H. Takesue and Y. Noguchi, “Implementation of quantum state tomography for time-bin entangled photon pairs,” *Opt. Express*, vol. 17, pp. 10976–10989, Jun 2009.
- [109] R. T. Thew, K. Nemoto, A. G. White, and W. J. Munro, “Qudit quantum-state tomography,” *Phys. Rev. A*, vol. 66, p. 012303, Jul 2002.
- [110] P. Walther, K. J. Resch, T. Rudolph, E. Schenck, H. Weinfurter, V. Vedral, M. Aspelmeyer, and A. Zeilinger, “Experimental one-way quantum computing,” *Nature*, vol. 434, pp. 169–176, Mar 2005.
- [111] Y. Tokunaga, S. Kuwashiro, T. Yamamoto, M. Koashi, and N. Imoto, “Generation of high-fidelity four-photon cluster state and quantum-domain demonstration of one-way quantum computing,” *Phys. Rev. Lett.*, vol. 100, p. 210501, May 2008.
- [112] X. Zou and W. Mathis, “Generating a four-photon polarization-entangled cluster state,” *Phys. Rev. A*, vol. 71, p. 032308, Mar 2005.
- [113] M. Bourennane, M. Eibl, C. Kurtsiefer, S. Gaertner, H. Weinfurter, O. Gühne, P. Hyllus, D. Bruß, M. Lewenstein, and A. Sanpera, “Experimental detection of multipartite entanglement using witness operators,” *Phys. Rev. Lett.*, vol. 92, p. 087902, Feb 2004.
- [114] D. L. Zhou, B. Zeng, Z. Xu, and C. P. Sun, “Quantum computation based on d-level cluster state,” *Phys. Rev. A*, vol. 68, p. 062303, Dec 2003.
- [115] C. Schmid, N. Kiesel, W. Wieczorek, and H. Weinfurter, “The entanglement of the four-photon cluster state,” *New J. Phys.*, vol. 9, pp. 236–236, Jul 2007.
- [116] O. Gühne and G. Tóth, “Entanglement detection,” *Physics Reports*, vol. 474, no. 1, pp. 1 – 75, 2009.
- [117] R. Raussendorf, D. E. Browne, and H. J. Briegel, “Measurement-based quantum computation on cluster states,” *Phys. Rev. A*, vol. 68, p. 022312, Aug 2003.
- [118] M. A. Nielsen and C. M. Dawson, “Fault-tolerant quantum computation with cluster states,” *Phys. Rev. A*, vol. 71, p. 042323, Apr 2005.

- [119] E. Knill, R. Laflamme, and G. J. Milburn, “A scheme for efficient quantum computation with linear optics,” *Nature*, vol. 409, pp. 46–52, Jan 2001.
- [120] R. Prevedel, P. Walther, F. Tiefenbacher, P. Böhi, R. Kaltenbaek, T. Jennewein, and A. Zeilinger, “High-speed linear optics quantum computing using active feed-forward,” *Nature*, vol. 445, pp. 65–69, Jan 2007.
- [121] P. Kok, W. J. Munro, K. Nemoto, T. C. Ralph, J. P. Dowling, and G. J. Milburn, “Linear optical quantum computing with photonic qubits,” *Rev. Mod. Phys.*, vol. 79, pp. 135–174, Jan 2007.
- [122] P. Walther, M. Aspelmeyer, K. J. Resch, and A. Zeilinger, “Experimental violation of a cluster state Bell inequality,” *Phys. Rev. Lett.*, vol. 95, p. 020403, Jul 2005.
- [123] B. M. Terhal, “Bell inequalities and the separability criterion,” *Physics Letters A*, vol. 271, pp. 319 – 326, Jul 2000.
- [124] M. Lewenstein, B. Kraus, J. I. Cirac, and P. Horodecki, “Optimization of entanglement witnesses,” *Phys. Rev. A*, vol. 62, p. 052310, Oct 2000.
- [125] D. Bruss, J. I. Cirac, P. Horodecki, F. Hulpke, B. Kraus, M. Lewenstein, and A. Sanpera, “Reflections upon separability and distillability,” *Journal of Modern Optics*, vol. 49, pp. 1399–1418, Dec 2002.
- [126] A. Dutta, J. Ryu, W. Laskowski, and M. Żukowski, “Entanglement criteria for noise resistance of two-qudit states,” *Physics Letters A*, vol. 380, pp. 2191 – 2199, Jun 2016.
- [127] D. Kaszlikowski, L. C. Kwek, J.-L. Chen, M. Żukowski, and C. H. Oh, “Clauser-Horne inequality for three-state systems,” *Phys. Rev. A*, vol. 65, p. 032118, Feb 2002.
- [128] D. J. Saunders, A. J. Bennet, C. Branciard, and G. J. Pryde, “Experimental demonstration of nonbilocal quantum correlations,” *Science Advances*, vol. 3, Apr 2017.
- [129] A. Pe’er, B. Dayan, A. A. Friesem, and Y. Silberberg, “Temporal shaping of entangled photons,” *Phys. Rev. Lett.*, vol. 94, p. 073601, Feb 2005.

- [130] C. Bernhard, B. Bessire, T. Feurer, and A. Stefanov, “Shaping frequency-entangled qudits,” *Phys. Rev. A*, vol. 88, p. 032322, Sep 2013.
- [131] M. Ferrera, L. Razzari, D. Duchesne, R. Morandotti, Z. Yang, M. Liscidini, J. E. Sipe, S. Chu, B. E. Little, and D. J. Moss, “Low-power continuous-wave nonlinear optics in doped silica glass integrated waveguide structures,” *Nature Photonics*, vol. 2, p. 737, Nov 2008.
- [132] P. Roztockii, M. Kues, C. Reimer, B. Wetzal, S. Sciara, Y. Zhang, A. Cino, B. E. Little, S. T. Chu, D. J. Moss, and R. Morandotti, “Practical system for the generation of pulsed quantum frequency combs,” *Opt. Express*, vol. 25, pp. 18940–18949, Aug 2017.
- [133] A. Christ, K. Laiho, A. Eckstein, K. N. Cassemiro, and C. Silberhorn, “Probing multimode squeezing with correlation functions,” *New J. Phys.*, vol. 13, p. 033027, Mar 2011.
- [134] M. Förtsch, J. U. Fürst, C. Wittmann, D. Strekalov, A. Aiello, M. V. Chekhova, C. Silberhorn, G. Leuchs, and C. Marquardt, “A versatile source of single photons for quantum information processing,” *Nat. Commun.*, vol. 4, p. 1818, May 2013.
- [135] L. G. Helt, Z. Yang, M. Liscidini, and J. E. Sipe, “Spontaneous four-wave mixing in microring resonators,” *Opt. Lett.*, vol. 35, pp. 3006–3008, Sep 2010.
- [136] I. A. Walmsley and M. G. Raymer, “Toward quantum-information processing with photons,” *Science*, vol. 307, pp. 1733–1734, Mar 2005.
- [137] C. Finot, “40-ghz photonic waveform generator by linear shaping of four spectral sidebands,” *Opt. Lett.*, vol. 40, pp. 1422–1425, Apr 2015.
- [138] A. V. Oppenheim, A. S. Willsky, and S. H. Nawab, *Signals & systems*. Prentice Hall Signal Processing Series, 1997.
- [139] M. Karpinski, M. Jachura, L. J. Wright, and B. J. Smith, “Bandwidth manipulation of quantum light by an electro-optic time lens,” *Nat. Photonics*, vol. 11, pp. 53–57, Nov 2016.

- [140] P. Kumar and A. Prabhakar, “Evolution of quantum states in an electro-optic phase modulator,” *IEEE Journal of Quantum Electronics*, vol. 45, pp. 149–156, Feb 2009.
- [141] J. Capmany and C. R. Fernández-Pousa, “Quantum model for electro-optical phase modulation,” *J. Opt. Soc. Am. B*, vol. 27, pp. A119–A129, Jun 2010.
- [142] Y. Xuan, Y. Liu, L. T. Varghese, A. J. Metcalf, X. Xue, P.-H. Wang, K. Han, J. A. Jaramillo-Villegas, A. A. Noman, C. Wang, S. Kim, M. Teng, Y. J. Lee, B. Niu, L. Fan, J. Wang, D. E. Leaird, A. M. Weiner, and M. Qi, “High-Q silicon nitride microresonators exhibiting low-power frequency comb initiation,” *Optica*, vol. 3, pp. 1171–1180, Nov 2016.
- [143] P. Imany, J. A. Jaramillo-Villegas, O. D. Odele, K. Han, M. Qi, D. E. Leaird, and A. M. Weiner, “Demonstration of frequency-bin entanglement in an integrated optical microresonator,” *Conference on Lasers and Electro-Optics*, p. JTh5B.3, 2017.
- [144] C.-Y. Lu, X.-Q. Zhou, O. Gühne, W.-B. Gao, J. Zhang, Z.-S. Yuan, A. Goebel, T. Yang, and J.-W. Pan, “Experimental entanglement of six photons in graph states,” *Nat. Phys.*, vol. 3, pp. 91–95, Jan 2007.
- [145] R. Ceccarelli, G. Vallone, F. De Martini, P. Mataloni, and A. Cabello, “Experimental entanglement and nonlocality of a two-photon six-qubit cluster state,” *Phys. Rev. Lett.*, vol. 103, p. 160401, Oct 2009.
- [146] X.-C. Yao, T.-X. Wang, H.-Z. Chen, W.-B. Gao, A. G. Fowler, R. Raussendorf, Z.-B. Chen, N.-L. Liu, C.-Y. Lu, Y.-J. Deng, Y.-A. Chen, and J.-W. Pan, “Experimental demonstration of topological error correction,” *Nature*, vol. 482, pp. 489–494, Feb 2015.
- [147] M. P. A. Branderhorst, J. Nunn, I. A. Walmsley, and R. L. Kosut, “Simplified quantum process tomography,” *New J. Phys.*, vol. 11, p. 115010, Nov 2009.
- [148] K. Życzkowski, P. Horodecki, A. Sanpera, and M. Lewenstein, “Volume of the set of separable states,” *Phys. Rev. A*, vol. 58, pp. 883–892, Aug 1998.
- [149] G. Weihs, M. Reck, H. Weinfurter, and A. Zeilinger, “All-fiber three-path mach-zehnder interferometer,” *Opt. Lett.*, vol. 21, pp. 302–304, Feb 1996.

- [150] J. Bavaresco, N. H. Ferrera, C. Klöckl, M. Pivoluska, P. Erker, N. Friis, M. Malik, and M. Huber, “Measurements in two bases are sufficient for certifying high-dimensional entanglement,” *Nat. Phys.*, pp. 1032–1037, Jul 2018.
- [151] M. Gell-Mann, “Symmetries of baryons and mesons,” *Phys. Rev.*, vol. 125, pp. 1067–1084, Feb 1962.
- [152] M. A. Ciampini, A. Orioux, S. Paesani, F. Sciarrino, G. Corrielli, A. Crespi, R. Ramponi, R. Osellame, and P. Mataloni, “Path-polarization hyperentangled and cluster states of photons on a chip,” *Light: Science & Applications*, vol. 5, p. e16064, Apr 2016.
- [153] Y. Soudagar, F. Bussi eres, G. Berl ın, S. Lacroix, J. M. Fernandez, and N. Godbout, “Cluster-state quantum computing in optical fibers,” *J. Opt. Soc. Am. B*, vol. 24, pp. 226–230, Feb 2007.
- [154] S. Loranger, V. Karpov, G. W. Schinn, and R. Kashyap, “Single-frequency low-threshold linearly polarized DFB Raman fiber lasers,” *Opt. Lett.*, vol. 42, pp. 3864–3867, Oct 2017.
- [155] P. Roztockı, C. Reimer, M. Kues, R. Helsten, Y. Jestin, and R. Morandotti, “System and method for phase-readout and active stabilization of optical interferometers,” Jun 2016. US20180180401A1.
- [156] X.-L. Wang, Y.-H. Luo, H.-L. Huang, M.-C. Chen, Z.-E. Su, C. Liu, C. Chen, W. Li, Y.-Q. Fang, X. Jiang, J. Zhang, L. Li, N.-L. Liu, C.-Y. Lu, and J.-W. Pan, “18-qubit entanglement with six photons’ three degrees of freedom,” *Phys. Rev. Lett.*, vol. 120, p. 260502, Jun 2018.
- [157] D. Alsina, A. Cervera, D. Goyeneche, J. I. Latorre, and K. Życzkowski, “Operational approach to Bell inequalities: application to qutrits,” *Phys. Rev. A*, vol. 94, p. 032102, Sep 2016.
- [158] G. Tóth and O. G uhne, “Detecting genuine multipartite entanglement with two local measurements,” *Phys. Rev. Lett.*, vol. 94, p. 060501, Feb 2005.
- [159] J. E. G. Farina, “Variance and covariance in quantum mechanics and the spreading of position probability,” *Int. J. Theor. Phys.*, vol. 21, pp. 83–103, Feb 1982.

- [160] R. Feynman, R. Leighton, and M. Sands, *The Feynman lectures on physics*. Addison–Wesley, 1965.
- [161] C. Cohen-Tannoudji, D. Bernard, and L. Frank, *Quantum mechanics*. John Wiley and Sons, 1977.